Dipl.-Ing. Bernhard Müller, BSc.

Fluoroionophores for Optical Ion Sensing – From Synthesis to Applications

DISSERTATION

zur Erlangung des akademischen Grades

Doktor der technischen Wissenschaften

eingereicht an der

Technischen Universität Graz

Betreuer

Univ.-Prof. Dipl.-Chem. Dr.rer.nat. Ingo Klimant

Institut für Analytische Chemie und Lebensmittelchemie
Technische Universität Graz

Graz, Juli 2017

EIDESSTATTLICHE ERKLÄRUNG

Ich erkläre an Eides statt, dass ich die vorliegende Arbeit selbstständig verfasst, andere als die angegebenen Quellen/Hilfsmittel nicht benutzt, und die den benutzten Quellen wörtlich und inhaltlich entnommenen Stellen als solche kenntlich gemacht habe. Das in TUGRAZonline hochgeladene Textdokument ist mit der vorliegenden Dissertation identisch.

Datum

Unterschrift

Acknowledgement

It is difficult to write this acknowledgment because I have to sum up in a few sentences not only three of my best years, but also my last nine years in Graz before my new life chapter begins. There are so many people who made walking to Uni every day feel not like work but like visiting friends and I want to try to thank all people who helped making the time unforgettable for me.

I am grateful to my supervisor Ingo Klimant for giving me the opportunity to work in this environment and to give me the opportunity to work on this topic. Thank you Ingo for guiding me throughout this thesis and for teaching me how to be a good researcher, but also for all the freedom and trust you gave me in my work.

Sergey you are the best supervisor I could ever imagine. You always had time and were always present if I had questions or troubles. It is the dream for a PhD student to always have somebody with your expertise, motivation and enthusiasm around him.

Gü, thank you for getting me into the SCHeMA Project and thank you for supervising me in the first year. I learned more from you than you would probably think. No matter how the project went, I will always have that year in good memory and I still continue to learn from you in all other aspects of life.

Christoph, without you I would not have a thesis. We started together at the Institute in 2013 and I think there is not one experiment that we haven't discussed together since then. You just always helped me with everything at any time.

David, thank you for choosing ACFC! I am so happy that I could work with you in this group and I am so proud of you and how you manage things here. I hope we will have a lot of future Posaune Beers in our lives.

Martin, you became one of my best friends over the last years and I could always complain about everything with you. Your amazing politeness and creative expressiveness made every day a highlight.

A big thank you to my office. Fips, Heidi and Silvia, you all have the strongest nerves to endure my moods. Silvia and Heidi you had always an open ear for me to listen to my complaints. Fips, I am always impressed by how you deal with all kind

of situations and I still try to learn from you. With you in the office I always feel like I am working on a construction site.

A special thanks goes to my master students Luki, Tanja and Nici. Although I had to learn a lot concerning my supervising skills, you were sufficiently patient and kept being motivated even when my instructions were confusing.

Additionally, I want to thank my bachelor/project students Bianca, Seppi, Luki, Beate and Christian for helping me in the lab. I hope you learned something other than my chaotic way to work.

I have to thank all other people in the Institute for so many good memories. Thank you for all the Dachterrassen beers and coffees, for all the food, for all the activities (cross-country skiing, hiking, ice-hockey, Christmas parties, Institute parties, Fasching, conferences, ASCOS). I enjoyed all the discussion of topics with different levels of sophistication and you all made it to the best place to work. Thank you Eveline for always listening and getting stuff done. Thank you also Ulli and Klaus for opening Tintenfass to give our group a second social room.

Also, I want to thank people from other Institutes and Unis for having discussions together or helping with measurements. A big thanks to Dr. Ruslan Dmitriev from University College Cork for starting a collaboration, for teaching me basic skills in cell culturing and for showing me around in Ireland.

Thank you Marko, Manuel, and David for all the help in the synthesis parts of my thesis and frustration beers when I needed them. Thank you Gill for correcting all my writing stuff and for motivating me in the last months of the thesis.

Additionally, I have to thank all my close 08er friends for everything in the last years. For all the travelling together but also for the visits in Graz. With you it was possible to talk about work but also to forget about it. Thank you Maria for supporting me in my decisions at the beginning of the thesis.

Am meisten möchte ich mich bei meiner Familie bedanken. Bei meinen Eltern, dass sie mich meinen Weg haben gehen lassen und mich immer unterstützt haben. Sandra – du hast schon mehr erreicht und erlebt in deinem Leben als ich es jemals werde. Ich bin stolz auf dich und deine junge Familie und du wirst immer mein Vorbild bleiben und möchte dir diese Arbeit widmen.

Abstract

In this thesis, novel sensors for the measurement of cations are presented. The sensors are based on fluorescent molecules (fluoroionophores) which change their spectral properties upon interaction with ions. Fluoroionophores consist of two building blocks: the receptor and the chromophore. The receptor is based on an aza-crown ether which acts as the recognition unit for cations and can quench the fluorescence of the chromophore by photoinduced electron transfer (PET). Upon interaction with ions, this PET is inhibited leading to an increase of fluorescence which is determined by the chromophore. Both building blocks of the fluoroionophore can be independently modified leading to a modular design of new sensing molecules. The versatility of this concept is demonstrated by preparation of new BODIPY dyes with adjusted photophysical properties (green to red excitation, red to NIR emission) and diverse crown-ethers, capable of sensing a variety of analytes (e.g. Na^+, K^+).

Immobilisation of the fluoroionophores could be achieved by physically entrapping them in various hydrogel matrices and polymer based nanoparticles. This yields in robust and high performance sensing materials, which are capable of the continuous measurement of clinically important analytes such as K^+ or Na^+. Moreover, we were also able to develop an innovative new sensing method for the selective measurement of highly toxic NH_3.

Finally, practical applicability of the new sensors is exemplified by measurement of K^+ in serum, determination of seawater salinity using Na^+ Optodes and visualisation of K^+ fluxes in live cell imaging, making them valuable new analytical tools in clinical diagnostics, marine research and life sciences.

Kurzfassung

In dieser Arbeit werden neuartige Sensormaterialien für die Messung von Kationen präsentiert. Diese Sensoren bestehen aus fluoreszierenden Molekülen (Fluoroionophore), welche bei Interaktion mit einem Ion ihre optischen Eigenschaften verändern. Die Fluoroionophore bestehen aus zwei Einheiten: dem Rezeptor und dem Farbstoff. Die Basis des Rezeptors bildet ein aza-Kronenether, der einerseits als Erkennungselement für Kationen dient, sowie andererseits verantwortlich für die Löschung der Fluoreszenz des Farbstoffes durch den photoinduced electron transfer (PET-) Effekt ist.

Die Interaktion des Rezeptors mit einem Kation hebt den PET-Effekt auf und führt zu einer Steigerung der Fluoreszenz, welche durch die Farbstoffeinheit gesteuert wird. Beide Einheiten der Fluoroionophore können unabhängig voneinander modifiziert werden, welches zu einem modularen Design neuer Indikatoren führt. Die Vielseitigkeit dieses Konzepts konnte durch die Herstellung verschiedener BODIPY Farbstoff demonstriert werden, wobei die photo-physikalischen Eigenschaften (grüne bis rote Anregung, rote bis nahinfrarote Fluoreszenz) eingestellt und die Sensitivität gegenüber verschiedener Analyten durch den Einsatz unterschiedlicher Kronenether gesteuert werden konnte (z.B. Na^+, K^+).

Durch die Immobilisierung der Fluoroionophore, die durch physikalische Einbettung in verschiedenen Hydrogel Matrizen und Polymer-Nanopartikel erfolgte, konnten neue leistungsfähige Sensormaterialien hergestellt werden. Diese Sensoren ermöglichen das kontinuierliche Messen von klinisch relevanten Parametern wie K^+ oder Na^+. Des Weiteren konnten wir erfolgreich eine neue und innovative Messmethode für die selektive Messung von Ammoniak (NH_3) entwickeln.

Praktische Anwendungsbeispiele der neuen Sensoren konnten durch die Messung von K^+ im Serum, die Bestimmung der Salinität im Meerwasser mittels Na^+-Optoden und durch die Visualisierung von K^+-Strömen in neuronalen Zellen mittels Fluoreszenzmikroskopie demonstriert werden. Die in dieser Arbeit entwickelten Sensoren sind wertvolle und neue analytische Werkzeuge für die vielseitige Anwendung in den Bereichen der klinischen Diagnostik, der Marineforschung und der Biowissenschaften.

Contents

Part I Introduction

Part II Results

Part I

Introduction

1 Scope and Outline of the Thesis

Given the physiological and ecological relevance of metal cations such as sodium (Na^+), potassium (K^+) and calcium (Ca^{2+}), it is not surprising that they belong amongst the most popular targets for the development of new sensors. Even though potentiometric sensors such as ion selective electrodes are well established, fluorescent sensors offer numerous advantages concerning miniaturisation, cost-effectiveness and multi-analyte sensing. Moreover, they enable fluorescence imaging applications which is of major relevance in biomedical research.

Although there are many fluorescent dyes for cation sensing reported, high performance dyes, solid state sensors and real applications are not yet fully developed. The aim of this thesis was to address this and to develop new sensors and sensing concepts based on cation-sensitive fluorescent dyes.

This thesis is written in a cumulative manner and the manuscripts presented are already accepted, under revision or are prepared for submission in peer reviewed journals. Additionally, a preface to the manuscripts will explain the framework of the work and will refer to important section in the theoretical part. Also, it will describe important unsuccessful experiments which led to the positive results presented in the publications afterwards. Future prospect and outlooks after each manuscript will describe follow up work and results, but also present new ideas and concepts for future work.

First, a theoretical background will give a basics knowledge about optical sensing, fluorescence and supramolecular chemistry which is necessary for understanding the concepts dealt with in this thesis.

Chapter 3 (p. 33) presents the foundation of all newly developed sensing materials throughout this thesis. Hereby, a family of new fluoroionophores based on differently substituted BODIPY chromophores and an 18-crown-6 ether as receptor were prepared. The indicators possess tuneable optical properties (green to red excitation, red to NIR emission) and PET efficiencies. By immobilisation of them into biocompatible hydrogel matrices or polymer based nanoparticles we obtained stable and fast responding sensor materials for various applications. This is demonstrated by measurement of K^+ in fetal bovine serum.

Chapter 4 (p. 69) describes the development of a Na^+ sensor. Substituting the 18-crown-6 of the K^+ sensor with a smaller sized 15-crown-5 makes the sensor reversible respond to Na^+ ions in water. Using the same immobilisation concepts as presented in chapter 3, we successfully prepared a referenced sensor (Optode) which was then used in a field trip in Kiel (Germany) to determine seawater salinity.

Chapter 5 (p. 99) demonstrates the applicability of the elaborated nanoparticle based K^+ sensors in collaboration with the University College Cork in Ireland. Together with Dr. Ruslan Dmitriev we were able to show for the first time, that polymeric RL100-based nanoparticles provide efficient staining of primary neural cells (astrocytes and neurons) and 3D tissue cancer and stem cell-based models. Additionally, detailed evaluation of the K^+ nanosensors in quantitative live cell imaging and *in vivo* brain imaging applications were performed.

Chapter 6 (p. 137) introduces a new innovate sensing mechanism for measurement of dissolved ammonia (NH_3). By taking advantage of the acid/base equilibrium between NH_3/NH_4^+ and the ability of the fluoroionophore to complex NH_4^+, we were able to design a highly selective NH_3 sensor over other volatile bases.

Finally, **chapter 7** (p. 153) will present a critical evaluation of the detection of the marine biotoxin Saxitoxin using fluoroionophores. During our work to improve published results, we identified an interfering artefact during measurements and were able to identify a fluorescent degradation product of STX caused by UV illumination. Additionally, a possible new route of STX detection using highly reactive singlet oxygen ($^1O_2$) generated by photosensitizer is presented.

Chapter 3

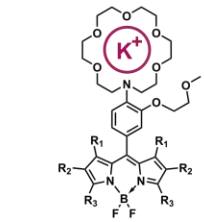

A palette of new BODIPY indicators with crown ether receptors were prepared

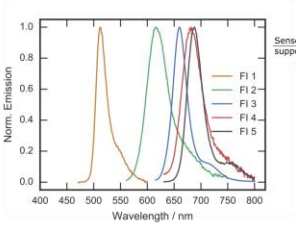

Spectral properties could be tuned by changing structural elements

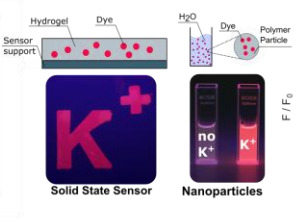

New indicator dyes can be incorporated in various polymeric materials

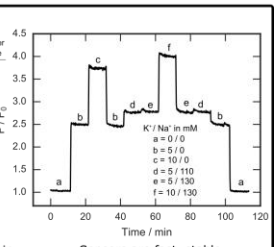

Sensors are fast, stable and highly selective

Chapter 4

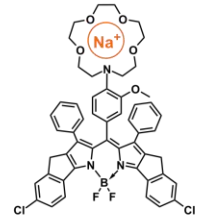

Attaching a smaller crown-ether makes the dye sensitive for Na^+ ions

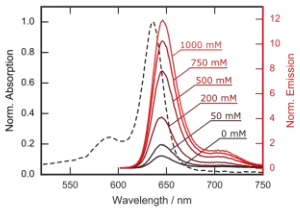

Indicator exhibits red to NIR Fluorescence

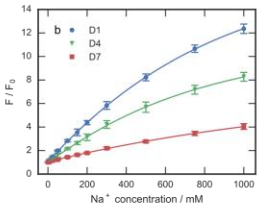

Sensitivity can be controlled by the hydrogel polymer used

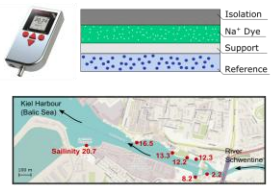

Salinity of the seawater can be measured with the Na^+ Sensor

Chapter 5

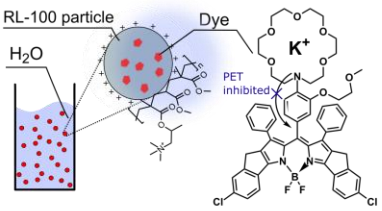

Indicator can be entrapped in water-dispersable nanoparticles

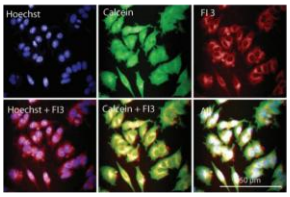

Nanoparticles can be uptaken by different cells

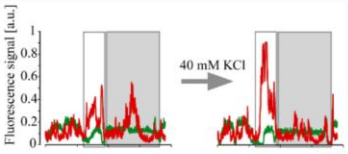

K^+ fluxes can be visualized with fluorescence microscopy

Chapter 6

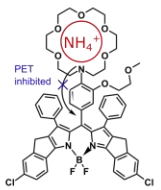

K^+ seletive dye can also complex NH_4^+

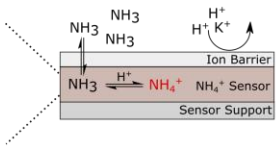

Ion Barrier and internal buffer transforms a K^+ Sensor to a highly selective NH_3 Sensor

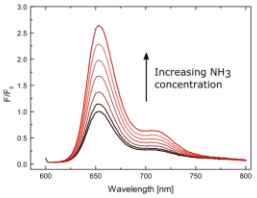

Sensor respsonds to dissolved NH_3

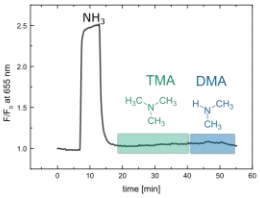

Substituted Amines can not be complexed and do not increase fluorescence

Chapter 7

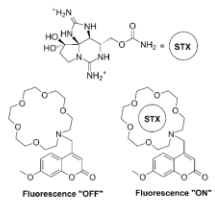

A Saxitoxin Sensor was developed based on reported sensing mechanism

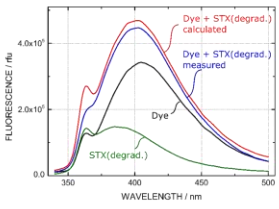

Reproducing literature lead to the finding of a fluorescence artefact

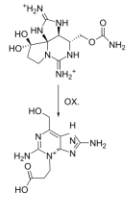

Saxitoxin gets oxidized to a fluorescent product during measurements

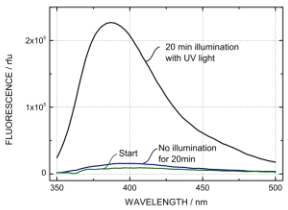

UV light catalyses the oxidation

2 Theoretical Background

2.1 Chemical Sensors

Chemical sensors are miniaturized analytical devices capable of delivering real-time and on-line information on the presence of a specific compound (analyte) in a sample. The typical layout of a chemical sensor is a receptor unit and a transducer unit. The receptor reacts to the presence of the analyte or interacts with the analyte itself and the transducer converts the obtained chemical information into a measurable electrical or optical signal. In recent years, there has been a growing interest in the development of chemical sensors, as they allow for continuous monitoring of various analytes in applications such as industrial processes, environmental monitoring or academia research.[1]

An ideal sensor should fulfil certain criteria:

- Conversion of chemical information to an electrically measurable signal
- Fast and reversible response to the change of the analyte concentration
- High selectivity and sensitivity towards the analyte of interest
- A low-cost small device which is simple to fabricate and is user-friendly
- Good stability both operational and a shelf life

Traditional analytical chemistry involves the manual collection of a sample, transport and the subsequent analysis in a laboratory. This is labour and time intensive, expensive, and can only be performed by qualified personnel. In contrast, a sensor can be brought directly to the sample or to the field and enables immediate measurement. Additionally, tedious sample preparation can be overcome by the use of a sensor. This makes sensors perfect candidates for on-line or in-line monitoring of industrial processes or environmental monitoring over a long period of time, leading to a huge and growing demand for low-cost sensors. In general, sensors take advantage of a wide range of measurement principles and are typically classified by the applied transduction method. In this thesis, there will be a focus on optical sensors which are based on the phenomenon of fluorescence and will be described in more detail. An overview of other methods for ion sensing will additionally cover electrochemical sensors as they represent the state-of-the art technology for ion sensors.

2.2 Optical Chemical Sensors

In an optical sensor, the component responsible for the analyte recognition is called the *receptor*, whereas the component responsible for generating a measurable signal depending on this analyte recognition is called the *transducer*. This transduction can be based on the change of optical proprieties such as refractive index, absorption (infrared or UV-VIS), luminescence or Raman spectroscopy and are comprehensively described in several reviews. [2,3,4,5,6,7,8,9,10]

In the case of luminescent sensors, the sensor typically consists of a light source (e.g. LED), the sensing material and a detector (photodiode) to quantify the received signal. Additional optical elements such as filters are placed between the sensing material and the detector, which can provide different light properties before and after interaction with the sensing material (e.g. wavelength selection). Not all parts are essential for an optical sensor, but generally, optical sensors are based on the measured parameter as an optical signal which is altered by the transducer in the sensing material.[2,11]

A clear advantage of optical sensors over electrical and electrochemical sensors is that they function without the need of a reference electrode. This makes them robust against electromagnetic influences and makes miniaturisation of the sensor possible. For this reasons, optical sensors can be fabricated in various formats ranging from nanoscale (e.g. nanoparticles)[12] to macroscale (e.g. sensor foils for imaging over a big area)[13]. Moreover, as light is used for the transport of information about the analyte, it is possible to separate the sensing unit entirely from the read out unit. As they are physically separated, the requirements for the read-out device are less pronounced when measuring in sterile samples or in applications where elevated temperatures, pressures or chemically aggressive environments can occur.

Some of the significant parameters of an optical sensor are:

- *Selectivity*, meaning that only the analyte of interest should generate a signal in the transducer. This is usually controlled by a receptor.
- *Sensitivity*, which is described as the increase of the generated signal with increasing analyte concentration. This parameter effects further characteristics such as *dynamic range*, *detection limit* and *resolution* of the sensor.

- *Reversibility* is given if the analyte is not consumed by the sensor and the measured signal of the sensor is according to the concentration of the analyte.
- *Response time* of a sensor is typically described as t_{90}, which is the time until 90% of the final signal is obtained. Fast response of a sensor is crucial for real-time analysis.
- *Stability* of the measured signal is highly important for long-term measurements. If the signal changes over time without a change in the analyte concentration, it is called *drift* of the sensor.

2.2.1 Fundamentals of Luminescence

A large number of optical sensors are based on the concept of luminescence. Luminescence is the process of a highly sensitive de-excitation pathway via light emission after the excitation of an electron. All processes occurring during this phenomenon can be visualised by the Jablonski diagram (**Figure 2.1**). Excitation of an electron to a higher electronic energy level usually occurs after absorption of energetically suitable light (suitable wavelength) by the molecule. The electron is then in the excited singlet state (S_1), which is the basis of various subsequent pathways that can occur. The term fluorescence is used when the electron relaxes back to the ground state (S_0) via emission of photons, and occurs approximately nanoseconds after absorption of the light. Phosphorescence, on the other hand, is the relaxation pathway from an excited triplet state (T_1) back to S_0 after the electron changed its spin, which is possible due to spin-orbit coupling. This spin change is called intersystem crossing and is a slow process, therefore phosphorescence lifetimes are usually in the range of microseconds to seconds. Delayed fluorescence is the emission from S_1 to S_0 after ISC to T_1 and a following reverse ISC back to S_1. The emission occurs from the excited singlet state, therefore the spectrum is the same as in normal fluorescence, whereas the lifetime is much longer as ISC occurs two times. This process is highly depending on temperature, therefore delayed fluorescence can be utilized for temperature sensing.

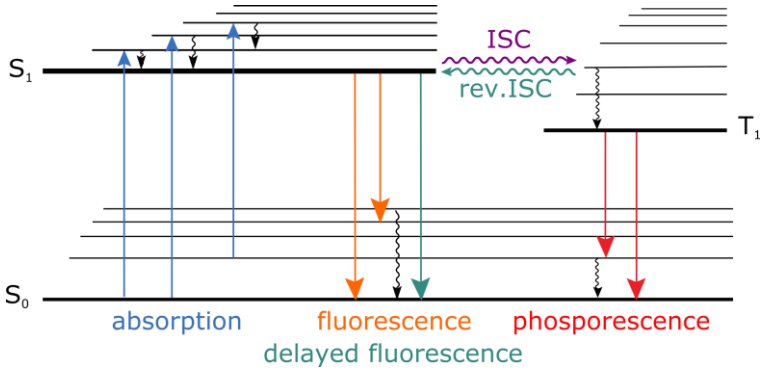

Figure 2.1: Jablonski diagram with the visualisation of absorption, fluorescence and phosphorescence. S_0 and S_1 represent the singlet ground state and the excited state respectively. T_1 represents the excited triplet state. Intersystem crossing (ISC & reversed ISC) is the transition between states of unlike multiplicity.

One of the important terms in luminescence is the *luminescence brightness*, which combines the ability of a molecule to absorb light (*molar absorption coefficient*) and the *quantum yield (QY)*. The latter describes how efficiently the molecule emits photons after excitation, as luminescence always competes with non-radiative de-excitation processes. *Luminescence lifetime* describes the time in which 63 % of the excited electrons relax back to the ground state. *Stokes shift* is the energy difference between the maxima of the absorption and the emission spectra. A change in any of these properties upon interaction with either another compound or with the luminescent dye itself, is called *quenching*. This can be used for the development of optical sensors, as a measurable change in an optical property is generated.[14,15]

In recent years, optical sensors based on luminescent indicator dyes have been receiving more attention. This type of sensor reversibly changes the emission intensity, wavelength or lifetime after interaction with the analyte. Luminescence sensors can utilize both fluorescent and phosphorescent dyes for sensing. Phosphorescent dyes with a typically long-lived excited state (triplet state) can be dynamically quenched by oxygen upon their collision. Immobilisation of these molecules (e.g. metalloporphyrines) into oxygen permeable polymers yields oxygen sensors.[16] In the case of fluorescent indicators, the quenching process can occur via different interactions and will be described in the next section.

2.2.2 Photo Induced Electron Transfer

For fluorescent dyes, quenching can occur via different analyte-indicator interactions. Most commonly, the effect of intramolecular charge transfer (ICT) or photoinduced electron transfer (PET) is used.[17,18,19,20] Attachment of a functional group (PET-group) to the fluorophore results in a redox process between the PET group and the excited chromophore. Typically, an electron is transferred from the PET group to the chromophore and occupies S_0, subsequently inhibiting radiative relaxation via fluorescence ("off"-state) (**Figure 2.2 a**).

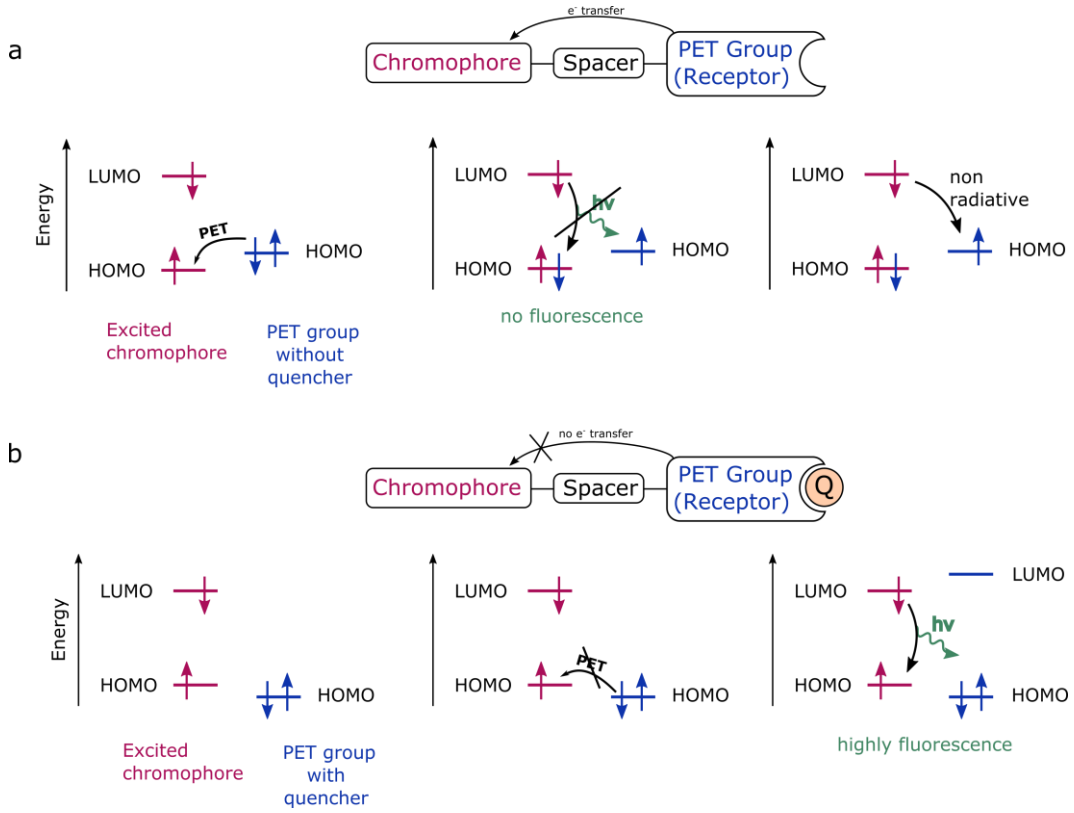

Figure 2.2: (**a**) Schematic illustration of the photoinduced electron transfer (PET) and (**b**) the inhibition of the PET effect due to a binding event with a receptor group and a resulting change in the molecular orbitals of the PET group.

If the free electron pair of the PET group is electronically lowered, PET is no longer possible and fluorescence emission is observed ("on"-sate) (**Figure 2.2 b**).

In most cases a reductive PET effect occurs, although there are few examples where an electron transfer from the fluorophore to the PET group is reported (oxidative

PET).[19] Employed functional groups for PET sensors are mostly amines[21], phenolates[22] or carboxylates[23]. Effective quenching is achieved by the combination of a strong electron-donating PET group with a strong electron-accepting chromophore. Besides having suitable redox potentials for both groups, PET is also more likely in a polar environment, meaning that it can even be used for polarity sensors.[24]

Protonation or deprotonation of a PET group is one of the most commonly used sensing concepts for pH probes. These chromophores can be used as pH probes with a pH sensitivity close to the pK_A value of the PET group.

As the PET can also be inhibited simply by perturbation of the electron pair's environment, the sensing ability of such probes can be extended for other analytes that do not depend on protonation/deprotonation. For instance, aza-crown-ethers can be applied for selective sensing of ions where PET translates the molecular recognition into a measurable fluorescence signal. This will be discussed in more detail in **section 2.4.3**.

PET groups are usually electronically separated from the indicator via a spacer bridge to break the conjugation. Therefore, the excited and ground state of the fluorophore are not affected by PET quenching, leading to a change in emission intensity only, while the shape or wavelength of the absorption and emission spectra are not influenced. Applying such indicators lead to simple "turn-on" - "turn-off" sensor system.

In contrast, probes based on intramolecular charge transfer (ICT) undergo changes in spectral properties (e.g. colour) as the sensitive functional group is in direct contact with the conjugation of the chromophore influencing the HOMO-LUMO levels of the dye.

The development of PET based probes for use in optical sensors is highly versatile. Combining intrinsically insensitive fluorescence dyes with PET groups yields new sensing molecules.[20] This enables a modular design of new indicators, as it is possible to change the spectral properties (chromophore) and sensitivity (PET group) independently. Therefore, sensors with different PET groups but the same chromophore basis can be used for sensing of a variety of different analytes without changing any optical parts of a measurement device. This enables simple multiparameter sensing.

In this thesis, we took advantage of this modularity and developed different fluoroionophores for K^+ sensing and studied the influence of different chromophores (**chapter 3** (p. 33)). Using the most promising chromophore basis and simply exchange of the PET group led to new different sensing materials for Na^+ ions and is described in **chapter 4** (p. 69).

2.3 Host-Guest Chemistry

The key component in optical ion sensors is the receptor, which belongs to a research area called host-guest chemistry. It describes complexes which are formed upon noncovalent binding of two molecules or ions which are held together due to suitable structural relationships.[25] This leads to the concept of molecular recognition which has been successfully applied in the last few decades in catalysis, functional materials, electronic devices, sensors, nanomedicine etc.[26] The host unit is typically an organic molecule that provides binding sites and a cavity, whereas the guest component can be any molecule or ion that fits in this cavity and is in noncovalent interaction with the host. Usually, the host is a highly functional molecule that is designed for a special application and the guest is a simple, abundant compound. An enormous amount of host molecules were developed over the last few decades, including cyclodextrines[27], cyclophanes[28], cucurbiturils[29], pillararenes[30] and crown ethers[31] (**Figure 2.3**).

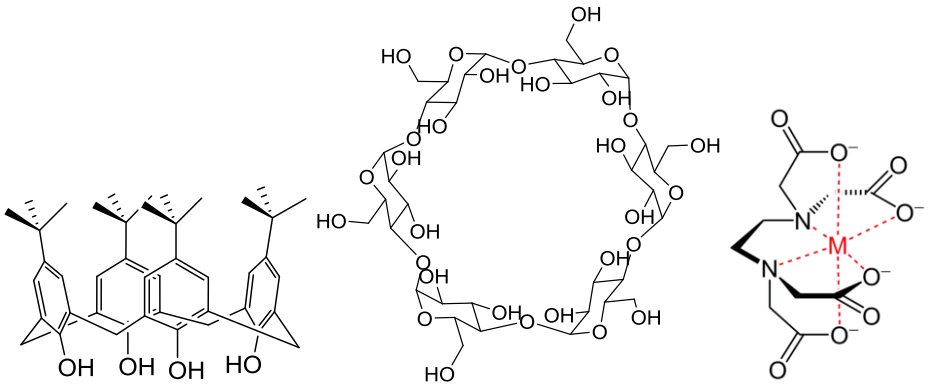

Figure 2.3: Exemplar host molecules. **left:** calixarene **middle:** cyclodextrine **right:** chelator EDTA.

As the complexation is a non-covalent binding event, there is a need for other interactions in order to form a stable complex. This usually includes coulomb interactions if there are charged compounds, Van-der-Waals interactions for non-

charged compounds and hydrogen bonds between guest and host molecules. Another important factor is the solvophobic force, which describes the contribution of the complexation concerning the enthalpy and entropy. Guest molecules are usually solvated, meaning molecules of the solvent surround them. In order to be complexed in the cavity of the host molecule, it must strip off this solvent molecules, which subsequently leads to an increase of entropy ΔS^0. This entropy contributes to the Gibbs free energy and is most pronounced in aqueous solutions. Host-guest complex formation usually shows a decreasing affinity in increasing solvent polarity due to stronger solvation of the host molecule.[32]

The degree of stability of the host-guest complex is expressed by the stability constant (K_S) which is described by the simple equilibrium constant of the host (H) and guest (G) to form the complex (HG) (**Equation 2.1**). The binding constant must be determined for the quantitative analysis of the complex formation. K_S and binding stoichiometry can be determined via titration of the host with the guest molecule through detection of the concentration of the uncomplexed and complexed compounds. This can either be performed by measurement of electrochemical properties such as conductivity or potential[33], but also NMR[34], mass spectrometry[35], and UV-VIS spectroscopy[36] can be applied. As the complexation is always accompanied by a change of the temperature, it is possible to determine the equilibrium constant K and the enthalpy of the complexation (ΔH) using a calorimeter.[37]

$$H + G \rightleftharpoons HG \qquad K_S = \frac{[HG]eq}{[H]eq + [G]eq} \qquad \text{Equation 2.1}$$

Complex binding constants were a key parameter for the critical evaluation of the development of a sensor for the marine biotoxin Saxitoxin, which can be found in **chapter 0** (p. 153).

2.3.1 Crown Ethers and their Derivatives

Crown ethers are the simplest form of host molecules in supramolecular chemistry.[38] They consist of a cyclic repeating ethyleneoxy unit to form crown ethers in various sizes (**Figure 2.4**). As they have hydrophobic (ethylene groups) and hydrophilic (heteroatoms such as oxygen) structural elements, they behave in aqueous solution similar to a fat droplet in water. Moreover, as they possess high

flexibility in their molecular backbone, they can act reversibly in lipophilic media (e.g. water droplet in oil). This hydrophilic interior of the crown ether is ideally suited for interactions with alkali cations.[39] Upon complexation, crown ethers form a two-dimensional complex where the oxygen atoms donate a fraction of their electron density to the alkali cation, which is electron deficient. There is an enormous variety of crown ether structures and derivatives, with different distribution, quantity and types of donor-heteroatoms (e.g. sulphur or nitrogen instead of oxygen atoms).

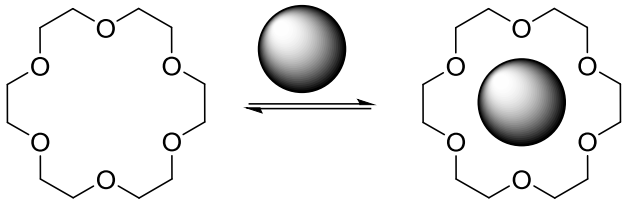

Figure 2.4: 18-crown-6 ether which is usually used for complexation of K^+ ions.

Cryptands have a three-dimensional structure and additional oxygen atoms for complexation (**Figure 2.5**). Due to their multi-dentate nature, cryptands usually show a better selectivity and a higher strength of binding compared to crown ethers. They typically consist of two bridge-head nitrogen atoms which are connected via additional ethyleneoxy units in order to obtain a bicyclic ligand (**Figure 2.5**).

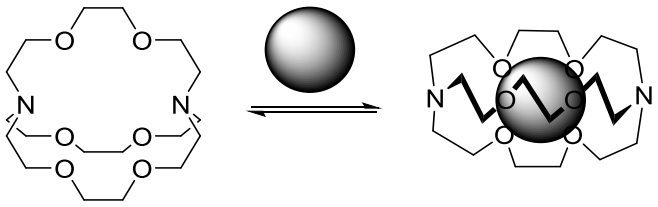

Figure 2.5: Exemplar cryptand ether. The additional "bridge" ligand additionally complexes an alkali ion.

Lariat ethers are a blend of crowns and cryptands. They exhibit the three-dimensionality of cryptands which leads to a better complexation, but still have fast complexation behaviour like normal crown ethers.[40] Upon encapsulation of

the ion, the side arm can fold and contribute as a donor to the macro ring and therefore stabilize the guest (**Figure 2.6**).

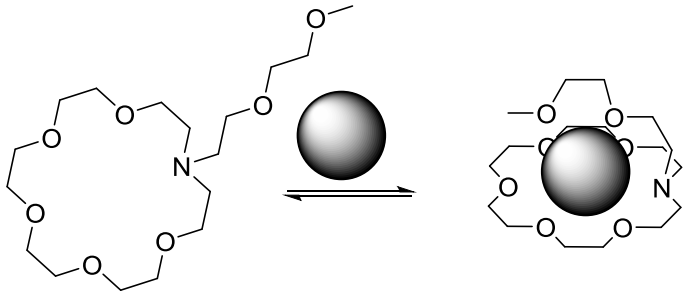

Figure 2.6: Lariat ether with additional arm to enhance complexation stability.

2.3.2 Hole-Size Fitting Concept

The high selectivity for cations is mainly caused by the "hole-size fitting concept" which describes the relationship between the "naked" cation diameter and the size of the crown cavity.[25] If the de-solvated ion is too big or too small for the cavity, it will not have optimal interaction with the host heteroatoms and therefore insufficient electronic interaction to stabilize the guest. Consequently, complex stability constants confirm that there is a relationship between the size and the stability of complexation.[41] Comparison of ion and cavity diameter indicates which crown ether will have the highest interaction and stability with the ion (**Figure 2.7** and **Table 2.1**). However, affinity and selectivity towards certain ions cannot be fully and satisfactorily explained by this concept as complexation is dependent on a variety of different factors, as mentioned previously.[42] Additionally, it is possible for crown ethers to form "sandwich" or "double decker" complexes with a 2:1 stoichiometry in order to enhance the stability of the complexation if the host and guest do not have suitable sizes.[43]

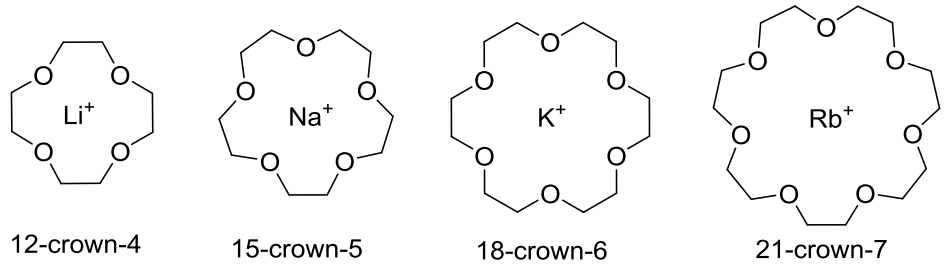

Figure 2.7: Crown ethers with different sizes.

Table 2.1. Crown ether ring sizes and ionic diameters.[44]

Cation	Cation diameter / Å
Li^+	1.36
Na^+	1.90
K^+	2.66
NH_4^+	2.68
Rb^+	2.94
Cs^+	3.38

Crown ether	Cavity diameter / Å
12-crown-4	1.2 - 1.5
15-crown-5	1.7 - 2.2
18-crown-6	2.6 - 3.2
21-crown7	3.4 - 4.3

By applying different sized crown ethers the selectivity towards an analyte ion is changed. As we successfully developed a sensor for K^+ ions (**chapter 3** (p 33)), we were able to prepare Na^+ sensitive materials by simply decreasing the size of the crown ether receptor (**chapter 4** (p. 69)). Additionally, **Table 2.1** shows that the sizes of K^+ and NH_4^+ ions are almost similar and that both would be efficiently complexed by the same receptor. This was the basis for the development of a novel ammonia sensor, presented in **chapter 6** (p. 137).

2.4 Concepts of Ion Sensors

2.4.1 Ion Selective Electrodes (ISE)

Among various classes of chemical sensors, ion-selective electrodes (ISE) are one of the most frequently used potentiometric sensors. The necessary equipment required

for measurements include an ion selective electrode, a reference electrode and a potential-measuring device (**Figure 2.8**). The ion selective electrode is the indicator electrode, which is based on a membrane that interacts selectively with the analyte and yields a change in the membrane potential. As this potential cannot be measured directly, a reference electrode is required, which provides a highly stable potential. Comparison of the detected potential of the ion selective electrode to the reference electrode determines a net potential, which is directly proportional of the activity of the selected ion. The relationship between the activity and the electrode potential can be described by the Nernst equation (**Equation 2.2**).[45,46]

$$E = E^0 - \frac{R \cdot T}{n \cdot F} \cdot \ln(a_i) \qquad \text{Equation 2.2}$$

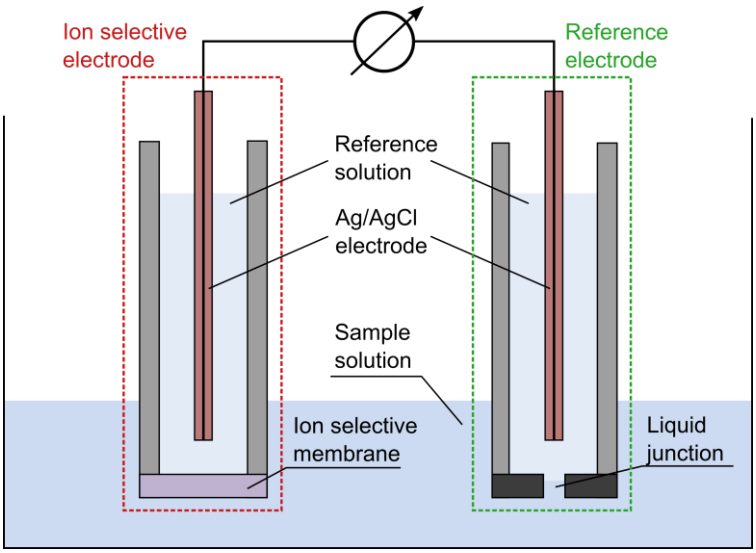

Figure 2.8: Functioning principle of an ion selective electrode (ISE). A reference electrode provides a stable potential whilst the ion selective electrode changes its potential due to the activity of a specific ion in the sample solution with the ion selective membrane.

The membrane is the key component for potentiometric ion measurements. Depending on the analyte of interest, different membranes must be used, as this determines the selectivity of the sensing material. The three main membrane types can be divided into glass, crystalline and liquid membranes.[47]

Glass membrane electrodes consist of an ion-exchange glass which is selective for monovalent ions such as H^+ or Na^+. Typically, these glasses are based on silicate

with different additions of metal oxides (e.g. Na, K, Li, Al) or chalcogenide matrices based on a network of AsS, AsSe or AsTe in order to enhance the selectivity of the membrane. Their main application is the determination of pH.

Crystalline electrodes are typically made of mono- or polycrystallites of a single compound where only the analyte can incorporate into the crystal structure, leading to a high selectivity. The use of Ag-crystals makes them suitable candidates for measuring anions such as Cl^-, Br^-, or I^-. The most commonly used membrane is based on LaF_3 crystals which can selectively measure F^- ions.

Liquid membrane electrodes are the most widespread electrodes for ion selective sensing.[48,49] The essential part of this electrode is an ion-sensitive polymer membrane placed between the sample solution and an inner reference solution. The polymer membrane incorporates a neutral or charged compound (host molecule) which can complex ions as described in **section 2.3**. Moreover, the host molecule (ionophore) must be capable of complexing the intended ion selectively and reversibly to obtain a sensing material. Typical polymer membranes consist of poly(vinylchloride) (PVC) with a high amount of plasticizer (dioctyl sebacate (DOS)) to ensure mobility of both the complexed and free ionophore inside the membrane. The diffusion coefficient in such membranes is similarly high as that in liquid phases and is therefore sometimes referred to as "solid liquid phase membrane".

Ions in the sample solution are extracted into the boundary layer of the PVC membrane, where they accumulate and cause a potential difference between the inner reference solution and the outer sample solution (**Figure 2.9**). As the selectivity of those electrodes is dependent on the ionophore used, it is possible to design ISEs for a wide variety of cations and anions, both monovalent and bivalent. Commercially available ISEs based on this membrane type are available for K^+, Na^+, NH_4^+, Ca^{2+}, Mg^{2+}, etc. and are commonly used in clinical diagnostics.[50,51]

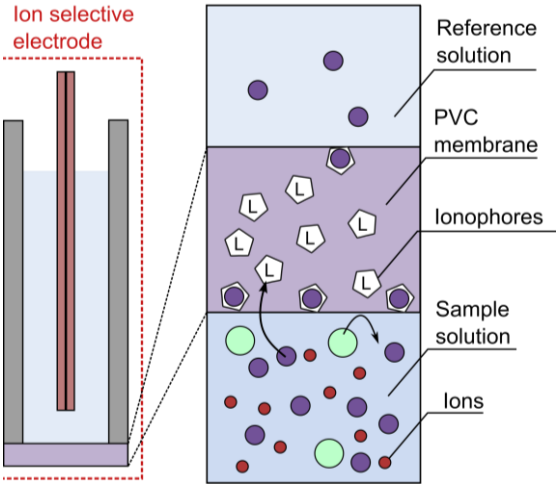

Figure 2.9: Schematic working principle of a liquid membrane based ion selective electrode. A membrane containing an ionophore extracts the ion of interest from the sample solution to the boundary layer of a polymer membrane where it causes a potential difference.

As the ISE measures the activity of the ion, it is highly dependent on the ionic strength of the solution. Therefore, it is necessary to adjust the salinity to a high ionic strength using a TISAB (total ionic strength adjustment buffer) to mask minor changes of the ionic strength. Additionally, the electrode can be fragile, have a limited shelf life and cannot be miniaturised down to the nanoscale due to the dimensions of the electrodes. The reference electrode is prone to drift as the junction potential can change over time. Optical sensors can overcome these limitations and will be described in the following sections.

2.4.2 Ionophore Based Optical Sensors (IBOS)

The working principle of ionophore based optical sensors is similar to ISEs. Both use a solid liquid phase membrane (PVC/DOS) with an incorporated ionophore that selectively and reversible binds the intended ions. At the ion selective electrode, interaction of the ion and the ionophore happens on the surface of the membrane and therefore develops a potential difference between an inner reference solution and an outer sample solution. Inside the membrane, a change in any component's concentration does not occur. In contrast, in IBOS a signal change cannot be induced by a surface interaction, but with a change in the concentration of one component inside the polymer matrix (inside the bulk) (**Figure 2.10**). Hereby, recognition is accomplished by the ionophore and an optical signal is obtained by a lipophilic pH indicator which is also immobilized in the PVC matrix. Complexation of an analyte is accompanied by a competitive ion exchange or a carrier-mediated co-extraction to

keep electro-neutrality inside the membrane. This leads to a change in the protonation degree of the pH indicator which acts as the transducer. Therefore, a change in optical signal (absorption or fluorescence emission) can be detected.[52]

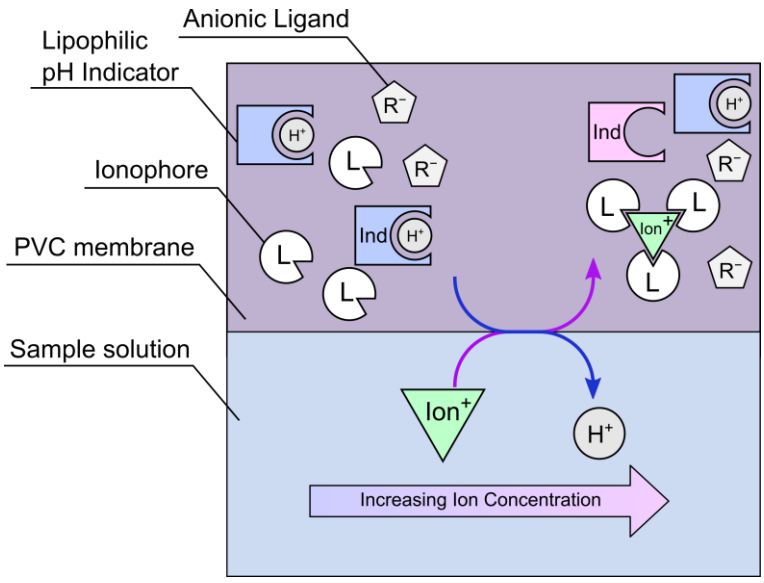

Figure 2.10: Schematic working principle of an ionophore based optical sensor. Extraction of ions into the sensor layer via selective ionophores trigger a proton release to the sample to keep the charge neutrality. This leads to a measurable change in the degree of protonation of a pH indicator dye.

As this is not based on a surface effect, these sensors are often referred to as bulk optodes. Depending on the charge of the analyte, pH indicator and ionophore, it is necessary to introduce charged ionic sites to ensure electro-neutrality inside the bulk and to facilitate ion transport (e.g. lipophilic anions such as tetraphenyl borates). Due to this, several membrane set-ups are possible, as shown in **Figure 2.11**.

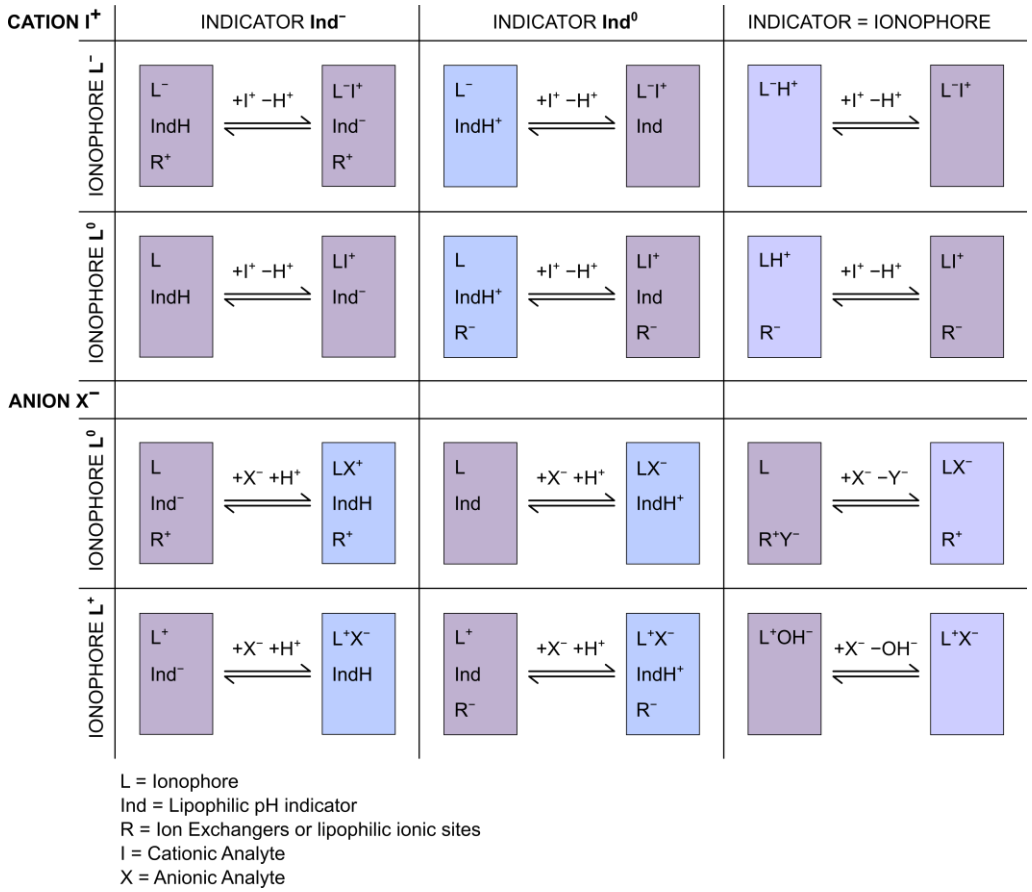

Figure 2.11: Schematic representation of possible combinations of ionophore (L), lipophilic pH indicator (Ind), ionic sites (R) and the analytes (I or X).

Commonly used pH indicators are derived from Nile blue or azo-compounds with various lipophilic residues and different pKa values. They were mainly developed at ETH Zürich by the research group of Simon and are commercially available as "ETH dyes".[53]

The selection of an ionophore can be conveniently adapted based on experience with ISEs, and yield the same number of measurable ions using IBOS. A comprehensive list of available ionophores, indicators and lipophilic ionic additives was prepared by Bühlmann et al.[54] The high versatility concerning available ionophores and pH indicators is one of the major advantages of IBOS. Moreover, as there is no need for bulky reference electrodes it is possible to fabricate sensors in the nanoscale.[55]

The commonly used read out modes for IBOS are based on absorption or fluorescence. As just measuring the intensity of parameters is error-prone, IBOS also

require a referencing system in order to obtain a robust sensor which can work reliably. This frequently used technique is based on a two wavelength ratiometric readout, but decay times or colorimetric approaches were also applied successfully.[56]

However, a major drawback of these sensors is their pH cross-sensitivity, which limits the practical applicability of IBOS. This can be overcome by simultaneous measurement of the pH of the sample, but leads to more complex instrumentation. Several strategies to overcome this pH dependency were reported, such as co-extraction of solvatochromic dyes[57,58,59] or applying fluoro- or chromogenic ionophores[60,61,62]. Fluorogenic ionophores (or fluoroionophores) combine the transducer element of the pH indicator dye and the recognition element of the ionophore in one molecule. This leads to a new generation of optical sensitive dyes for ionic species which were topic of this thesis, and will be discussed in more detail in the following section.

2.4.3 Fluoroionophore Based Optical Sensors (FBOS)

In contrast to ionophore based optical sensors, fluoroionophores combine the recognition unit (ionophore) and the transduction unit (chromophore) into one molecule.

FBOS are based on fluorescence quenching using an intramolecular charge transfer (ICT) or photoinduced electron transfer (PET) mechanism, which is described in detail in **section 2.2.2**. Briefly, the receptor is covalently coupled to the chromophore indicator dye. If they are electronically separated via a methylene bridge then PET is present, whereas direct connection of the receptor and the conjugated system of the chromophore is the basis for ICT.[63,64] In certain cases, it is difficult to draw a clear line between them, and a mixture of ICT and PET can be observed. Fluoroionophore based sensors can incorporate all presented host molecules from **section 2.3**, yet mainly crown ethers are used as they are easily accessible and show good selectivities.[65,66]

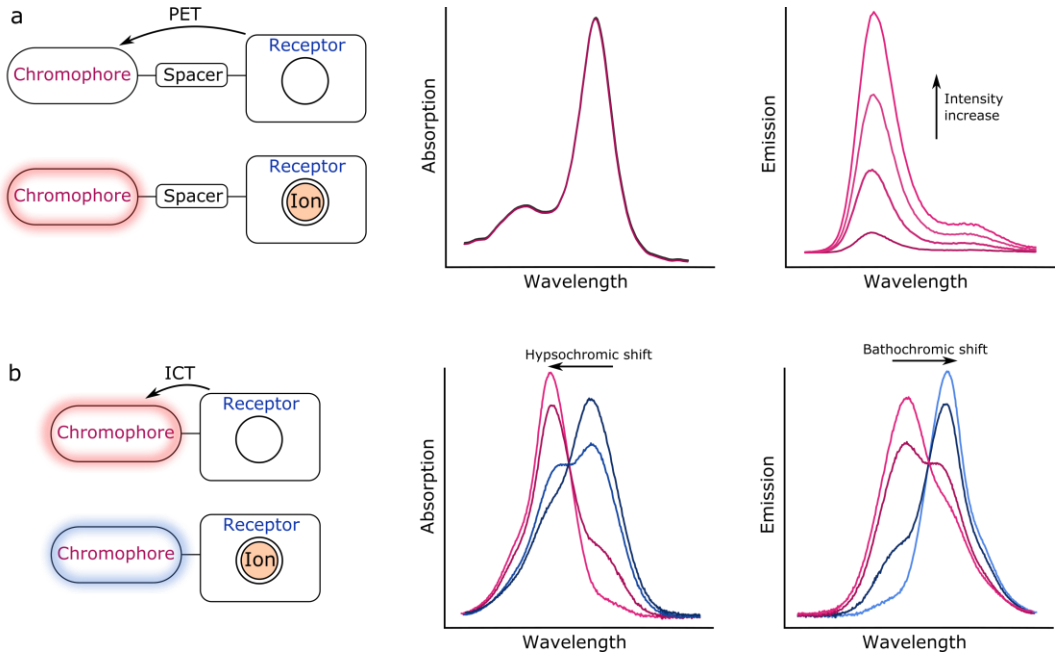

Figure 2.12: (**a**) Schematic illustration of the photoinduced electron transfer (PET). The absorption and emission spectra do not change position or the shape. Emission intensity is increased upon inhibition of the PET effect. (**b**) intramolecular charge transfer (ICT) leads to a change in the shape and position of both the absorption and the emission spectra.

In contrast to the ionophore based systems, it is possible to employ fluoroionophores for a wider range of applications as there is no need for a hydrophobic matrix. Combining simple cellular uptake of a fluoroionophore with well-known imaging techniques using fluorescence microscopy, it is possible to explore the influence of ions in biological processes.[67]

Typical analytes include biological essential ions such as Li^+, Na^+, K^+, Mg^{2+} or Ca^{2+}, as well as environmentally relevant ions Ag^+, Hg^{2+}, Cu^{2+} or Cd^{2+}. The latter can be detected by utilizing crowns with nitrogen or sulphur as the heteroatom.[31] There is a wide range of chemosensors for recognition of ionic species based on luminescence effects which are comprehensively described in several reviews.[68,65,31,69]

2.4.3.1 ICT based sensors

Sensors based on ICT (also called chromogenic or colorimetric dyes) are very simple systems where crown ethers are directly coupled to a chromophore and complexation yields a change in colour (e.g. change of absorption spectrum) (**Figure 2.12 b**). This is due to the destabilization of the excited state of the chromophore caused by a

positively charged ion inside the crown. Subsequently, the transfer of electron density from the crown electron donor to the electron accepting chromophore is influenced by this interaction, leading to a hypsochromic or bathochromic shift of the absorption band. This enables read out in the absorption and emission mode and enables ratiometric dual wavelength measurements. Direct coupling with the conjugated system of the dye can be realized via several different approaches (**Figure 2.13**).[70,71,72]

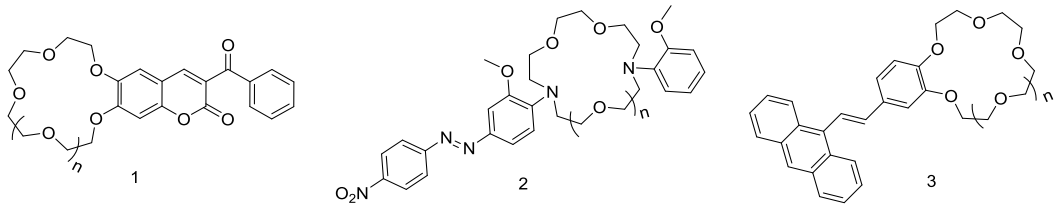

Figure 2.13: Exemplar fluoroionophores based on ICT quenching mechanism for sensing cations.

2.4.3.2 PET based Sensors

Utilization of PET usually involves aza-crown ethers bound to the chromophore, where the nitrogen electron pair is then responsible for the quenching. As the absorption spectrum is not altered, it is only possible to measure the fluorescence emission intensity, which shows ON-OFF response (**Figure 2.12 a**). Use of this system enables the utilisation of simple crown ethers (compound 4)[73], cryptants (compound 5)[74] or even more than one receptor for complexation (compound 6)[75].

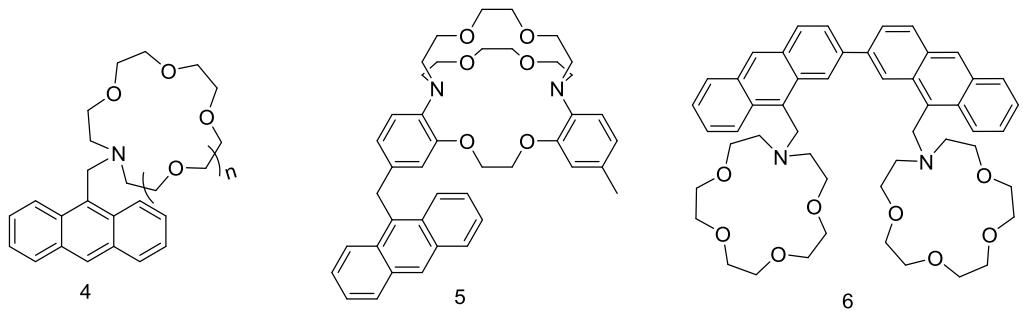

Figure 2.14: Exemplar fluoroionophores based on the PET quenching mechanism.

2.4.4 From Probe to Sensor

In order to obtain a sensor which is capable of continuous monitoring, it is necessary to immobilize fluoroionophores into polymeric matrices. Unfortunately, finding a suitable polymer matrix for ion sensing is not a simple task. The polymer must ensure that no leaching of the dye occurs in order to keep a constant concentration of indicator. Moreover, the polymer must be sufficiently hydrophilic to ensure mobility and permeability of ions inside the sensor membrane, but still remain sufficiently hydrophobic to prevent the fluoroionophore from aggregation. Hydrogel matrices are already commonly used in fluorescence pH sensors and can be adapted for ion sensing.[76] Sensor fabrication in the simplest case is achieved by simple dissolving of the hydrogel matrix in an organic solvent. Further processing steps include knife coating, spin coating, screen printing or spray coating on transparent sensor supports to obtain planar sensor foils (**Figure 2.15 a**). Sensor fibers can be produced by dip coating of the material onto the end of an optical fiber (**b**). Sensors described in this thesis are typically prepared by one of this two methods to yield robust ion sensing materials.

Alternatively, water dispersible nanosensors can be made by incorporating the sensing chemistry into polymer nanoparticles which can then be used for biological applications, as nanoparticles can be taken up by cells (**c**).[77] This was successfully conducted in this thesis by applying K^+ sensitive nanoparticles with a variety of different cell lines to study intracellular K^+ dynamics and is described in **chapter 5** (p. 99).

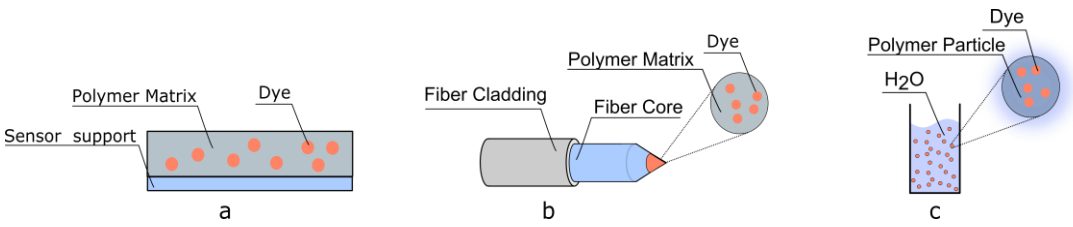

Figure 2.15: Different sensor layouts for FBOS sensors. (**a**) planar sensor foil on a transparent support. (**b**) dip-coated optical fiber. (**c**) water dispersible nanoparticles with encapsulated indicator dye.

To date, solid state sensing materials incorporating fluoroionophores are not common and the vast majority of published dyes were simply used as probes in solvents. Reported solid state ion sensors used methacrylate based hydrogels.[78,79] In contrast to

IBOS, these polymers must be water swell-able. As mentioned in **section 2.3**, the complexation is highly dependent on the environmental conditions surrounding the ion or guest molecule, and binding constants are usually higher in organic solvents than in aqueous media due to strong hydration of the ion.[80] Consequently, this system suffers from poor binding stabilities of the analyte to the receptor inside a hydrogel, which would explain the lack of solid state sensing materials to date.[41]

2.5 BODIPY Fluorophores

Among various classes of fluorescence dyes, BODIPY indicators possess perhaps the highest potential and are hugely popular. They were described for the first time by Treibs and Kreuzer in 1968, but were recognized to be suitable candidates for sensing applications in the 1990s.[81] BODIPY dyes possess many remarkable characteristics that are responsible for the high popularity of these dyes, such as

- High photo- and chemical stability
- Relatively high molar absorption coefficients (>50,000)
- High quantum yields
- Sharp excitation and emission spectra
- Tuneable spectroscopic and photophysical properties
- Good solubility and resistance to self-aggregation
- Versatile synthetic pathways to prepare BODIPY dyes

Due to this remarkable properties, we decided to use BODIPY dyes as universal chromophore basis for the development of ion sensors. There are three widely used synthetic routes towards BODIPY dyes.[82,83] The first approach is based on an acid catalysed condensation between a pyrrole (7) and an aromatic aldehyde (8) to yield dipyrromethane (9) (**Figure 2.16**). These are rather unstable compounds as they are light, air and acid sensitive. Oxidation of 9 using DDQ (2,3-dichloro-5,6-dicyano-*p*-benzoquinone) or *p*-chloranil (2,3,5,6-tetrachloro-*p*-benzoquinone) and complexation using BF_3 yields the final, robust chemical fluorescent dye (11).

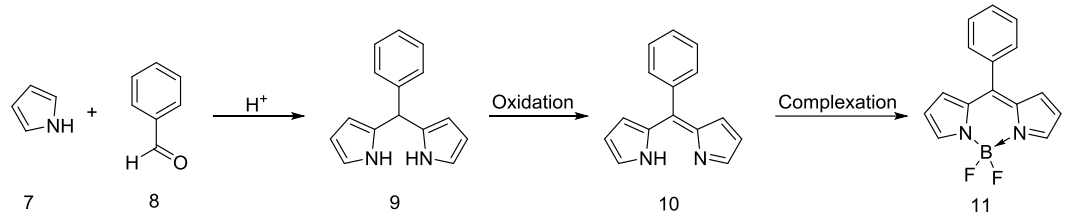

Figure 2.16: Synthetic pathway for the preparation of BODIPY dyes via condensation of an aromatic aldehyde and a pyrrole and subsequent oxidation and complexation.

The second route is a condensation between pyrrole (7) with an acylium (12) which yields a non-stable intermediate acylpyrrole (13). This further reacts with different pyrroles to a dipyrrinium salt (14) which then is complexed to form the final product. With this pathway, it is possible to prepare asymmetric dyes, as it enables the use of a second different pyrrole moiety (14) during the condensation step.

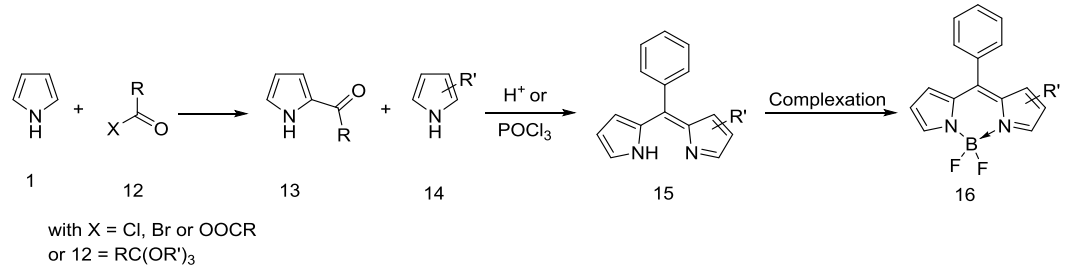

Figure 2.17: Synthesis of BODIPY via an acylation of a pyrrole and a subsequent condensation and complexation.

The third route is a simple one-pot condensation of two equivalents of pyrrole-2-carbaldehyde (17) using $POCl_3$ (**Figure 2.18**). Products synthesised via this route are typically obtained in high yields and require little purification.

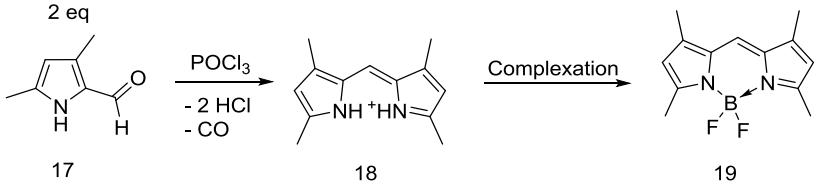

Figure 2.18: One-pot reaction to form BODIPY dyes based on a condensation and decarbonylation of pyrrole-2-carbaldehydes.

BODIPYs in general are highly chemically robust and therefore allow subsequent modifications after complexation, such as oxidation, reduction or nucleophilic substitutions, without destroying the former dye. The possibility of modifying the boron center, extending the degree of the conjugated system and performing further reaction at the BODIPY core creates enormous potential for structural tuning.[84]

Due to this immense versatility, crown ethers or similar ion-receptors were already coupled to different positions at the BODIPY dye.[82] There are two main routes to introduce analyte sensitive groups, as illustrated in **Figure 2.19**. Receptors were introduced either during the preparation of the BODIPY via an aromatic aldehyde bearing the receptor unit to obtain a PET sensor (Route 1)[85], or via additional condensation to form a styrylated fluorophore which acts as ICT probe (Route 2)[86,87]. However, the vast majority of the reported BODIPY based fluoroionophores for cation measurements were only used in solution and no solid state sensing material was prepared.[82,88]

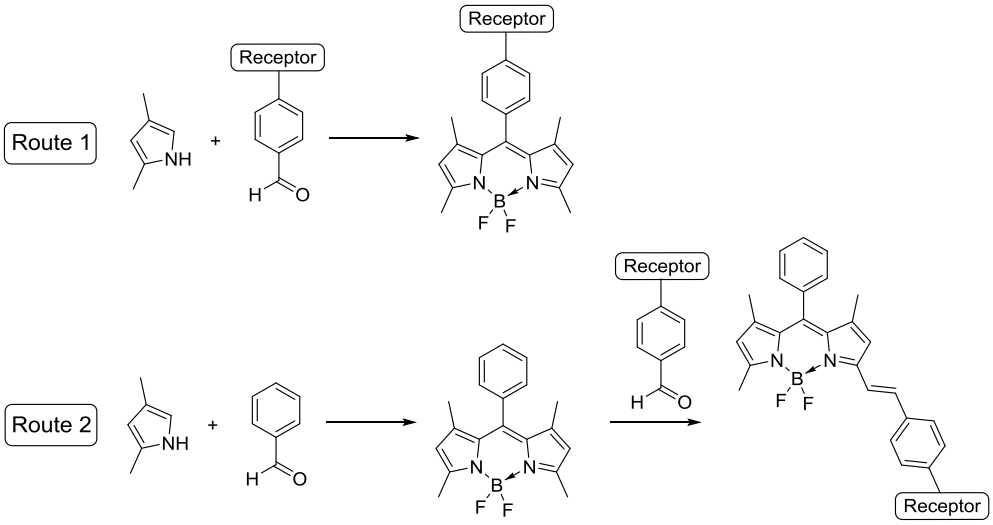

Figure 2.19: Commonly applied routes to introduce receptor units to BODIPY dyes. Route 1 yield PET-based indicator dyes whereas route 2 yield ICT-based dyes.

BODIPYs allow for a simple control of the photophysical properties via synthetic modifications of the dye. Introducing electron withdrawing or electron donating groups to the BODIPY dye or further aromatic groups, which will expand the conjugated system, can have a direct effect on the spectral properties of the dye. BODIPYs with absorption and emission spectra which span the visible range, but also to longer wavelengths in the NIR region, can be prepared. This makes BODIPY

probes the preferred choice as fluorescent labels or markers in biological research.[89] The tuning of spectral properties was performed in the context of K^+ sensitive fluoroionophores and will be the topic of the first publication described in the next chapter and was the basis for all further developments in ion sensors presented in this thesis.

Part II

Results

Chapter 3

Red- to NIR- Emitting, BODIPY Based, K^+ - Selective Fluoroionophores and Sensing Materials

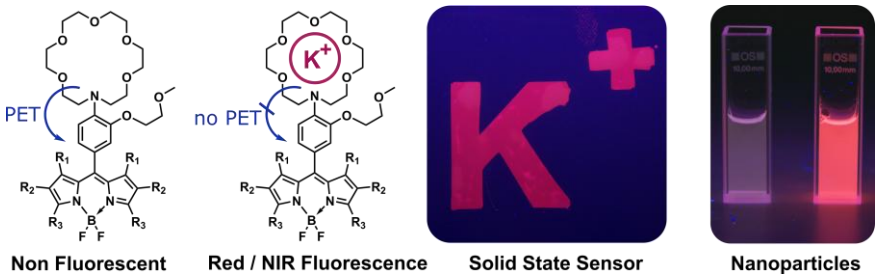

Preface for the Manuscript

This publication represents the foundation of all newly developed sensing materials throughout this thesis. The sensing materials presented here can be used for determination of K^+ in aqueous solution and represent promising new sensing tools for various applications.

First, we synthesized a known receptor unit which was published in 2013, just recently before this work started.[90] This crown-ether receptor unit was coupled to a coumarin derivate and a high K^+/Na^+ selectivity and a sensitivity in the micromolar concentration range was reported. However, the fluoroionophore showed only moderate photophysical properties.

We aimed to take advantage of this new receptor unit, but develop a new set of indicator dyes with superior photophysical properties, such as high molar absorption coefficient, high quantum yield and good chemical- and photostability. Moreover, we intended to develop a building block system which simplifies the synthesis of indicator dyes for individual demands. BODIPY chromophores meet these criteria as they are simply prepared by condensation of the receptor unit and pyrroles (more detailed explanations about BODIPY synthesis can be found in **section 2.5** (p. 27). Using this method, we were able to synthesize five new fluoroionophores which show efficient excitation and emission ranging from green to NIR light. Moreover, we could show that different substituents have a major effect on the photoinduced electron transfer (PET) effect and studied this using cyclovoltametric measurements. These findings were of major importance for the development of new fluoroionophores throughout this entire thesis.

Additionally, we successfully immobilized fluoroionophores into various polymer matrices, such as hydrogels for planar sensor foils or nanoparticles to obtain water-dispersible nanosensors. To demonstrate potential applicability in clinical diagnostics, we prepared referenced fiber optic sensors and measured K^+ in fetal bovine serum with ICP-OES measurements for reference. The fabricated nanoparticle based sensors were then used in a collaboration with University College Cork to study intracellular K^+ fluxes. These results are shown in **chapter 5** (p. 99).

Manuscript

Red to NIR Emitting BODIPY Based K^+ Selective Fluoroionophores and Sensing Materials

This chapter was published as *Full Paper* in

Advanced Functional Materials, 2016, *26* (42), 7697–7707.

doi: 10.1002/adfm.201603822

Authors: Bernhard J. Müller, Sergey M. Borisov* and Ingo Klimant

Graz University of Technology, Institute of Analytical Chemistry and Food Chemistry, Stremayrgasse 9, 8010 Graz, Austria

E-mail: sergey.borisov@tugraz.at

Keywords: Sensors, Photoinduced electron transfer, Potassium, Nanoparticles, Fluorescence

Abstract Novel optical sensing materials for the selective measurement of potassium ions (K^+) in water are presented. Signal enhancement of the fluoroionophores is caused by the reduction of photoinduced electron transfer (PET) upon complexation with K^+ ions. The indicator dyes are based on an aza-crown ether as a receptor and BODIPY dyes as fluorophores. This family of new indicators possess tuneable optical properties (green to red excitation, red to NIR emission) and PET efficiencies. They exhibit high brightness with a quantum yield between 0.20 and 0.47 in the "on" state and a molar absorption coefficient between 30,000 and 290,000 $M^{-1}cm^{-1}$. These new indicator dyes are immobilized in biocompatible hydrogel matrices to obtain stable non-leaching and fast responding (t_{90} ~ 10s) sensor materials for continuous measurements of extracellular potassium prepared in various formats such as planar optodes or fiber-optic sensors. Water dispersible polymer-based nanoparticles are prepared for imaging applications. Apart from fluorescence intensity measurement, self-referenced read-out of fluorescence decay time is demonstrated. All sensor materials display a high K^+/Na^+ selectivity and are not influenced by pH within the physiologically relevant range. Practical

applicability of the new materials is emphasized by application of a fiber-optic sensor to quantification of K^+ in serum which shows excellent correlation with the reference measurements.

3.1 Introduction

Potassium (K^+) plays a central role in the human body and is necessary for the function of all living cells. Inside the cell K^+ is the main ion with an approximate concentration of 150 mM while extracellular concentrations are about 5 mM. [91,92] The difference in concentration causes a disparity in electric potential between the interior and exterior of cells, known as the membrane potential. [93] It takes part in substantive processes and functions such as the regulation of cell growth, acid-base equilibrium and maintaining the normal blood pressure. [94,95,96] Cells can control this potential by opening or blocking K^+ channel transmembrane proteins. [97] This regulation of intra- and extracellular K^+ concentration plays a key role in metabolic processes and is of high interest for pharmacological research. However, the molecular mechanism of potassium physiology and pathology are still insufficiently understood, partly due to the lack of tools for measuring K^+.

Extracellular potassium (whole blood, serum) is the key analyte in clinical diagnostics as elevated K^+ concentrations (hyperkalemia) is an indication for cardiac arrhythmia which can lead to sudden heart failure. [98] The crucial requirement and greatest challenge for potassium sensors for clinical diagnostics is the selective detection of the low extracellular K^+ (5 mM) over a high Na^+ concentration (150 mM). [99] Apart from good selectivity, inertness to variations of pH in the relevant range is of extreme importance.

Fluorescence-based measurements offer several advantages compared to other analytical techniques (e.g. electrochemical measurements with ion selective electrodes) as they are free of electromagnetic interferences and are non-invasive. Fluorescent sensors are available in various formats including planar sensors and spots, fiber-optic sensors and (nano)particles. Nano-scale sensing materials can be incorporated into small objects such as cells to gain information in real time or enable high-resolution imaging. [100] Conventional fluorescence and laser-scanning microscopes can be used for this purpose. [13,12]

A fluorescent indicator dye typically consists of a fluorophore linked to a recognition unit (receptor/ionophore) leading to a fluoroionophore. Fluoroionophores based on intramolecular quenching due to photo-induced electron transfer (PET) have been applied successfully for sensing cations in the last years. [101] Typically, the receptor unit bears a tertiary amine group which is responsible for the emission enhancement in presence of ions, due to the reduction of the PET effect (**Figure 3.1**).

PBFI (potassium binding benzofuran isophthalate) consisting of a diaza-18-crown-6 ether as a receptor and a benzofuran derivative as a fluorophore is the most popular indicator dye for molecular biology studies and the only commercially available fluoroionophore. [102] However, this PBFI indicator suffers from a poor K^+/Na^+ selectivity and is expensive. A triazacryptand (TAC) receptor designed by He et al. [103] shows excellent K^+ selectivity and sensitivity, but its preparation is very tedious due to extensive multistep synthesis. Hence, there is a high demand for simple, sensitive and selective receptors.

Recently, Ast et al. introduced a phenylaza-[18]crown-6 with ortho-substituted 2-methoxyethoxy group as receptor which has a good K^+/ Na^+ selectivity and is simpler to prepare than the TAC receptor. [90] Combining this receptor with a coumarin fluorophore enabled measurement of K^+ in the range of 2-100 mM with a negligible cross-sensitivity to Na^+ under physiological conditions and a 2.5-fold fluorescence enhancement at 160 mM K^+ at 493 nm. The fluorophores used for optical K^+ sensing included derivates of coumarins,[90] xanthene dyes, [104,105,106] naphthalimides, [103,107] borondipyrromethenes (BODIPYs) [108,86,85,109,110,111] and other dyes. [112] Most of them are excitable below 600 nm (Fehler! Verweisquelle konnte nicht gefunden werden.). However, indicator dyes with longer wavelength of absorption and emission (> 600 nm) are of particular interest as they allow measurements in highly scattering and absorbing media (e.g. tissues) as well as in autofluorescent media (e.g. biological samples).

The fluoroionophores for intracellular imaging of K^+ reported by the groups of Verkman and Meldrum were modified with charged groups in order to facilitate the solubility in water and to enable cell uptake. Application of such probes is limited to essays in small volumes (such as cells) since they have to be added to the analysed media. Thus, immobilization of the fluoroionophores into polymeric matrices is necessary to design sensors for continuous monitoring of the analytes (e.g. in diagnostics). Despite seemingly straightforward, this can be a challenging task since (i) it should be ensured that the material possesses good permeability for the analyte

i.e. is sufficiently hydrophilic; (ii) the indicator should be compatible to the matrix to prevent aggregation; (iii) it should not leach out of the matrix which is not unlikely for the dyes bearing hydrophilic receptors. Last but not least, not all indicators which work properly in solution show a response when immobilized in a hydrogel, as the environmental polarity plays an important role in the PET effect. In fact, very few sensors based on immobilized indicators have been reported so far. [103,90,107] They employed fluoroionophores which show excitation and emission at shorter wavelength and only moderate brightness. Thus, preparation of novel high performance sensing materials for K^+ remains of utmost importance.

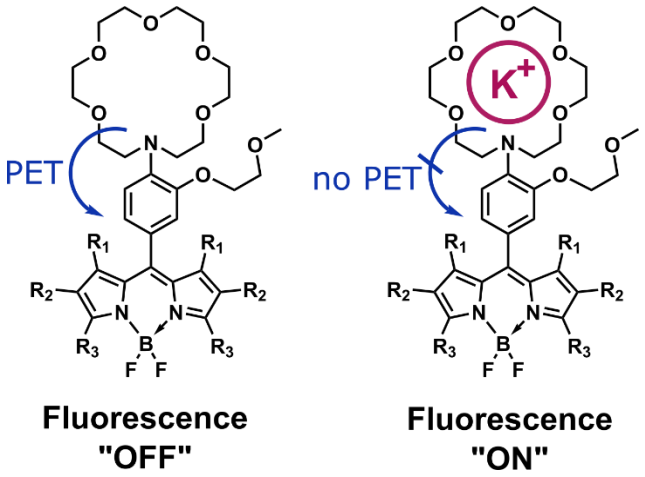

Figure 3.1: Operating principle of a fluorescent K+ probe. Fluorescence enhancement is caused by complexation of K+ and a reduction of the photoinduced electron transfer (PET).

In this contribution we report a palette of K^+ fluoroionophores based on BODIPY dyes having tuneable spectral properties, good brightness, insensitivity to pH in the relevant conditions and tuneable sensitivities. They incorporate a selective, yet conveniently accessible aza-crown-ether receptor. We will report on preparation and properties of novel materials (solid state optical sensors and potassium-sensitive nanoparticles) which enable numerous applications in science and technology exemplary demonstrated for measurement in fetal bovine serum samples.

3.2 Results and Discussion

3.2.1 Synthesis of BODIPY Fluoroionophores

The new fluoroionophores (**FIs**) represent a highly modular system consisting of two building blocks – the receptor and the chromophore. The spectral properties are controlled by the pyrroles and the sensitivity is controlled by the receptor which enables high flexibility of the design. The synthesis of the receptor (o-(2-methoxyethoxy)phenylaza-[18]crown-6 lariat ether) was performed as described by Ast et al.[90] (**Figure S - 3.1**). Importantly, this convenient procedure relies on readily available reagents and allows preparation of multi-gram quantities of the receptor. All the BODIPY indicators are prepared via condensation of a pyrrole and the aromatic aldehyde from the receptor, subsequent oxidation with DDQ and complexation using a base and BF_3-etherate. We prepared differently substituted pyrroles in order to tune the optical properties and optimize the PET efficiencies of the indicators (Fehler! Verweisquelle konnte nicht gefunden werden.). Whereas 2,4-dimethylpyrrol is commercially available, other pyrrols can be conveniently prepared from the respective ketones and 3-phenyl-2H-azirene. [113] A different route is necessary for preparation of furan-fused pyrrols. [114]

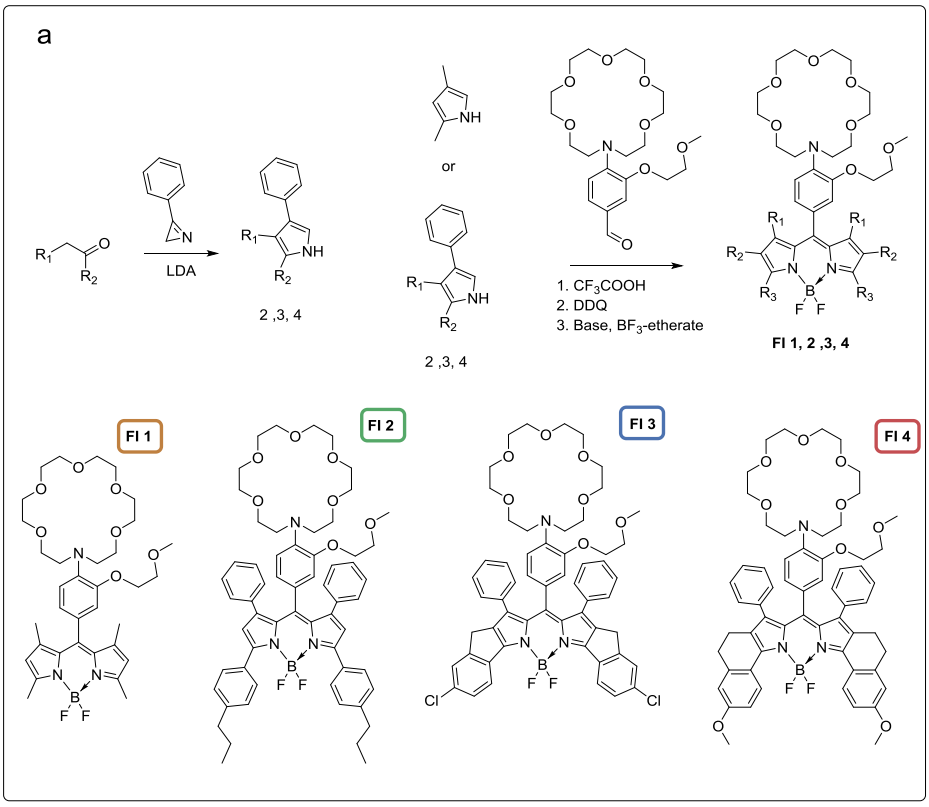

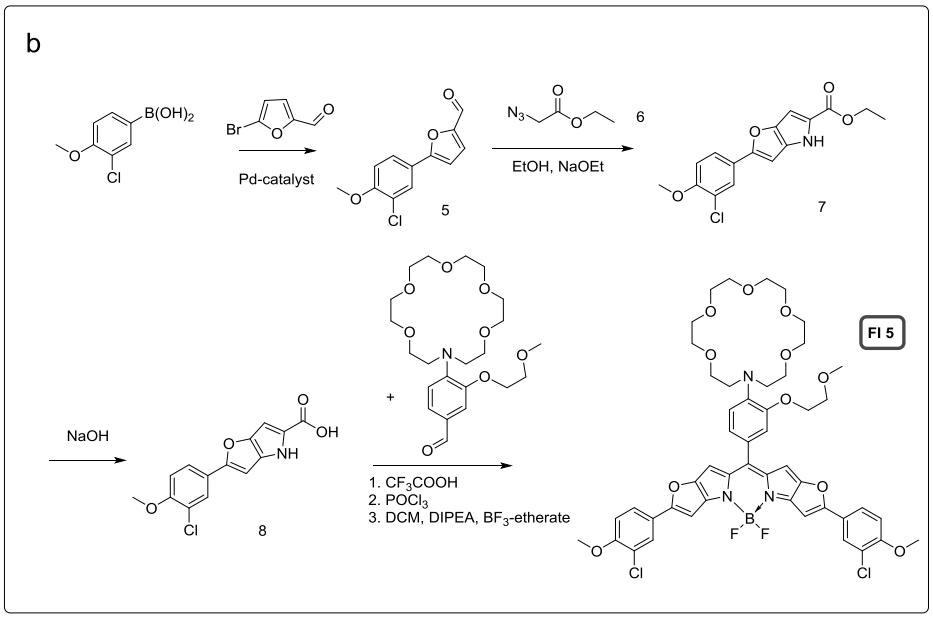

Figure 3.2: (**a**) Synthesis of different pyrroles and BODIPY indicators. (**b**) Synthetic pathway to FI 5.

3.2.2 Spectral and Electrochemical Properties of the Fluoroionophores

FI 1 prepared from 2,4-dimethylpyrrol is a commonly used BODIPY dye with absorption in the blue and emission in the green region of the electromagnetic spectrum (**Figure 3.3Fehler! Verweisquelle konnte nicht gefunden werden.**, **Table 3.1**). A bathochromic shift of about 70 nm is obtained via extension of the aromatic system to tetraphenyl-BODIPY **FI 2**. Rigidization results in an even further bathochromic shift of the absorption and emission (about 70 nm), higher molar absorption coefficients and fluorescence quantum yields (**Table 3.1**). As expected **FI 4** absorbs at longer wavelength compared to **FI 3** due to the electron-donating character of the methoxy-group. **FI 3** and **FI 4** can be efficiently excited using red light and show emission in the red/NIR part of the spectrum. **FI 5** includes a fused furan ring and belongs to the so called Keio Fluors variation of BODIPYs. [115] This dye class has extraordinarily high molar absorption coefficients and high quantum yields. Indeed, the indicator **FI 5** demonstrates ε of 195 600 M^{-1} cm^{-1} and QY of 60% in the "on" state. (**Table 3.1**). BODIPY indicators are well known for their sharp and narrow absorption and emission spectra [82] which is also the case for all new fluoroionophores except **FI 2**. It shows a very broad absorption and consequently a lower molar absorption coefficient. This can be attributed to the rotation of the phenyl rings, since aggregation of the dye was not observed. **FI 2** already shows an

appreciable quantum yield of 35 % in solution when protonated with trifluoracetic acid whereas the quantum yields for BODIPYs **FI 1, 3, 4** and **5** in solution are significantly higher. Luminescence lifetimes in the "on"-state (fully protonated) vary from 3.1 ns to 5.1 ns. To conclude, all the new fluoroionophores feature excellent fluorescence brightness (BS) which is particularly high for **FI 5**.

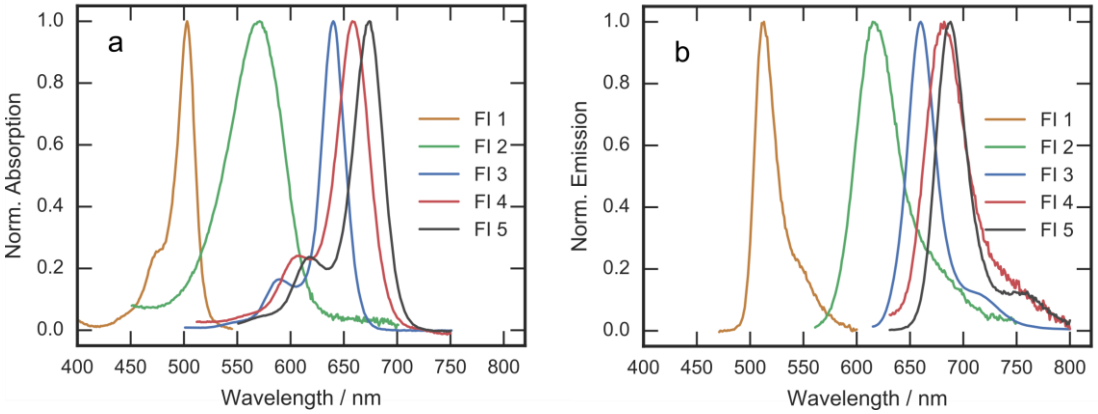

Figure 3.3: Normalized absorption (**a**) and emission (**b**) spectra of the fluoroionophores in dichloromethane.

Cyclovoltammetric measurements (**Figure S - 3.4**, **Table 3.1**) show that **FI 2** and **FI 3** are more difficult to oxidize than **FI 4** and **FI 5** which indicates more electron-rich character of the latter. **FI 1** bearing 4 electron-donating methyl groups instead of electron-withdrawing aryls shows significantly lower oxidation potential compared to other FIs. The trend in the ground state reduction potentials is less evident. However, the reduction potentials estimated for the excited state ($E_{1/2}$red*) from the reduction potential in the ground state ($E_{1/2}$red) and the energy of the excited state (E_{00}) clearly show that **FI 1-3** in the excited state are more powerful oxidants than **FI 4** and **FI 5**. In the same conditions, the oxidation potential of the free aza-crown receptor ($E_{1/2}$ox(rec)) was estimated to be 0.817 V. Thus, ΔG of the electron transfer reaction ($\Delta G_{PET} = E_{1/2}ox(rec) - E_{1/2}red^*(FI)$[17]) is negative for **FI 1-FI 3** but close to zero for **FI 4** and **FI 5**. An increase in $E_{1/2}$ox(rec) by at least 0.1V is detectable in presence of K^+ (**Figure S - 3.4g**) indicating the increase in ΔG of quenching reaction. It should be mentioned that the absolute values are just a very rough estimation due to the fact that the ion pairing energy describing charge generation and separation within the electron-transfer complex is neglected and E_{00} was estimated from fluorescence maxima and not on the edge of the spectra.

Table 3.1: Photophysical and electrochemical properties of the fluoroionophores in solutions and immobilized in a hydrogel matrix (D4)

Fluoro-ionophore	λmax abs (ε), nm ($M^{-1}cm^{-1}$)	λmax em, nm	QY in THF[(a)]	BS, ε·QY	QY in D4 with 1M KCl	QY in D4 with 0.1 M HCl	Lifetime in THF[(a)], ns	$E_{1/2}$ ox, V	$E_{1/2}$ red, V	$E_{1/2}$ ox*, V [(b)]	$E_{1/2}$ red*, V [(c)]
FI **1**	504 (53 600)	513	0.66	35 376	n.d.	n.d.	5.1	0.44	-1.27	-1.98	1.15
FI **2**	571 (29 900)	615	0.35	10 465	0.20	0.64	3.5	0.93	-0.95	-1.09	1.07
FI **3**	640 (109 300)	660	0.68	74 324	0.47	0.76	5.0	1.08	-0.82	-0.80	1.06
FI **4**	655 (87 200)	682	0.53	46 216	0.47	0.46	4.1	0.80	-1.03	-1.02	0.79
FI **5**	670 (195 600)	688	0.60	117 360	0.42	0.41	3.1	0.88	-0.88	-0.92	0.92

(a) contains 3% v/v trifluoroacetic acid

(b) calculated as $E_{1/2}\ ox^* = E_{1/2}\ ox - E_{00}$; E_{00} is estimated from the $\lambda_{max\ em}$

(b) calculated as $E_{1/2}\ red^* = E_{1/2}\ red + E_{00}$; E_{00} is estimated from the $\lambda_{max\ em}$

3.2.3 Polymer Based Sensing Materials

In order to prepare solid state sensing materials the fluoroionophores have to be immobilized in a hydrogel matrix (**Figure 3.4**). This was achieved by simply dissolving the dyes and the polymer in organic solvent and coating the resulting "cocktail" onto a transparent inert polyethylene terephthalate support. Hydromed D4 was chosen as a suitable matrix due to its capability to take up about 100 % water, good ion permeability, biocompatibility and commercial availability. As can be seen from **Figure 3.4** immobilized **FI 1** leaches continuously out of the sensor matrix into the analysed solution. Leaching of the dye can be attributed to very hydrophilic nature of the receptor which is particularly pronounced in presence of K^+ due to the charged nature of the resulting complex. In contrast to **FI 1**, indicators **FI 2 – 5** are significantly more hydrophobic which completely eliminates leaching (**Figure 3.4** and **Figure S - 3.3**). Due to instability of **FI 1**-based sensors only materials based on **FI 2 - 5** were characterized. The calibration curves for the sensors were obtained in

20 mM TRIS buffer at pH of 7.4 (representing the pH of blood) with different KCl concentrations (**Figure 3.5**).

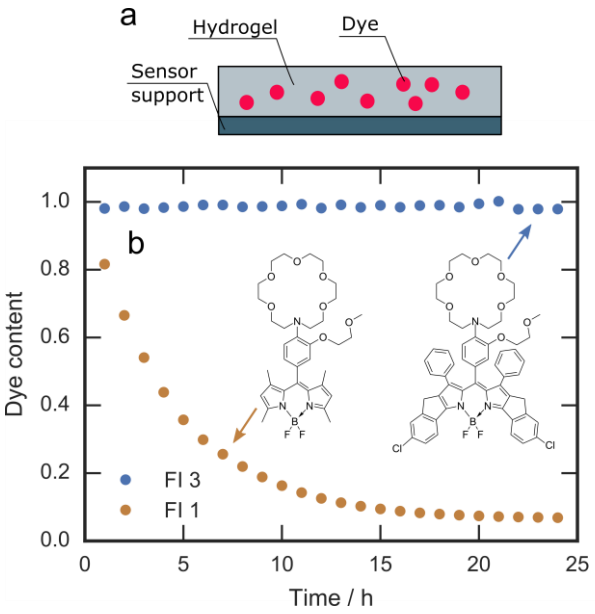

Figure 3.4: (**a**) Scheme of a polymer-based sensing material. The fluoroionophores are physically immobilized in a polymer hydrogel matrix. (**b**) Normalized absorption maxima of the fluoroionophores immobilized in hydrogel D4. 100 mM KCl solution was pumped through a flow-through cell for 24 hours.

As can be seen, the fluorescence intensity greatly increases in presence of the analyte due to decreased efficiency of photoinduced electron transfer (PET) from the amino group of the receptor to the chromophore. For **FI 2** and **FI 3** the relative fluorescence enhancement in presence of K^+ is higher than for **FI 4** and **5**. This behaviour is attributed to the electron-donating effect of the methoxy groups in both indicators (**FI 4** and **5**) which decrease the PET efficiency in the absence of K^+. Therefore, these fluoroionophores show emission in the absence of K^+ whereas the emission of **FI 2** and **3** is "switched off" almost completely in the same conditions (**Figure 3.5c, f; Figure S - 3.5b, d).** These findings show good correlation with the results of the electrochemical investigation.

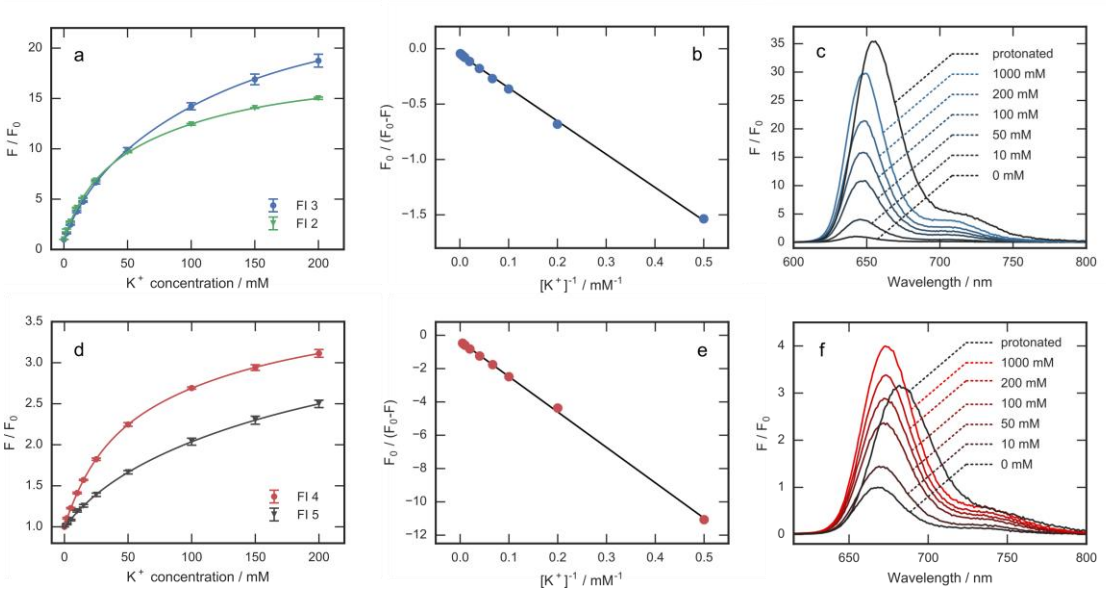

Figure 3.5: (**a**) and (**d**): F/F_0 calibration curves for **FI 2 – 5** immobilized in hydrogel D4. The values of F and F_0 were taken at λ = 605 nm, 645 nm, 668 nm and 685 nm for **FI 2**, **FI 3**, **FI 4** and **FI 5**, respectively . (**b**) and (**e**): Exemplar Benesi-Hildebrand plot for **FI 3** and **FI 4** for the determination of Kd via the slope. Benesi-Hildebrand plots for **FI 2** and **FI 5** are shown in the supporting information. R^2 of the linear fit is >0.989 for all materials. (**c**) and (**f**): Exemplar normalized emission spectra of **FI 3** and **FI 4** with different K^+ concentrations and protonation with 0.1 M HCl. The insert in (**a**) shows the photographic image (λexc 365 nm) of hydrogel D4 foil based on **FI 3** with the emission switched on with 150 mM K^+.

The emission spectra (**Figure 3.5**) show only a minor bathochromic shift in presence of K^+ and upon protonation of the receptor in acidic media, which indicates that the PET effect is predominant over intramolecular charge transfer (ICT).

Comparison of the very similar rigid chromophores **FI 3** and **FI 4** reveals that systematic tuning of the PET efficiency is easily possible. Significant increase in the dynamics for **FI 4** and **FI 5** is expected if further electron-withdrawing substituents (halogens, sulphonamides) are introduced into the chromophore. The normalized F/F_0 values at 5 mM K^+ (typical extracellular concentration), 150 mM K^+ (typical intracellular concentration), and at saturation of the sensor (1 M K^+) as well as Kd values for each sensing material are listed in **Table 3.2**.

Table 3.2: Fluorescence enhancement factors and Kd values for all sensing materials. [(a)] with 150 mM Na^+ background

Sensor Material	F/F_0 at 5 mM K^+	F/F_0 at 150 mM K^+	F/F_0 at 1 M K^+	Kd / mM
FI 2 in D4	2.8	14.1	18.4	24.1
FI 3 in D4	2.5	16.9	25.5	67.7
FI 4 in D4	1.2	2.9	3.7	37.1
FI 5 in D4	1.0	2.3	3.4	102.7
FI 3 in RL100	1.3	6.7	23.0 (at 800 mM)	177.4
FI 3 in PS/PVP	1.7	5.0	11.9	15.6
FI 3 in D4[(a)]	2.5	17.5	26.0	66.8

The Kd value of the indicators inside the polymer membrane were determined using the Benesi-Hildebrand equation as described in literature [112] (**Equation S1**). Almost ideal linear fit (**Figure 3.5 e and f**) indicates a 1:1 complexation behaviour. Kd can be calculated using the slope of the fit. The relative fluorescence enhancement in case of **FI 2** and **3** is very good at low K^+ concentrations and the dynamic range extends beyond 150 mM making these two fluoroionophores promising for both intra- and extracellular measurements.

Since the polymer environment can affect the photophysical properties of the indicators, the QYs of the fluoroionophores in hydrogel D4 were also investigated (**Table 3.1**). **FI 2** and **3** show an increased QY in foil when fully protonated (PET off) which can be attributed to a more rigid environment where non emissive deactivation processes are minimised. However, the QY in 1 M KCl is lower than for the protonated form indicating that K^+ does not fully inhibit the PET effect with these indicators. **FI 4** and **5** have a lower QY in foil than in solution, but the QY of the protonated indicator dyes and the dyes in 1 M K^+ are similar indicating an efficient inhibition of the PET effect by K^+. In general, all indicators show a high QY upon complexation with K^+ in the sensor matrix. Combined with a high molar absorption coefficient this results in very bright sensors. Therefore, indicator dyes

can be used for preparation of thin sensor layers which subsequently improves the response time of the sensor.

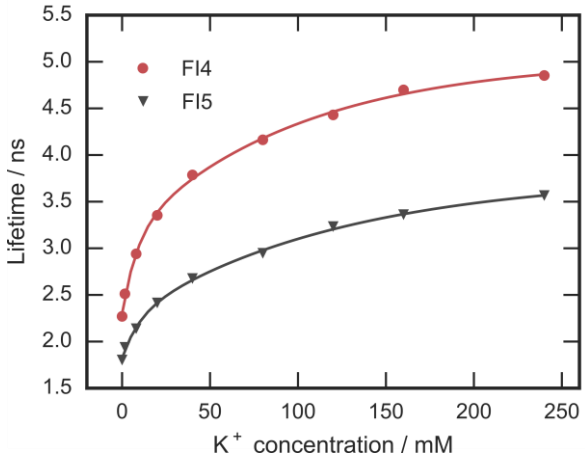

Figure 3.6: Calibration of **FI 4** and **FI 5** immobilized in hydrogel D4 using fluorescence decay time read-out.

Since the fluorescence of **FI 4** and **FI 5** is not fully quenched in the absence of K^+ (both free and complexed forms are emissive), self-referenced measurements of the luminescence lifetime become possible (**Figure 3.6, Figure S - 3.9**). This enables fluorescence lifetime imaging (FLIM) measurements which is of high interest for biological applications.

3.2.4 Selectivity of the Sensor

Inertness to changes of pH in the physiologically relevant range is essential for practical applications of the sensors. As can be seen (**Figure 3.7a**), the calibration curves are identical at pH 7.1, 7.4 and 7.7. Investigation of the acid-base equilibrium of the aromatic amine of the receptor (**FI 3** in D4) reveals an apparent pK_a value of 3.2 (**Figure 3.7b**). Thus, the receptor can be used in the pH range of 5.5 – 9 without any pH cross-talk i.e. it is suitable for intra- or extracellular measurements. [116]

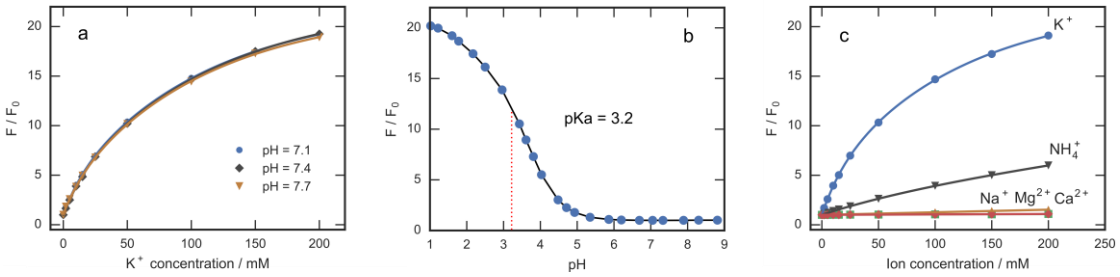

Figure 3.7: (**a**): Calibration curve for **FI 3** in hydrogel D4 at different pH values. (**b**): Determination of the pKa of the receptor for **FI 3** in hydrogel D4. (**c**): Exemplar determination of the selectivity for **FI 3** immobilized in hydrogel D4.

FI 3 shows no response to Ca^{2+} or Mg^{2+} (**Figure 3.7c**). On the other hand, the indicator dye shows high cross sensitivity to NH_4^+ since the size of NH_4^+ is comparable to that of K^+. However, NH_4^+ does not occur in biological samples in an interfering concentration (except urine) whereas sodium is the main ion present in the extracellular space (150 mM). Therefore, the high K^+/Na^+ selectivity of the sensors is of great importance. In fact, **FI 3** shows a fluorescence enhancement of 1.3 at 150 mM Na^+ compared to 16.89 at 150 mM K^+ and to 2.46 at 5 mM K^+. When simulating extracellular conditions (150 mM Na^+ background) the F/F_0 and Kd value are only slightly increased compared to 0 mM Na^+ background (**Table 3.2**). It should be considered that in most applications the concentration of Na^+ does not vary drastically (**Figure S - 3.8**).

To demonstrate sufficient selectivity over Na^+ ions, we measured the response of a sensor at different K^+ concentrations in presence of 110 and 130 mM Na^+. Buffer solutions with different K^+ and Na^+ concentrations were pumped through a flow through cell to imitate extracellular K^+ measurements. **Figure 3.8** shows that the response of the sensor is fast and fully reversible (a - c). Variation of the Na^+ background from 110 mM to 130 mM at constant K^+ concentration (e - f) does not result is a noticeable cross-talk. Therefore, it is possible to reliably measure K^+ at varying background of Na^+ in the concentration range typical for extracellular measurements. The sensor shows a fast response and recovery (t_{90} = 10s) and no hysteresis at any concentration. Leaching or aggregation of the dye was not observed either. Interestingly, hydrophobic perylene-based pH indicators previously showed slow response and hysteresis when physically embedded in hydrogel D4.[117] We do not observe such behaviour for the potassium fluoroionophores. Therefore, it is likely

that the hydrophobic part of the fluoroionophore remains fixed in the hydrophobic domains of the hydrogel whereas much more hydrophilic receptor is localized in the hydrophilic domains.

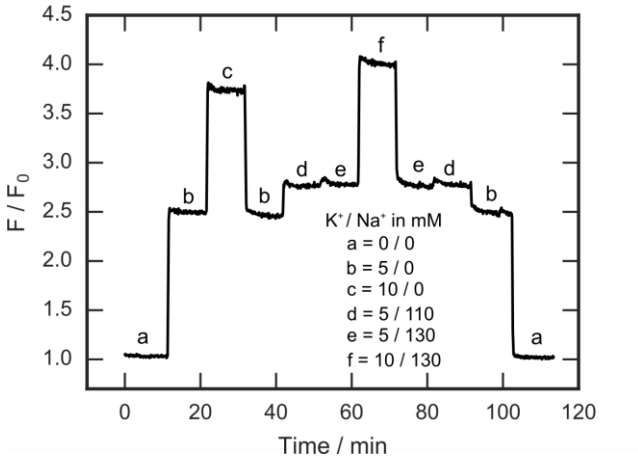

Figure 3.8: Normalized fluorescence of **FI 3** in hydrogel D4 fixed in a flow - cell while pumping solutions with different K^+ and Na^+ concentrations through it.

3.2.5 Water Dispersible Nanoparticles

Analyte-sensitive nanoparticles represent versatile analytical tools that are attractive for sensing and imaging in small volumes such as cells. Therefore, additionally to planar sensor foils we prepared two different kinds of nanosensors based on commercially available polymers. RL100 is a copolymer of different acrylates with quaternary ammonium groups which are responsible for the excellent cell-penetrating properties of the nanobeads. [118] It is frequently used for drug delivery due to the positive charge and its non-biodegradability. [119,120,121] Particles can be prepared in a very simple procedure by dissolving the polymer and the indicator dye in an organic solvent (e.g. acetone) followed by precipitation in water, forming particles with a positive charge outside and the lipophilic indicator entrapped inside. [118,122] The particles show an average size of approx. 30 nm and due to the positive charge on the surface the nanoparticle show water uptake and ion permeability.

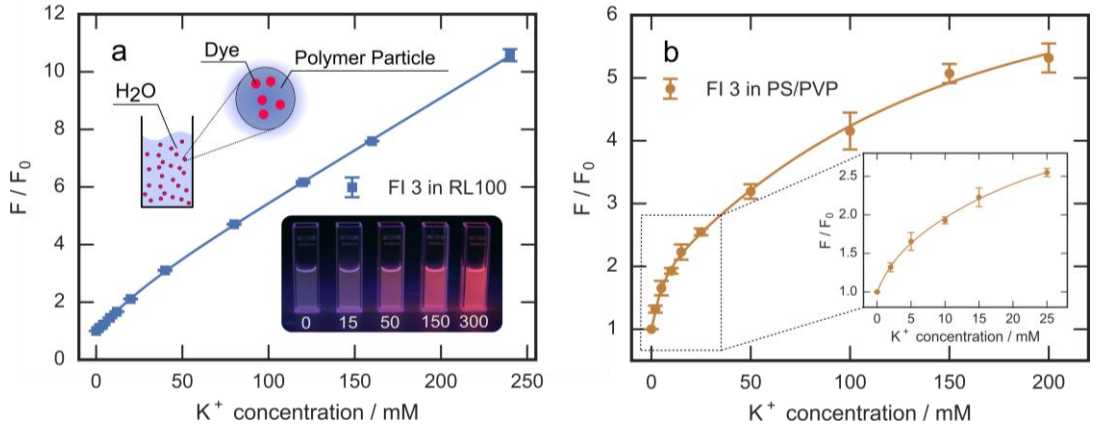

Figure 3.9: (**a**): Sensing properties of **FI 3** immobilized in positively charged RL100 nanoparticles dispersed in an aqueous solution. The insert shows a photographic image of the aqueous dispersions of the nanoparticles at varying K^+ concentration under 365-nm excitation. (**b**): Sensing properties of PS-PVP nanoparticles stained with **FI 3**. Benesi-Hildebrand plots for both materials are shown in **Figure S - 3.7**.

Figure 3.9a shows a calibration curve for **FI 3** entrapped in the particles. The sensor material has a higher Kd (177.4 mM) compared to hydrogel D4 (67.7 mM) which can be attributed to the positive charge of the particles lowering the equilibrium of positively charged K^+ ions inside the particle. Furthermore, the polarity of the polymer is different to Hydrogel D4 affecting the PET efficiency. It should be emphasized that the dynamic range, the spectral properties and the cell penetration of this material match the requirements for intracellular measurements.

Poly(styrene-block-vinylpyrrolidone) (PS/PVP) is a highly versatile particle platform for optical sensors. [123] These commercially-available uncharged particles have an average size of 245 nm and core-shell architecture, which can be used for incorporation of (indicator) dyes into these two domains. Physical entrapment of the dyes is achieved via swelling the particle with an organic solvent, adding the indicator and then removing the solvent.

We entrapped **FI 3** in the shell in order to allow interaction of the analyte with the indicator. The calibration of the sensor material shows a large dynamic range and a Kd of 15.6 mM K^+ (**Figure 3.9b**). The most attractive feature of this material is the possibility of incorporating a second dye in the core (e.g. an oxygen indicator for dual sensing or an inert dye for referencing). Also the neutral nature of the particles enhances the sensing options in complex media (e.g. cell cultures) since they do not

absorb interfering species, are not incorporated by cells and do not aggregate in samples with high ion concentration. [123]

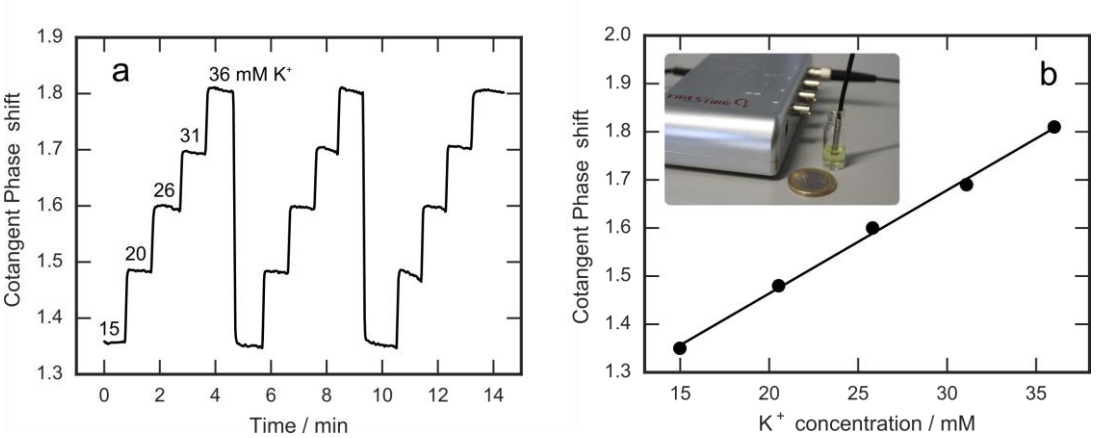

Figure 3.10: (**a**): Recorded phase shift values of the referenced sensor in BSA samples with different K^+ concentrations. (**b**): Calibration curve of the referenced sensor. The K^+ concentrations were determined using ICP-OES. The inlet shows the phase fluorometer (PyroScience Firesting) and an optical plastic fiber with a sensor spot attached to the distal end of the fiber with help of a metal cap.

To demonstrate the possible application of the newly developed sensing materials, we fabricated a fiber-optic sensor suitable for read-out with a commercially available phase fluorometer (Firesting, **Figure 3.10**). In order to ensure a reliable performance the fluorescence intensity of the **FI 3** was referenced against luminescence of Egyptian blue [124] using the so called dual lifetime referencing (DLR) scheme. [125] Briefly, the overall phase shift is determined only by the ratio of the intensities of the fluoroionophore and the analyte-insensitive long-lived reference luminophore. The sensor material was mounted on the top of an optical fibre using a metal ferrule (**Figure 3.10**). Fetal bovine serum (FBS) was used to demonstrate an application of this compact sensor in a complex sample solution. For calibration different FBS samples were prepared by spiking them with KCl solution and determining the real K^+ concentration via ICP-OES since the obtained FBS already contains a certain amount of K^+. The optical sensor shows reproducible performance in serum (**Figure 3.10a**). The calibration curve in the low mM range can be fitted linearly ($R^2 = 0.998$, **Figure 3.10b**). Three serum samples with unknown K^+ concentration were prepared and measured with the calibrated optode and reference measurements were performed again on ICP-OES. The values obtained with the optodes (21.42, 23.52 and 32.59 mM K^+ for samples 1, 2 and 3, respectively) showed excellent match with

the reference data (21.53, 23.71 and 32.27 mM, respectively) demonstrating ability of the sensor to accurately measure K^+ concentration in a complex sample media within the mM range. It should be also considered that optical components of Firesting currently show only limited compatibility with the emission spectrum of the **FI 3** so that simple modification of the emission filter is expected to dramatically (about 10-fold) improve already very good signal-to-noise ratio.

3.3 Conclusion

In this contribution we presented a straightforward and efficient strategy leading to optical K^+ sensors with tuneable properties. A palette of new fluoroionophores combines a selective aza-crown receptor and bright and photostable tetraaryl-BODIPY chromophores. Several representatives show absorption and emission in the red/NIR part of the spectrum, high molar absorption coefficients and fluorescence quantum yields. For the first time, the K^+ sensors were obtained by simple immobilization of the fluoroionophores into a stable and biocompatible hydrogel. Despite the simple design, the sensors show no leaching of the indicators, and feature fast and reproducible response. The "off" - "on" enhancement factor can be tuned over a broad range via introduction of electron-donating and electron-withdrawing substituents into the chromophore. The materials show excellent response to K^+ in aqueous solution with a very good selectivity over possible competing ions (e.g. Na^+) and no pH dependency in physiologically relevant conditions. Importantly, the new materials are applicable in a variety of formats, including planar sensor foils and spots, fiber-optic (micro)sensors and water-dispersible nanosensors and reliably operate even in complex samples such as serum. The nanoparticles are prepared via a simple procedure and enable extra- and intracellular quantification of potassium. We believe that the above properties of the new high-performance materials will make them valuable analytical tools in biomedical research and diagnostics.

Acknowledgements

The authors would like to thank Georg Michelitsch, Bianca Hörler, Josef Lechner, Nicole Steinmann and Lukas Heupl for support in synthesis of the indicators and receptors. We greatfully acknowledge Stefan Freudenberger and Nika Mahne from

the Institute for Chemistry and Technology of Materials (TU Graz) for the help with the cyclovoltametry measurements. Helmar Wiltsche and Monika Winkler of the Institute of Analytical Chemistry and Food Chemistry (TU Graz) are thanked for the help with the ICP-OES measurements. Financial support from European Commission ("Schema" Project No. 614002) is gratefully acknowledged.

3.4 Materials and Methods

^{1}H NMR spectra were recorded on a 300 MHz instrument from Bruker. MALDI-TOF mass spectra were recorded on a Micromass TofSpec 2E in refectron mode at an accelerating voltage of +20 kV. Absorption measurements were performed on a Cary 50 UV-Vis spectrophotometer from Varian. Luminescence spectra, calibrations, quantum yields and lifetimes (TCSPC) were measured on a Fluorolog-3 luminescence spectrometer (Horiba). Calibrations were performed using a peristaltic pump and a home-made flow through cell. Quantum yields were measured using the absolute method in an integrating sphere. QY and lifetimes of the indicators in solution were acquired in THF in presence trifluoroacetic acid (0.3 mM) to fully protonate the indicator. QYs for the foils were measured at 1000 mM aqueous KCl and 0.1 M aqueous HCl. Leaching was investigated by recording the absorption spectra of a foil during continuous pumping a 100 mM KCl solution (20 mM TRIS, pH 7.4) through the flow-through cell (10 ml/min). pKa determination was performed using a 20 mM universal buffer (citrate, acetate, BIS-TRIS and TRIS); pH was adjusted with HCl with help of a digital pH meter (Seven Easy, Mettler Toledo, www.mt.com) calibrated at 25 °C with standard buffers of pH 7.0 and 4.0 (WTW, www.wtw.com). K^+ concentrations of the fetal bovine serum were quantified with an axially viewed ICP-OES (Ciros Vision EOP, Spectro, Germany) using a cross-flow nebulizer, a Scott type spray chamber and a standard ICP torch with a 2.5 mm inner diameter injector. 1200 W RF power, 12 l min^{-1} outer gas flow, 0.7 l min^{-1} intermediate gas flow and 0.83 l min^{-1} nebulizer gas flow were used. K 404.721 nm emission line was used for quantification. Scandium (Sc 361.384 nm) was used as an internal standard at a concentration of 1 mg l^{-1}. Serum measurements with the optode were performed with a Firesting phase fluorometer (www.pyroscience.com) with at a modulation frequency of 4 kHz.

Electrochemical measurements were performed using a VMP3 electrochemical workstation (Biologic). The measurements were carried out at room temperature. A 1

mm diameter gold disc was employed as the working electrodes. A platinum wire served as the counter electrode. Measurements were performed using a Ag/AgCl reference electrode (BAS Inc). Ferrocene was used as reference.

Eudragit RL-100 copolymer (poly-(ethylacrylate-co-methylmethacrylate-co-trimethyl-aminoethyl methacrylate), M.W. ≈ 150 000 Da, 8.8 - 12% of quaternary ammonium groups) was from Degussa, Germany (www.evonik.com). Hydrochloric acid 37% (HCl), sodium sulfate anhydrous (Na_2SO_4) and all other solvents including the deuterated solvents were from VWR (www.vwr.com). Polyurethane hydrogel (Hydromed D4) was purchased from AdvanSource biomaterials (www.advbiomaterials.com). Poly(ethylene terephthalate) (PET) support Melinex 505 was obtained from Pütz (www.puetz-folien.com). Poly(styrene-blockvinylpyrrolidone) emulsion in water (38% w/w emulsion in water), lithium diisopropylamide (LDA) (2M in THF), 2,3-dichloro-5,6-dicyano-p-benzoquinone (DDQ), trifluoracetic acid, $Pd(dppf)Cl_2$, boron trifluoride etherate (BF_3OEt_2), water-free dichloromethane and Fetal Bovine Serum were purchased from Aldrich (www.sigmaaldrich.com). 5-Bromo-2-furaldehyde was purchased from ABCR (www.abcr.de). Buffer substances, KCl, NaCl, $CaCl_2$, NH_4Cl, $MgCl_2$ were from Roth (www.carlroth.com). Silica gel (0.04-0.063 mm) was acquired from Acros Organics (www.fishersci.com). Silanized Egyptian blue microparticles (trimethylsilyl form) were prepared according to a literature procedure. [124] All other chemicals were purchased from TCI Europe (www.tcichemicals.com). PMMA fibers (∅ 1 mm) were from Ratioplast (www.ratioplast.com).

3.5 Experimental

3.5.1 Synthesis

N-(4-Formyl-2-methoxyethoxyphenyl)aza-[18]crown-6 ether Synthesis of compound **S3** was performed according to literature procedure[103] and subsequent preparation of compound **S6** was performed according to Ast et at. [90]

3-Phenyl-2H-azirene Synthesis was performed according to literature using styrene as starting material. [126]

2-(4-Propylphenyl)-4-phenylpyrrol (2) 4'-Propylacetophenone (5.00 g, 30.8 mmol, 1 eq) was dissolved in 90 ml dry THF and cooled down to -78 °C. LDA (2M in THF) (17.05 mL, 1.1 eq) and 3-phenyl-2H-azirene (3.61 g, 30.8 mmol, 1 eq) were added dropwise. The mixture was stirred at -78 °C for 3 h, warmed up to RT, quenched with water and neutralized with diluted HCl. THF was removed under vacuum and the mixture was extracted with DCM, dried over Na_2SO_4 and the solvent removed under vacuum. Purification was performed by column chromatography (silica gel, eluent: CH+DCM = 1+1) to obtain the product as white crystals (5.687 g, 18.6 %). ^{1}H NMR (300 MHz, CD_2Cl_2) δ 8.49 (bs, 1H), 7.64 – 7.54 (m, 2H), 7.49 – 7.39 (m, 2H), 7.44 – 7.32 (m, 2H), 7.23 (d, J = 7.9 Hz, 3H), 7.16 – 7.08 (m, 1H), 6.87 – 6.79 (m, 1H), 2.63 (t, J = 7.7 Hz, 2H), 1.67 (p, J = 7.4 Hz, 2H), 0.99 (t, J = 7.3 Hz, 3H). DI-EI: m/z: [M^+] calcd for $C_{19}H_{19}N$, 261.1518; found, 261.1508

5-Chloro-3-phenyl-1,4-dihydroindeno[1,2-b] pyrrole (3) The synthesis of **3** was performed analogously to that of **2** but 1.0 g (6.0 mmol) of 5-chloro-1-indanone and 0.70 g (6.0 mmol) of 3-phenyl-2H-azirene were used instead. The product was isolated as white crystals (486 mg, 30 %). ^{1}H NMR (300 MHz, CD_2Cl_2) δ 8.56 (bs, 1H), 7.66 – 7.59 (m, 2H), 7.48 (s, 1H), 7.43 – 7.36 (m, 2H), 3.76 (s, 2H). DI-EI: m/z: [MH^+] calcd for $C_{17}H_{12}ClN$, 265.0658; found, 265.0656.

4,5-Dihydro-7-methoxy-3-phenylbenzo[g]indole (4) The synthesis of **4** was performed analogously to that of **2** but 5.06 g (28.7 mmol) of 6-methoxy-1-tetralone and 3.36 g (28.7 mmol) of 3-phenyl-2H-azirene were used instead. The product was isolated as greenish crystals (2.04 g, 25.8 %). ^{1}H NMR (300 MHz, CD_2Cl_2) δ 8.40 (bs, 1H), 7.51 – 7.44 (m, 2H), 7.43 – 7.35 (m, 2H), 7.29 – 7.20 (m, 1H), 7.13 (d, J = 8.4 Hz, 1H), 6.93 (d, J = 2.7 Hz, 1H), 6.84 (s, 1H), 6.76 (dd, J = 8.4, 2.6 Hz, 1H), 3.81 (s, 3H), 2.97 – 2.89 (m, 4H). DI-EI: m/z: [M^+] calc for $C_{19}H_{17}NO$, 275.1310; found, 275.1305.

Fluoroionophore FI 1 N-(4-Formyl-2-methoxyethoxyphenyl) aza-[18]crown-6 ether (357 mg, 0.809 mmol, 0.5 eq) and 2,4-dimethylpyrrole (169 mg, 1.78 mmol, 2.2 eq) were dissolved in 5 mL of anhydrous dichloromethane and 1 drop of trifluoroacetic acid was added. The mixture was shielded from light and stirred at RT for 48 hours,

DDQ (367 mg, 1.61 mmol, 2 eq) was added. After stirring for another 60 min, N,N-diisopropylethylamine (2.15 ml, 12.3 mmol, 15 eq) and BF_3OEt_2 (1.50 ml, 12.3mmol, 15 eq) were added and stirred for 60 min. The mixture was extracted with water, dried over Na_2SO_4 and the solvent removed in vacuo. The final product was purified by column chromatography and was obtained as purple crystals (117 mg, 22%). UV-VIS (DCM): λ_{max} (ε), nm ($M^{-1}cm^{-1}$) = 504 (53600). ^1H NMR (300 MHz, $CDCl_3$) δ 7.25 (m, 1H), 7.06 – 6.82 (m, 2H), 6.00 (s, 2H), 4.35 – 4.14 (m, 2H), 3.80 – 3.23 (m, 29H), 2.55 (s, 6H), 1.47 (s, 6H). MALDI-TOF: m/z: [MH^+] calcd for $C_{34}H_{49}N_3O_7$, 660.364; found, 660.389.

Fluoroionophore FI 2 The synthesis of **FI 2** was performed analogously to that of **FI 1** but 100 mg (0.226 mmol) of N-(4-formyl-2-methoxyethoxyphenyl) aza-[18]crown-6 ether and 120 mg (0.459 mmol) of 2-(4-propylphenyl)-4-phenylpyrrole were used instead. The product was isolated as purple crystals (58 mg, 26 %). UV-VIS (DCM): λ_{max} (ε), nm ($M^{-1}cm^{-1}$) = 571 (29900). ^1H NMR (300 MHz, CD_2Cl_2) δ 7.68 (d, J = 7.8 Hz, 4H), 7.21 (d, J = 7.9 Hz, 4H), 6.91 – 6.81 (m, 10H), 6.49 (s, 2H), 3.65 – 3.27 (m, 31H), 2.62 – 2.54 (m, 4H), 1.66 – 1.58 (m, 4H), 0.91 (t, J = 7.3 Hz, 6H). MALDI-TOF: m/z: [MK^+] calcd for $C_{60}H_{68}BF_2N_3O_7K$, 1030.4766; found, 1030.4915.

Fluoroionophore FI 3 The synthesis of **FI 3** was performed analogously to that of **FI 1** but 256 mg (0.582 mmol) of N-(4-formyl-2-methoxyethoxyphenyl) aza-[18]crown-6 ether and 299 mg (1.164 mmol) of 5-chloro-3-phenyl-1,4-dihydroindeno[1,2-b]pyrrole were used instead. The product was isolated as green crystals (125 mg, 21 %). UV-VIS (DCM): λ_{max} (ε), nm ($M^{-1}cm^{-1}$) = 640 (109300), 589 (20000). ^1H NMR (300 MHz, CD_2Cl_2) δ 8.32 (d, J = 8.3 Hz, 2H), 7.52 (d, J = 7.1 Hz, 4H), 7.06 – 6.85 (m, 10H), 6.75 – 6.57 (m, 2H), 6.47 – 6.29 (m, 1H), 3.78 – 3.34 (m, 31H), 1.27 (s, 4H). MALDI-TOF: m/z: [MH^+] calcd for $C_{56}H_{55}BF_2Cl_2N_3O_7$, 1000.3488; found, 1000.3410.

Fluoroionophore FI 4 The synthesis of **FI 4** was performed analogously to that of F**I 1** but 100 mg (0.226 mmol) of N-(4-formyl-2-methoxyethoxyphenyl) aza-[18]crown-6 ether and 124 mg (0.452 mmol) of 4,5-dihydro-7-methoxy-3-

phenylbenzo[g]indole were used instead. The product was isolated as green crystals (41 mg, 18 %). UV-VIS (DCM): λ_{max} (ε), nm ($M^{-1}cm^{-1}$) = 655 (87200), 601 (22000). ^{1}H NMR (300 MHz, CD_2Cl_2) δ 8.74 (d, J = 8.9 Hz, 2H), 7.11 – 6.70 (m, 17H), 3.89 (s, 6H), 3.73 – 3.34 (m, 31H), 2.91 – 2.68 (m, 4H), 2.44 – 2.32 (m, 4H). MALDI-TOF: m/z: [MNa^+] calcd for $C_{60}H_{65}BF_2N_3O_9Na$, 1020.4792; found, 1020.4977.

5-(3-Chloro-4-methoxyphenyl)-furan-2-carbaldehyde (5) 5-Bromo-2-furaldehyde (3.00 g, 0.017 mol, 1 eq), 3-chloro-4-methoxyphenyl) boronic acid (3.20 g, 0.017 mol, 1 eq) and Na_2CO_3 (60 ml of 2 M solution) and) were dissolved in 300 ml toluene and 60 ml ethanol. The mixture was degassed for 20 minutes by vigorously stirring under heavy Ar flow. After addition of the catalyst [1,1′-bis(diphenylphosphino)ferrocene] dichloropalladium(II) ($Pd(dppf)Cl_2$) (20.0 mg, 0.15 mol%) the reaction mixture was heated up to 80 °C and stirred for 18 hours under inert atmosphere. After cooling, the organic phase was washed with water and brine, dried over Na_2SO_4 and evaporated. The resulting residue was purified by column chromatography (silica gel, eluent: CH+DCM = 1+1 to 1+5) to obtain 5-(4-methoxyphenyl)-furan-2-carbaldehyde as a yellow solid (2.89 g, 71.1 %). ^{1}H NMR (300 MHz, $CDCl_3$) δ 9.63 (s, 1H), 7.84 (d, J = 2.2 Hz, 1H), 7.71 (dd, J = 8.6, 2.2 Hz, 1H), 7.31 (d, J = 3.7 Hz, 1H), 6.99 (d, J = 8.6 Hz, 1H), 6.74 (d, J = 3.7 Hz, 1H), 3.96 (s, 3H).

Ethyl-2-azidoacetate (6) Ethyl 2-bromoacetate (11.50 ml, 0.10 mol, 1 eq) and NaN_3 (13.20 g, 0.20 mol, 2 eq) were stirred in 300 ml acetone and 100 ml H_2O. After one hour the reaction solution was extracted with DCM and brine (3x), the organic phase dried with Na_2SO_4 and concentrated under vacuum and yields in a colourless liquid (12.53 g, 93.9 %). ^{1}H NMR (300 MHz, $CDCl_3$) δ 4.27 (q, J = 7.1 Hz, 2H), 3.87 (s, 2H), 1.32 (t, J = 7.1 Hz, 3H).

2-(3-Chloro-4-Methoxyphenyl)-4H-furo[3,2-b] pyrrole-5-carboxylic acid ethyl ester (7) 5-(3-Chloro-4-methoxyphenyl)-furan-2-carbaldehyde (2.02 g, 8.54 mmol, 1 eq) and ethyl 2-azidoacetate (4.0 ml, 34.7 mmol, 4 eq) were dissolved in 120 ml anhydrous ethanol and cooled down to 0 °C. Sodium ethoxide (20 w% in ethanol, 25 ml, 34.7 mmol, 4 eq) was added dropwise over 30 min and stirred for 3 h. The

reaction mixture was poured on 250 ml sat. NH_4Cl solution, the precipitate collected and washed with H_2O. The intermediate product was dissolved in 85 ml toluene, refluxed for 4 hours. A precipitation forms after cooling down to RT and the solvent was removed using rotary evaporator. Column chromatography (silica gel, eluent: CH+EE = 5+1 to 1+1) was performed and the product was obtained as an orange solid (1.44 g, 52.7 %). ^{1}H NMR (300 MHz, $CDCl_3$) δ 8.86 (bs, 1H), 7.73 (s, 1H), 7.58 (d, J = 8.6 Hz, 1H), 6.95 (d, J = 8.7 Hz, 1H), 6.79 (s, 1H), 6.59 (s, 1H), 4.36 (q, J = 7.1 Hz, 2H), 3.93 (s, 3H), 1.39 (t, J = 7.2 Hz, 3H). DI-EI: m/z: [M^+] calcd for $C_{16}H_{14}NO_4Cl$, 319.0611; found, 319.0599.

2-(3-Chloro-4-Methoxyphenyl)-4H-furo[3,2-b] pyrrole-5-carboxylic acid (8) 2-(3-Chloro-4-methoxyphenyl)-4H-furo[3,2-b] pyrrole-5-carboxylic acid ethyl ester (780 mg, 2.44 mmol, 1 eq) was dissolved in 25 ml ethanol and a NaOH (7 ml of 2.5 M solution) was added and the mixture was refluxed for 1 h. After cooling, HCl conc. was added resulting in a green precipitate. The resulting precipitate was filtered and washed with H_2O and dried in the oven at 60 °C overnight (548 .7 mg, 70 %). 1H NMR (300 MHz, DMSO-d6) δ 11.60 (bs, 1H), 7.87 (d, J = 2.2 Hz, 1H), 7.74 (dd, J = 8.7, 2.2 Hz, 1H), 7.21 (d, J = 8.7 Hz, 1H), 7.11 (s, 1H), 6.71 (s, 1H), 3.89 (s, 3H). DI-EI: m/z: [M+] calcd for $C_{14}H_{10}NO_4Cl$, 291.0298; found, 291.0299.

Fluoroionophore FI 5 2-(3-Chloro-4-methoxyphenyl)-4H-furo[3,2-b] pyrrole-5-carboxylic acid (127.9 mg, 0,438 mmol, 1 eq) and N-(4-formyl-2-methoxyethoxyphenyl) aza-[18]crown-6 ether (96.2 mg, 0.218 mmol, 0.5 eq) were dissolved in 3 ml conc. trifluoroacetic acid under Ar atmosphere. The mixture was stirred at 50 °C for 1 h, $POCl_3$ (0.50 mL) was added, the stirred for 10 min at 50 °C and precipitated slowly into cold water. The precipitate was collected and transferred into a Schlenk tube and dried via vacuum and 5 ml water-free DCM was added under an Ar atmosphere. N,N-Diisopropylethylamine (305 µl, 1.75 mmol, 4 eq) and BF_3OEt_2 (220 µL, 1.75 mmol, 4 eq) were added to the solution and after 60 min stirring, the solution was extracted with H_2O, dried over Na_2SO_4 and concentrated under vacuum. The crude product was purified using column chromatography (silica gel, eluent: DCM+MeOH = 100+1 to 100+20) to obtain the dye as green blue crystals (35 mg, 8.3 %). UV-VIS (DCM): λ_{max} (ε), nm ($M^{-1}cm^{-1}$) = 670 (195600), 616 (48500). ^{1}H NMR (300 MHz, $CDCl_3$) δ 7.80 (d, J = 2.2 Hz, 2H), 7.66 (dd, J =

8.6, 2.2 Hz, 2H), 7.16 (d, J = 4.8 Hz, 2H), 6.98 (d, J = 8.8 Hz, 2H), 6.87 (s, 2H), 6.34 (s, 2H), 4.22 (s, 2H), 3.94 (s, 6H), 3.82 – 3.49 (m, 26H), 3.43 (s, 3H). MALDI-TOF: m/z: [MNa^+] calcd for $C_{48}H_{50}BCl_2F_2N_3O_{11}Na$, 986.2789; found, 986.4067.

3.5.2 Preparation of Sensing Materials

Planar Sensor Films An appropriate amount of the indicator was dissolved in a hydrogel D4 stock solution (10 wt. % in THF). Sensor films were prepared by knife coating of these "sensor cocktails" onto dust-free PET foils (25 µm wet film thickness). Dye concentrations for calibrations and QY determination were 0.2 wt. % and for leaching experiment 1 wt. % in respect to the polymer.

Fiber-Optic Sensor 0.5 mg FI 3, 20 mg of silanized Egyptian blue and 100 mg hydrogel D4 were dissolved in 1 g THF. The "cocktail" was knife coated onto a dust-free PET foil (75 µm wet film thickness). A sensor spot (approx. 2 mm diameter) was stamped out and fixed with a metal cap on a 1 m PMMA fiber.

RL100 Particles 100 mg Eudragit RL100 were dissolved in 50 ml acetone, and indicator dye FI 3 (1 mg) was added. 250 ml water was added quickly under vigorous stirring (3 s); acetone was removed using rotary evaporator and the particle dispersion was further concentrated to a volume of 50 ml. For calibrations 0.5 ml of particle dispersion were added to 2 ml of KCl aqueous solutions.

PS/PVP Particles 213 mg of the PS/PVP emulsion (38 % emulsion in water) was diluted with 25 ml H_2O and 20 ml EtOH. FI 3 (1 mg, 1 wt.%) was dissolved in 20 ml EtOH and was added dropwise under vigorous stirring into the emulsion of the polymer. The emulsion was concentrated under reduced pressure to remove all ethanol and partly water. It was then diluted with water up to 10 mL overall volume. For calibration 20 µl of the solution were added to 1980 µl buffered KCl solution.

3.6 Supporting Information

Synthesis of the Receptor

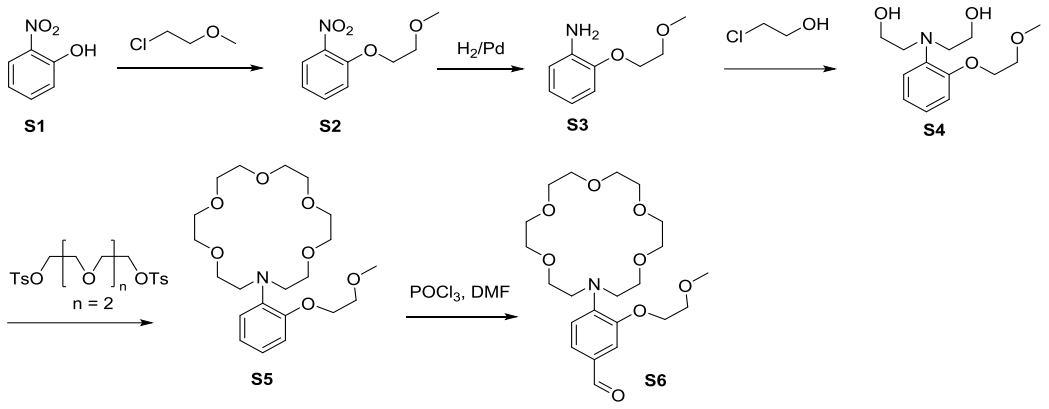

Figure S - 3.1: Synthesis of **S3** was performed according to literature procedure[103] and subsequent preparation of **S6** was performed according to Ast et. al.[90]

Table S-3.1: Summary of spectral properties of published fluoroionophores.

Indicator	Absorption Maxima / nm	Emission Maxima / nm	Extinction Coefficient / ($M^{-1}cm^{-1}$)	QY / %	Solvent / Sensor Format	Ref.
Coumarin Fluorophore 1	420	493	n.d.	18.4 at 160 mM K^+	1% DMSO / water	90
Coumarin Fluorophore 2	422	500	n.d.	6.4 at 160 mM K^+	1% DMSO / water	90
TAC-Lime dex = TAC-BODIPY derivate	n.d.	535 *	n.d.	n.d.	water	111
TAC-Red	550 *	570 *	n.d.	n.d.	water	106
KS6 (styrylated BODIPY)	567	572	30 500 at 567 nm	14.4 at 150 mM	water	127
Di-BODIPY	498	512	140 000 at 509 nm	n.d. with K	EtOH	109
TAC-BODIPY	n.d.	512	n.d.	43 at 150 mM K^+	water/MeCN 4/1	85
4-amino-naphthalimide	450 *	525 *	n.d.	n.d.	PHEMA -PAM	78
TAC-Crimson (xanthythilium derivate)	578	597	n.d.	n.d.	water	105
2-dicyanomethylene-3-cyano-4,5,5-trimethyl- 2,5-dihydrofuran derivate	560	650	38 400 at 560 nm	0.52 at 150 mM	water	112

* Determined by the corresponding spectra.

Single Photon Counting of the Fluoroionophores

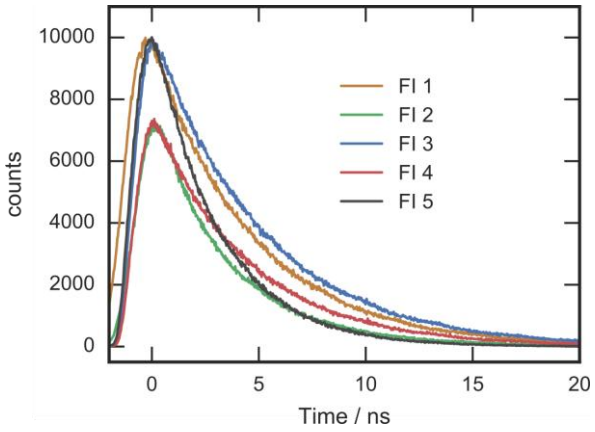

Figure S - 3.2: Single photon counting measurements of the fluoroionophores in THF with TFA. The decay curve was fitted mono-exponentially.

Leaching Experiment

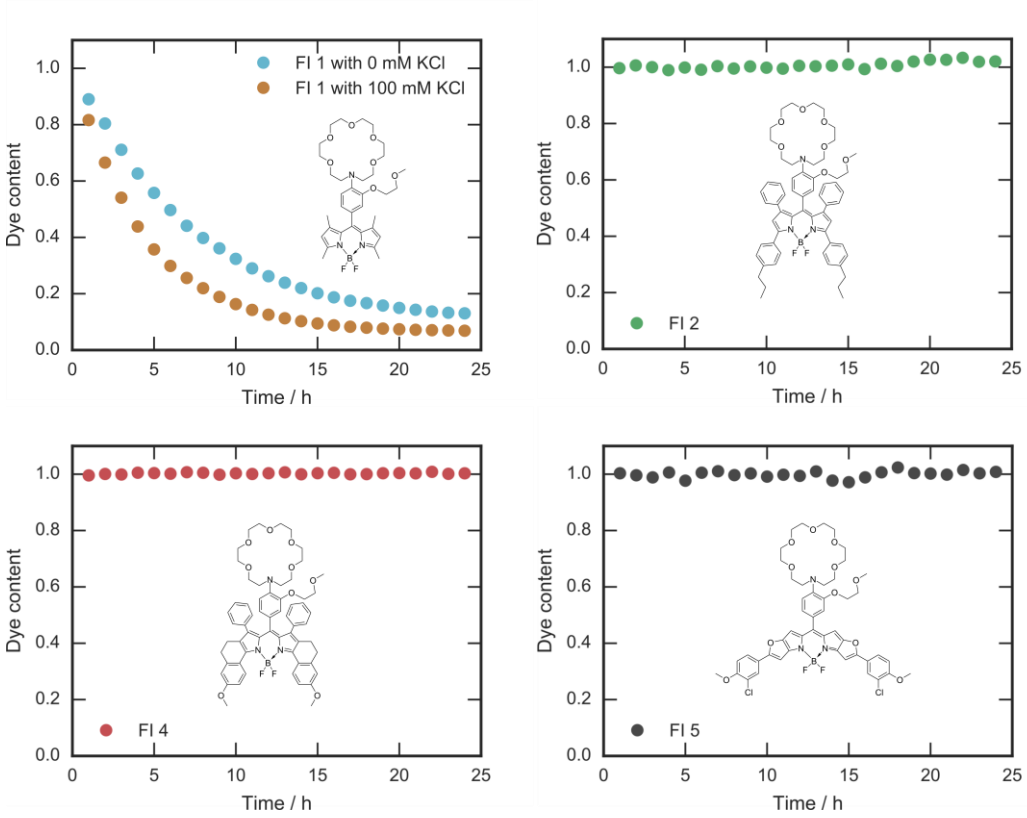

Figure S - 3.3: Normalized absorption maxima of fluoroionophores immobilized in hydrogel D4. 100 mM KCl solution was pumped through a flow-through cell for 24 hours.

Cyclic Voltammetry Measurements

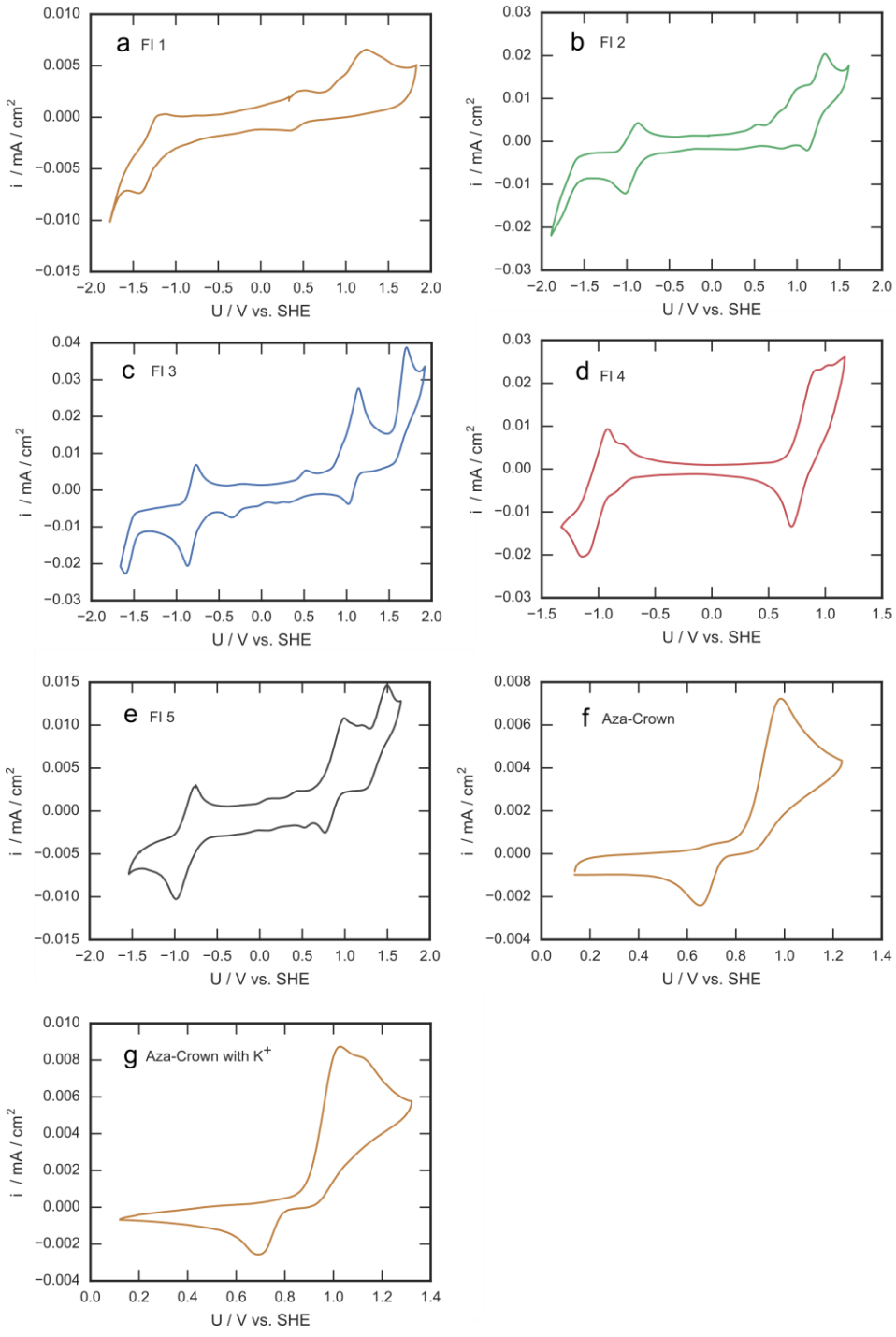

Figure S - 3.4: Cyclic voltammograms of different fluoroionophore (**a**)-(**e**) and the aza-crown ether (compound S5) without K^+ (**f**) and with 10 eq $KClO_4$ (**g**) in DCM.

Benesi-Hildebrand Equation

$$\frac{F_o}{F_o - F} = \frac{F_o}{F_o - F_{complex}} + \frac{F_o}{F_o - F_{complex}} \cdot K_d \cdot \frac{1}{[M]}$$ Equation S3.1

Benesi-Hildebrand Plots

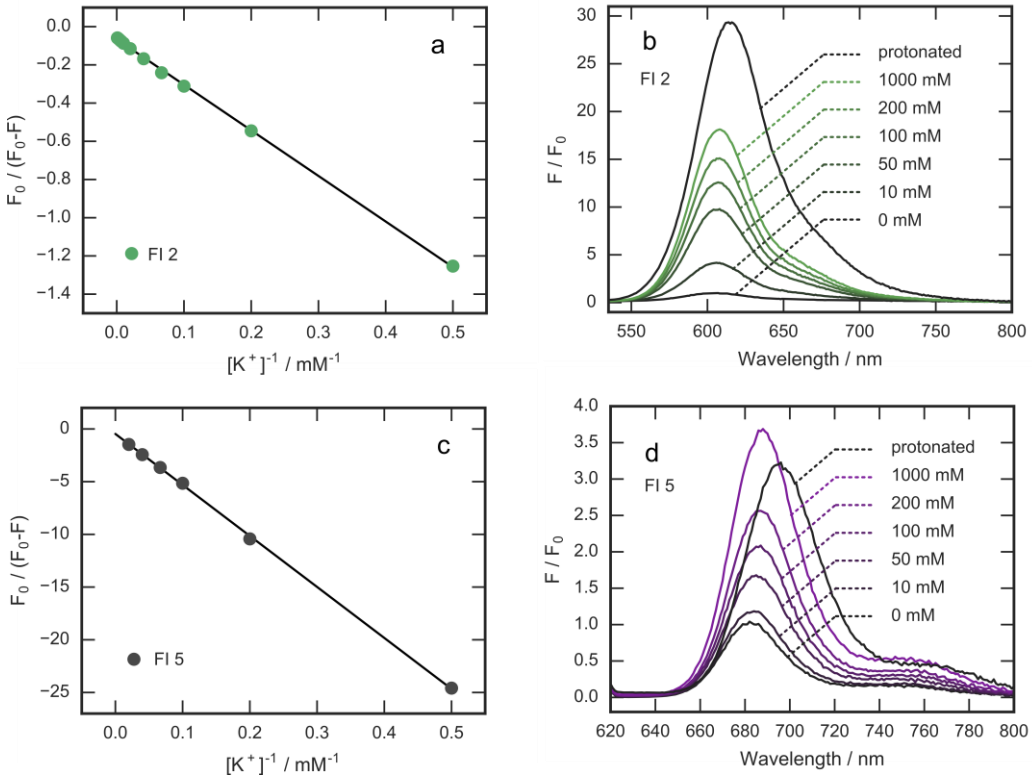

Figure S - 3.5: (**a**) and (**c**): Benesi-Hildebrand plot for **FI 2** and F for the determination of Kd via the slope. R^2 of the linear fit is >0.989 for all materials. (**b**) and (**d**): Exemplar normalized emission spectra of **FI 2** and **FI 5** with different K^+ concentrations and protonation with 0.1 M HCl.

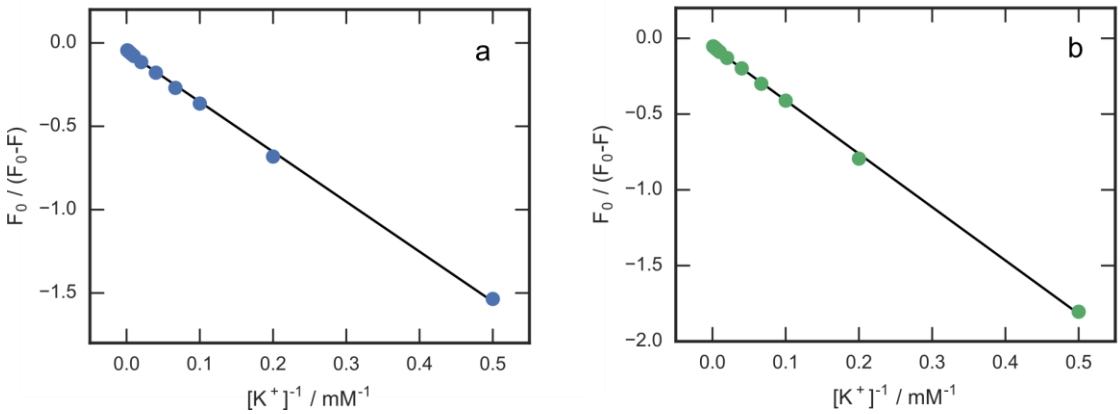

Figure S - 3.6: Benesi-Hildebrand plot for **FI 3** immobilized in D4. R^2 of the linear fit in the Benesi Hildebrand plot is > 0.998 for both. (**a**) with 0 mM NaCl background (**b**) with 150 mM NaCl background.

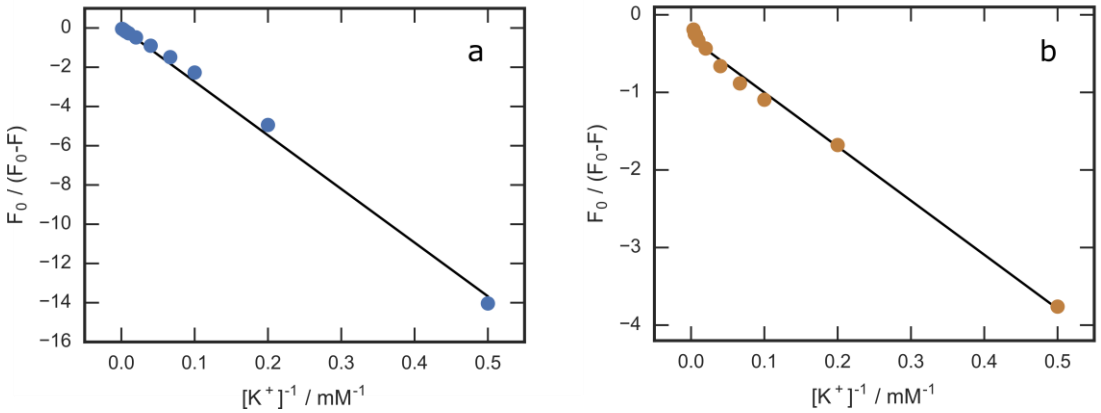

Figure S - 3.7: (**a**) Benesi-Hildebrand plot for **FI 3** immobilized in positively charged RL100 particles. R^2 of the linear fit of the Benesi Hildebrand plot = 0.999. (**b**) Benesi-Hildebrand plot for **FI 3** immobilized in PS/PVP particles. R^2 of the linear fit of the Benesi Hildebrand plot = 0.977.

Na^+-Cross Sensitivity

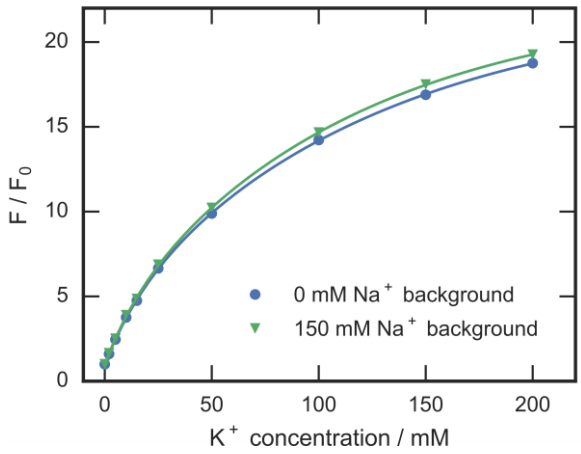

Figure S - 3.8: Influence on the calibration curve of 150 mM NaCl compared to 0 mM NaCl solutions.

SPC in Hydrogel D4

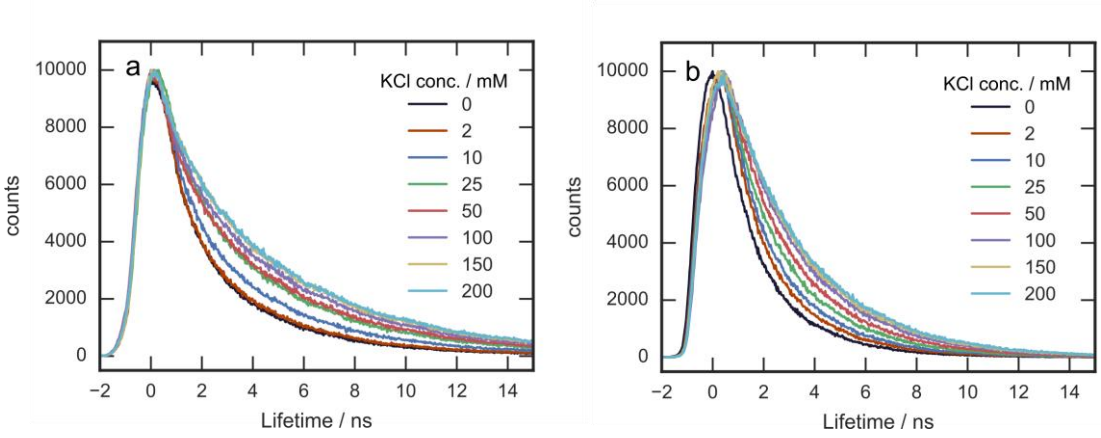

Figure S - 3.9: Single photon counting measurement of **FI 4** (**a**) and **FI 5** (**b**) in hydrogel D4. The decay curve was fitted mono-exponentially

Future Prospect and Outlook

In this publication we developed a series of new fluoroionophores and prepared novel solid state sensing materials. The fluoroionophores were based on the same receptor unit but differed by the chromophore. Different structural elements and substituents of the chromophore had major influence on the PET efficiency and spectral properties. FI3 (rigidified pyrrole with electron withdrawing chlorine substituent) proved to be the best candidate for future projects.

Using the FI3 fluoroionophore, we were able to show a proof of concept experiment for its potential use in clinical diagnostics. The sensor requirements within this application are for the selective measurement of low K^+ concentration (5 mM) with a high Na^+ background (150 mM). The sensitivity of the FI3 based sensing material is not ideal for measuring such low concentrations (**Figure 3.5**). The main factor determining the sensitivity is the binding stability of the crown ether receptor with the K^+ ion. Therefore, we decided to start a project dealing with the synthesis and characterisation of new receptors and to study the suitability for measuring K^+ in extracellular media. This was conducted by Tanja Rappitsch during her master thesis and will be briefly summarized here.[128]

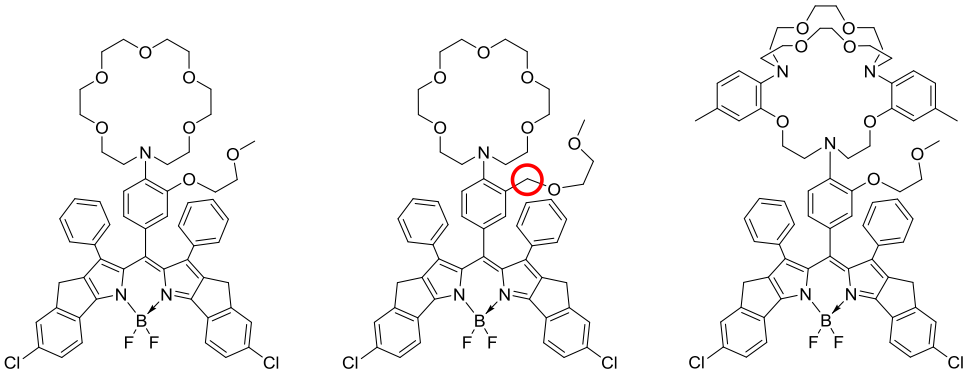

Figure 3.11: Prepared fluoroionophores with different receptor units for the measurement of K^+ ions.

It is known, that the side arm of the receptor used in FI3 is a crucial structural element for increasing the binding stability and selectivity towards K^+.[90] As the size of the crown ether is already suitable and should remain unchanged, we aimed to improve the complexation behaviour by making synthetic modifications to the side arm.

The initial idea was to incorporate an additional methylene group between the aromatic ring and the ether group. This should enhance the flexibility of the side arm and consequently provide more degrees of freedom to adjust the arm for perfect interaction with a complexed ion. This receptor was successfully synthesized and a fluoroionophore with the same chromophore moiety as used with FI 3 was prepared ($K^{2n\ Gen}$-FI3, **Figure 3.11**).

The state-of-the-art optical detection of extracellular K^+ currently utilizes a triazacryptand receptor (TAC) which was developed by He et al. and is commercially available.[103] Thereupon, we also prepared an indicator using the TAC crown to have a comparison to commonly used K^+ sensors (TAC-FI3, **Figure 3.11**).

Calibration of the new fluoroionophores were performed in buffered solution with additional ethanol for solubility of the dye. Measurements were performed with and without a constant 150 mM NaCl background to receive information about the cross sensitivity towards Na^+ ions (**Figure 3.12**).

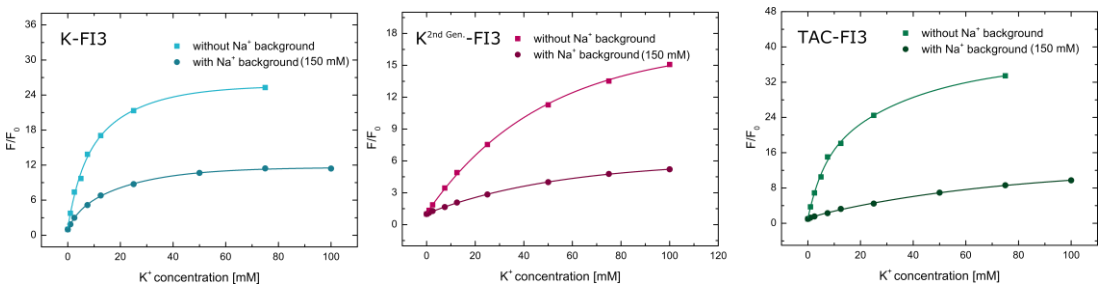

Figure 3.12: F/F_0 calibration curves for K-FI3, $K^{2nd\ Gen.}$-FI3 and TAC-FI3 dissolved in $EtOH/H_2O$. The values of F and F_0 were taken at λ = 645 nm.

All of the presented indicators show good fluorescence increase with increasing K^+ concentration. Furthermore, when Na^+ is present the sensor response and sensitivity is decreased as Na^+ can also be complexed in the crown ether and therefore blocks the receptor for K^+. The increase of flexibility of the side arm in $K^{2nd\ Gen}$-FI3 does not yield a higher sensitivity. In contrast, the sensitivity of the sensor in lower K^+ concentration is reduced, compared to K-FI3. Surprisingly, comparison of K-FI3 with the state-of-the-art receptor (TAC-FI3) reveals that the sophisticated structure and additional complexing structural elements of the TAC crown do not increase the binding stability.

However, as the TAC receptor was never compared to any other receptor unit, it was always assumed that simpler crown ethers have worse sensitivity. In this project, it could be shown that a simple lariat ether group yielded in similar or better binding constants.

Chapter 4

Sodium-Selective Fluoroionophore-based Optodes for Seawater Salinity Measurements

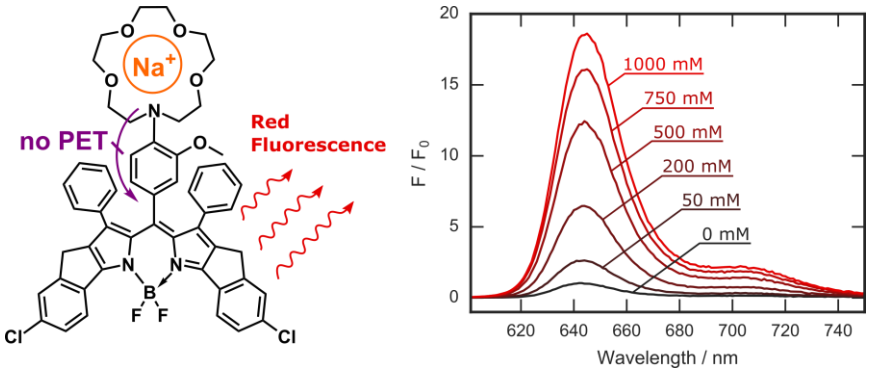

Preface for the Manuscript

This manuscript describes the development of novel Na^+-sensitive fluoroionophores and the application of this sensing material in marine research.

The fluoroionophores presented in this thesis are based on two separate units (the receptor and the chromophore) which can be exchanged independently and therefore represent a simple building block system. For this work, we used the chromophore moiety already introduced in the last publication (**chapter 3**) that showed the most suitable sensing properties. As already explained in **section 2.3.2**, the sensitivity of a crown ether towards a cation is mostly dependent on the size of the cavity. With this in mind, we synthesized a smaller crown ether compared to the K^+-selective indicator to obtain a Na^+ selective fluoroionophore.

Additionally, we conducted a study into the influence of different polymer hydrogels on sensor performance as the sensing mechanism is highly dependent on the environment of the fluoroionophore.

To show a potential application of the sensor, we prepared referenced sensors which were used for the determination of seawater salinity in the Baltic Sea during a field trip. Hereby, we could demonstrate salinity measurements in surface water, but also conducted profiling measurements. Both were in good agreement with reference measurements.

This manuscript demonstrates the versatility of the building block system of the developed fluoroionophores during this thesis.

Manuscript

Sodium-Selective Fluoroionophore-based Optodes for Seawater Salinity Measurements

This chapter was published as *Full Paper* in

Analytical Chemistry

Authors: Bernhard J. Müller, Tanja Rappitsch, Christoph Staudinger, Christian Rüschitz, Sergey M. Borisov* and Ingo Klimant

Graz University of Technology, Institute of Analytical Chemistry and Food Chemistry, Stremayrgasse 9, 8010 Graz, Austria

E-mail: sergey.borisov@tugraz.at

Keywords: Optical Sensor, Sodium, Salinity, Photoinduced Electron Transfer, Fluoroionophore, Hydrogel, Fluorescence

Abstract A new fluorescent sensor for Na^+ is presented. The sensor relies on a Na^+ selective fluoroionophore based on a bright red-emitting BODIPY chromophore. The fluorescence of the fluoroionophore is enhanced upon binding of Na^+-ions to the highly selective aza-crown ether receptor due to reduction of the photoinduced electron transfer (PET) quenching. Solid state sensing materials were prepared by physically embedding the fluoroionophore into water-swellable biocompatible polymer matrices (polyurethane hydrogels), thus enabling continuous measurements of aqueous samples. Despite the simple design, the sensor showed no leaching of the indicator and featured fast and reversible response. Among different polyurethane hydrogels investigated, the hydrogel D1 featuring the highest water uptake was found to be the most suitable due to the highest dynamics between "off" and "on" states. Due to little or no cross sensitivity to other ions (e.g. Mg^{2+}, Ca^{2+}, K^+) and its insensitivity to potential changes in pH, this sensor is promising for use in clinical diagnostics and for biological and marine applications. Fiber optic sensors based on referenced read-out with a compact phase fluorimeter were prepared. To demonstrate

their practical applicability, the sensors were used to determine the salinity in the seawater and brackish water of the Baltic Sea.

4.1 Introduction

Optical sensors (Optodes) are promising analytical tools for *in situ* measurements, with several properties making them advantageous to the conventional analytical methods. They are non-invasive, disposable, can be miniaturized easily and when combined with other sensors, they enable multi-analyte measurements.[129] Moreover, they allow imaging of analytes over a certain area or even in small volumes (e.g. cells).[13,130] Optical sensing materials are widely used in various formats such as mini- and microsensors [131,132,133,134], planar sensor foils [135,136] and nanoparticles [137,77].

There is significant interest in development of new optical sensors for a variety of analytes, for instance oxygen, pH, carbon dioxide, reactive oxygen species or ions.[76] Ions play an essential role in all living organisms and natural processes.[68] Sodium is a crucial factor for physiological pathways in the biomedical field. It is the most abundant ion in the extracellular medium (more than 100 mM) and is maintained at a low intracellular concentration, creating an osmotic pressure which is crucial for the transmission of nerve impulses.[138] Determination and visualisation of the transport of ions between the inner and outer compartment of the cell is of high interest for biological research and can be achieved by utilizing fluorescent probes. [127,78,139,140] Optical sensors for cations can be divided into two main groups. The first group relies on use of hydrophobic membrane (poly(vinyl chloride) with plasticizer) containing an analyte selective ionophore and a pH indicator. Selective extraction of the target

analyte into the lipophilic membrane triggers a release of an equivalent amount of protons out of the sensing film, thereby changing the pH which can be measured by a lipophilic pH indicator.[56]

In the second group the fluorescent reporter and the receptor are combined in a single molecule (fluroionophore, FI). FIs operate in aqueous media and have been mostly applied as water-soluble probes. Several FI-based probes for Na^+ have been reported [141,142,71,143,66,82,144,145] primarily in the context of intracellular measurements. The sensing mechanism is based on intramolecular quenching via photoinduced electron transfer (PET).[101,146,147] The most popular and commercially available sodium FIs are

SBFI (sodium binding benzofuran isophthalate) and SG (sodium green).[138,148] They consist of a diaza-15-crown-5 ether as a receptor coupled to a benzofuran or a fluorescein fluorophore, respectively. However, all of these indicators possess a relatively short excitation wavelength (below 500 nm), leading to high (and variable) levels of background fluorescence from optical components, carrier polymers, and biological samples. Fluorescein is known for its poor photostability. Therefore, new FIs with longer wavelengths of absorption and emission (> 600 nm) are of particular interest as they allow measurements in highly scattering and absorbing media (e.g. tissues) as well as in autofluorescent media (e.g. biological samples).

Design of FI-based ion sensors is a challenging task since the FI should not only retain its sensitivity upon immobilization but also show no leaching out of the matrix. Thus, the matrix should be hydrophilic enough to ensure sufficient PET efficiency (which is known to decrease in a low polarity environment) but hydrophobic enough to be a good solvent for the non-covalently immobilized amphiphilic FI or contain functionalities for the covalent coupling of a hydrophilic FI. So far, only very few published indicators were immobilized in a polymer matrix, all of them short wavelength FIs.[149,79,150]

In this contribution, we present a novel sensor for Na^+-ions based on hydrogel-immobilized fluoroionophore. We take advantage of the complexation properties of a crown ether receptor that has an appropriate size to selectively bind Na^+-ions. This receptor is linked to a red light emitting BODIPY chromophore which features high brightness and excellent photostability. The aromatic amino group in the receptor acts as efficient fluorescence quencher in the absence of the analyte but the fluorescence is dramatically enhanced upon complexation. Based on the correlation between Na^+ concentration and seawater salinity, we demonstrate applicability of the new optical sensor for oceanographic applications.

4.2 Results and Discussion

4.2.1 Synthesis and Photophysical Properties of the New Fluoroionophore

The synthesis of the fluoroionophore is based on a convenient approach previously demonstrated for K^+ FIs.[151] The sensitivity towards the analyte is controlled by the aromatic crown-ether receptor unit, whereas the spectral properties are determined by the BODIPY chromophore. Condensation of the pyrrole and the aromatic aldehyde, subsequent oxidation using DDQ and complexation with BF_3-etherate yields the new fluoroionophore (**Na-FI**) in a simple one-pot reaction (**Figure 4.1**).

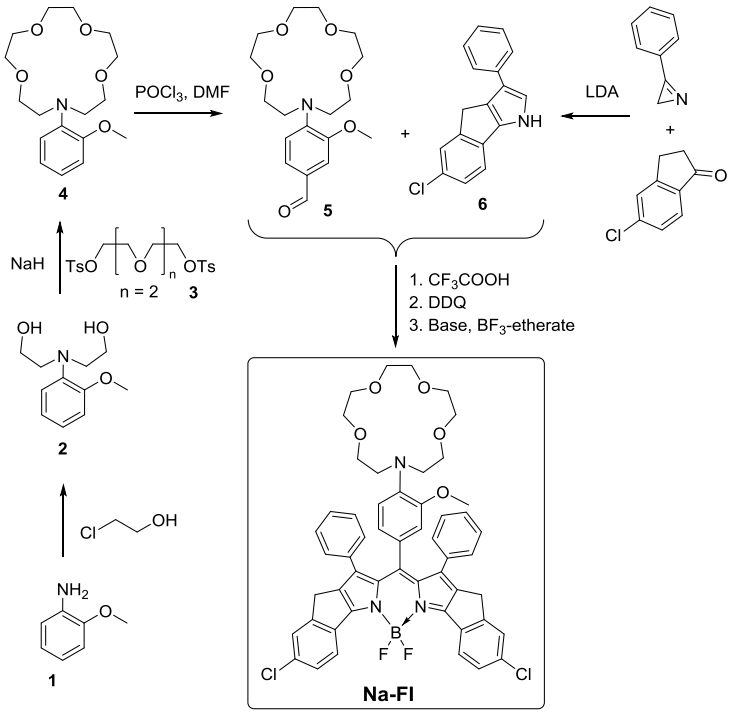

Figure 4.1: Synthesis of the Na^+ fluoroionophore (**Na-FI**).

As a receptor, we chose a methoxy-substituted N-phenyl-aza-crown ether due to its optimal binding constant towards Na^+ ions.[152] This crown ether was already used as the recognition unit in Na^+ FIs based on naphthalimide [150] and triazole–coumarin derivates.[79] Based on our experience with K^+ FIs, a rigid tetraaryl-BODIPY dye was selected since the rigidification and planarization of the chromophore results in a bathochromic shift of absorption and emission and ensures excellent fluorescence

brightness.[151] Indeed, the FI shows efficient absorption and emission in the red/NIR region of the electromagnetic spectrum (**Figure 4.2**). The absorption and emission bands are very sharp which is typical for BODIPY dyes.[82] It also features excellent luminescence brightness due to high molar absorption coefficient (130,000 $M^{-1}cm^{-1}$) and a quantum yield of 69 % in the "on" state (fully protonated in THF using trifluoroacetic acid). The introduction of chlorine favourably affects the PET efficiency, as the electron withdrawing character enhances the reduction potential of the fluoroionophore in the excited state.[151] Therefore, the fluorescence is almost completely "switched off" when no analyte is present.

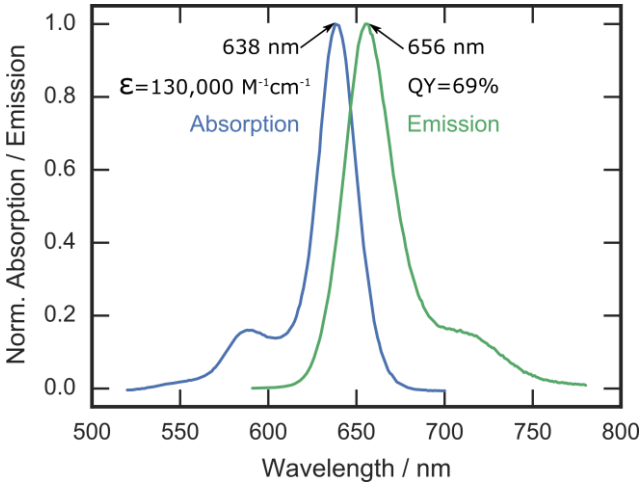

Figure 4.2: Normalized absorption and emission spectra of the fluoroionophore dissolved in dichloromethane. Molar absorption coefficient was determined in dichloromethane and the quantum yield in tetrahydrofuran with 0.3 mM trifluoroacetic acid to ensure full protonation of the crown ether.

4.2.2 Solid State Sensing Materials

To enable continuous measurement, it is necessary to immobilize the FI into a polymer matrix. Although covalent coupling represents the most efficient strategy to eliminate indicator migration and leaching, several additional synthetic steps would be necessary to introduce the required functionalities which in turn may negatively affect the photophysical properties of the FI. Therefore, we preferred non-covalent immobilisation.

This can be achieved by simply dissolving the indicator dye and the polymer in an organic solvent and knife-coating of the solution onto a transparent and inert poly(ethylene-terephthalate) foil, which acts as sensor support. The polymer matrix

acts as a solvent for the indicator dye and therefore cannot be too hydrophobic (due to poor PET in hydrophobic environment) or too hydrophilic, as the FI can either leach out of the matrix or aggregate. Therefore, we chose commercially available water swellable hydrogels (known under the name Hydromed D1, D4 and D7) which are ether-based polyurethanes with hydrophobic and hydrophilic blocks. Depending on the ratio of the blocks, they show different swelling (water uptake) behaviour: swollen hydrogels D1, D4 and D7 contain 70 %, 50 % and 30 % water, respectively.[153] Importantly, no leaching or aggregation of the immobilized FI was observed upon continuous rinsing of the sensor foil with a 500 mM NaCl solution for several hours even in case of the most hydrophilic hydrogel D1 and high dye concentration (1 wt.%). (**Figure S - 4.1** and **Figure S - 4.2**, Supporting Information).

4.2.3 Influence of the Polymer Matrix

As expected, the immobilized FIs show low fluorescence intensity in the absence of the analyte (**Figure 4.3**). The fluorescence intensity of the indicator dye is enhanced in the presence of Na^+ due to the decrease of the PET effect. The sensing behaviour of the FI is strongly influenced by the hydrophilicity of the hydrogel used. The fluorescence enhancement factor is the highest (12-fold at 1000 mM Na^+) in more hydrophilic hydrogel D1. In case of the most hydrophobic hydrogel D7, fluorescence is enhanced only 4-fold in the same conditions. Hydrogel D4 occupies intermediate position (**Table 4.1**, **Figure S - 4.3,** Supporting Information).

In the absence of Na^+, fluorescence quantum yields are very similar for all the hydrogels (**Table 4.1**). However, at high Na^+ concentration (1000 mM), the quantum yields are very different: D1 > D4 > D7. The same trend is observed for fluorescence enhancement in acidic media. pH calibration curves show, that the FI is completely "switched on" only in case of hydrogel D1 and D4 (QY of 86 % and 84 % respectively in 0.1 M HCl) (**Figure S - 4.4**, Supporting Information). In case of D7, a QY of 50 % was determined in 0.1 M HCl. However, it was not possible to fully protonate the FI with even highly concentrated HCl solutions (**Figure S - 4.4**, Supporting Information). The dye appears to be located in more hydrophobic domains, which are not fully accessible to Na^+-ions or protons. This difference in analyte accessibility is indicated by the decrease of the apparent pK_a value and decrease of QYs in 1000 mM Na^+ with increase in the hydrogel hydrophobicity (**Table 4.1**). Among the investigated hydrogels, D1 has the highest degree of swelling and therefore best accessibility of the FI to Na^+. Even though the QY in

hydrogel D1 in presence of 1000 mM Na^+ is 23 %, the overall brightness is very good considering high molar absorption coefficients. High brightness allows reduction of the thickness of the sensing layer which is beneficial for the development of sensors with fast response time. An LOD of 1.3 mM Na^+ was calculated when using hydrogel D1 (3 x standard deviation of the blank). Due to the best performance, the sensing material based on hydrogel D1 was chosen for further experiments.

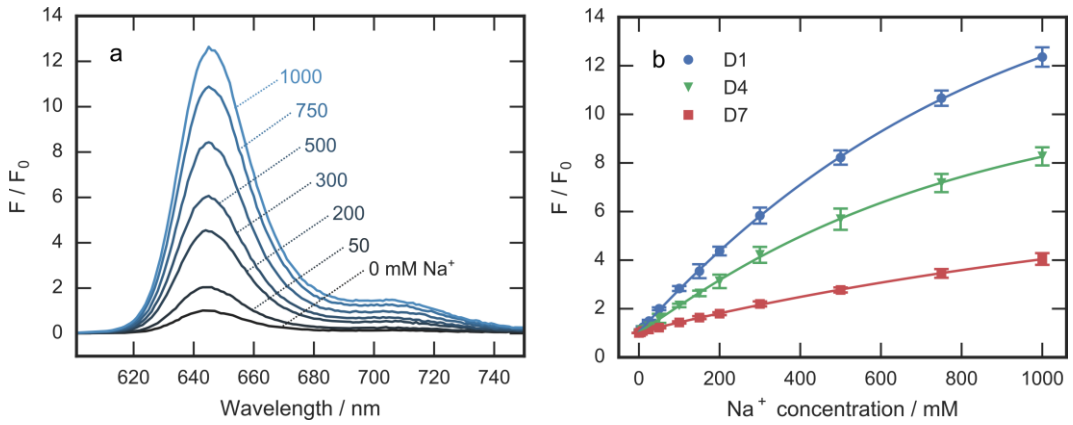

Figure 4.3: a: Exemplar normalized emission spectra of Na-FI in hydrogel D1 at different Na^+ concentrations (20 mM TRIS buffer pH 7.4) **b:** F/F_0 calibration curves for the indicator immobilized in hydrogel D1, D4 and D7. The values of F and F_0 were taken at λ = 645 nm.

Table 4.1: Fluorescence intensity ratios F/F_0 at 645 nm and fluorescence quantum yields for Na-FI in different hydrogel matrices.

	F/F_0 at 1000 mM NaCl	QY at 0 mM NaCl	QY at 1000 mM NaCl	QY at 0.1 M HCl	Apparent pK_a value
Hydrogel D1	12.4	0.01	0.23	0.86	3.03
Hydrogel D4	8.3	0.01	0.16	0.84	2.60
Hydrogel D7	4.0	0.02	0.09	0.50	1.46*

*pK_a was estimated assuming a QY of 0.85 in the fully protonated state to enable a sigmoidal fit.

4.2.4 Cross-Sensitivity of the Sensing Material to Cations and Protons

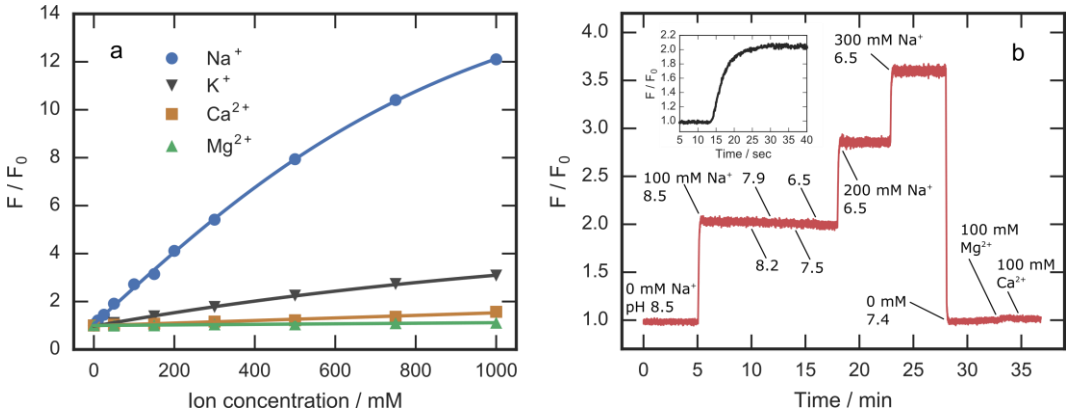

Figure 4.4: a: Cross-sensitivity of Na-FI/D1 to common cations at pH 7.4 (20 mM TRIS buffer). **b:** Fluorescence response detected in the kinetic mode of the fluorimeter. A foil of Na-FI in hydrogel D1 was fixed in a flow-cell and solutions with different Na^+, Mg^{2+}, Ca^{2+} concentrations or pH values were pumped through it. The insert shows a zoom of the response from 0 mM to 100 mM NaCl (t_{90} < 20 sec).

The selectivity of the indicator dye is mostly determined by the size of the recognition unit (crown ether). The cross-talk to cations depends on the size and charge of the ions. The aza-15-crown-5 used in this study is well known for complexing Na^+ and shows good selectivity against other alkali ions. **Figure 4.4a** shows the selectivity of the FI/ D1sensor. Some cross-talk to K^+ is visible at very high concentrations. However, this interference is not problematic for envisaged applications as very low K^+ is present (e.g. ~ 5 mM in blood and 10 mM in seawater) whereas the concentration of Na^+ is much higher (~150 mM and 500 mM, respectively). In fact, addition of 5 or 10 mM KCl to a solution of 150 mM NaCl does not result in a statistically significant increase of the fluorescence intensity. Addition of as much as 150 mM K^+ shows some enhancement of the signal that would correspond to an increase in Na^+ concentration from 150 to ~160 mM. Additionally, the ionic strength of the solution is doubled in this test which may also contribute to the observed changes.

Notably, virtually no cross-talk to Ca^{2+} and Mg^{2+} is observed (**Figure 4.4**). Interestingly, BODIPYs with aza-15-crown-5 without side arms were reported to have rather high cross sensitivity to Ca^{2+} and Mg^{2+}.[154,155,156] Therefore, the side arm of the receptor is likely to be necessary for elimination of this cross sensitivity.

Inertness to pH changes is of major importance for applications of optical ion sensors. Aza-crown ethers based on aromatic amines are advantageous to those containing aliphatic amines due to lower pK_a value (~ 5), which further decreases upon immobilization in the hydrogels (**Table 4.1**, **Figure S - 4.4**Supporting Information) which enables measurements in the physiological pH range without any influence from pH. Indeed, no cross-sensitivity to pH in the range 6.5-8.5 is observed (**Figure 4.4b**). As can be seen, the response to Na^+ is fully reversible without hysteresis or drift. The dynamic response of about 2.5 µm-thick sensing foil was very fast (t_{90} < 20 seconds).

4.2.5 Miniaturized Referenced Na^+ Optode

All measurements discussed above are intensity based. Fluorescence intensity is affected by many parameters which makes it unsuitable for practical applications. To overcome this limitation dual lifetime referencing (DLR) ratiometric scheme was applied.[125] This method requires a phosphorescent reference dye featuring a long decay time, spectral properties similar to those of the indicator and inertness towards the analyte and other substances. The DLR scheme can be applied both in frequency and in time domain.[125] In the case of the former, the overall phase shift measured by a phase-fluorimeter is determined only by the ratio of the amplitudes of the FI (A_{ind}) and the reference material (A_{ref}) (**Eq. 4.1**). For instance, if the fluorescence intensity of the indicator is low, mostly the luminescence intensity of the reference material can be detected, and a low cotangent of the overall phase shift (ϕ) is measured. As a reference material, we utilized Egyptian blue, an inorganic phosphor excitable in the green-red part of the electromagnetic spectrum and emitting in the NIR. A good quantum yield of 10 %,[157] a luminescence lifetime of ~107 µs and its high photostability make it an almost ideal reference material for DLR.[158]

$$\frac{A_{ind}}{A_{ref}} = cot\phi \cdot cot\varphi_{ref} - cot\phi_{ref} \qquad \textbf{(Eq. 4.1)}$$

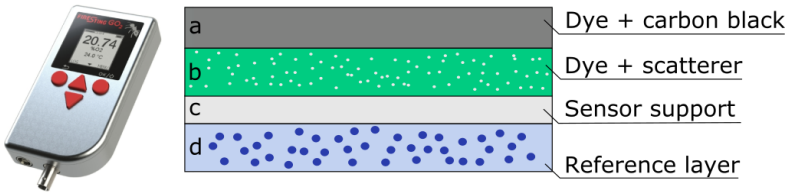

Figure 4.5: Miniaturized phase fluorimeter FirestingGO_2 from Pyro Science and the cross-section of the sensor for referenced read-out using a phase fluorimeter. **a:** Hydrogel D1 with immobilized indicator dye and carbon black for optical isolation. **b:** Hydrogel D1 with immobilized indicator dye and diamond powder for enhancing signal by light scattering. **c:** sensor support. **d:** Egyptian blue microparticles immobilized in polysulfone.

The referenced sensor consists of three layers coated onto a transparent polyester support (**Figure 4.5**). Silanized Egyptian blue particles were immobilized in polysulfone (**d**) and coated on the support (**c**). To prevent potential interaction between the reference layer and the sensing layer, we chose to coat the latter on the opposite side, in order to have the polyester foil as a barrier. The other side of the support foil has a layer of hydrogel D1 incorporating the indicator dye and diamond powder for signal enhancement caused by light scattering (**b**). A further hydrogel D1 layer consisting of **Na-FI** and carbon black was used as the final layer (**a**). Carbon black acts as optical isolation in order to prevent interference from ambient light. The dye was added in the same concentration as in layer **b** in order to prevent migration from one layer to the other, thus changing the signal intensities. As both "cocktails" are dissolved in THF, applying the second layer yield to some mixing of the layers. However, as only one type of polymer and the same amount of indicator dye is used in both, this mixing of layers will not cause any disturbing effects. Notably, diamond powder and carbon black are not necessary in order to obtain a referenced sensor, but they improve the sensors performance by elimination of potential interferences caused by background fluorescence and ambient light (which may saturate the photodetector). A sensor spot was stamped out from this material and was mounted either directly onto PMMA fibers using a metal cap, or glued on a plastic screw-cap which could be fixed directly onto the read-out device. A commercially available phase-fluorimeter (FirestingGO_2 from Pyro Science) was used for measurement of the phase shift (**Figure 4.5**).

4.2.6 Application of Na^+ Optode for Measurement of Seawater Salinity

The salinity of water is an important measure of water quality. The survival of different species of animal and plant life depends on the salinity range within their habitat. The most abundant cations in seawater are Na^+, Mg^{2+}, Ca^{2+} and K^+, while Cl^-, SO_4^{2-}, Br^- and HCO_3^- are the predominant anions (**Table 4.2**).[159] The sum of masses of these ionic species is referred to as salinity; it is expressed as practical salinity unit (PSU) which is the mass fraction of salts in water (grams salt per kilogram solution).[160,161,162] The average practical salinity in the open ocean is 35, and typically varies between 33 and 37 PSU, while much lower salinities are found in brackish waters where the seawater is diluted by a high quantity of freshwater (between 0-30 PSU).[159,163] Since the only change occurring to seawater is a change in the entire concentration of dissolved ions (e.g. dilution with water), the ratio of the different ion concentrations is not affected. Consequently, the composition stays the same, enabling the determination of salinity by simply measuring one component of the seawater.[164]

Seawater salinity is typically measured with a conductivity sensor. An optical sensor for determination of salinity via measurement of Cl^- concentration has been reported.[164] Here we propose an alternative method based on quantification of Na^+ concentration.

The dynamic range of the new sensing material based on **Na-FI**/D1 matches very well the concentration of Na^+ present in seawater. As discussed above, the minor cross-sensitivity of the sensor to K^+ is not critical for seawater measurement since the concentration of K^+ is too low to be detected by the sensor (**Table 4.2**). Advantageously, comparably high concentrations of Mg^{2+} occurring in seawater do not trigger any fluorescence response.

Table 4.2: Summary of mean composition of seawater with salinity 35 at 25 °C.[164]

Cations	g/kg	mM	Anions	g/kg	mM
Na^+	**10.77**	**479**	Cl^-	19.37	559
Mg^{2+}	1.30	54.4	SO_4^{2-}	2.71	28.9
Ca^{2+}	0.409	10.5	CO_3^{2-}	0.0026	2.33
K^+	0.388	10.4	Br^-	0.065	0.86
Sr^{2+}	0.010	0.09	F^-	0.0013	0.075

Determination of temperature cross-talk of the optical sensor is essential for *in situ* monitoring of seawater salinity. A high dependency towards temperature was observed within the relevant concentrations (**Figure 4.6**). This can be attributed to the influence of temperature on the stability constant of the crown ether-Na^+ complex. At higher temperatures, the complexation of the analyte is less favourable, and therefore less fluorescence emission is observed (lower cotangent ϕ). In addition to the complexation equilibrium, Egyptian blue contributes to the temperature dependency, as the emission intensity and lifetime decrease with increasing temperature.[158] This dependency can be compensated for with simultaneous temperature measurements and with the introduction of the temperature coefficient into the calibration equation (**Eq. 4.2**). A is the upper limit of the fit (PSU 45), B the minimum value (PSU 0) and k describes the increment of the fit. A_T, B_T and k_T are linear temperature coefficients for the three parameters and T represents temperature.

$$\cot(d\phi) = (A + A_T \cdot (T - 20)) \cdot (1 - e^{(-(k + k_T \cdot (T-20)) \cdot Na)}) + (B + B_T \cdot (T - 20)) \quad \textbf{(Eq. 4.2)}$$

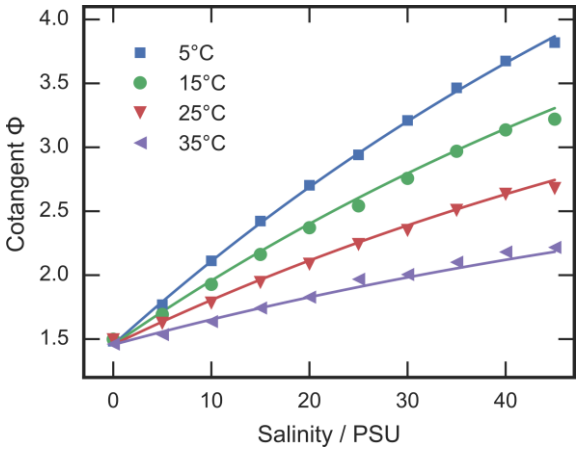

Figure 4.6: Temperature-dependent calibration of the salinity optode based on Na^+ transduction performed with a phase fluorimeter and an optical plastic fiber with a sensor spot attached to the distal end of the fiber.

4.2.7 Measurement of Salinity in the Baltic Sea

The applicability of this novel sensor was demonstrated in *in situ* measurements of the salinity in the Baltic Sea. We used two different read-out devices for three different application areas. A commercially available handheld phase fluorimeter (FirestingGO_2, Pyro Science) incorporating a PMMA fibre with the sensing material coated on the tip was used for quick *in situ* salinity measurements. Additionally, we conducted salinity profiling measurements up to a depth of 25 m and surface salinity measurements. For this purpose, the stand alone phase fluorimeter was embedded into a polyoxymethylene (POM) pressure housing to enable autonomous long term measurements. The module is also equipped with an internal temperature sensor, and the Na^+ sensitive material is mounted on the optical feedthrough with a screw-cap system.

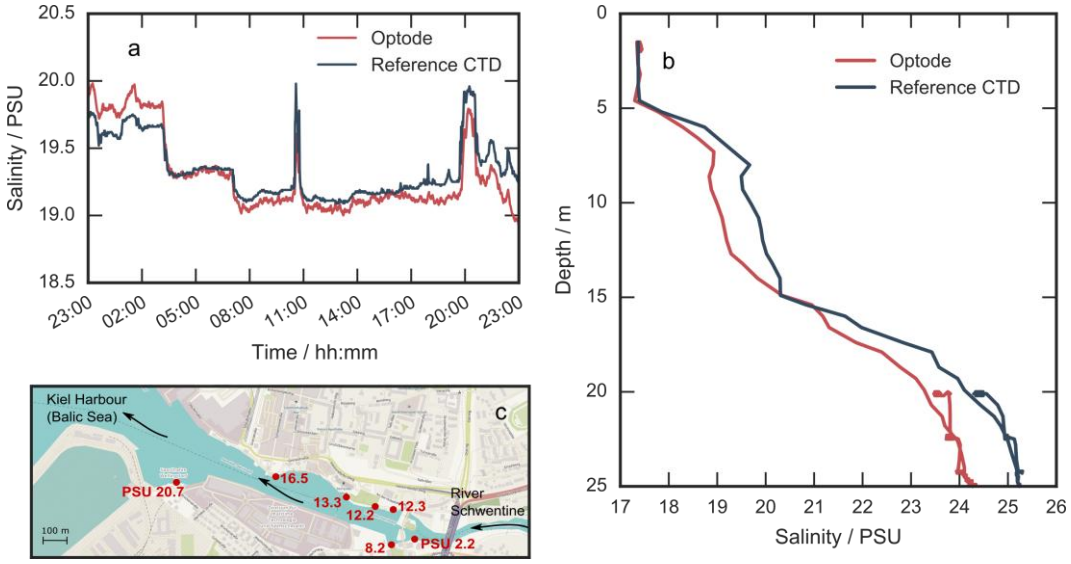

Figure 4.7: Measured salinity in the Baltic Sea compared to reference conductivity measurements from the CTD rosette. a: Measurement performed in surface water for one day (Kiel, 54.3301°N , 10.1498°E). b: Profiling measurement with a speed of 0.15 m/s and stops of 10 min at 24, 22 and 20 m acquired at Boknis Eck (54.5° N, 10.0° E). c: Measurement points and salinity values determined with the sensor material and a handheld phase fluorimeter as the read-out device.

Figure 4.7a shows the 24 h measurement of salinity in surface water. The temperature varied between 18.5 °C and 20 °C during the measurement time. The sensor was calibrated at room temperature before deployment with appropriate salinity solutions containing Na^+ ranging from 0 to 1000 mM. Our data is in good agreement with the reference data obtained via conductivity measurements (CTD). The sensor responds sufficiently fast to detect small changes in salinity. **Figure 4.7b** shows profiling measurements up to 25 m depth. Contrary to the surface measurement, the first measured point of the CTD at the surface was used as a reference calibration point for the optode, as it showed an offset of around 4 PSU. The trend of salinity measured by the sensor is in good agreement with the reference measurement. However, there is a disparity beyond a depth of 5 m. A possible explanation for this is the reduction in response time at lower temperatures. A combination of the high speed of profiling (0.15 m/s) and the change in temperature at greater depths (from 19.4 °C at 5 m to 11.3 °C at 25 m) could cause this variation to the reference. Preparing thinner sensor foils featuring faster response may overcome this issue.

Several point measurements along the mouth of river Schwentine (Kiel) have also been performed (**Figure 4.7c**). The lowest salinity (2.2 PSU) was measured in the river before a bridge. There was a gradient in the altitude of about 1-1.5 m with water flowing in the direction of the sea, which prevents movement of the salt water upwards to the river. As the river gets wider, measurements at locations closer to the harbour indicated an increase in the salinity. The last point of measurement is virtually a fjord and the widest location of all measurements, with the highest salinity of 20.7 PSU. This is in good agreement with commonly measured salinity values in the harbour. Using this optode, it was possible to perform *in situ* salinity measurements along a river in minimal time, effort and equipment.

4.3 Conclusion

A highly selective optical sensor material for the measurement of Na^+-ions in aqueous media was presented. The new fluoroionophore is based on a aza-crown ether receptor unit coupled to a BODIPY chromophore which shows emission in the red region of the spectrum and good fluorescence brightness. By incorporating this fluoroionophore into a polymer matrix a robust and fast responding sensor is obtained. Among different polyurethane hydrogels tested as matrices the most hydrophilic D1 hydrogel proved to be the most suitable. The material showed the highest dynamics between the "off" and "on" state and the highest fluorescence quantum yield in the "on" state. The sensor displays high selectivity over other competing ions (e.g. Mg^{2+}, Ca^{2+}, K^+) and is not affected by pH changes in the relevant range. As all chemosensors, the sensor shows cross-talk to temperature which can be easily compensated for.

A referenced sensing material has also been prepared to enable measurements with a commercially available compact phase fluorimeter. These sensors were used to determine the salinity of seawater and brackish water in the Baltic Sea, and show good correlation with reference measurements. They demonstrate the potential of optical technology for measuring of this very important parameter. It should be emphasized that the new indicator and sensing materials can also be used for a variety of other applications, such as clinical diagnostics or biological imaging.

Acknowledgment

We thank Prof. Eric Achterberg and the GEOMAR team for their assistance in field measurements. Financial support from the European Union FP7 Projects SenseOcean (Grant Agreement Number 614141) and SCHeMA (Grant Agreement Number 614002) is gratefully acknowledged.

4.4 Materials and Methods

^{1}H NMR and ^{13}C spectra were recorded on a 300 MHz instrument from Bruker. MALDI-TOF mass spectra were recorded on a Micromass TofSpec 2E in reflectron mode at an accelerating voltage of +20 kV. Absorption measurements were performed on a Cary 50 UV-Vis spectrophotometer from Varian. Luminescence spectra and absolute quantum yields were measured on a Fluorolog-3 luminescence spectrometer (Horiba). Calibrations were performed by fixing a sensor foil diagonally in a quartz cuvette filled with different buffer solutions. QY of the indicator in solution (THF in presence of 0.3 mM trifluoroacetic acid) and in sensor foils (at 1000 mM NaCl and 0.1 M aqueous HCl) were acquired with an integrating sphere from Horiba. Leaching was investigated by recording the absorption spectra of a foil during continuous pumping a TRIS-buffered (7.4) solution with 500 mM NaCl through a flow-through cell (15 ml/min). Measurements of the referenced sensors were performed with FirestingO_2 and FirestingGO_2 phase fluorimeters (www.pyro-science.com) at a modulation frequency of 4 kHz and a LED intensity of 80 %. Optical plastic fibers (1 mm core diameter) were obtained from Ratioplast-Optoelectronics GmbH (www.ratioplast.eu). Polyurethane hydrogels (Hydromed D1, D4 and D7) were purchased from AdvanSource biomaterials (www.advbiomaterials.com). Poly(ethylene terephthalate) support Melinex 505 was obtained from Pütz (www.puetz-folien.com). Hydrochloric acid 37% (HCl), anhydrous sodium sulfate and all other solvents including the deuterated solvents were from VWR (www.vwr.com). Polysulfone (Mn=16000, Mw=35000), 2,3-dichloro-5,6-dicyano-p-benzoquinone (DDQ), trifluoroacetic acid, boron trifluoride etherate ($BF_3{\cdot}O(C_2H_5)_2$), DMF, $POCl_3$ and water-free dichloromethane (DCM) were purchased from Aldrich (www.sigmaaldrich.com). Buffer substances, NaCl, KCl, $CaCl_2$, $MgCl_2$, K_2CO_3, KI, KOH and chloroform (analytical grade) were from Roth (www.carlroth.com). Silica gel (0.04-0.063 mm) was acquired from Acros Organics

(www.fishersci.com). Carbon black was obtained from Kremer Pigments (www.kremer-pigmente.com). Monocrystalline diamond powder was purchased from Microdiamant (www.microdiamant.com). Silanized Egyptian blue microparticles (trimethylsilyl form) were prepared according to a literature procedure.[158] All other chemicals were purchased from TCI Europe (www.tcichemicals.com). All chemicals were used as received.

4.5 Experimental

4.5.1 Synthesis

5-Chloro-3-phenyl-1,4-dihydroindeno[1,2-b]pyrrole (6)

This synthesis was performed according to the literature procedure.[151]

Triethylene glycol ditosylate (3)

Triethylene glycol (4.50 g, 30.0 mmol, 1 eq) and 4-toluenesulfonyl chloride (11.80 g, 61.8 mmol, 2.1 eq) were dissolved in 100 ml dichloromethane (DCM). The solution was cooled down to 0 °C and portions of KOH (13.60 g, 242.3 mmol, 8.1 eq) were added slowly over a period of 15 min and then allowed to warm up to RT over 4 hours. H_2O (60 ml) was added and the reaction mixture was extracted (DCM) (2x, 30 ml). The organic phase was dried over Na_2SO_4 and the solvent was removed using a rotary evaporator. The crude product was recrystallized from methyl tert-butyl ether (MTBE) to yield a white crystalline product (10.40 g, 75 %). ^{1}H NMR (300 MHz, $CDCl_3$) δ 7.79 (d, J = 8.2 Hz, 4H), 7.34 (d, J = 7.9 Hz, 4H), 4.16 – 4.11 (m, 4H), 3.67 – 3.63 (m, 4H), 3.52 (s, 4H), 2.44 (s, 6H). ^{13}C NMR (76 MHz, $CDCl_3$) δ 145.02, 130.02, 128.13, 70.87, 69.37, 68.93, 21.81.

***N*,*N*-bis(2-Hydroxylethyl)-2-methoxyaniline (2)**

A mixture of 2-anisidine (**1**) (21.84 g, 0.177 mol, 1 eq), 2-chloroethanol (52.8 g, 0.655 mol, 5 eq), $CaCO_3$ (17.75 g, 0.177 mol, 1 eq) and KI (2.27 g, 0,013 mol, 0.07 eq) was stirred in 300 ml H_2O at 90 °C until TLC indicated full conversion (eluent: cyclohexane (CH) + ethyl acetate (EA), 1+2). The reaction mixture was filtered, the

filtrate extracted with DCM and the organic phase dried over Na_2SO_4 before removing the solvent in vacuo. The crude product was purified using column chromatography (eluent DCM to EA and then EA + MeOH (90+10)) to yield the product as brown oil (15.36 g, 40.9 %). ^{1}H NMR (300 MHz, CD_2Cl_2) δ 7.25 – 7.08 (m, 2H), 7.02 – 6.90 (m, 2H), 3.85 (s, 3H), 3.50 – 3.44 (m, 4H), 3.20 – 3.15 (m, 4H), 3.10 (bs, 2H). ^{13}C NMR (76 MHz, CD_2Cl_2) δ 155.84, 138.90, 125.99, 125.24, 121.78, 112.08, 60.10, 57.60, 55.87.

2-Methoxyphenylaza-15-crown-5 (4)

NaH (3.243 g of 60% NaH suspension in mineral oil, 81.0 mmol, 2.5 eq) was added slowly to anhydrous tetrahydrofuran (THF) (150 ml) under an argon counterflow. The mixture was heated to reflux and a solution of N,N-bis(2-hydroxylethyl)-2-methoxyaniline (**2)** (6.719 g, 31.8 mmol, 1 eq) and triethylene glycol ditosylate (**3**) (14.66 g, 31.8 mmol, 1 eq) dissolved in 100 ml anhydrous THF was added dropwise over a period of 30 min and continued refluxing for 18 hours. After cooling down, the suspension was filtered and the solvent was removed under reduced pressure. The residue was dissolved in 20 ml MeOH, heated to reflux and $NaClO_4 \cdot H_2O$ (4.84 g, 34.45 mmol, 1.08 eq) dissolved in 10 ml MeOH was added. After 30 min, 20 ml EA was added and the solution was concentrated to a volume of 10 ml on the rotary evaporator. This suspension was refluxed and EA was added until a total volume of 450 ml. The clear solution was then put in the fridge for 18 hours. The obtained white crystals were filtered, dried in an oven and then dissolved in 10 ml DCM and extracted with H_2O (3x 10 ml) to obtain the free crown (2.80 g, 27 %). ^{1}H NMR (300 MHz, $CDCl_3$) δ 7.12 (dd, J = 7.5, 2.0 Hz, 1H), 6.98 – 6.81 (m, 3H), 3.83 (s, 3H), 3.73 – 3.64 (m, 16H), 3.52 – 3.44 (m, 4H). ^{13}C NMR (76 MHz, $CDCl_3$) δ 152.78, 140.08, 122.12, 120.84, 120.74, 111.77, 70.97, 70.60, 70.37, 70.18, 55.40, 53.00. MS (MALDI-TOF): m/z $[MNa]^+$ 348.1787 calcd, 348.1895 found.

4-Formyl-2-methoxyphenylaza-15-crown-5 (5)

2-Methoxyphenylaza-15-crown-5 (**4**) (2.51 g, 7.7 mmol, 1 eq) was dissolved in 4 ml DMF in a Schlenk flask, cooled down to -8 °C and $POCl_3$ (1.68 g, 16.1 mmol, 2.1 eq) was added slowly so that the temperature did not raise over 0 °C. Afterwards, the reaction mixture was allowed to warm up to RT and was stirred for 20 hours and

then heated to 60 °C for 2 hours. Aldehyde formation could be seen by TLC (DCM + MeOH, 75 + 5) and staining of the TLC with a solution containing dinitrophenylhydrazine (DNP). The solution was cooled down to RT, poured slowly over ice and neutralized with K_2CO_3 to pH 7. The reaction mixture was extracted with DCM (3x, 30 ml), the solvent was removed and the product purified by column chromatography (gradually from DCM to DCM + MeOH, 100+5) to yield the product as brown oil (1.12 g, 41 %). ^{1}H NMR (300 MHz, CD_2Cl_2) δ 9.73 (s, 1H), 7.38 – 7.28 (m, 2H), 6.98 (d, J = 8.3 Hz, 1H), 3.84 (s, 3H), 3.72 – 3.64 (m, 4H), 3.62 – 3.55 (m, 15H). ^{13}C NMR (76 MHz, CD_2Cl_2) δ 190.49, 151.36, 146.49, 129.04, 126.71, 116.80, 110.42, 71.3, 70.74, 70.56, 70.32, 55.91, 54.05. MS (MALDI-TOF): m/z $[MH]^+$ 354.1917 calcd, 354.1599 found.

BODIPY Fluoroionophore (Na-FI)

4-Formyl-2-methoxyphenylaza-15-crown-5 (**5**) (1.10 g, 3.11 mmol, 1 eq) and 5-chloro-3-phenyl-1,4-dihydroindeno[1,2-b]pyrrole (**6**) (1.69 g, 6.38 mmol, 2.05 eq) were dissolved in 5 mL of anhydrous DCM and 1 drop of trifluoroacetic acid was added. The mixture was shielded from light and stirred at RT for 48 hours and 2,3-dichloro-5,6-dicyano-1,4-benzoquinone (DDQ) was added (0.741 g, 3.26 mmol, 1.04 eq), changing the colour of the reaction mixture to dark blue. After stirring for another 15 min, N,N-diisopropylethylamine (DIPEA) (4.07 g, 31.4 mmol, 10 eq) and $BF_3{\cdot}O(C_2H_5)_2$ (6.9 g, 48.6 mmol, 15 eq) were added under argon counterflow. After 15 minutes stirring, the mixture was extracted with H_2O, the organic phase was dried over Na_2SO_4 and the solvent removed in vacuo. Purification was performed by column chromatography (2x, eluent DCM gradually to DCM + MeOH, 100+5) yielding the product as purple crystals (211 mg, 7.4 %). UV-VIS (DCM): λmax = 538 nm, ε = 130,000 $M^{-1}cm^{-1}$. ^{1}H NMR (300 MHz, CD_2Cl_2) δ 8.30 (d, J = 8.4 Hz, 2H), 7.54 – 7.45 (m, 4H), 7.05 – 6.83 (m, 10H), 6.66 – 6.58 (m, 2H), 6.39 – 6.31 (m, 1H), 3.82 – 3.45 (m, 27H). MS (MALDI-TOF): m/z $[MNa]^+$ 934.2782 calcd, 934.2747 found.

4.5.2 Preparation of Sensing Materials

Planar Sensor Films

Hydrogel polymers (Hydromed D1, D4 or D7) were dissolved in THF to yield a solution of 10 wt.%. An appropriate amount of the indicator was dissolved in the hydrogel solution. The sensor films were prepared by knife coating of these "sensor cocktails" onto dust-free polyester foils (25 µm wet film thickness). The sensor foils were allowed to dry for several hours at RT. Dye concentrations for calibrations and QY determination were 0.2 wt.% and for leaching experiment 1 wt.% in respect to the polymer.

Fiber-Optic Sensor for Ratiometric DLR Readout

The "cocktail" for the reference layer was prepared by dispersing 12 mg Egyptian blue and 100 mg polysulfon in 888 mg $CHCl_3$. This "cocktail" was knife coated onto dust-free polyester foils (25 µm wet film thickness) and allowed to dry in the oven at 60 °C for 2 hours. For the first sensing layer 0.5 mg **Na-FI**, 100 mg diamond powder and 100 mg hydrogel D1 were dispersed/dissolved in 566 mg THF. This "cocktail" was knife coated onto the back-side of the polyester support and allowed to dry for 2 hours at RT (75 µm wet film thickness). The cover layer was prepared by dissolving/dispersing 0.5 mg **Na-FI**, 100 mg carbon black and 100 mg hydrogel D1 in 566 mg THF (15 wt.% in respect to the polymer). This "cocktail" is knife coated onto the first sensor layer (25 µm wet film thickness) and allowed to dry for 2 hours at RT. A sensor spot was then either stamped out (2 mm diameter) and fixed with a metal cap on a 1 m PMMA fiber or stamped out (5 mm diameter) and glued on a plastic screw cap.

4.6 Supporting Information

Leaching Experiment

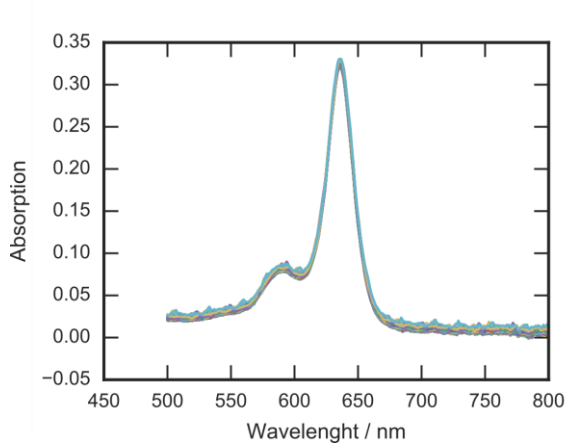

Figure S - 4.1: Recorded absorption spectra of the indicator immobilized in Hydrogel D1 during continuous rinsing the sensor foil with a solution containing 500 mM NaCl.

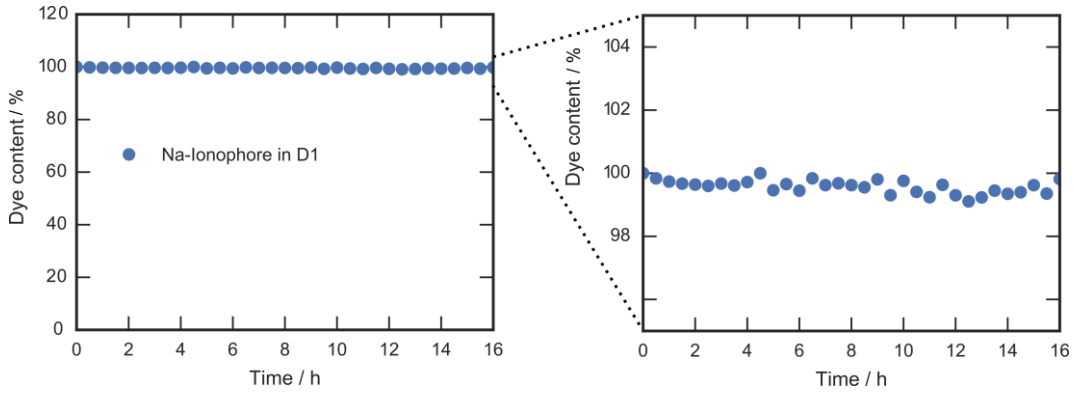

Figure S - 4.2: Left: Normalized absorption maxima of the recorded absorption spectra during the leaching experiment corresponding to Figure S1. Absorption maximum of the first measurement point was used for normalization to indicate % loss of dye. **Right:** Zoom in.

Normalized Emission Spectra of Na-FI in other Hydrogels

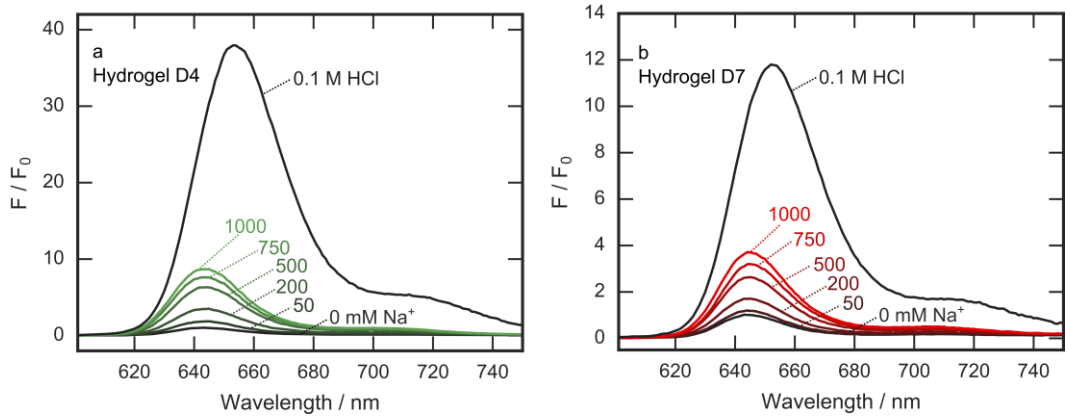

Figure S - 4.3: Normalized emission spectra of Na-FI in hydrogel D4 (**a**) and D7 (**b**) at different Na^+ concentrations (20 mM TRIS buffer pH 7.4) and in acidic media (0.1 M HCl). F0 was taken at 645 nm.

Determination of the pKa-Value

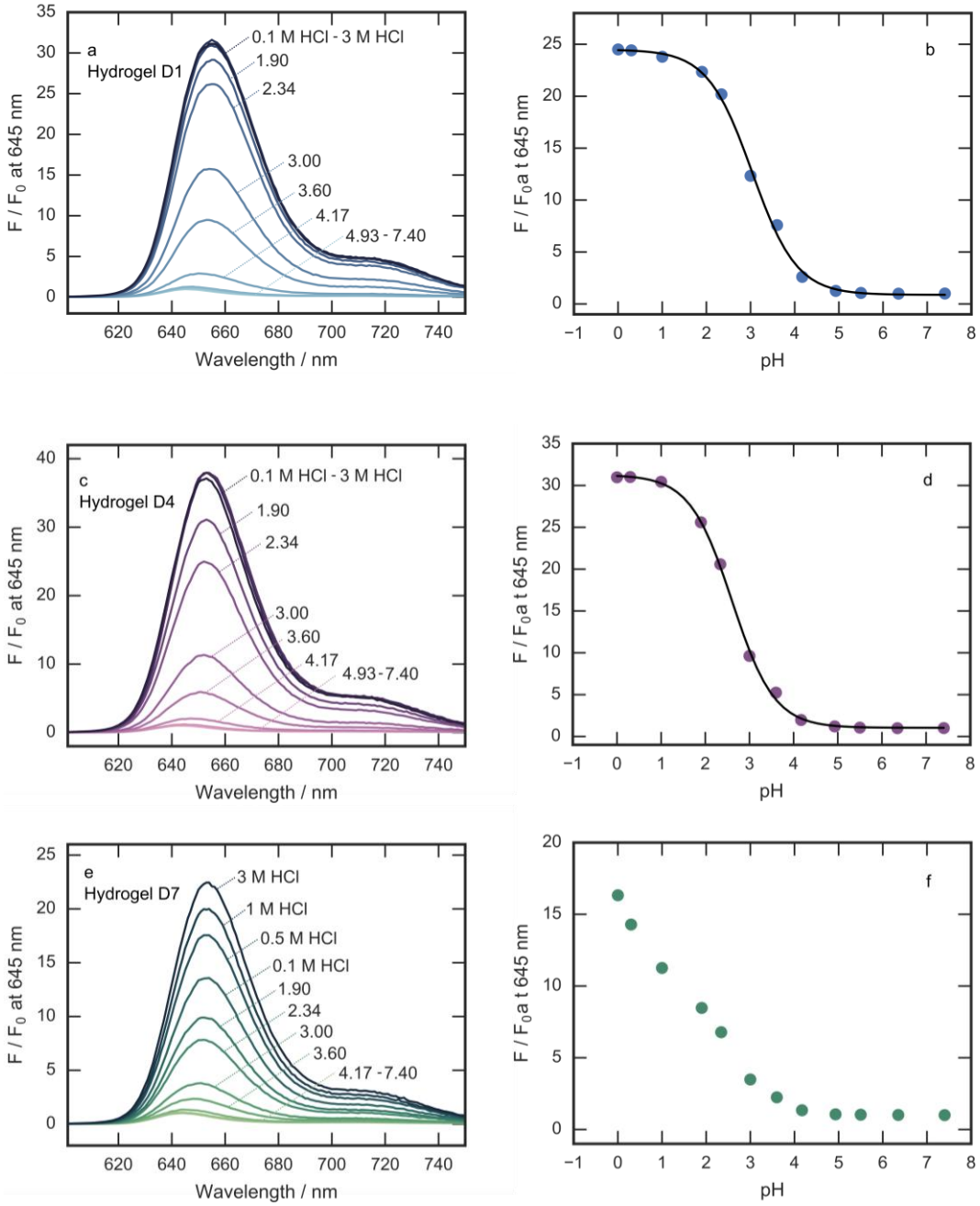

Figure S - 4.4: Normalized emission spectra of Na-FI in Hydrogel D1 (**a**), D4 (**c**) and D7 (**e**) at different pH values. **Right:** pH-Calibration of the corresponding sensor material.

MALDI-TOF Spectra

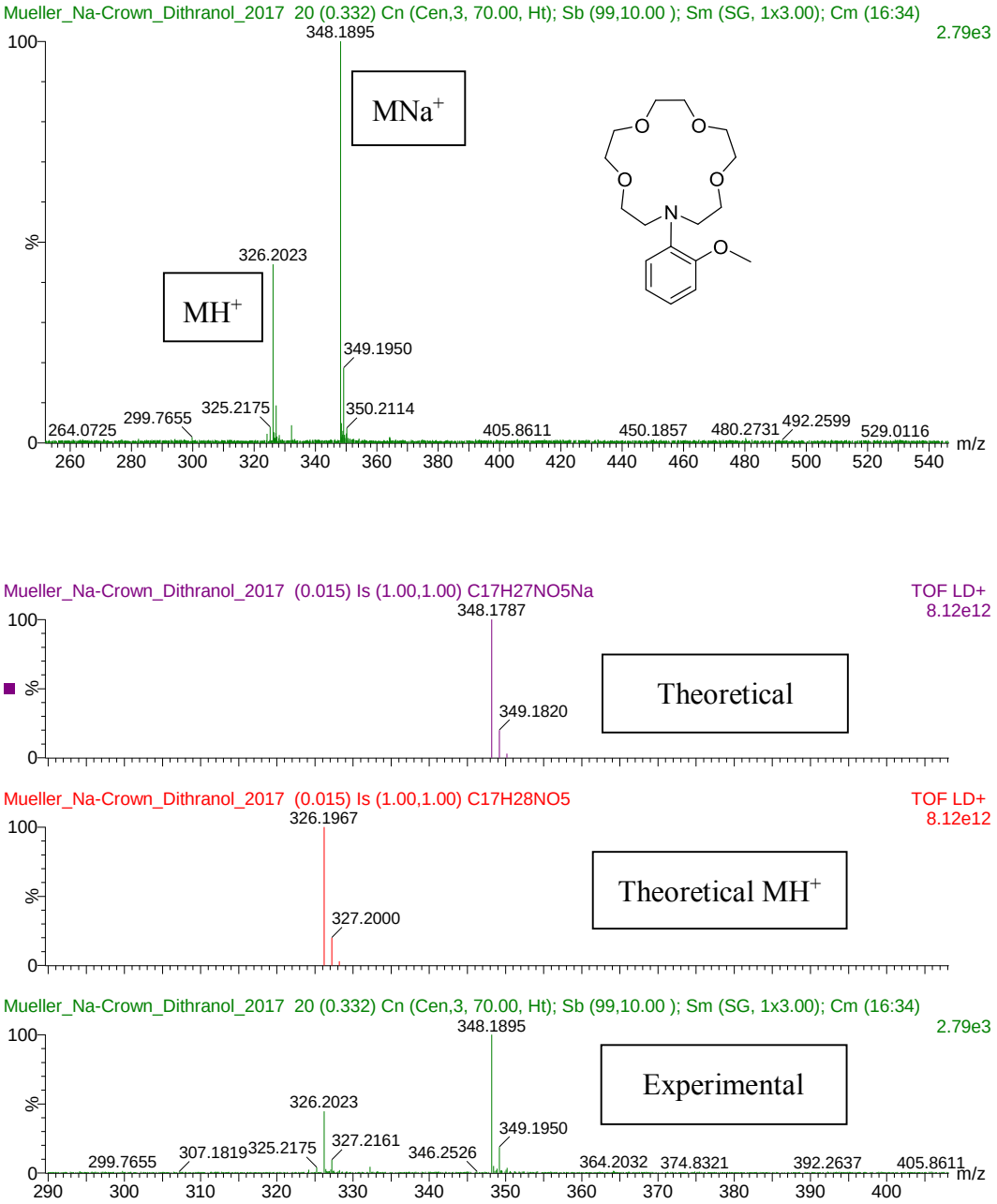

Figure S - 4.5: Mass spectra (MALDI-TOF) of 2-Methoxyphenylaza-15-crown-5 (4) in dithranol matrix.

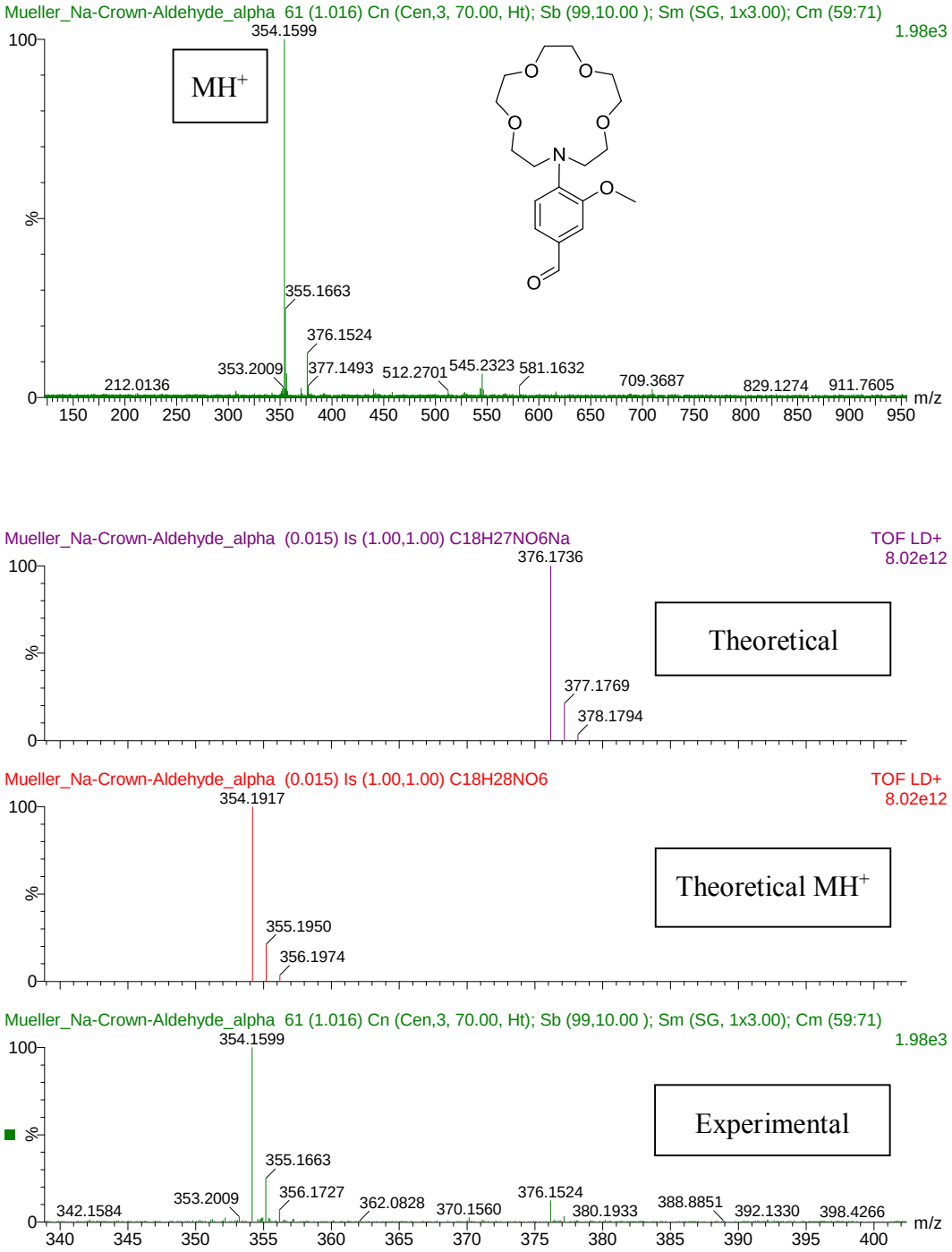

Figure S - 4.6: Mass spectra (MALDI-TOF) of 4-Formyl-2-methoxyphenylaza-15-crown-5 (5) in alpha-Cyano-4-hydroxycinnamic acid matrix.

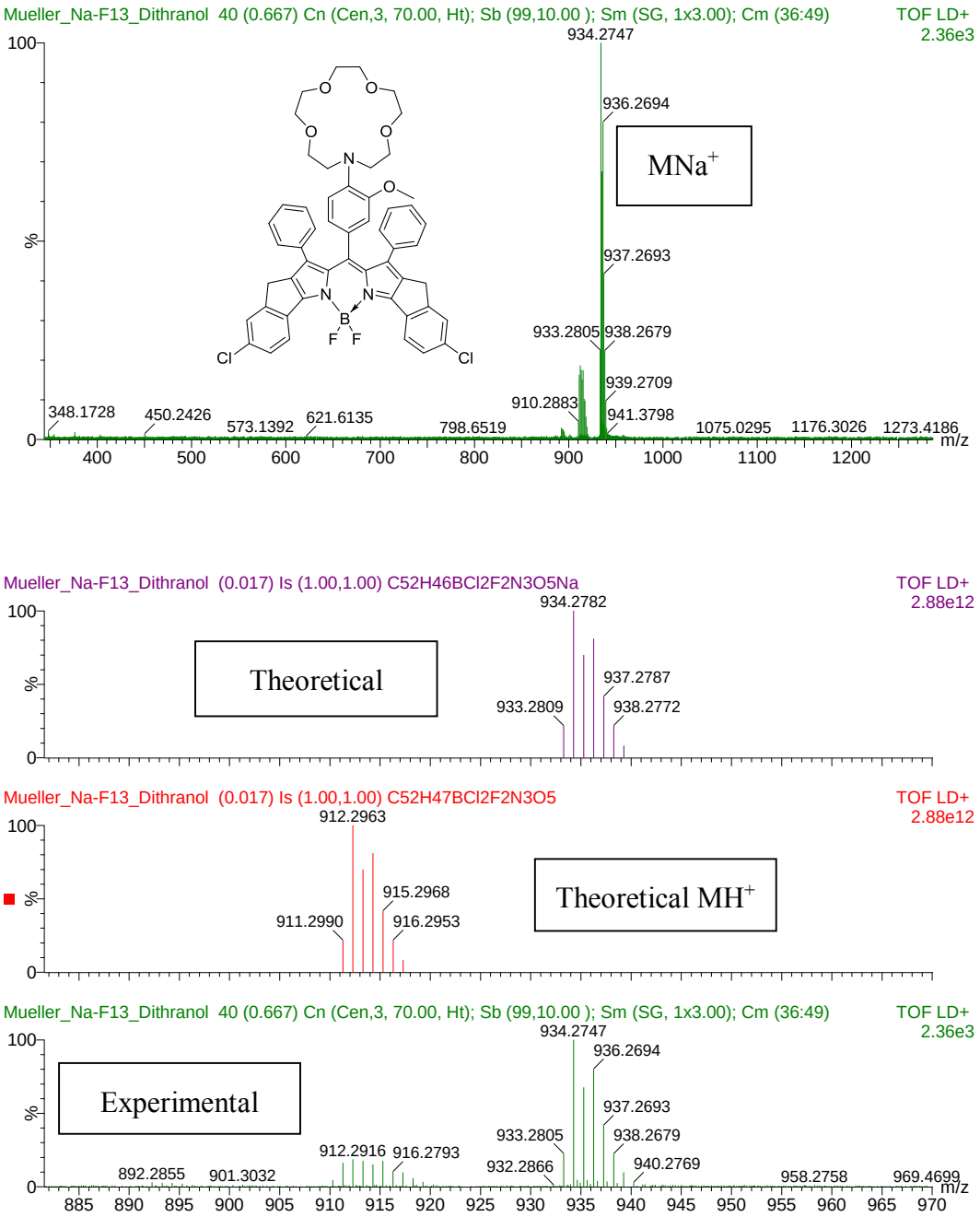

Figure S - 4.7: Mass spectra (MALDI-TOF) of Na-FI in dithranol matrix.

Future Prospect and Outlook

Optical sensors are already regularly used in marine research and oceanography. The salinity sensor herein presented is a valuable addition to other commonly measured compounds such as O_2, pH and CO_2 which are important analytes for monitoring ocean acidification. This acidification is creating an imbalance in $CaCO_3$-formation, thus making calcifying organisms, such as corals, vulnerable to dissolution. Hence, the measurement of Ca^{2+} in the sea is of great interest and is one of the missing items for fully understanding marine processes.

In addition to the salinity sensor, we made attempts to develop a Ca^{2+} sensor based on our PET-based indicators. In contrast to other presented fluoroionophores in this thesis, the Ca^{2+} receptor is not based on a crown ether. Here we utilize N-phenyliminodiethoxyacetic acid as the chelating agent, which was already reported to show efficient Ca^{2+} sensitivity.[165] This project was part of the master thesis of Lukas Tribuser, where he successfully synthesized Ca-FI3 (**Figure 2.1**).[166]

Preparation of solid state sensing materials by immobilizing this compound in hydrogel matrices is not as straight forward as with fluoroionophores with crown ether receptors due to the highly hydrophilic receptor. Coupled with a very hydrophobic chromophore, this resulted in a fluoroionophore with amphiphilic properties. Further attempts on immobilization are currently under investigation.

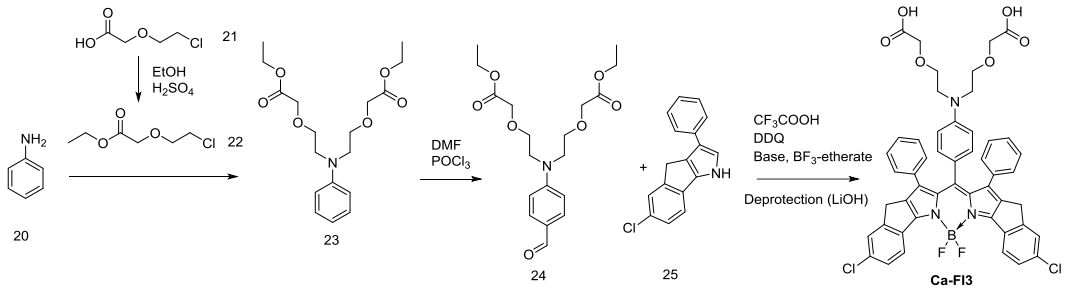

Figure 4.8: Synthetic pathway towards a Ca^{2+} sensitive fluoroionophore (Ca-FI3).

The presented Na^+ sensor is also part of further projects. Similar to K^+ fluoroionophores, our research is currently directed towards the synthesis of new receptors for improving the stability constants. The lariat side arm of K-FI3 seemed to be of particular importance to improve binding in the context of K^+ sensors as shown in **Figure 3.12** (p. 66).

For this reason, we started the synthesis of a 15-crown-5 using this structural element (**Figure 4.9**). The synthesis is analogous to the preparation of the K^+ receptor, but using triethylene glycol (30) for the ring closing reaction instead of tetraethylene glycol. Further reaction can be conducted analogous to the reported synthesis.[151] At this stage, compound 31 is available and will be used for the preparation of a new fluoroionophore (Na $^{2nd\ Gen}$ - FI3) in the future.

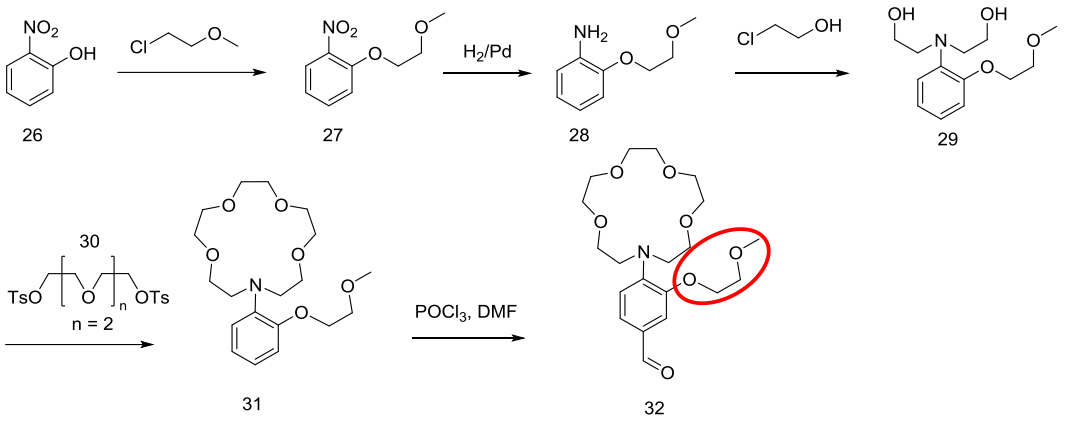

Figure 4.9: Synthetic Scheme towards a new Na^+ sensitive receptor unit utilizing the same side arm as in presented K^+ sensors to increase the binding stability with the complexed ion.

Chapter 6

Nanoparticle-based Fluoroionophore for Analysis of Potassium Ion Dynamics in 3D-Tissue Models and In Vivo

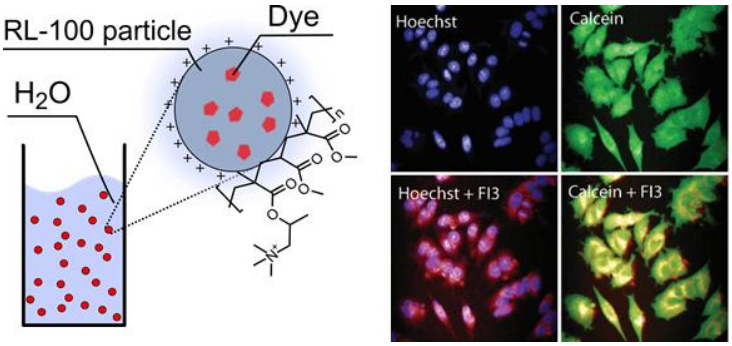

Preface for the Manuscript

In this project the practical applicability of the developed ion sensors is tested for live cell imaging. As shown in **chapter 3**, K^+ indicators can be physically entrapped inside commercially available RL-100 nanoparticles (**Figure 3.9** (p. 49)). The outside layer of these particle have positively charged quaternary ammonium groups which makes them water dispersible while still exhibiting fluorescence response to changes in K^+ concentration. These particles were already successfully used for cellular imaging with entrapped oxygen[118], pH[167] and temperature[168] sensitive indicators.

K^+ is the main ion inside the human cell with an approximate concentration of 150 mM while extracellular concentrations are about 5 mM. This difference creates the membrane potential which cells can control by opening or blocking K^+ channel transmembrane proteins. Understanding K^+ fluxes is of high importance for biological research. Indeed, most reported fluoroionophores were used as molecular probes (e.g. water soluble indicator dye) for fluorescence imaging. As we developed the first nanoparticle based sensor, we aimed to show new potential of our fluoroionophores. Our group already has a successful collaboration with Prof. Dmitri Papkovsky and Dr. Ruslan Dmitriev from University College Cork (UCC) in Ireland, who are experts in the application of fluorescent sensing materials for imaging of biological samples. Together with UCC, we started a project on K^+ nanosensors.

Our goal was to determine and quantify K^+ fluxes in neuronal cells. For quantification, it is necessary to incorporate a second reference dye which shows emission at a different wavelength than the fluoroionophore dye. For measurement in biological samples, it is always beneficial to apply dyes which can be excited and show emission in the red to NIR part of the electromagnetic part of the spectrum to reduce interferences from autofluorescence or scattering of the sample. Therefore, we chose FI3 as the suitable candidate for this project.

Four different referenced nanoparticles were prepared using two conjugated polymers and two perylene based dyes (**Figure 5.1**). They are all insensitive towards K^+ and show strong emission < 600 nm.

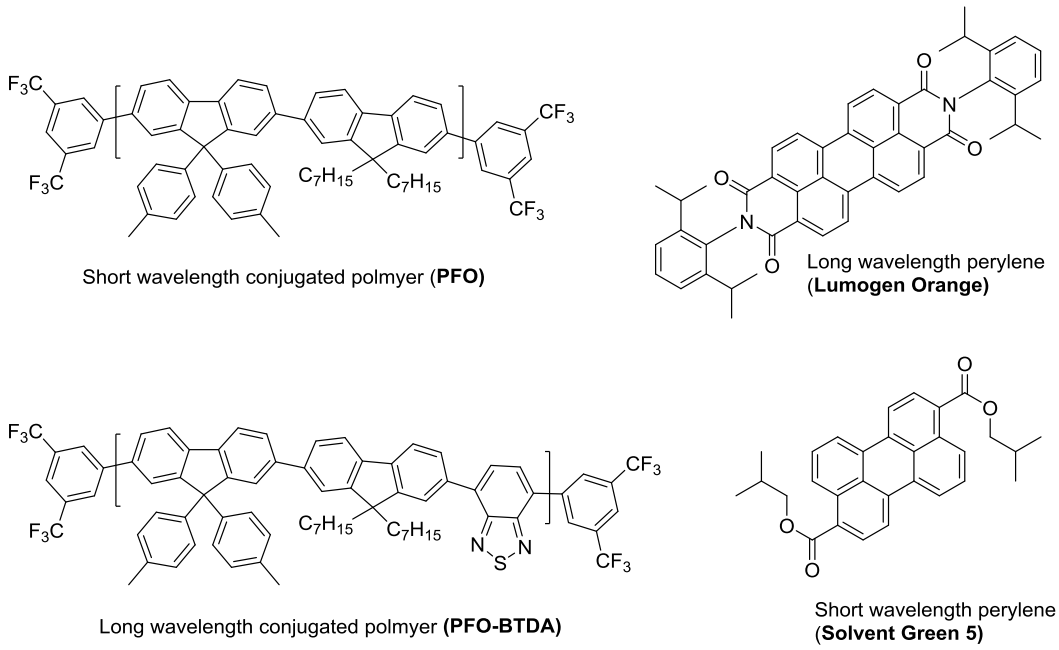

Figure 5.1: Fluorescent compounds used as reference for K^+ sensitive nanoparticles. **Left:** Conjugated polymers. Short wavelength emission of **PFO** (λ_{em} = 420 nm) can be bathochromically shifted by additional incorporation of benzothiadiazole (**PFO-BTDA**, λ_{em} = 530 nm). **Right:** Commercially available perylene deviates **Lumogen Orange** (λ_{em} = 530 nm) and **Solvent Green 5** (λ_{em} = 475 nm).

The referenced fluorescence spectra are shown in **Figure 5.2**. Evidently, particles with perylene show a much higher F/F_0 with increasing K^+ compared to particles with conjugated polymers (F/F_0 at 500 mM ~12 and ~3 respectively). This could be attributed to the high amount of conjugated polymer used (5 wt.%) compared to perylene (0.5 wt.%), therefore changing the environmental conditions inside the particle.

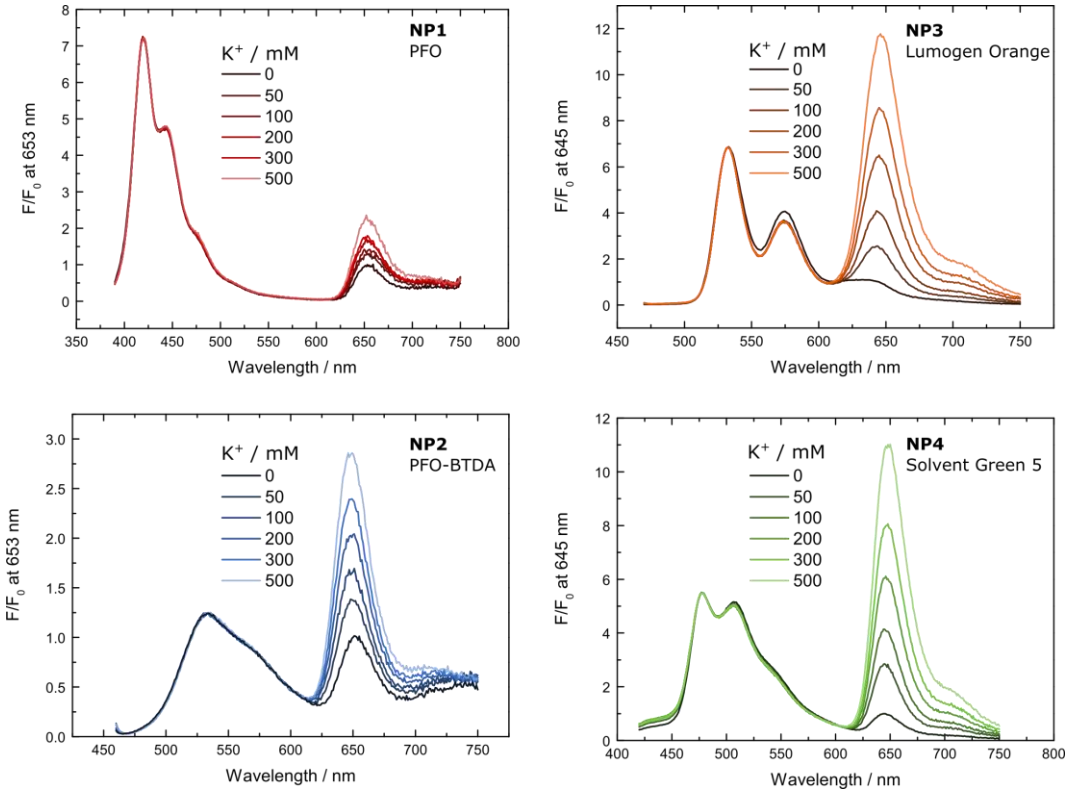

Figure 5.2: Emission spectra of the referenced nanoparticles (NPs). NP1 / NP4 were excited at 380 nm and NP2 / NP3 at 450 nm respectively. NP1 and NP2 contained 5 wt.% reference dye and 1 wt.% indicator dye FI3. NP3 and NP4 contained 0.5 wt.% reference dye and 1 wt.% indicator dye FI3.

To test their suitability for cell imaging, neuronal origin cancer cells (PC12) were stained with the particles for 16 h (10 µg/ml). Fluorescence emission of treated cells was then measured on a widefield microscope with various emission filters to detect the emission of the reference and the indicator dye (**Figure 5.3**). All particles show cellular uptake both intracellular and extracellular aggregates. However, the overlap of both the emission of the reference and FI3 indicates that there is no co-localisation of the compounds. This means that the ratio between both dyes within a particle is not constant and therefore this material is not suitable for quantitative measurements. This can be caused by i) leaching of either FI3 or the reference out the particle over time or ii) inhomogenous particle mixture caused by the production step. Covalent coupling of both dyes could prevent this and potential synthetic routes are presented in the outlook (p. 134).

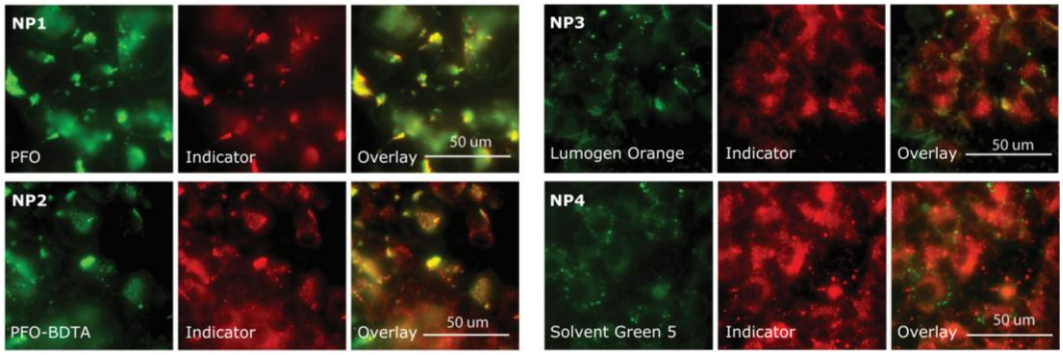

Figure 5.3: Widefield microscopy of the NPs uptaken by PC12 cells. Staining was performed with 10 µg/ml for 16 h. Reference dyes: λ_{ex}= 470 nm and λ_{em} = 530.nm. Indicator λ_{ex}= 350 nm and λ_{em} = 635.nm. Overlay of both indicates no co-localisation of the reference and the indicator.

All particles showed efficient intracellular uptake- RL-100 particles are known to efficiently stain cells such as fibroblasts or HeLa, but staining of 'hard' cell lines such as neural cells is not reported. For this reason, we decided to investigate the staining efficiency of RL-100 particles with only FI3 incorporated with different cell lines. Initial tests for staining of PC12 and SHSY5Y cells gave promising results (**Figure 5.4**) and were the basis for the following publication.

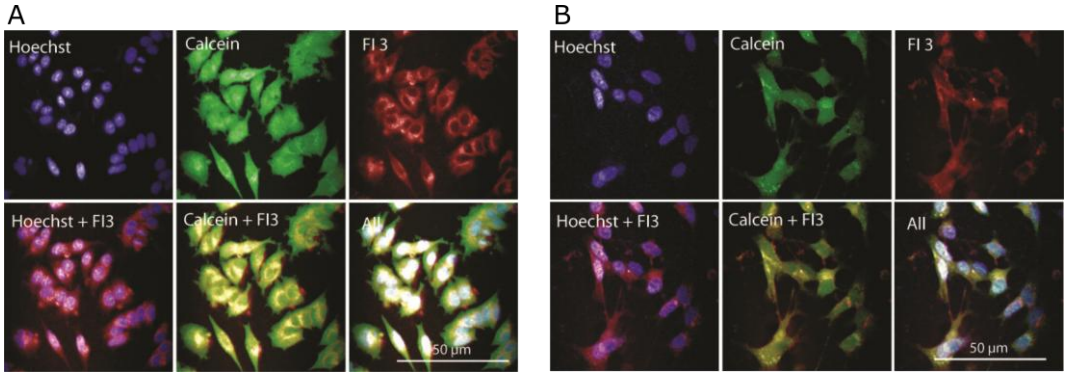

Figure 5.4: Staining of cells with RL-100 particles with incorporated FI3 fluoroionophore. Counterstaining of the cells with Hoechst (DNA staining) and Calcein (cell body). Overlay indicators efficient intracellular uptake of FI3-nanosensors. **A:** PC12 cell line, **B:** SHSY5Y cell line.

Manuscript

Nanoparticle-based Fluoroionophore for Analysis of Potassium Ion Dynamics in 3D-Tissue Models and *In Vivo*

This chapter was submitted as *Full Paper* in

Nature Materials

Authors: Bernhard J. Müller[1,$], Alexander V. Zhdanov[2,$], Sergey M. Borisov[1], Tara Foley[3], Irina A. Okkelman[2], Vassiliy Tsytsarev[4], Qinggong Tang[5], Reha S. Erzurumlu[4], Yu Chen[5], Haijiang Zhang[6], Claudio Toncelli[6], Ingo Klimant[1], Dmitri B. Papkovsky[2] and Ruslan I. Dmitriev[2*]

[$] these authors contributed equally to this work.

[1]Institute of Analytical Chemistry and Food Chemistry, Graz University of Technology, Stremayrgasse 9, 8010 Graz, Austria

[2]ABCRF, School of Biochemistry and Cell biology, University College Cork, Cork, Ireland

[3]Department of Anatomy and Neuroscience, University College Cork, Cork, Ireland

[4]Department of Anatomy and Neurobiology, University of Maryland School of Medicine, Baltimore, MD, USA

[5]Fischell Department of Bioengineering, University of Maryland, College Park, 20740 MD, USA

[6]Empa, Swiss Federal Laboratories for Materials Science and Technology, Laboratory for Biomimetic Membranes and Textiles, Lerchenfeldstrasse 5, CH-9014 St. Gallen, Switzerland

E-mail: r.dmitriev@ucc.ie

Keywords: Fluorescence microscopy; *In vivo* brain imaging; Live cell imaging; Nanoparticles; Potassium;

Abstract The imaging of real-time fluxes of K^+ ions in live cell with high dynamic range (5-150 mM) is of paramount importance for neuroscience and physiology of the gastrointestinal tract, kidney and other tissues. In particular, the research on high-performance deep-red fluorescent nanoparticle-based biosensors is highly anticipated. We found that BODIPY-based FI3 K^+-sensitive fluoroionophore encapsulated in cationic polymer RL100 nanoparticles displays unusually strong efficiency in staining of broad spectrum of cell models, such as primary neurons and intestinal organoids. Using comparison of brightness, photostability and fluorescence lifetime imaging microscopy (FLIM) we confirmed that FI3 nanoparticles display distinctively superior intracellular staining compared to the free dye. We evaluated FI3 nanoparticles in real-time live cell imaging and found that it is highly useful for monitoring intra- and extracellular K^+ dynamics in cultured neurons. Proof-of-concept in vivo brain imaging confirmed applicability of the biosensor for visualization of epileptic seizures. Collectively, this data makes fluoroionophore FI3 a versatile cross-platform fluorescent biosensor, broadly compatible with diverse experimental models.

5.1 Introduction

Potassium (K^+) is one of the principal ions in living cells and multicellular organisms[91,169]. Its concentration is dynamically regulated through numerous membrane protein-based channels and transporters, to maintain a gradient of ~ 150 mM inside vs. ~ 5 mM outside the cell. The essential processes of cell growth, acid-base equilibrium, maintenance of electrolyte balance and transmembrane transport are all regulated by potassium. In tissue-specific manner, potassium regulation is crucial for brain (resting potential, firing, interactions between astrocytes and neurons)[170,171], gut[172], muscle[173], kidney[174] and implicated in progression of numerous diseases such as cancer[175] and ischemia[176]. Understanding molecular mechanisms of these processes and monitoring of potassium ion fluxes in different tissues and cellular compartments are important tasks for biochemistry, physiology, pathology and bioanalytical sciences. In particular, development of sensitive, non-invasive and efficient fluorescent chemical sensors for K^+ is in high demand[112,177,106,178,179,180,151,181]. Various optical and fluorescence microscopies allow for high-resolution, fast and quantitative readout, with minimal interferences from electrochemical gradients of other ions present in the cell. Recent developments in high-resolution and super-resolution selective plane illumination, FLIM, confocal

and two-photon microscopies demand for bright, highly selective and photostable probes[182,183,184].

Over the last decade the 'traditional' method of synthesizing ion-selective dyes is slowly being replaced by their modification with functional and targeting groups and encapsulation in nanoparticles[185,186]. Nanoparticle technology helps improving the functional properties of fluorophores (brightness, photostability, minimal cross-interferences to other ions and environment) and brings additional features of targeting and bio-delivery. For instance, encapsulation in nanoparticles can help solving problems of selectivity of the chemical probe, introduce second (reference) dye and improve its ability to stain cells and tissues[186,187]. Various methods such as precipitation of biocompatible polymers allow preparing nanoparticles with virtually any possible specificity and appropriate photophysical properties[188]. However, the control of interaction of nanoparticles with cells and tissues still represents a challenging task[188,189]: nanoparticles display complex interactions at the nano-bio interface (e.g. salt-induced agglomeration or formation of 'protein corona'), often resulting in endocytosis-dependent transport of nanoparticles across the cell membrane, and their subsequent entrapment in endosomes, lysosomes and other intracellular organelles[188,190]. Compared to small molecule dyes, cell staining with nanoparticles is usually 10-20 times slower, rarely leads to cytoplasmic localization and is often cell-specific. Consequently, staining of more complex cell models such as 3D spheroids or tissues becomes more problematic, limiting the progress in use of fluorescent nanosensors. Significant research is now directed towards modifying the size, charge, shape and surface with functional groups, and understanding the structure-activity relationships[188,191,192].

The positively charged polymeric nanoparticles based on Eudragit RL100[193] encapsulated with hydrophobic Pt(II)-porphyrins and other fluorescent dyes display cell-specific intracellular staining[118,194,167,195]. Such nanoparticles stain well a number of adherent cell lines (fibroblasts, HeLa, HCT116, HepG2) but display poor staining efficacy of neural cells and multicellular spheroids[196,197]. While these issues can be addressed by changing to negatively and mixed-charged polymers[187,198], it is interesting and equally important to understand how the properties of nanoparticles based on this cationic polymer can be improved.

Here, we report the use of RL100-based nanoparticles, impregnated with a red emitting K^+-sensitive fluoroionophore FI3[151]. As the chemical modification with targeting groups can represent multi-step and laborious procedure[192,199,200,201], we

examined how the presence of this amphiphilic sensor dye, conjugated with crown ether affects the cell staining properties of RL100-based nanoparticles. Surprisingly, we found that FI3 nanoparticles have improved ability to internalize in a number of 'hard' cell types and models, including primary neurons and 3D models in a manner, superior to the free (non-encapsulated) dye. We studied the mechanisms of internalization and demonstrated biological application of FI3 in monitoring of K^+ fluxes in *in vitro* and *in vivo*. This report provides new framework for design of sensing and labeling nanoparticle agents and demonstrates its high practical application potential.

5.2 Results and Discussion

5.2.1 FI3 nanoparticles display versatile intracellular staining pattern across the range of 2D and 3D tissue models

Recently, we reported a family of new fluoroionophores based on borondipyrromethenes (BODIPY) and aza-crown ether-based sensing unit, emitting in green to near-infrared parts of electromagnetic spectrum. The compound FI3 showed attractive properties with high molar absorption (109,300 M^{-1} cm^{-1} at 640 nm), deep red fluorescence (λ_{max} exc./ em. 640/ 660 nm), high quantum yields (47-76%) and selectivity towards K^+, independent from pH, within the relevant range[151] (**Figure 5.5**). We found that the dye is relatively easy to impregnate in polymer nanoparticles, however their physical properties and interaction with cells were not studied in detail[151]. The amphipathic nature of fluoroionophore suggests that the sensing part (crown ether) must be exposed externally, together with positively charged groups of RL100 polymer[151], unlike the other RL100-based nanosensors, in which the impregnated material represents highly hydrophobic dyes[118,194,168]. This results in an indented surface of the agglomerated nanoparticles as evidenced by scanning transmission electron microscopy (STEM). Interestingly, such agglomerates were still of nanoscale dimensions (i.e. 91.1 ± 31 nm) and low fractal dimension (d_f) (**Figure S - 5.1**).

For assessment of cell staining efficacy, we chose a number of previously tested adherent cell lines, including human colon cancer HCT116 cells, mouse embryonic fibroblasts (MEF), neuronal origin cancer cells (PC12, SHSY5Y) and mixed culture of rat primary neural cells (**Figure 5.6A**). When analyzed by confocal fluorescence

microscopy, we found efficient and bright staining of cells, including culture of primary neural cells. Bright intracellular fluorescence was observed for both differentiated (not shown) and non-differentiated SHSY5Y neuroblastoma cells and for two principal types of neural cells present in primary culture, astrocytes and neurons. With mixed culture of primary neurons we also observed some degree of extracellular staining, which can be caused by simply non-specific aggregation of nanoparticles or their interaction with dead cells or cell debris; however, at the same time, the bright cytoplasmic staining of both cell bodies and neuritis was evident, proving efficient intracellular staining of neural cells (**Figure 5.6**). This is in contrast with the poor staining efficacy anticipated from positively charged RL100-based nanoparticles: for control, we stained primary neurons with RL100-nanoparticles impregnated with hydrophobic metalloporphyrin PdTFPP (**Figure S - 5.2A**). In this case we observed mostly extracellular aggregates, in agreement with our previous data[198].

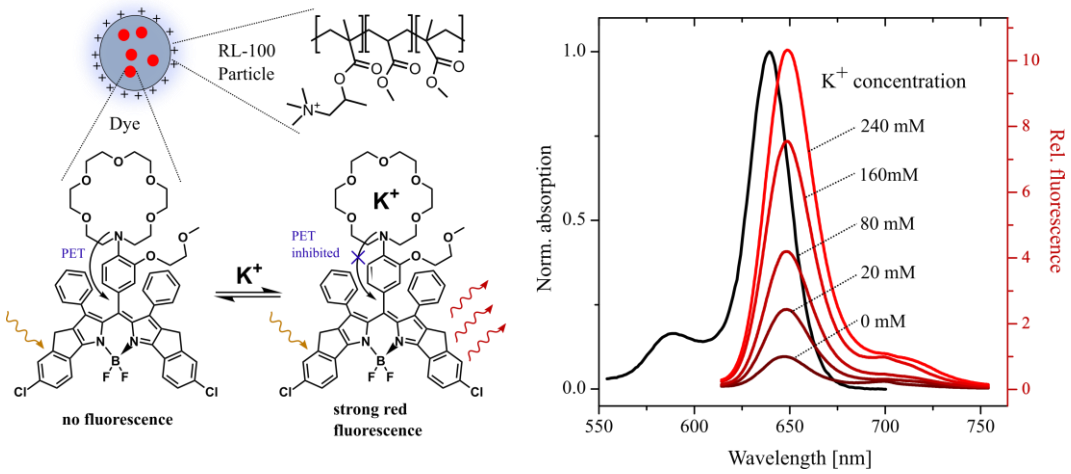

Figure 5.5: Scheme and spectral properties of K^+-sensitive FI3 dye encapsulated in RL100 nanoparticles.

The unusually efficient staining of neural cells with FI3 nanoparticles prompted us to test them with 3D tissue models. We produced neurospheres from rat primary neurons (E18) and observed efficient in-depth staining achieved in 6-16 h incubation time (**Figure 5.6B**). With more complex mouse intestinal organoid model[202] we observed comparably efficient staining of epithelium and lumen and some degree of aggregation (**Figure 5.6**). In comparison, two other types of nanoparticle biosensors,

based on anionic polymer (PA1)[198] and RL100 polymers (NanO2)[118] lacked the ability to stain intestinal organoids under similar conditions (**Figure 5.6B**): instead, only strong autofluorescence of lumen compartment was observed. Since FI3, PA1 and NanO2 are all emitting in the same spectral window, the luminal fluorescence can be related to strong red autofluorescence, which we reported before[203]. FI3 showed rather homogeneous staining of epithelium with enrichment in certain cell types (showing a 5-6 times higher fluorescence), which can be explained most likely by the cell-specific difference in staining efficiency (**Figure 5.6B**).

We also evaluated relative staining efficacy of FI3 nanoparticles with culture of tumor spheroids from HCT116 cells. Using optical sectioning we found strong fluorescent signals at 40-50 μm depths, indicating similar or higher staining efficacy than with conventional Calcein Green dye (**Figure 5.6C**).

Thus, we observed highly efficient and unique (in comparison to previously reported RL100-based probes) staining with FI3 nanoparticles of all tested cell models, from 'simple' adherent to multicellular aggregates and intestinal organoids, containing multiple cell types. This finding can be explained by the specific morphologies of FI3 nanoparticles (**Figure S - 5.1**), promoting disaggregation during interaction with lipid membranes.

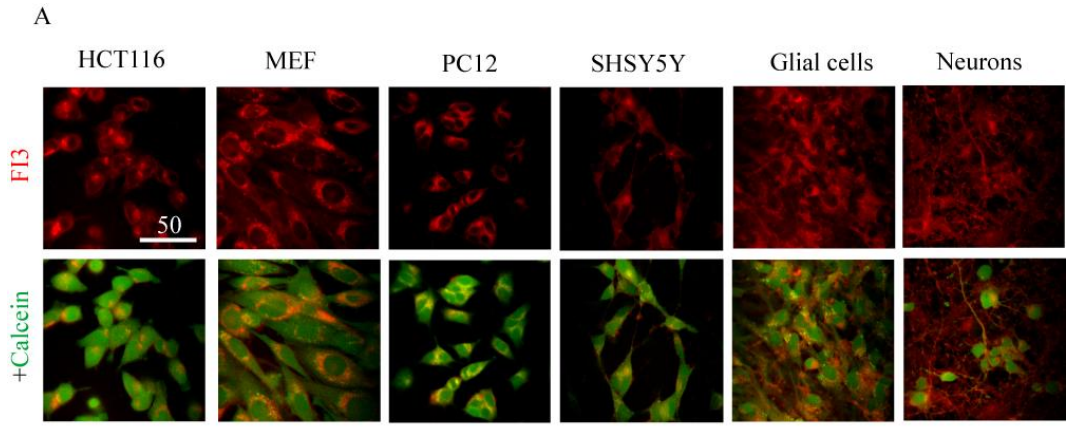

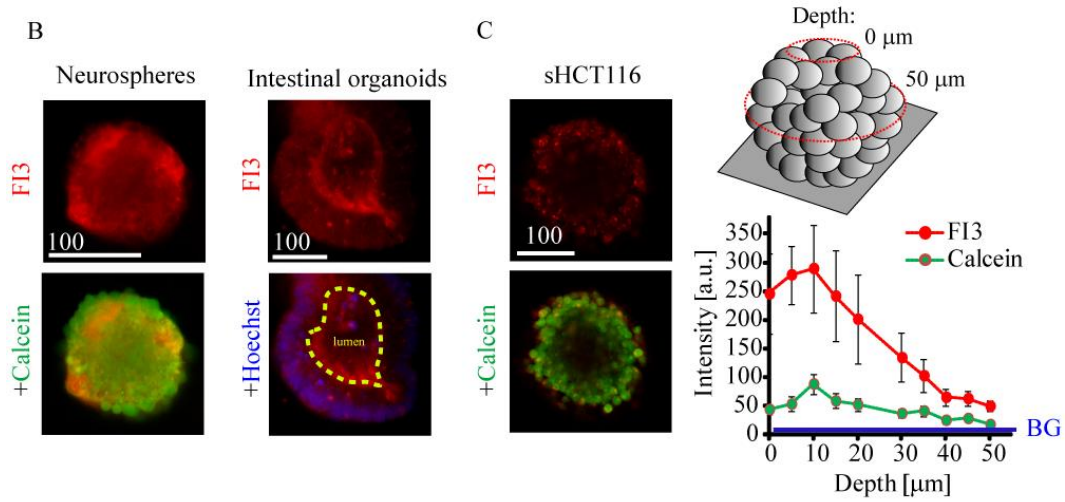

Figure 5.6: FI3 nanoparticles provide efficient staining of various 2D and 3D tissue models. **A:** adherent cell models of neuronal and non-neuronal origin. Live cells were incubated with FI3 nanoparticles (10 µg/ml, 16 h), washed and counter-stained with Calcein Green AM (1 µM, 0.5 h) and imaged. **B:** staining of rat primary neurospheres and mouse intestinal organoids. Live neurospheres and organoids were incubated with FI3 nanoparticles (10 µg/ml) for 16 h and 3 h, respectively, counter-stained with Calcein Green or Hoechst 33342 and imaged. **C:** staining of tumor spheroids from HCT116 cells. Formed tumor spheroids were incubated with FI3 nanoparticles (3 h) and counter-stained with Calcein Green. The image represents cross-section at 50 µm depth, as indicated. Right graph shows distribution of fluorescence intensity in the center of spheroids at depths 0-50 µm. BG indicates background intensity. Scale bar is in µm.

5.2.2 Intracellular staining differs between FI3 nanoparticles and non-encapsulated dye

The amphipathic nature of FI3 dye can potentially lead to its leakage from nanoparticles upon or prior to the cell internalization and thus explain the observed 'efficient' intracellular staining pattern. To reveal if this is the case, we performed a number of additional experiments. First, we compared the staining of neural cells with the free dye and encapsulated in RL100 nanoparticles (**Figure 5.7**): free dye displayed intracellular staining only of certain cells in culture and with lower intensity (not shown). The comparison of average brightness inside the cells showed that the dye impregnated in nanoparticles displayed 3-5 times higher brightness (0.1 µM of free dye corresponds to 10 µg/ml concentration of nanoparticles). The staining with free dye did not reach saturation at 0.1-0.2 µM, implying at difference in cell uptake mechanisms between the free dye and RL100 nanoparticles (**Figure 5.7A**).

Next, we found that FI3 encapsulated in nanoparticles displayed higher photostability than free dye and Calcein Green dye (**Figure 5.7B**). While testing other cell lines (HCT116, MEF, PC12) we saw comparable efficacy of staining between nanoparticles and free dye (not shown), however with mixed culture of neural cells we observed the differences in cell specificity (**Figure 5.7C**). We found that free dye stained predominantly certain neuron-like cells, while nanoparticles provided efficient staining of all the cells in population (both neurons and astrocytes). We attempted to confirm the cell specificity of free dye using immunofluorescent staining of fixed cells with respective antibodies but found that dye and nanoparticles did not remain visible after this procedure (not shown).

Further, we reasoned that after internalization into the cell different environments of the free dye (directly exposed to proteins, lipids or other biomolecules) and protected by nanoparticle shell can affect the fluorescence lifetime of FI3. Using fluorescence lifetime imaging microscopy (FLIM) we found that both free dye and RL100 nanoparticles displayed fluorescence decays, which could be fit with mono-exponential function (**Figure 5.7C-F**). We found that dye encapsulated in nanoparticles showed narrower distribution (±0.2 ns) of fluorescence lifetimes across the imaged areas, than the free dye (twice broader, ±0.4 ns) in mixed culture of neurons (**Figure 5.7E**) and in other cells, such as HCT116 (**Figure 5.7F**).

This data suggests that: (1) the fluorescence lifetime of FI3 is environment-sensitive; (2) encapsulation in RL100 nanoparticles helps minimizing the effect of biological environment on the fluorescence lifetime; (3) the dye does not leak from the nanoparticles. Collectively, these results demonstrate the improvement of photophysical properties of FI3 encapsulated in nanoparticles, in the staining of neural cells.

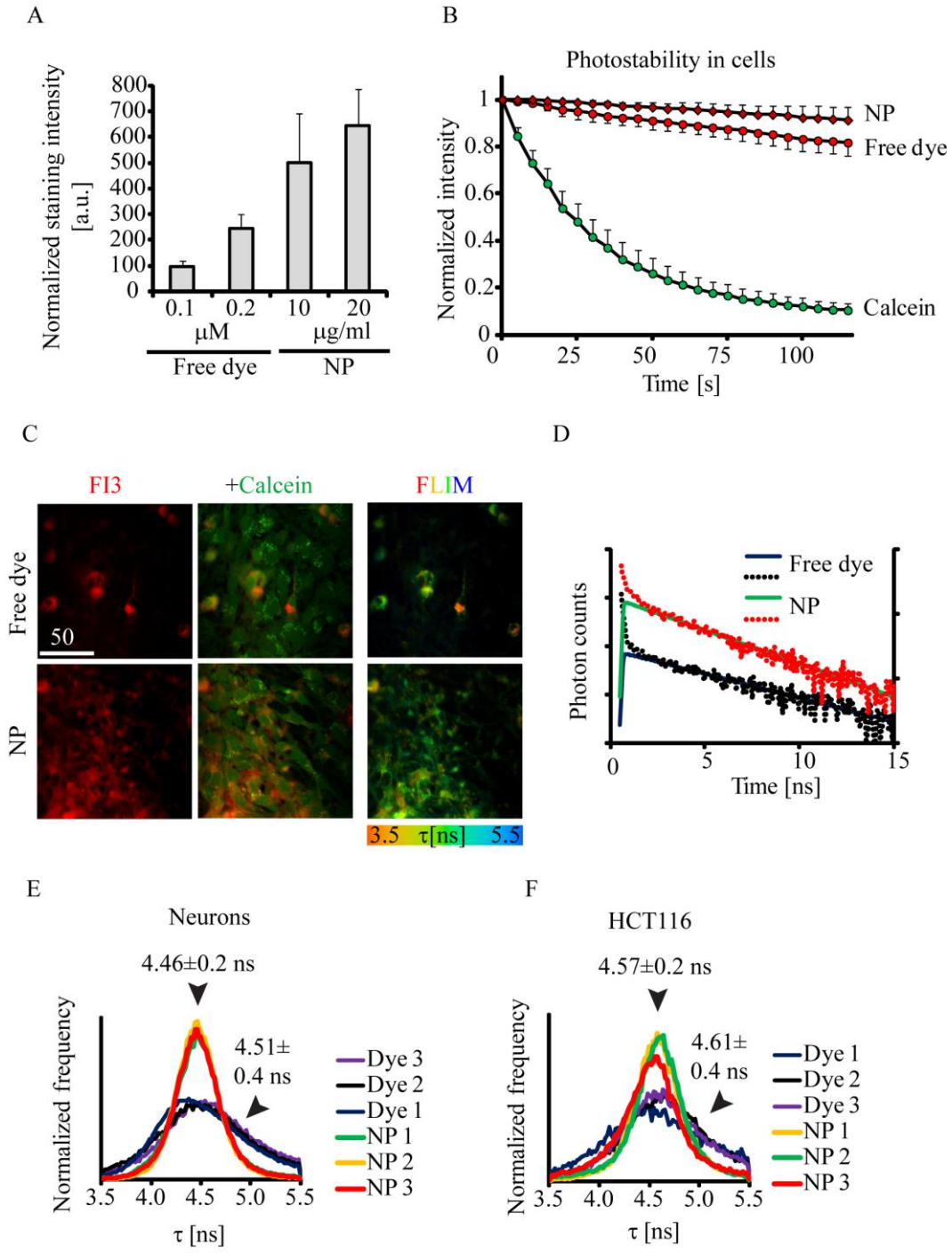

Figure 5.7: FI3 dye remains encapsulated in the nanoparticles after cell internalization. **A-B**: comparison of staining efficiency of live primary neurons with FI3 as free dye and encapsulated in nanoparticles (NP). The dye concentration of 0.1 µM equals to 10 µg/ml of nanoparticles. Cells were incubated with dye and dye/NP at indicated concentrations (16 h), washed and imaged. **A**: Comparison of fluorescence intensity in cells for the free dye and NP at different concentrations. **B**: Comparison of photostability between free dye, NP and Calcein Green. N=8. **C-F**: The differences in fluorescence lifetimes observed in cells stained with free dye and NP, measured by FLIM. **C**: characteristic images of mixed culture of astro-glial cells and neurons stained with FI3. Intensity (red

fluorescence), co-staining with Calcein Green and FLIM images are shown. **D**: typical fluorescence lifetime decay curves (dots) and the respective fits (lines), shown in logarithmic scale. **E, F**: distribution histograms for free dye and NP, observed for primary neurons and HCT116 cells. N = 3. Scale bar is in μm.

5.2.3 Mechanism of intracellular accumulation of FI3 nanoparticles

With culture of primary neural cells, FI3 nanoparticles displayed relatively fast intracellular accumulation different from the free dye (**Figure 5.8A**). Although this was still slower than with regular small molecule dyes such as Calcein Green, TMRM and fluorescent conjugates of transferrin or cholera toxin, it was comparable or better than loading with other nanoparticle-based biosensors[198,204], allowing shortening the incubation time with cells to as little as 3 h. Staining time of 3 h allowed us to study the mechanism of intracellular accumulation of FI3 nanoparticles using the culture of primary neural cells (**Figure 5.8B-D**). As expected, we observed that intracellular staining with FI3 was nearly completely inhibited by decreasing temperature to 4 ^{o}C (**Figure 5.8B**) and was mainly energy-dependent (**Figure 5.8D**). The incomplete blocking of uptake can be explained by partial depletion of cell energy sources (both glycolytic and oxidative phosphorylation ATP production pathways were blocked). Staining of cells with FI3 nanoparticles in presence of endocytosis inhibitors[205] revealed reliance of cell uptake on macropinocytosis (EIPA) and largely on clathrin-mediated endocytosis (chlorpromazine, CPZ) (**Figure 5.8C**). The treatment with methyl-β-D-cyclodextrin (MβCD) resulted in extensive cell condensation (round phenotype) and apparent increase of brightness, allowed to conclude that there was no effect of lipid raft-mediated endocytosis on cell uptake. This data shows with culture of primary neurons FI3 nanoparticles utilize mostly clathrin-dependent endocytosis (main energy dependent delivery route for small molecules), with lower degree of macropinocytosis. Thus, with culture of primary neural cells, FI3 nanoparticles employ different cell entry pathway than negatively charged polymeric nanoparticles[198].

We wondered if the K^+-sensitive sensor groups exposed at the surface of nanoparticles could participate in the improvement of cellular uptake. To test this, we stained neural cells with Na^+-sensitive FI3 analog (Na-FI3) under the same conditions and analyzed them by microscopy (**Figure 5.8E**). We found that both K^+ and Na^+-sensitive nanoparticles displayed comparable ability to stain live cells suggesting the active role of crown ether in improving the cell staining efficiency of RL100-based nanoparticles. With Na-FI3 we observed expected ~50% 'lower' signal

intensities inside the cells, which can be explained by much lower concentration of Na^+ in the cells.

Collectively, this data confirms that FI3 nanoparticles show different kinetics of staining than free dye, utilizing endocytic, energy-dependent cell entry pathway. The charge of nanoparticles and their complexation with K^+ unlikely plays significant role in their cell entry but the presence of crown ether is seemingly beneficial.

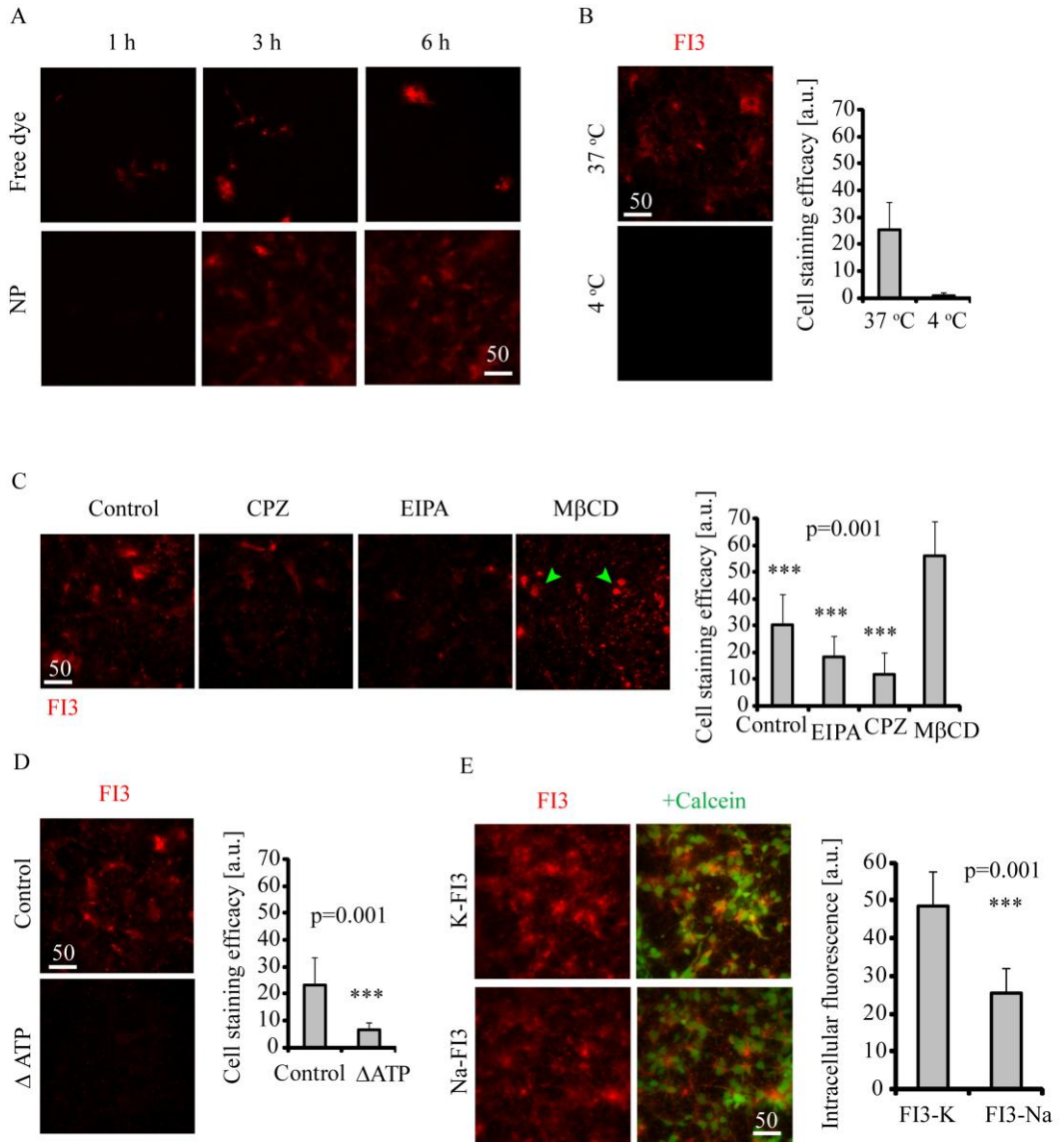

Figure 5.8: Mechanism of cell entry for FI3 nanoparticles. **A**: Staining kinetics for FI3 (0.1 µM free dye or 10 µg/ml RL100 nanoparticles) in live rat primary neural cells. Cells were incubated with FI3 for indicated time intervals, washed and immediately imaged. **B-D**: Staining of primary neural cells with FI3 nanoparticles (10 µg/ml, 3 h). **B**: Effect of temperature on staining efficiency. **C**: Effects of various endocytosis inhibitors on cell staining with FI3. Cells were pre-treated with inhibitors (50 µM EIPA, 10 µg/ml CPZ and 5 mg/ml MβCD) for 30 min, followed by staining procedure. MβCD-treated

cells displayed round morphology, indicated with green arrows. N= 17. **D**: Effect of ATP depletion on cell staining efficiency. For ATP depletion, cells were pre-incubated in no-glucose medium and treated with oligomycin (10 μM), followed by staining procedure. N=20. **E**: Cell staining efficacy for K-FI3 and Na-FI3. Cells were incubated with nanoparticles (10 μg/ml, 16 h) washed, counter-stained with Calcein Green and imaged. Scale bar is in μm.

5.2.4 Evaluation of FI3 nanoparticles as K^+ nanosensor with primary neural cells

The previously unseen ability of RL100-based FI3 nanoparticles to stain neural cells prompted us to evaluate it as a functional tool in monitoring of intra- and extracellular K^+ dynamics in mixed culture of primary neural cells. First, we tested whether the successful staining of cells with this fluoroionophore has any effects on cell viability. Using analysis of total cellular ATP, primary marker of cell viability, we found minor or no toxicity of nanoparticles at up to 20 μg/ml concentrations (6 and 25 h staining times) (**Figure S - 5.3A**). Similarly, we did not see toxic effects of FI3 nanoparticles when analyzed the membrane integrity (not shown). However, prolonged staining time and increase of concentration resulted in some toxic effects, more profound than for free dye. We also further tested if the toxicity increases at higher cell density (100%) and upon metabolic stimulation (cells exposed to glucose-free galactose medium or treated with mitochondrial uncoupler FCCP), when the effects of FI3 ionophore activity on cell function can become more profound: in this case we observed strong toxicity (25 h incubation time), reflected in loss of cell mass (cell detachment) and overall inhibition of mitochondrial function (**Figure S - 5.3B**). The potential effect on cell energy metabolism at high doses of FI3 nanoparticles (20 μg/ml, 25 h incubation time) was also confirmed with analysis of glycolytic flux (extracellular acidification rate) (**Figure S - 5.3C**). While our data showed minimal toxicity upon short incubation time and small concentrations of FI3, it should be kept in mind that use of FI3 (and any other fluoroionophore) at high concentrations can indeed have adverse effects on cell function. However, the high brightness, quantum yield and cell staining efficiency with FI3 allow for use of minimal doses of these nanoparticles for cell-based measurements.

Next, we evaluated the performance of FI3 in monitoring of K^+ dynamics with mixed culture of neural cells. Using confocal fluorescence microscopy, we observed nearly equal staining efficacy of both astro-glial cells and neurons in mixed culture (**Figure**

S - 5.4). Astrocytes showed stronger punctate staining of cytoplasm with FI3 than neurons (diffuse cytoplasmic staining), which can be attributed to their higher capacity[170] in storing intracellular K^+. To demonstrate the responses of FI3 nanoparticles in kinetic measurements, we treated neural cells with KCl (increases extracellular K^+) and then with ionophore valinomycin (increases membrane permeability and equalizes extra- and intracellular K^+) (**Figure 5.9A-C**). We found that application of KCl led to cell contraction, changing cell shape and size. In order to interpret the differences between extra- and intracellular (visualized by co-staining with Calcein Green) pools we used line profiles across optical sections and integrated peak areas (grey boxes indicate extracellular signals, see Methods for details and **Figure 5.9B**). As expected, we observed overall increase in extracellular K^+ after addition of 40 mM KCl and subsequent decrease after applying valinomycin (**Figure 5.9C**). Upon such treatment, application of external KCl resulted in minor decrease of intracellular pool of K^+, potentially due to partial depolarization of cell membrane, while adding valinomycin helped to slightly 'restore' it. In another experiment, we reversed the order of these treatments and monitored only intracellular K^+: we added first valinomycin and observed ~40% decrease in K^+, and again slightly 'restored' it by applying KCl (**Figure 5.9D**, **Figure S - 5.5**).

We also looked at the effects of treatment with nigericin (H^+/K^+ ionophore) and ouabain (inhibitor of Na^+/K^+-ATPase)[174]. Treatment with these drugs led to decrease of intracellular K^+ (**Figure S - 5.6**).

These results demonstrate that FI3 can be successfully used for monitoring of intracellular K^+ fluxes in live cells, by high-resolution live cell confocal fluorescence microscopy. The counter-staining with markers of cytoplasm and simultaneous monitoring of FI3 can be also used for analysis of extracellular K^+. The quick response time and the molecular structure of BODIPY dye[206] constituting FI3 nanoparticles allow for advanced two-photon excited imaging applications and multi-color imaging[207].

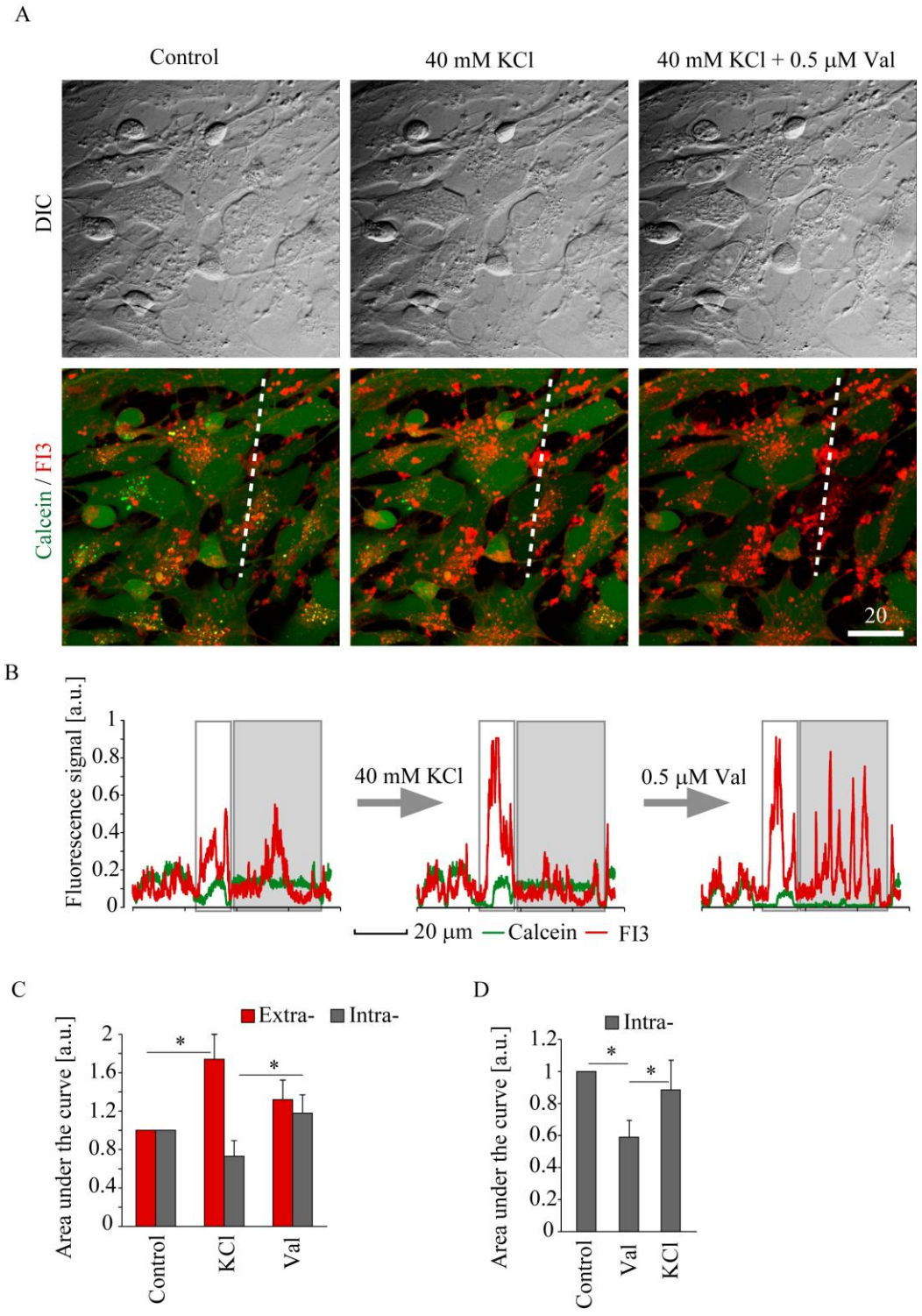

Figure 5.9: Monitoring of extra- and intracellular K^+ in neural cells with FI3 nanoparticles. The live rat primary neural cells were stained with nanoparticles (10 µg/ml, 16 h), counter-stained with Calcein Green and treated with KCl and valinomycin (Val). **A**: Representative transmission light (DIC) and superimposed confocal fluorescence images of FI3 and Calcein before and after treatment with KCl (40 mM) and valinomycin (Val, 0.5 µM). **B-C**: Line profile analysis of the changes in FI3 and Calcein

fluorescence signals, induced by treatments in (**A**). The areas of intra- and extracellular FI3 pools are highlighted in (**B**) in grey and white, respectively. **D**. Results of line profile analysis of the changes in intracellular FI3 signal, induced by the sequential addition of Val and KCl. Images (**A**) represent stacks of 2 confocal planes taken with 0.5 μm step. Error bars indicate SEM. Asterisks indicate significant difference ($p < 0.01$, U test). N = 4 (**D**). Scale bar is in μm.

5.2.5 Application of FI3 nanoparticles to brain imaging

To further evaluate the application potential of FI3 we tested more complex biological models, such as live brain slices and intact brain. Using confocal fluorescence microscopy of live organotypic rat brain slices (*ex vivo*), we observed efficient staining of cortex, different from distribution of cholera toxin-positive cells (**Figure 5.10A-B**). This confirmed that FI3 can be used for staining of intact live tissue and prompted us to apply FI3 nanoparticles in functional brain imaging.

Using previously described *in vivo* imaging setup[208] we applied FI3 nanoparticles to live mouse brains (intracortical administration) and recorded the responses to electrical stimulation. Functional pseudocolor maps images of recorded optic signal were constructed using 'the first frame analysis' (**Figure 5.10C**). Due to short incubation time, we expected that FI3 nanoparticles partially localized inside the cells and predominantly in the brain parenchyma. The changes of FI3 fluorescence were observed near the electrode tip immediately following the stimulation onset, reaching a maximum at 40–50 ms after stimulation onset and then decaying during the subsequent frames. This response occurred simultaneously but its intensity was proportional to the distance from the electrode tip (**Figure 5.10C-D**). In another experiment, we looked if the drug-induced epileptic seizures can be monitored with FI3 in intact mouse brain. To do this, we applied 4-aminopyridine (4-AP) and monitored fluorescence changes together with EEG (**Figure S - 5.7**): thus, we found periodic responses lasting for 2 – 3 h (30 – 200 s with few min intervals). **Figure S - 5.6** shows pattern of the *EEG* typically observed during *epileptic seizures.* Epileptic seizure on the EEG signal (30 seconds window) and profound changes in fluorescence were well correlated with each other.

Thus, we demonstrated for the first time that K^+-sensitive FI3 nanoparticles are useful for *in vivo* mapping of epileptic seizures with high spatial and temporal resolution in animal model. This suggests that FI3 can become a new tool for mapping neural activity in various areas of brain imaging.

The resolution of the used optical system is about 50 μm per pixel, and the obtained data represents 2D projection of the 3D object. Therefore, each pixel reflects averaged fluctuations of intra- and extracellular K^+ in the particular volume of the brain tissue. It is well known that electrical stimulation of the cortical tissue causes an increase in extracellular K^+ concentration[209] and thus positive and negative fluorescence changes in particular pixels can be observed on a micro scale. Overall, the brain activity patterns obtained in our experiments are very similar to voltage-sensitive dye optical imaging (VSDI)[210]. Altogether, measured relative changes in FI3 fluorescence displayed the responses, concomitant with the evoked neural activity, within the useful scale of milliseconds. FI3 showed good sensitivity, reproducibility of signals, selectivity and thus can be applied for functional brain imaging and such applications as development of better therapy against epileptic seizures.

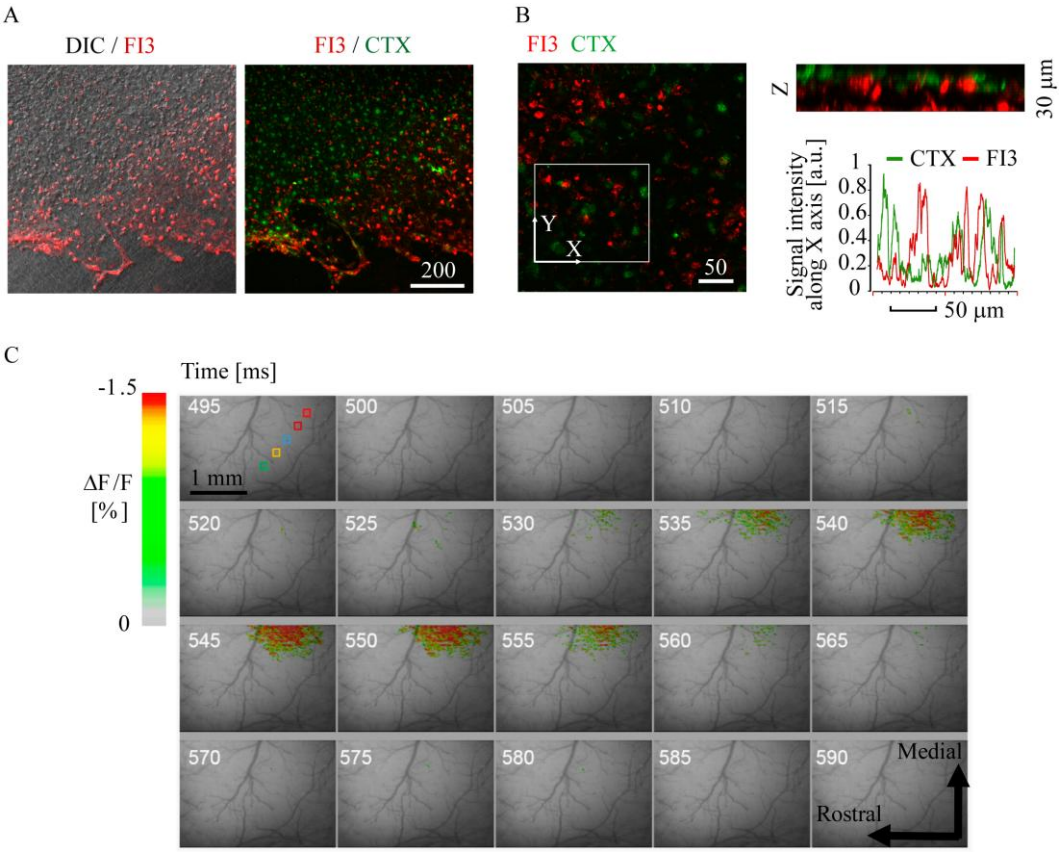

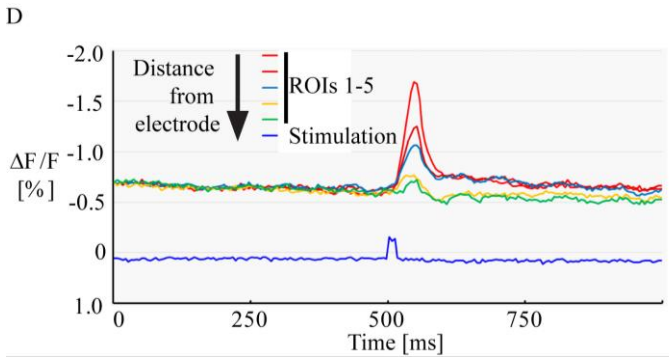

Figure 5.10: Application of FI3 nanoparticles to ex vivo and in vivo brain imaging. **A-B**: staining efficiency and distribution of FI3 (10 µg/ml, 6 h) in live organotypic rat brain slices. Cortex region is shown. Staining with FI3 (red) and cholera toxin-Alexa Fluor 488 conjugate (green) is shown. **B**: 3D reconstruction (the views of XY and Z projections) of FI3 and CTX localization in the tissue, and corresponding line profile analysis. Images represent stacks of 21 (**A**) and 16 (**B**) confocal planes taken with 2 µm step. **C-D**: In vivo imaging of stained mouse brain. **C**: Pseudocolor images of the cortex before and after stimulus onset. Time (ms) after beginning of the trial is indicated by numbers. **D**: Time-course of recorded response at the locations (depicted in **C**) having different distances from the electrode.

5.3 Conclusion

We discovered improved cell permeability of RL100-based nanoparticles, when combined with crown ether-based BODIPY FI3 dyes. For the first time, we show that polymeric RL100-based nanoparticles provide efficient staining of primary neural cells (astrocytes and neurons) and 3D tissue cancer and stem cell-based models (spheroids, organoids and *ex vivo* tissue sections). The encapsulation of FI3 in cationic RL100 polymer facilitated brighter cell staining, with no observable cell specificity, via energy-dependent clathrin-mediated endocytosis. These features and relatively short cell staining time (3 h) demonstrate that FI3 nanoparticles are as easy to use as small molecule fluorescent dyes. We also performed detailed evaluation of FI3 nanoparticles in quantitative live cell imaging and *in vivo* brain imaging applications. The sensitivity, brightness and versatility of the described nanoparticles make them a promising tool as a versatile K^+-sensitive biosensor and as a prototype for advanced design of polymer-based nanoparticles, helping to solve the problem of their efficient bio-distribution.

Acknowledgments

This work was supported by Science Foundation Ireland (SFI) 13/SIRG/2144 (RID), NSF CBET-1254743 'Career award' (YC) and National Institutes of Health (NIH) NS084818 (RSE) grants. We thank E. Keomani and Dr. C. Waeber for help with brain slice culture, and B. Okura, T. Sakuraba and K. Tsubokura (Sci-Media Company) for their help with MiCAM-02 data analysis and experimental design.

Author Contributions

BJM, AVZ, SMB and RID conceived the study, performed experiments, analyzed the data and wrote the manuscript. BJM, SMB and IK designed and synthesized the nanoparticles. AVZ and RID performed evaluation with cells and 3D tissue models by microscopy. TF and IAO performed experiments with organoid culture. TF assisted in preparation of culture primary neural cells. VT, YC, QT and RSE performed in vivo imaging experiments. HZ and CT performed the analysis of nanoparticles. DBP and IK helped the data interpretation and drafting the manuscript. All authors read, and edited the manuscript.

5.4 Materials and Methods

CellTox Green™ and CellTiter-Glo™ viability assay kits were from Promega (MyBio, Ireland). Lipidure™ 96-well plates were from Amsbio (UK). Palladium (II) meso-tetra(pentafluorophenyl)porphine (PdTFPP) was from Frontier Scientific (Inochem Ltd, Lancashire, UK). IntestiCult organoid growth medium (mouse) kit and Gentle dissociation reagent were from StemCell technologies (UK). Matrigel™ matrix with reduced growth factors was from Corning (USA). Eudragit RL100 was from Evonik Industries (Germany). MitoImage-NanO2™ and pH-Xtra™ probes were from Luxcel Biosciences (Cork, Ireland). PdTFPP/RL100 nanoparticles and PA1 O_2-sensitive nanoparticles were prepared as described previously[198]. FI3 free dye and RL100-based nanoparticles were prepared as described previously[151]. Na-FI3 was synthesized as described before. Cholera toxin, subunit B, Alexa Fluor 488 conjugate and B-27 serum-free media supplement were from Thermofisher (BioSciences, Dublin, Ireland). Fibroblast growth factor (FGF), Epidermal growth factor (EGF), R-spondin and MilliCell membranes were from Millipore (Cork,

Ireland). Galactose, valinomycin, oligomycin, Calcein Green AM, bis-benzimide Hoechst 33342, chlorpromazine, 5-(N-ethyl-N-isopropyl)amiloride, methyl-β-cyclodextrin and all the other reagents were from Sigma-Aldrich (Dublin, Ireland). Standard cell culture grade plasticware was from Sarstedt (Wexford, Ireland), glass bottom mini-dishes were from MatTek (Ashland, USA) and Ibidi µ-slide 8/12-well chambers were from Ibidi (Martinsried, Germany).

5.5 Experimental

5.5.1 Cells, tissues and organoids

HCT116, PC12, MEF and SHSY5Y cells (ATCC) were handled and differentiated as described before[187,211]. Typically, cells cultured at 30-50% confluence were incubated with dyes and nanoparticles in regular growth medium (McCoy 5A supplemented with 10% heat-inactivated fetal bovine serum, penicillin-streptomycin, 10 mM HEPES-Na, pH 7.2 for HCT116 cells; RPMI 1640 supplemented with 1% heat inactivated horse serum, penicillin-streptomycin, 10 mM HEPES-Na, pH 7.2 for differentiated PC12 cells; high-glucose DMEM supplemented with 10% heat-inactivated fetal bovine serum, penicillin-streptomycin, 10 mM HEPES-Na, pH 7.2 for MEF and SHSY5Y cells) at indicated concentrations and staining time, washed three times with growth medium and immediately proceeded to live cell imaging.

In studies of cell entry mechanism, cells were pre-incubated with respective drugs for 30 min (or 1.5 h in glucose-free DMEM supplemented with 10 mM galactose, followed by 15 min pre-incubation with 10 µM oligomycin, for ATP depletion), followed by incubation in the same medium with FI3 (10 µg/ml, 3 h), washing and analysis. Tumor spheroids were produced by seeding in Lipidure^{TM} plates (300 cells, 3 days growth per spheroid) essentially as described previously[168].

All the procedures with animals were performed under the license issued by the Department of Health and Children (Ireland) and in accordance with the Directive 2010/63/EU adopted by the European Parliament and the Council of the European Union. Cultures of embryonic rat (E18) neurons, neurospheres and organotypic brain slices were produced and handled as described previously[198,197]. Mixed culture of primary neurons and astro-glial cells (primary neural cells) were allowed to differentiate in DMEM F12 Ham medium supplemented with 1% heat-inactivated fetal bovie serum, 2% B-27 and penicillin-streptomycin for 4-8 days, before

experiments. To obtain the culture enriched in astrocytes, cells were first grown in neurospheres, then trypsinized and seeded for additional 5 days differentiation[197]. Neurospheres were typically grown in suspension state for 5-7 days before staining and analysis. For staining and microscopy, they were collected, washed in Hanks' balanced salt solution and allowed to attach under differentiation conditions (1% FBS, 2% B-27) for 3 h on poly-D-lysine pre-coated glass or plasticware as described previously[204]. Organotypic brain slices were cut at 300 μm thickness on a vibratome and cultured on MilliCell (0.4 μm) membranes for 7-9 days prior the staining and analysis, essentially as described previously[204].

Mouse intestinal organoids were produced, grown in Matrigel and handled as described before[203]. Organoids were incubated with FI3 nanoparticles (10 μg/ml, 16 h), washed and imaged directly in Matrigel™ in growth medium.

5.5.2 Microscopy

Cell staining kinetics, comparison of efficiency of staining, photostability and mechanism of cell internalization were studied on widefield live fluorescence microscope Axiovert 200 (Carl Zeiss)[7] equipped with 40x/1.3 Plan Neofluar oil-immersion objective, integrated T/ CO_2 climate control (PeCon), pulsed LED excitation module (390, 470, 590 nm), gated CCD camera, respective green (FITC) and red (635LP) emission filters and image acquisition and processing ImSpector software (LaVision Bio-Tec).

Comparative analysis of staining of different cell models (including neurospheres, tumor spheroids and organoids) and FLIM were performed on an upright laser scanning Axio Examiner Z1 (Carl Zeiss) microscope[187] equipped with 20x/1.0 and 63x/1.0 W-Plan Apochromat dipping objectives, integrated T and Z-axis control, ps diode BDL-SMC 405 nm (Becker & Hickl GmbH) and ps supercontinuum SC400-4 (Fianium, UK) lasers, DCS-120 confocal TCSPC scanner, photon counting detector and dedicated SPCM and SPCImage software (Becker & Hickl GmbH). Calcein Green dye was excited using 4488 nm laser (emission collected at 512-536 nm), Hoechst 33342 was excited using 405 nm laser (emission collected at 428-468 nm), FI3 was excited using either 405 nm or 632 nm lasers (emission collected at 635-675 nm). FLIM measurements of FI3 (excited at 632 nm) were performed essentially as described previously[168], with application of mono-exponential decay (longer component) fitting function.

Analysis of brain slices and monitoring of kinetic responses of primary neural cells to drug stimulation were performed on an inverted Olympus FV1000 confocal laser scanning microscope[212] with controlled temperature, CO_2 and humidity. Calcein Green and CTX were excited at 488 nm (2-8% of laser power) with emission collected at 500-560 nm. FI3 was excited at 633 nm (5-20% of laser power); emission was collected at 560-600 nm. Acquisition of each spectral signal was done using UPLSAPO 20x/0.75 and UPLSAPO 60x/1.35 oil immersion Super Apochromat objectives in sequential laser mode to avoid spectral overlap. In all experiments differential interference contrast (DIC) images were collected to complement fluorescence images. In kinetic experiments, images (8-12 focal planes) were collected with approximately 3 min intervals before and after stimulations. The changes in FI3 intensity signals (Fig. 5C-D and S5) were quantified as areas under the curve (from line profiles), calculated according to the equation S *(the area)* = $\Sigma[(X_{(n+1)}-X_n)\times(Y_n+Y_{(n+1)})/2]$, where X_n is the position on the analyzed line (μm) and Y_n is the value of corresponding fluorescence signal.

Analysis of cellular responses to ouabain (50 μM) and nigericin (10 μM in the presence of 20 mM KCl) was performed in a kinetic mode, with 3 focal planes imaged repeatedly with 30 s intervals before and after addition of drugs. The resulting single plane and z-stacked images were analysed using FV1000 Viewer software (Olympus) and assembled using Adobe Photoshop and Illustrator software.

Scanning transmission electron microscopy (STEM) was performed on a FEI Talos F200X at the Scope M facility (Zürich, Switzerland). The nanoparticle solution (1 mg ml^{-1}) was first desalted (to eliminate glycerol) using a PD MiniTrap G-25 column (GE Healthcare) and then diluted 1:10 (v/v) with ethanol. 1 μL of the resulting solution was drop-casted on a carbon support film copper grid Cu 400 and used for measurements.

5.5.3 Assessment of toxicity

The effects of cell staining with FI3 (free dye and nanoparticles) were evaluated by using analysis of membrane integrity (staining of cells with 0.2% CellTox Green), total cellular ATP (CellTiter-Glo assay) and extracellular acidification (unsealed system), as described before[187]. Briefly, primary neurons grown on poly-D-lysine pre-coated microplates were incubated with FI3 at indicated concentration and time, washed and either measured in presence of pH-Xtra probe on Victor2 time-resolved

fluorescence microplate reader (PerkinElmer) over 1 h at 37 ºC or lysed using CellTiter-Glo reagent and measured for total luminescence. For normalization, cells were lysed with buffer containing 50 mM HEPES-Na, pH 7.4, 150 mM NaCl, 1 mM EDTA, 1% Igepal CA630, protease inhibitor cocktail (Sigma P2714) and total protein concentration was determined using BCA protein assay kit (Pierce, Thermofisher, Ireland)[213].

5.5.4 *In vivo* imaging

All the procedures with animals were performed in accordance with the NIH Guide for the Care and Use of Laboratory Animals (NIH Publications No. 80-23) revised in 1996 and a protocol approved by the University of Maryland School of Medicine Institutional Animal Use and Care Committee. The *in vivo* imaging experiments were performed on C57BL/6N (Charles River Laboratory, MD) mice (weight 25–35 g, 3–6 months old, N=4) using a MiCAM-02 optical imaging system (SciMedia, Ltd). Animals were anesthetized with urethane (IP injection, 1.15 g/kg), fixed on a stereotaxic frame and proceeded to surgical removal of the skin of the dorsal part of the head. The exposed area was washed with a hemostatic sponge with the artificial cerebrospinal fluid (ACSF). A cranial opening (~4–5 mm^2) was made using a dental drill and the exposed *dura mater* surface was cleaned with ACSF. After each experiment, the animal was euthanized. After craniotomy, FI3 nanoparticles (1 µl of 2 mg/ml solution) were injected into 3-5 sites in the cortex. For electrical stimulation experiments a bipolar tungsten electrode MX216TW(VT1) (FHC Inc.) was introduced into the cortical tissue at a 0.3–0.4 mm depth using XYZ manipulator. A 100 µA stimulus was generated by A-M Systems stimulator (Model 2100), controlled by computer and consisted of a 10 ms train of 0.2 ms 300 Hz. For the epileptic seizures experiment, 4-aminopyridine (4-AP, 0.3 µL of 30 mM solution in ACSF) was injected into cortical layer III, using an injector mounted on a micromanipulator (Nanojet II) with a 20–30 µm diameter glass microcapillary as described previously[214]. A single-channel electroencephalogram (EEG) was recorded through a screw-type electrode placed in the operated hemisphere in the bone, then amplified by the differential amplifier (A-M Systems, Model 3000), digitized at 5000 Hz, and recorded using custom made computer software. The EEG data acquisition was initiated manually.

5.5.5 Data assessment

Plate reader data represent averaged values (obtained from >4 replicates) with standard deviation shown as error bars. For microscopy, the experiments were performed in triplicate. For quantification, images were processed in Fiji (ImageJ 1.49k) or FV1000 (Olympus) software, using analysis of independently taken ROIs (N indicated in figure legends). Where appropriate (normal distribution), an independent *t*-test was performed in Origin 6.0 software, with confidence level P=0.001 accepted as significant. FLIM data were processed using SPCImage and Microsoft Excel software, with mono-exponential tail-enhanced fitting function ($\chi^2 <$ 1.5) and binning factor as appropriate.

Distribution of fluorescent signals was evaluated using a cumulative histogram approach, as described before[215]. Where appropriate, an independent *t*-test and Mann-Whitney U-test were performed in Origin 6.0 (Microcal Software) and SPSS software, with confidence level P=0.05 or 0.01 deemed significant.

5.6 Supporting Information

Analysis of size of FI3 nanoparticles by electron microscopy

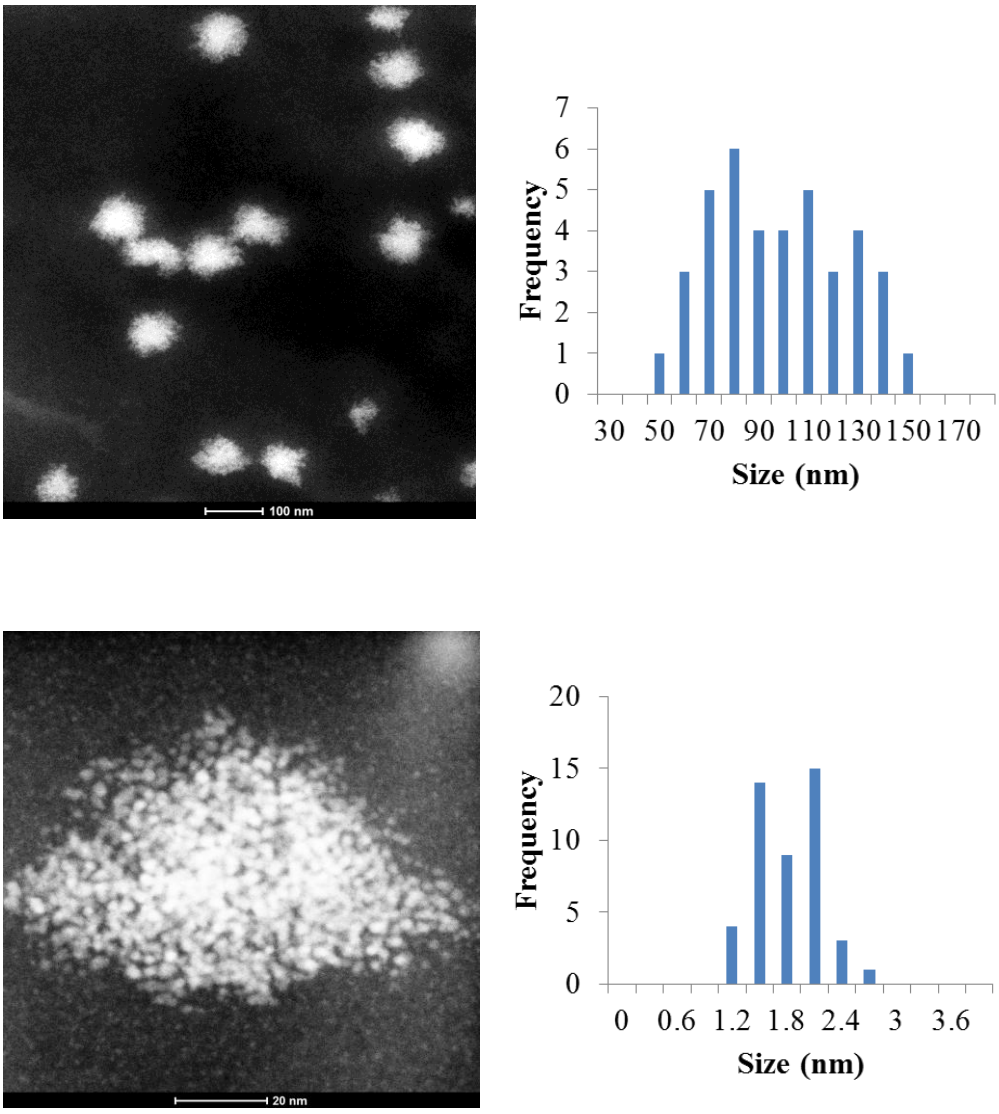

Figure S - 5.1: STEM images of the nanoparticle aggregates (top, scale bar 100 nm) and at higher magnification resolving the single nanoparticles (bottom, scale bar 20 nm). Size distribution histograms are shown on the right.

Efficiency of staining of primary neurons and intestinal organoids with other nanoparticles

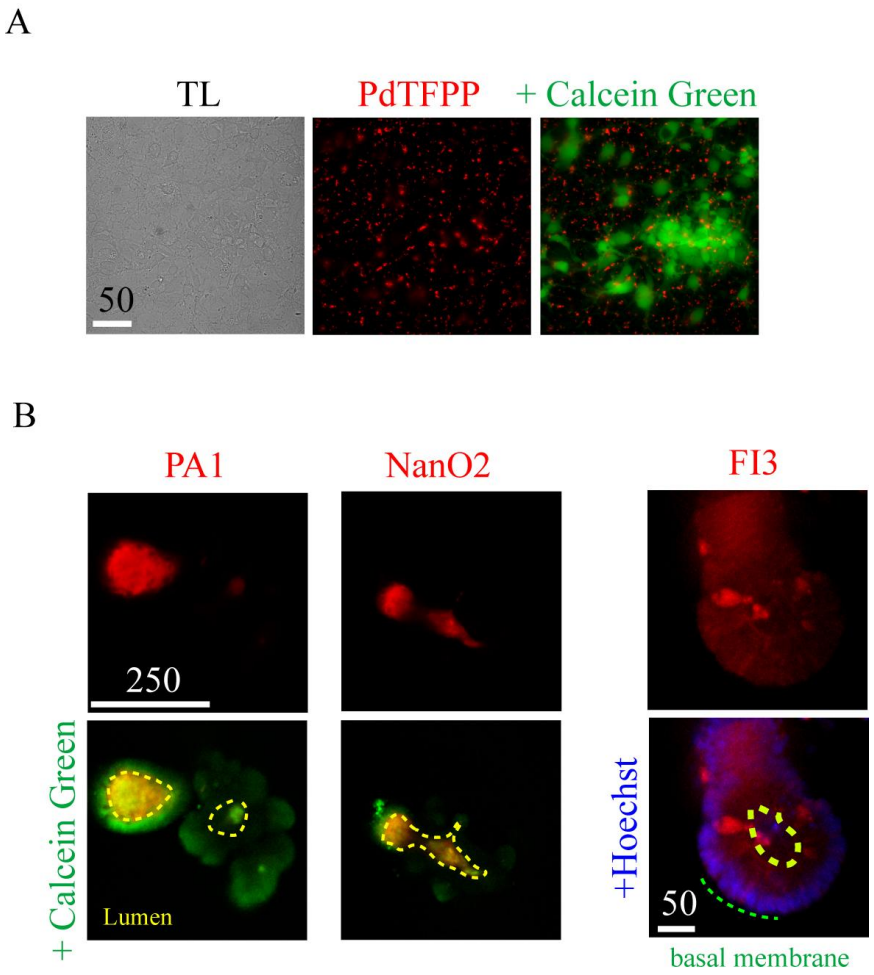

Figure S - 5.2 A: Staining of primary neurons with PdTFPP/ RL100 nanoparticles (10 µg/ml, 16 h), counter-stained with Calcein Green. **B**: Staining of mouse intestinal organoids with PA1 and NanO2 (10 µg/ml, 16 h), counter-stained with Calcein Green or Hoechst 33342 and FI3, for comparison. Scale bar is in µm.

Evaluation of toxicity of FI3 nanoparticles

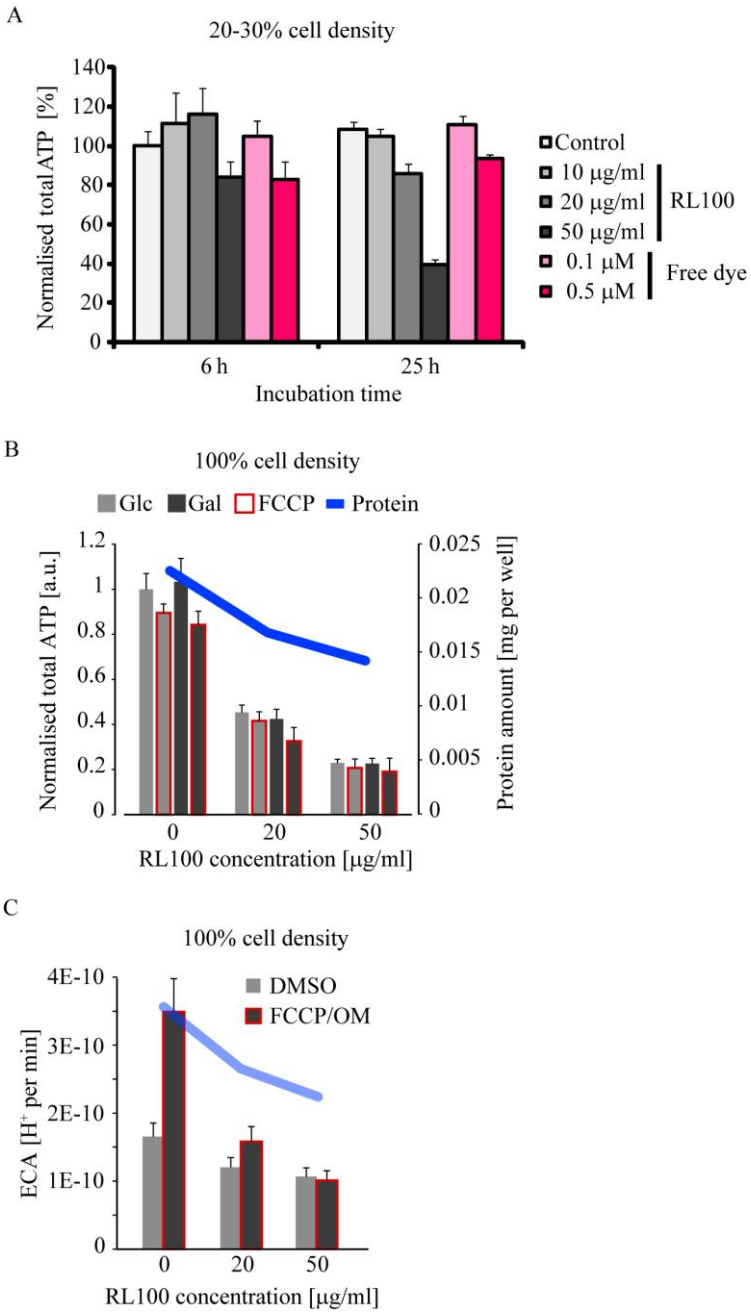

Figure S - 5.3: Evaluation of toxicity of FI3 nanoparticles with primary neural cells. Cells were grown on microplates, stained with FI3 at indicated concentration and times and then proceeded to analysis of cell energy budget by measuring total ATP and extracellular acidification. **A**: Total cellular ATP in cells cultured at regular 20-30% density. ATP data are normalized to total protein. **B, C**: Cells growing at high density and exposed to higher concentrations of FI3 and incubation in glucose- or galactose-containing media display stronger decrease of viability after treatment. **B**: Total cellular ATP. Blue line indicates total protein amount in the samples. **C**: Extracellular acidification (glycolytic

flux). To achieve maximal uncoupling, cells were treated with 1 µM FCCP and 10 µM oligomycin (FCCP/OM). Error bars indicate standard deviation (N=4).

Comparison of cell staining

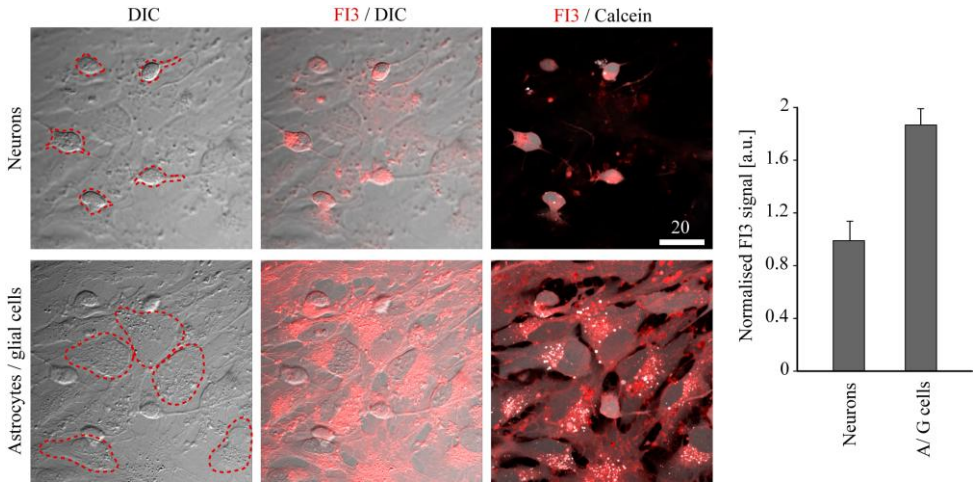

Figure S - 5.4: The live cells were stained with FI3 (10 µg/ml, 16 h), counter-stained with Calcein Green and imaged. Representative neurons (top) and astro-glial cell (bottom) are highlighted on transmission light (DIC) and combined fluorescence images. FI3 is shown in red, Calcein Green is shown in grayscale. For calculations, 4 confocal planes (0.5 µm each) were stacked together. N = 8 (neurons) and 21 astroglial cells. In the right panel, the calculated data are shown as m ± SEM. Scale bar is in µm.

Stimulation of rat primary neural cells

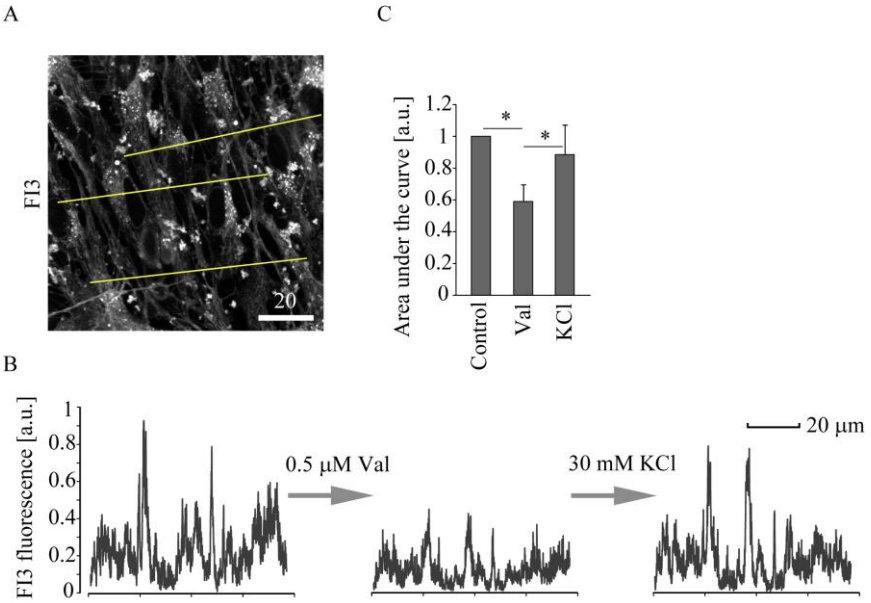

Figure S - 5.5: Stimulation of rat primary neural cells with Valinomycin and KCl. The live cells were stained with FI3 nanoparticles (10 µg/ml, 16 h) and treated with valinomycin (Val) and KCl as indicated. **A**: Fluorescence microscopy image (8 confocal planes taken with 0.5 µm step). **B**: Line profile analysis of the changes in FI3, induced by treatments and (**C**) calculated responses in intracellular K^+. Error bars show SEM. Asterisks demonstrate significant difference ($p < 0.01$, U test). *N*= 3. Scale bar is in µm.

Stimulation of rat primary neural cells with ouabain and nigericin

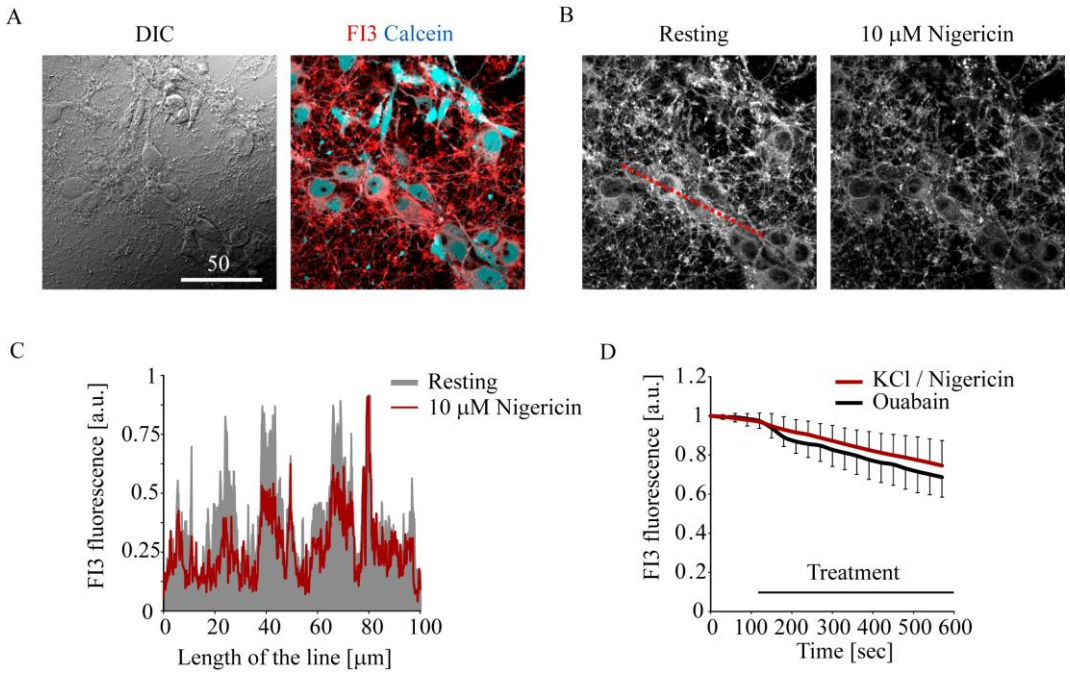

Figure S - 5.6: Stimulation of rat primary neural cells with ouabain and nigericin. Live cells were stained with FI3 (10 μg/ml, 16 h), counter-stained with Calcein Green and imaged. **A**: Representative image of cells shown as transmission light (DIC) and fluorescence (FI3 in red, Calcein Green in blue). Images represent stacks of 2 (DIC) or 3 (fluorescence) focal planes (0.5 μm). **B**. Examples of decrease in intracellular FI3 fluorescence upon addition of nigericin (10 μM, 7 min) in the presence of 20 mM KCl. **C**. Representative line profile analysis of the response to nigericin (dotted line is shown in B). **D**. Calculated reduction of intracellular FI3 fluorescence upon treatment of cells with nigericin (10 μM) and ouabain (50 μM). Scale bar is in μm.

In vivo brain imaging

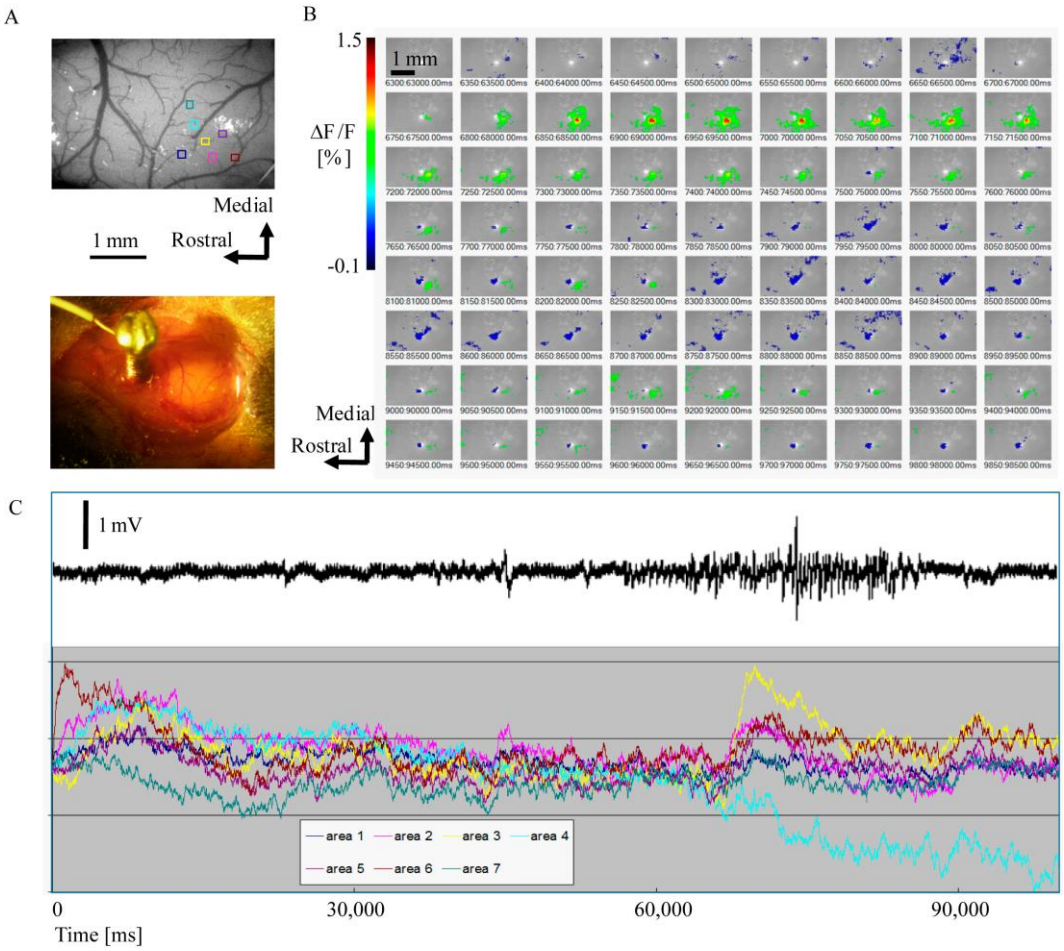

Figure S - 5.7: *In vivo* brain imaging of responses to epileptic seizures with FI3 nanoparticles. **A**: Region of imaging, with locations of ROI, where fluorescence was calculated. Bottom: photo of operated area (cranial window) with the screw-type electrode connected for the EEG. **B**: Pseudocolor images of the cortex before and after stimulus onset. **C**: calculated the epileptic seizures on the EEG (top) and the integrated fluorescence signal in the indicated ROI (bottom).

Future Prospect and Outlook

As shown in the preface to this manuscript , attempts to use ratiometric nanosenors were not successful due to the absence of co-localisation of the indicator and the reference (**Figure 5.3** (p. 103)). This can be overcome by having a covalent connection of the fluoroionophore and the reference dye, which would prevent leaching of one of the two components.

One possibility aims to couple the indicator dye onto a conjugated polymer reference dye via substitution of one boron–fluorine bond by an alcohol (**Figure 2.1**).This would lead to a high variability of potential indicator dyes that can be incorporated as the reactive group is always available in BODIPY and independent of the substitution pattern (e.g. recognition units, pyrrole) of the dye. Initial results of polymers with covalently coupled dyes via a boron–oxygen bond were successful and are currently under further investigation.

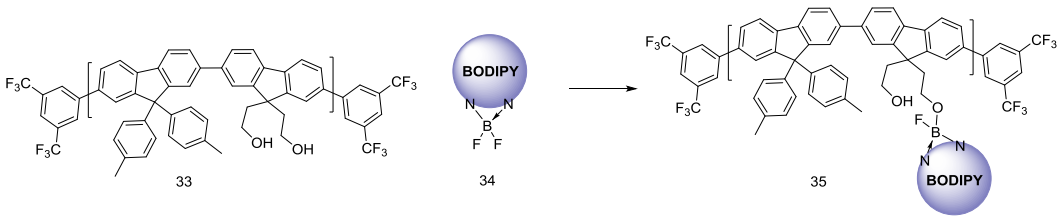

Figure 5.11: Schematic illustration of the covalent coupling of a BODIPY dye on a conjugated polymer.

As an alternative to nanoparticle based sensors, it is also possible to prepare molecular probes. In order to enable cell penetration, it is necessary to attach positively charged groups onto the indicator dye. BODIPYs with a triphenylphosphonium group (PPh_3) were already reported to show good cell uptake.[127] One attempt that is currently under investigation is the preparation of a brominated derivate of FI3 (**Figure 5.12**). Due to the increased reactivity of the bromine, the indicator can undergo further synthetic modifications. Initial attempts of Suzuki coupling reaction using a non-rigid brominated BODIPY (derivate of FI2 with bromine instead of propyl) were already successful.

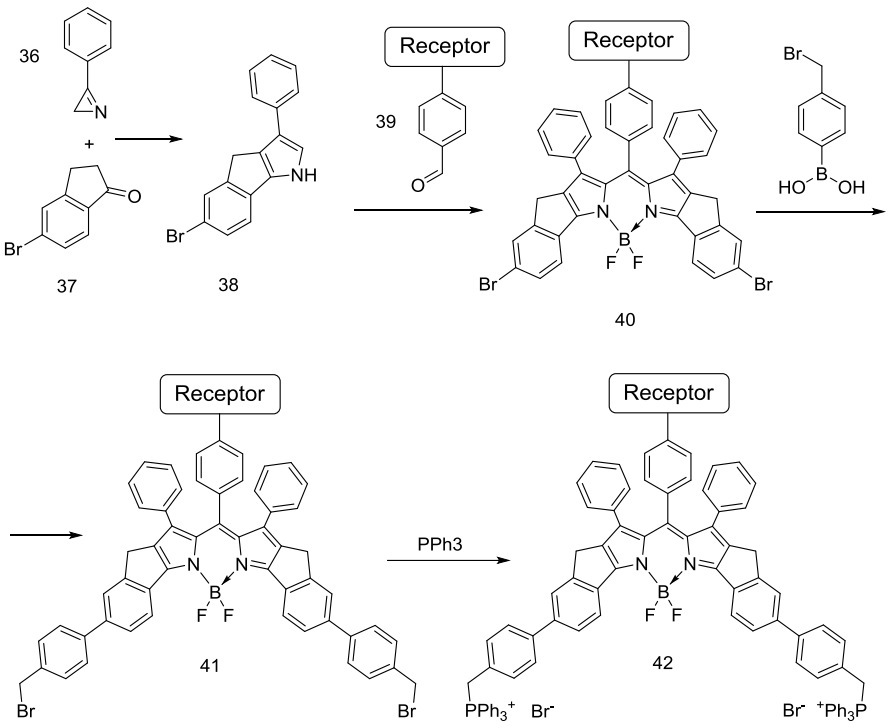

Figure 5.12: Possible synthetic route towards a K^+ sensitive molecular probe.

A bromine substituted BODIPY has great potential due to further modifications via Suzuki coupling. Another attractive material would be a conjugated polymer particle a with covalently coupled indicator (**Figure 5.13**). We previously reported a similar sensing scheme in the context of oxygen imaging.[187] This material is highly attractive as the conjugated polymer has three different functions which are combined in one material. Firstly, the conjugated polymer itself shows fluorescence and can be used for referencing. The emission maximum can be controlled by changing the ratio of short (**A** and **B**) and long (**C**) wavelength emitting monomers. Secondly, the polymer also includes charged groups (**D**) which make the preparation of nanoparticles possible. Similar to RL-100 particles, the polymer is dissolved in organic solvent and upon addition of water nanoparticles are formed with the charged groups on the outside and the residue conjugated polymer with bound indicator inside. Thirdly, when a particle is formed, the polymer and the indicator are in close contact leading to an efficient energy transfer to the indicator. Thus, the polymer acts as a donor and enhances the brightness of the indicator dye.

As mentioned already, this was successfully realized with oxygen indicators.[187] Adapting this concept to ion sensing requires further modification of the polymer as

it is necessary to gain a more hydrophilic polymer. This is necessary to achieve water uptake of a particle which subsequently enables penetration of ionic species into the particle towards the sensing molecule. This is crucial for the design of a sensing molecule that should be capable of sensing ions.

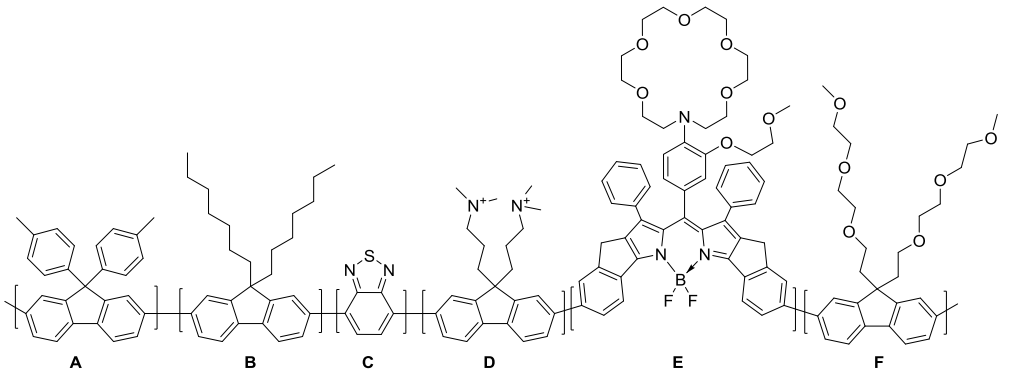

Figure 5.13: Structure of K^+-sensitive conjugated polymer.

Introducing this hydrophilicity can be achieved by additionally copolymerizing a PEGylated fluorine (**F**) with the other monomers. Fluorescent nanoparticles based on PEGylated polyfluorenes are already reported and display high potential for future projects.[216]

Chapter 6

Ammonia Sensing with Fluoroionophores – a Promising Way to Minimize Interferences Caused by Volatile Amines

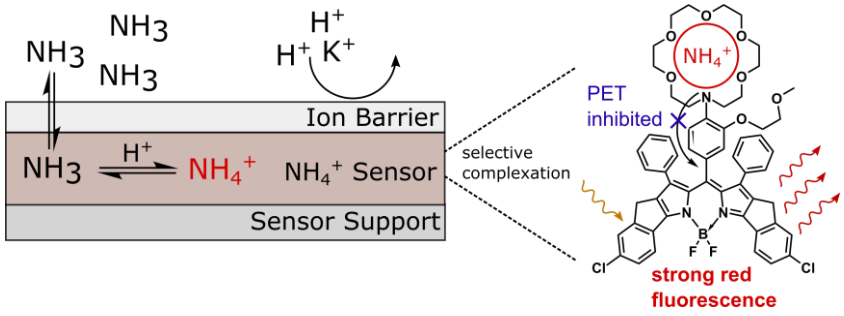

Preface for the Manuscript

This manuscript describes a novel sensing mechanism for the determination of dissolved ammonia (NH_3). Typical optical ammonia sensors are based on the deprotonation of a pH indicator dye caused by NH_3. The deprotonation causes a change in the optical properties of the indicator dye. However, this system is not selective towards NH_3 as other volatile bases can also deprotonate the pH indicator.

Our concept is based on fluoroionophores and represents a new sensing method for NH_3. As shown in **Table 2.1** (p. 17), NH_4^+ and K^+ possess a similar ion radius and are therefore complexed in the same crown ether. Hence, a K^+ selective fluoroionophore also responds to NH_4^+, which was already shown in the cross-selectivity experiment in the previous publication (**Figure 3.7**). The development of an optical NH_3 sensor was the master thesis topic of Nicole Steinmann and was based on a key publication by West et al.[217] In their work, they presented an optical NH_3 sensor based on a pH indicator dye in a hydrophobic matrix (PVC/DOS). In contrast to other NH_3 sensors, they incorporated an ionophore which can selectively complex the NH_4^+ which is generated inside the sensor membrane and has positive effects on selectivity and sensitivity. The idea was to utilize fluoroionophore indicators as they respond selectively and directly to NH_4^+ and therefore eliminate the need of a pH indicator. Initial attempts to immobilize the fluoroionophore in hydrophobic matrices did not yield a functional sensor. For this reason, we attempted to developed an NH_3 sensor using hydrophilic matrices such as water swellable hydrogels. The detailed study can be found in the master thesis of Nicole Steinmann.[218]

For this publication, we used this K^+ sensor and converted it into a highly selective NH_3 sensor by simply covering the sensor membrane with an ion impermeable layer, such as Teflone or silicone. This prevents a response of the sensor towards ionic species in the sample, but still allows NH_3 to diffuse into a sensor membrane. An additional internal buffer system converts NH_3 inside the sensor to the NH_4^+ ion which can then be detected by the fluoroionophore. This leads to a high selectivity, as other volatile bases (e.g. substituted amines) are too big to become complexed by the indicator dye.

Manuscript

Ammonia Sensing with Fluoroionophores – a Promising Way to Minimize Interferences Caused by Volatile Amines

This chapter was submitted as *Communication* in

Chemical Communication

Authors: Bernhard J. Müller, Nicole Steinmann, Sergey M. Borisov* and Ingo Klimant

Graz University of Technology, Institute of Analytical Chemistry and Food Chemistry, Stremayrgasse 9, 8010 Graz, Austria

E-mail: sergey.borisov@tugraz.at

Abstract A novel sensing concept for the selective detection of ammonia over amines is introduced. For the first time, the reversible fluorescence-based NH_3 sensor makes use of an ammonium-sensitive fluoroionophore instead of commonly used pH indicators. NH_3 diffuses into the sensor where a buffered internal electrolyte generates the corresponding ammonium ion, which is then detected by an ion selective fluoroionophore.

6.1 Introduction

Ammonia is an important analyte in agricultural, industrial, biotechnological and clinical industries. A high concentration of NH_3 has significant environmental impact and is toxic to both animals and humans.[219] Consequently, there is great interest in its continuous monitoring using low-cost analytical methods in various applications. State of the art optical ammonia sensors utilize pH indicators (IndH) immobilized in a polymer matrix and work for both absorption and fluorescence read out. Immobilization of the pH indicator can be carried out in both hydrophobic and hydrophilic matrices.

The signal transduction is based on a simple acid/base reaction of the pH sensitive dye with ammonia yielding an ammonium ion and deprotonated pH indicator (**Figure 6.1a**). A variety of different pH indicators for ammonia sensing are reported, such as fluorescein,[220] triphenylmethane,[221,222,223] xanthene dyes,[224,225,226]aza-BODIPYs[227] and coumarin derivates[228,229,230]. As the pH indicator is also prone to react to changes of the pH of the sample, it is necessary to immobilize them into a polymer matrix and prevent penetration of protons. This is achieved by using hydrophobic matrices such as silicone rubber[231,232,233], polyvinylchloride with various plastizers[234,235], sol-gels[225,236] and a variety of others[237,238,239,240,241]. When hydrophilic matrices are applied, it is necessary to cover the sensor membrane with a hydrophobic protective layer to gain pH robustness.[242]

The major drawback of pH indicator-based optodes is low selectivity for ammonia, since any other volatile base can also diffuse into the sensing layer and cause deprotonation of the dye. One way to improve the selectivity was shown by Simon and co-workers by incorporating a neutral ionophore (L) in addition to the pH indicator (IndH) in a hydrophobic PVC/DOS membrane (**Figure 6.1b**).[243,217] The ionophore acts as a cation trap and selectively binds and stabilizes the generated NH_4^+ ion, leading to a shift of the NH_3/NH_4^+ equilibrium inside the sensor. With increasing binding constant of the ionophore-NH_4^+ complex (L-NH_4^+), higher sensitivities could be achieved. In contrast to the ammonium ion, the substituted amines (methylamine, dimethylamine, trimethylamine) are too bulky to be strongly complexed by the ionophore and therefore no equilibrium shift occurs. However, also this sensing scheme requires the use of pH indicators, and therefore will respond to the amines at higher concentrations. The use of ionophores is still a highly interesting approach to overcome amine cross-sensitivity, but surprisingly was not further explored in optical ammonia sensing.

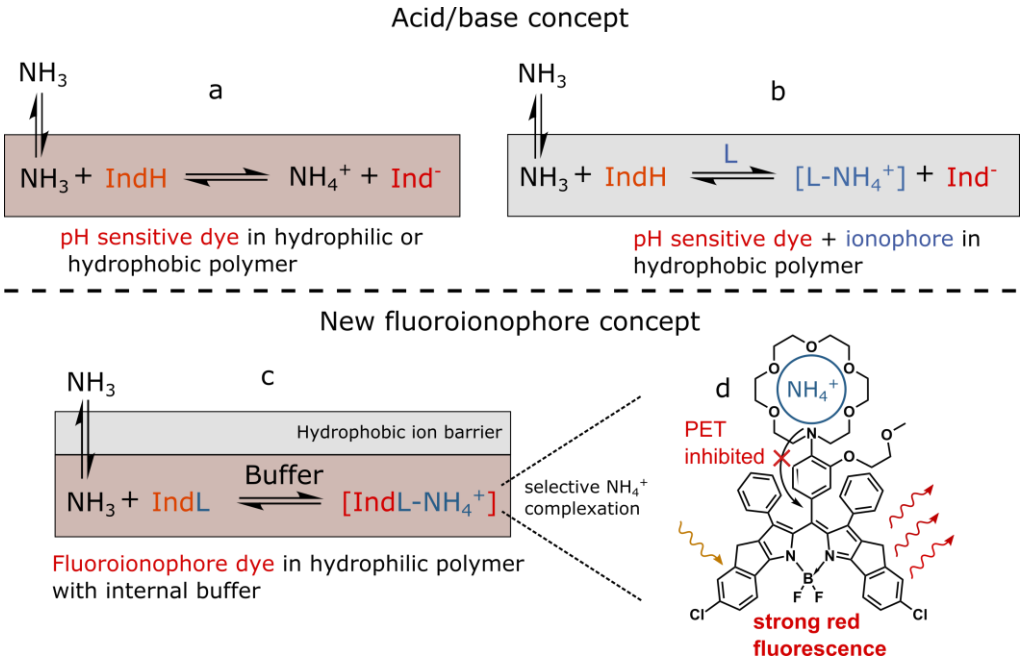

Figure 6.1: Different concepts of optical ammonia sensing. **a:** Diffusion of NH_3 into a hydrophobic or hydrophilic matrix causes deprotonation of an incorporated pH indicator (IndH). **b:** Additional incorporation of a neutral ionophore (L) which is able to selectively complex and stabilize the formed NH_4^+ ion leads to a higher selectivity and sensitivity towards NH_3. **c:** The new sensing concept based on an ion selective fluoroionophore embedded in a hydrophilic matrix and additional internal buffer. Diffused NH_3 gets protonated and the resultant NH_4^+ is selectively complexed by a crown ether which inhibits the photoinduced electron transfer (PET) and therefore results in an increase of fluorescence. **d:** Fluoroionophore indicator that was used.

In this contribution, we introduce a novel methodology for measuring ammonia using optical sensors. For the first time, ammonia is quantified via the direct measurement of NH_4^+ ions generated inside the sensor membrane. Contrary to the state-of-the-art sensors it is not based on the deprotonation of a pH indicator. The membrane itself consists of an NH_4^+ sensitive fluoroionophore (IndL) physically entrapped in a hydrophilic polyurethane hydrogel incorporating an internal buffer. In order to prevent any interaction of the sensitive layer with charged species, it is covered with a hydrophobic, gas permeable protective layer which acts as a proton and ion barrier (**Figure 6.1c**).

Ammonia molecules in the sample can freely diffuse across this protective membrane. Inside the sensor NH_3 is protonated by the low pH buffer and is converted to ammonium ions. A dynamic equilibrium is reached when the partial pressure of ammonia is equal inside the sensor and in the sample. Consequently, an

essential increase of NH_4^+ is facilitated in acidic media according to the Henderson-Hasselbalch equation:

$$pH = pKa - \log ([NH_4^+] / [NH_3])$$

The key component of this system is the fluoroionophore which complexes the generated NH_4^+ ions, leading to an increase of fluorescence emission.

6.2 Results and Discussion

6.2.1 Properties of the Fluoroionophore

The fluoroionophore combines both the transduction and the recognition element of the sensor in one molecule. The recognition unit (aza-crown ether) binds the guest molecule selectively and reversibly whereas the fluorophore unit is responsible for the signal transduction. This type of fluoroionophore makes use of the photo induced electron transfer (PET) which causes an intramolecular quenching by the nitrogen lone-pair of the aza-crown ether. The fluorescence of the indicator is supressed if no analyte is bound in the receptor unit, as PET can take place. Conversely, if the analyte molecule is complexed, it interacts with the nitrogen lone-pair of the aza-crown-ether inhibiting the PET, thus facilitating strong fluorescence.

An aza 18-crown-6 (**Figure 6.1d**) was chosen as a receptor since the dimensions of the cavity excellently match the size of ammonium ion. An additional ether side group also participates in complexation leading to enhanced selectivity and sensitivity of the binding event. Notably, the receptor is identical to the one used in K^+ fluoroionophores[151] due to very similar radii of both ions. Importantly, the aromatic amine on the crown ether shows a pKa value of around 3[151] so that it cannot be protonated by the buffer. A π-extended rigid BODIPY dye (**Figure 6.1d**) was chosen for its attractive spectral properties (long-wavelength absorption, high brightness and photostability). In fact, the fluoroionophore has a high molar absorption coefficient (109,300 $M^{-1}cm^{-1}$ at 640 nm) and a quantum yield of 68 % in the “on” state when dissolved in dichloromethane.

For the preparation of a sensor, it is necessary to immobilize the indicator dye in a polymer matrix Which acts as a solvent for the indicator dye. The polymer cannot be too hydrophilic or too hydrophobic. In the first case the dye may aggregate inside the polymer. In the second case, the performance of the sensor can be compromised by

the low polarity of the matrix since the PET is much more efficient in a polar environment than in hydrophobic media.[242] Consequently, a fluoroionophore in a hydrophobic medium is already fluorescent and therefore a complexation with ions does not lead to a significant increase in emission. Based on these considerations, we selected commercially available water swellable hydrogel (available under the name Hydromed D1) which is an ether-based polyurethane. It consists of distinct hydrophobic and hydrophilic areas and is able to take up 70 % water. Indeed, the immobilized fluoroionophore shows low fluorescence intensity in the absence of NH_4^+ ions and increasing intensity in the presence of the analyte due to the decrease of the PET (**Figure S - 3.1**). For this reason, this sensor membrane was a suitable candidate for preparing new ammonia sensors.

6.2.2 Design of the Sensor Membrane

An ammonia sensor requires a proton and ion impermeable protection layer in order to avoid cross-talk of the sensor to pH or ions (for instance K^+). Here, we chose to use a highly hydrophobic polytetrafluoroethylene (PTFE) membrane which possesses remarkably high permeability for ammonia due to its porous structure. Moreover, the white membrane surface increases the signal intensity due to light scattering effects. Upon diffusion of NH_3 into the sensing membrane, protons are required to generate NH_4^+ ions. An internal buffer system provides a constant pH value inside the membrane and facilitates the formation of NH_4^+ which complexation by the fluoroionophore yields in a strong fluorescence emission (λ_{max} 655 nm) (**Figure 6.2a**). A low pH value inside the sensor membrane will cause diffusing NH_3 to become protonated, forming NH_4^+, according to the Henderson-Hasselbalch equation. This generation of NH_4^+ will occur until the partial pressure of NH_3 inside and outside the sensor membrane is equal. If the pH value in the membrane rises, less NH_3 needs to diffuse inside to reach this equal partial pressure.

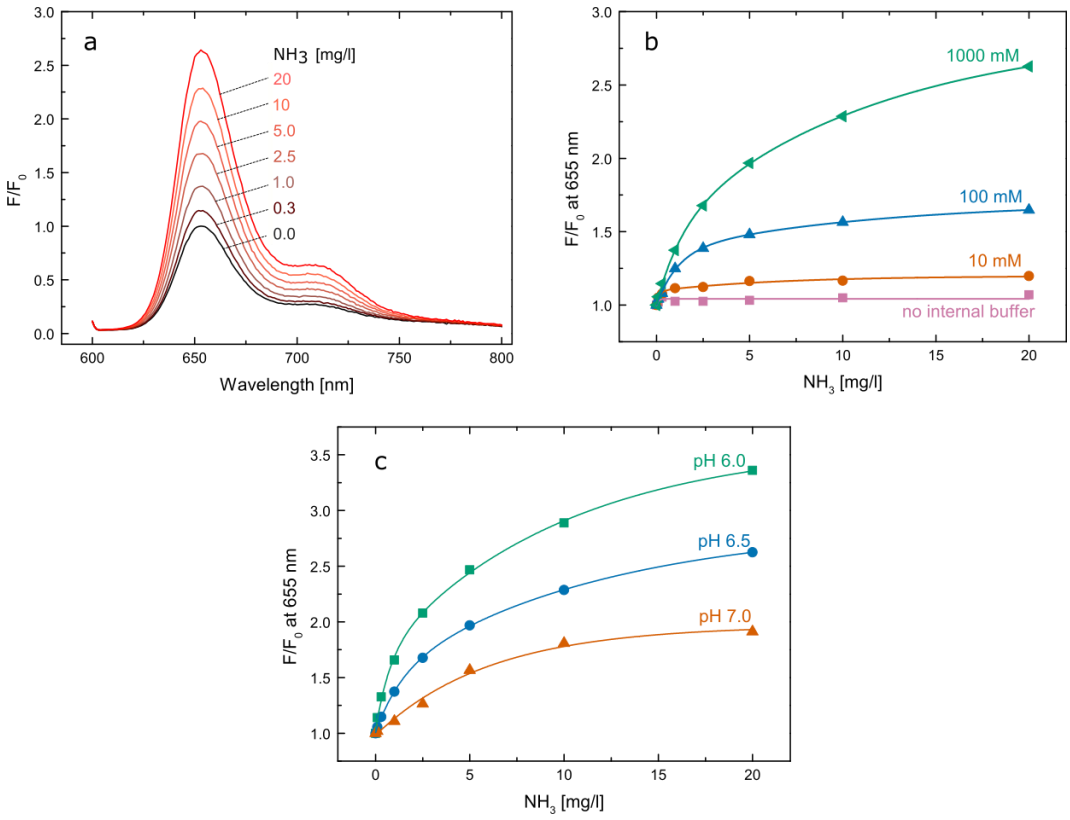

Figure 6.2: a: Normalized emission spectra of the sensor membrane at different ammonia concentrations. **b:** Calibration curves of the sensing material with different buffer capacities of the internal buffer solution (BIS-TRIS Buffer at pH 6.5). The values of F and F_0 were taken at λ = 655 nm. **c:** Calibration curves of sensors with different pH values of the internal buffer. Buffer capacity was 1000 mM.

Consequently, the generation of NH_4^+ inside the membrane depends on i) the pH value inside the membrane due to pH-dependent equilibrium between NH_4^+ and NH_3 and ii) the buffer capacity of the internal solution determining the degree of NH_4^+ conversion before the rise of pH and equilibration of pNH_3 on both sides of the protective layer.

Here, we decided to use BIS-TRIS as the buffer due to the suitable pKa value of 6.5 and good solubility in the hydrogel D1 polymer and absence of the interaction with the fluoroionophore. Other buffer substances containing Na^+ or K^+ ions would interfere with the measurement as the fluoroionophore is also highly sensitive to these ions. **Figure 6.2b** shows the influence of sensors with different internal buffer capacities. As expected, a non-buffered system displays no response to NH_3 since no NH_4^+ is generated due to lack of protons and stable internal pH. As the buffer capacity increases, an increase in sensor response is evident. This is due to an

increasing generation of NH_4^+ as the pH remains more stable with increasing diffusing NH_3. Once the buffer capacity is depleted, the pH value raises and the NH_3/ NH_4^+ equilibrium favours NH_3 and therefore an equal pNH_3 in the sample and the sensor is reached.

According to the Henderson-Hasselbalch equation, we aimed for the lowest possible pH value inside the sensor membrane to favour protonation of NH_3. **Figure 6.2c** displays calibration curves applying internal pH values of 6.0, 6.5 and 7.0. The lower the pH value is, the more NH_4^+ is generated and therefore a higher fluorescence increase is detected.

However, pH value of the internal buffer cannot be too low due to possible protonation of the crown ether of the fluoroionophore. As the PET effect is caused by disturbing the electron lone pair of the aza-crown, fluorescence increase is also caused by protonation, and not only by complexation of NH_4^+. The pKa value of this compound is 3.2 when immobilised in hydrogel matrices (**Figure S - 6.2**). Hence, a minor amount of the receptor can already be protonated at pH of 6.0 so that some fluorescence emission is already observed in the absence of ammonium (**Figure S - 6.3**). When this sensor is treated with a solution containing a substituted amine (e.g. trimethylamine (TMA)) deprotonation of the crown ether occurs resulting in the decrease of fluorescence intensity (**Figure S - 6.3**). Treating the sample again with buffer leads to an increase in fluorescence, as the amine is removed from the sensor membrane. Increasing the internal pH to 6.5 virtually completely eliminates the protonation of the receptor by the buffer which is the optimal pH for preparation of the sensing material.

6.2.3 Reversibility and Cross-Sensitivities

Figure 6.3a shows a typical response of a sensor membrane (internal buffer 1000 mM, pH 6.5). when treated with aqueous ammonia solutions. As can be seen, the sensor shows very fast response and recovery times (~1 min and 3 min, respectively) and is fully reversible.

Inertness to changes of the sample pH is crucial for real world applications. Due to the use of the PTFE based proton barrier, the sensors shows no response to tested samples with different pH values (4.0, 6.0, 8.0 and 10.3) (**Figure 6.3b**)

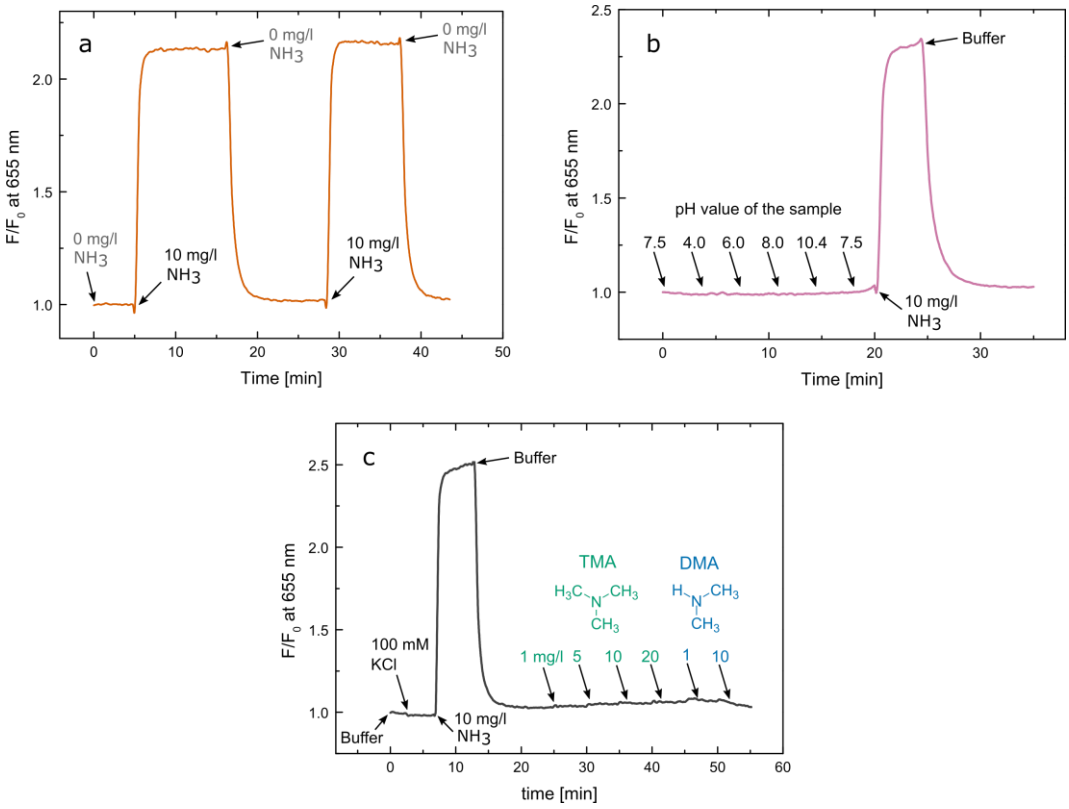

Figure 6.3: Fluorescence response of a sensor membrane (1000 mM buffer at pH 6.5). **a:** Reversibility of the sensor. **b:** Cross sensitivity of the sensing membrane to pH changes in the analysed solution. **c:** Cross sensitivity of the sensor to KCl and amines (trimethylamine (TMA), dimethylamine (DMA)) where the concentration of free amine is given in mg/l.

The major improvement compared to state-of-the art optical sensors is the insensitivity to other amines shown in **Figure 6.3c**. This is due to the fact that the sensing principle is not based on a simple deprotonation/protonation of a pH indicator, but on the selective complexation of ammonium. The ammonium ions of the substituted amines, such as trimethylamine or dimethyl amines, are too bulky to fit into the cavity of the crown ether. Therefore, the sensor does not show any signal increase and displays an outstanding selectivity over these compounds. This is of major importance for applications in fish farming, where trimethylamine occurs in high concentrations as it is a degradation product of fish. Currently used optical ammonia sensors are not capable of distinguishing between ammonia or trimethylamine.

6.3 Conclusion

To conclude, for the first time dissolved NH_3 was determined using fluorescent ion-selective chromophores. NH_4^+ ions formed inside the sensor membrane are selectively complexed by the crown-ether unit of the fluoroionophore and cause an increase in fluorescence due to decreasing PET. Both a high buffer capacity and a low pH value of the internal electrolyte increase the sensitivity of the sensor but the performance of the sensor deteriorates at too low pH values due to partial protonation of the receptor. The sensor displays fast response and recovery times, is fully reversible and shows no cross-talk to changes in pH. Importantly, the sensor is characterized by an insensitivity towards other substituted amines (trimethyl- or dimethylamine) due to the high selectivity o the crown-ether receptor for NH_4^+. This novel concept offers a new pathway for future research in the context of ammonia sensors and will be a valuable tool for applications in biotechnological and environmental applications. Further improvements may include design of an even more sensitive NH_4^+ -fluoroionophore and modification of the phenyl ring of the receptor with electron-withdrawing substituents (e.g. halogens) decreasing the pKa value of the receptor and therefore enabling using buffers with lower pH.

Acknowledgement

Financial support from the European Union FP7 Project SCHeMA (Grant Agreement Number 614002) is gratefully acknowledged. We thank Andreas Steinegger and Christoph Staudinger for proofreading the manuscript and helpful discussions.

6.4 Materials and Methods

Sodium dihydrogen phosphate, disodium hydrogen phosphate, CAPS, TRIS and BIS-TRIS, potassium chloride (KCl) were bought from Carl Roth GmbH (Karlsruhe, Germany). Polyurethane hydrogels (Hydromed D1) was purchased from AdvanSource biomaterials (advbiomaterials.com). Poly(ethyleneterephthalate) (PET) support Melinex 505 was obtained from Pütz (puetz-folien.com). biomaterials. FluoroporeTM membrane PTFE (0.45 µm pore) was from Merck Millipore Ltd. (Cork, Ireland). Methylamine hydrochloride, dimethylamine and trimethylamine hydrochloride were purchased from Acros (www.acros.com). Ammonium chloride

(NH_4Cl) was obtained from Sigma Aldrich (www.sigmaaldrich.at). Citric acid monohydrate was purchased from Merck (www.merckmillipore.com). All chemicals were used as received.

pH cross sensitivity experiments were performed using a 20 mM universal buffer (citrate, CAPS, BIS-TRIS and TRIS). The pH was adjusted with HCl with help of a digital pH meter (Seven Easy, Mettler Toledo, www.mt.com) calibrated at 25 °C with standard buffers of pH 7.0 and 4.0 (WTW, www.wtw.com).

Calibrations were performed by placing the sensor membrane in a home-made flow through cell pumping different buffers through it using a peristaltic pump. The temperature of the buffers and the measurement cell was held constant at 23°C using a thermostat. Corrected fluorescence spectra were recorded in front-face mode on a Fluorolog3 spectrofluorometer (Horiba Jobin Yvon) equipped with a NIR-sensitive photomultiplier R2658 from Hamamatsu (300 − 1050 nm).

The NH_4^+ sensitive BODIPY fluoroionophore was synthesized in our lab as described previously.[151]

6.5 Experimental

6.5.1 Preparation of Solutions

Amine containing buffer solutions were prepared by dissolving appropriate amounts of ammonium chloride, trimethylammonium hydrochloride, dimethylamime or methylamine hydrochloride in a 150 mM phosphate buffer (pH 7.5). The appropriate amounts to dissolve in each buffer resulting in a free amine concentrations were calculated by the Henderson-Hasselbach equation with the respective pKa values of the amines at a temperature of 23°C.

6.5.2 Preparation of Sensing Materials

NH_3 Sensor Membranes

Hydrogel polymer (Hydromed D1) was dissolved in EtOH+H_2O (9+1) to yield a stock solution of 10 wt.%. The water part consisted of the buffer substance (BIS-TRIS) with the required buffer capacity and pH value. An appropriate amount of the indicator was dissolved in this hydrogel stock solutions the sensor membrane to have

a dye concentration of 0.5 wt.% in respect to the polymer. This "cocktail" was knife coated onto dust-free PET foils (12.5 µm wet film thickness). Immediately after the knife-coating step, a Fluoropore membrane PTFE was carefully laid onto the still wet film to obtain a sensor membrane with a size of ~ 2 cm x 2 cm which can be placed in a home-made flow-through cell.

Planar sensor films for NH_4^+ calibrations

Hydrogel polymer (Hydromed D1) was dissolved in THF to yield a solution of 10 wt.%. The indicator (0.2 mg) was dissolved in 1 g of the hydrogel solution to yield a final dye concentration of 0.2 wt.% in respect to the polymer after drying. This "cocktail" was knife coated onto dust-free PET foils (12.5 µm wet film thickness) and allowed to dry at RT.

6.6 Supporting Information

Response of the Sensor to Ammonium

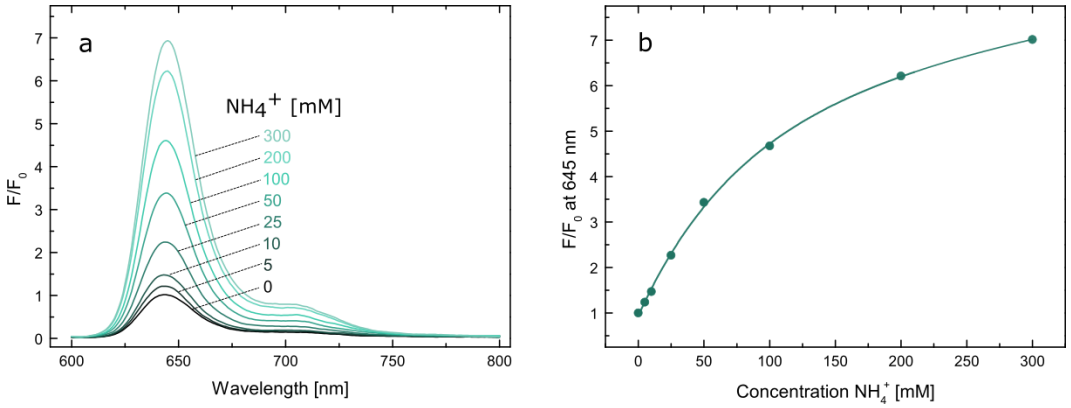

Figure S - 6.1: a: Normalized emission spectra of the fluoroionophore in hydrogel D1 without a teflone membrane at different NH_4^+ concentrations (20 mM TRIS buffer pH 7.4) **b:** F/F_0 calibration curves for the indicator immobilized in hydrogel D1. The values of F and F_0 were taken at λ = 645 nm.

Determination of the pKa Value

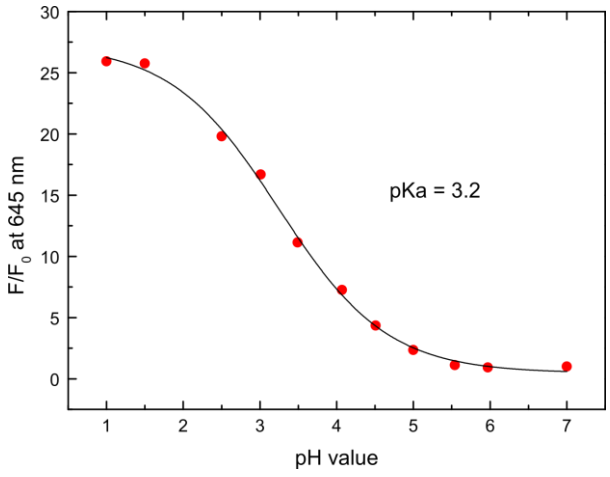

Figure S - 6.2: Determination of the pKa of the receptor in hydrogel D1 without the teflone membrane. The values of F and F_0 were taken at λ = 645 nm.

Influence of a Low Internal pH Value

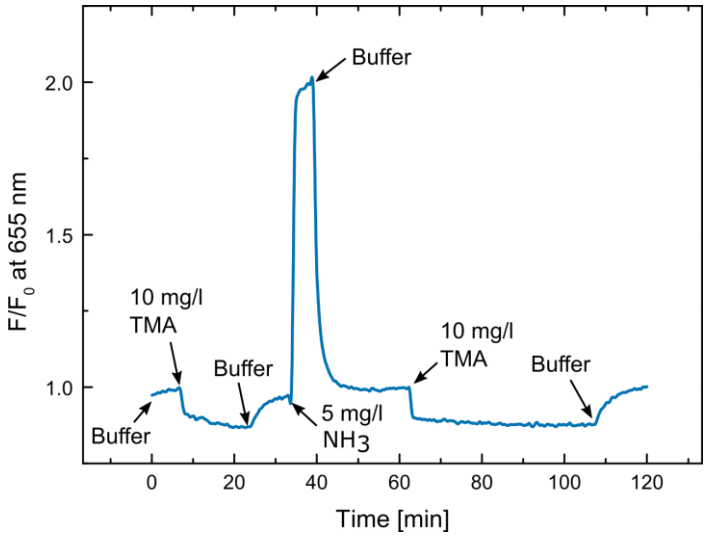

Figure S - 6.3: Fluorescence response of a sensor membrane (1000 mM buffer capacity) at an internal pH of 6.0.

Future Prospect and Outlook

This publication shows the first proof-of-concept experiments, describes the most important parameters for a fluoroionophore based NH_3 sensor and represents the first of this kind. Using this sensor, we were able to eliminate cross sensitivity caused by other volatile bases. For example, this is important for fish farming, where a high concentration of trimethylamine (TMA) occurs. However, the presented sensing material is not suitable for this application as a concentration of 25 µg/L NH_3 is already toxic for fish and therefore it is not sufficiently sensitive.

As shown in **Table 2.1** (p. 17), the NH_4^+ ion has a slightly larger ionic radius compared to K^+ ion. The fluoroionophore used in this publication was developed for the detection of K^+ ions and therefore does not have the optimal hole-size relationship with NH_4^+ ions. Therefore, we started the synthesis of a 19-crown-6 receptor unit in which the K^+ crown is increased by one methylene group. The synthesis pathway is shown in **Figure 6.4** and is currently under investigation. Compound 46 is already available and more specific experimental details and discussions are available in the master thesis of Nicole Steinmann.[218]

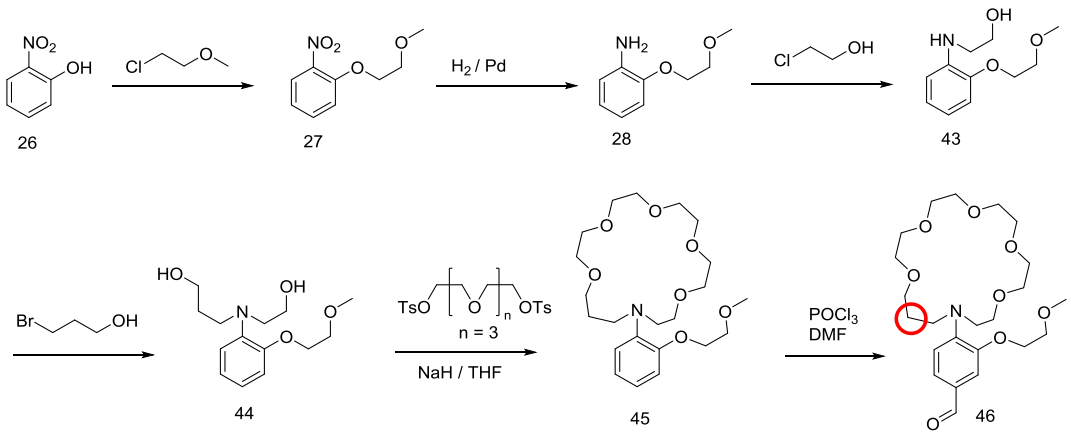

Figure 6.4: Synthetic pathway towards a new NH_4^+ sensitive crown ether receptor.

Chapter 7

New Insights in the Determination of Saxitoxin with Fluorogenic Crown Ethers in Water

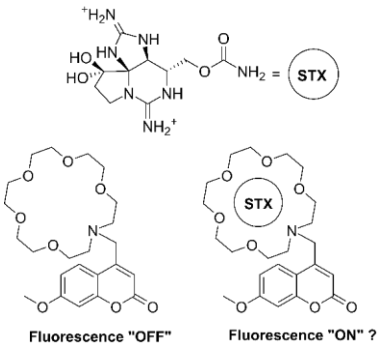

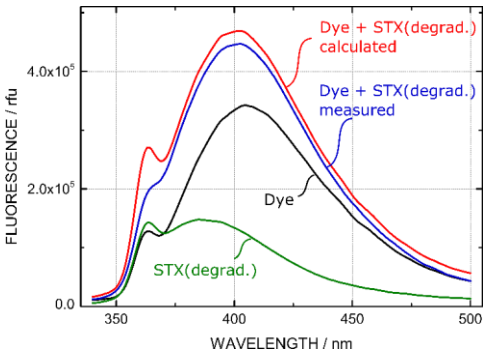

Preface for the Manuscript

This chapter deals with the determination of the marine biotoxin Saxitoxin (STX). The development of an optical sensor for STX was the goal of the EU FP7 project "SCHeMA" (Integrated in Situ CHemical MApping probes) which funded this thesis in the beginning.

Saxitoxin is one of the most toxic non-protein based substances and acts as a Na^+ channel blocker, leading to lethal paralytic shellfish poisoning. State of the art detection is based on tedious and expensive HPLC methods. Our approach was based on several publication of the group of Gawley et al., who developed a method to detect STX using fluoroionophores.[244] Hereby, different chromophore basis and differently sized aza-crown ethers were applied and STX could be measured in the low micromolar range.

We intended to develop a sensor based on this concept, but to additionally immobilize it into a polymer matrix and prepare a referenced sensing material for continuous long term measurements in the ocean. As STX only occurs in low concentrations, a pre-concentration unit was planned by the project partner at University of Geneva. It was based on aptamers immobilized into a microfluidic chip which can release the pre-concentrated STX upon stimulation with acid or heat.

However, we faced serious problems developing a sensor based on this concept. During our experiments, we found out that a fluorescence increase of fluorescence indicators when treated with STX is not caused by complexation of STX into a crown ether, but from a fluorescence degradation product of STX itself. This degradation product was then misinterpreted as sensor response.

In this publication, we report on this finding and additionally present a critical discussion about crown ether binding constants. Relevant theoretical background information can be found in **section 2.3.1** (p. 14).

Manuscript

New Insights in the Determination of Saxitoxin with Fluorogenic Crown Ethers in Water

This chapter was submitted as *Rapid Communication* in

Analytical and Bioanalytical Chemistry

Authors: Bernhard J. Müller*, Günter Mistlberger and Ingo Klimant

Graz University of Technology, Institute of Analytical Chemistry and Food Chemistry, Stremayrgasse 9, 8010 Graz, Austria

E-mail: b.mueller@tugraz.at

Keywords: Biotoxin, paralytic shellfish poisoning, optical sensor, fluorescence, PET

Abstract In this contribution we present new insights and a critical discussion in the optical detection of Saxitoxin (STX) using fluorophores with crown ethers. Fluorescence enhancement is caused by the reduction of photoinduced electron transfer (PET) upon complexation with the analyte. Our attempts to improve this detection method did not yield a functioning sensor nor were the attempts to reproduce published data in this area successful. Due to the fact that only low concentrations of STX are available, multiple surrogates were investigated at high concentrations. However, no turn-on response was observed. Moreover, a fluorescent decomposition product of STX that forms under UV light was discovered which was in our opinion misinterpreted as a sensor response by previous publications.

7.1 Introduction

Saxitoxin (STX) is one of the most toxic non-protein substances known and is responsible for the so called paralytic shellfish poisoning [245]. It is naturally produced by a variety of algal species such as cyanobacteria and dinoflagellates, which are consumed in large amounts by shellfish during red tide algal blooms [246]. This

accumulation of STX in shellfish which leads to the paralytic shellfish poisoning syndrome is a worldwide health problem. STX acts as a sodium channel blocker by binding to a receptor site on the outer surface of the cell-membrane and inhibits the permeation of Na^+ ions through the channel [247]. Consequently, action potentials are terminated and signal transmission between neutrons is inhibited, leading to paralysis [248].

Monitoring of this toxin by a mouse bioassay (MBA) is used in many countries [249]. For ethical reasons, alternatives such as HPLC methods were developed and are now routinely used [250] [251] [252]. The initial challenge in toxin detection is the lack of any UV absorption by STX. This can be overcome by oxidation of the toxin to a fluorescent derivate prior to or after separation on a HPLC column. The fluorescence can be observed at an excitation maximum of 330 nm and an emission maximum of 390 nm.

In recent years, a fluoroionophore based method for the detection of STX was developed by the group of Gawley et al. [244]. This method was based on a commonly used concept for measurement of cations, where a fluorescence indicator dye is linked to a recognition unit (e.g. crown ethers) [147]. Complexation of cations leads to a fluorescence enhancement caused by a reduced photo-induced electron transfer (PET) effect. It was assumed that STX could inhibit the PET effect as STX is a bis-guanidinium ion, and guanidiniums are known to bind to crown ethers [253] [254]. Different crown receptors and indicator dyes were tested for their response to STX in this group with different fluorophores, e.g. anthracene [244] [254], coumarin [255] [256] [257], acridine [258] and aza-BODIPY [259]. We attempted to improve this method by preparing new indicator dyes and immobilizing these dyes into a polymer matrix, in order to obtain robust sensor films, enabling continuous measurements in aquatic media without pH interference. However, during our work we faced challenges in developing new optical sensors for STX, as well as reproducing published results. Furthermore, we investigated the response of our sensors at high concentrations of different surrogates for Saxitoxin and discovered an artefact, which could have compromised previous experiments and has to be avoided in the future. This will be discussed in this contribution.

7.2 Results and Discussion

7.2.1 Fluorogenic Crown Ethers

The set-up for a fluorescence optical sensor for Saxitoxin is analogous to commonly used ion sensors. A fluorophore is linked to a recognition unit (receptor/ionophore) resulting in a fluoroionophore [101]. Typically, the receptor unit bears a tertiary amine group which is responsible for the emission enhancement in the presence of ions due to the reduced PET effect.

To date, receptors for STX detection were based on aliphatic aza-crown ethers. Those receptors are highly pH sensitive at physiological conditions because the amine can be easily protonated, which would result in a fluorescence enhancement similar to analyte binding. Moreover, most of the fluorophores which were used for the optical detection of STX were excitable in the UV region (330 to 390 nm), which can cause fluorescence background from biological samples (e.g. shellfish extract). Additionally, for measurements in the required low concentration ranges, the complex stability of crown ethers with analytes may be too weak in aqueous solutions. Complex stabilities in organic solvents are typically better and may be sufficient, however usually aqueous conditions are required for the measurement of environmental samples.

In order to improve the commonly used set up, we introduced a lariat-ether at the ortho position with respect to the nitrogen atom of the crown. This increases the binding efficiency of the analyte, since the two additional oxygen atoms also participate in the complexation [90]. We also decided to use an aromatic crown ether (substituted aniline) which is not sensitive to pH in the relevant range, since the pKa value of the tertiary amine is ~5.5. As indicator we used a commonly known BODIPY fluorophore which are excitable at > 400 nm, possess a high photostability and molar absorption coefficient, and show a high quantum yield.

Using this new indicator, the response to STX in solution was tested under similar conditions as in previously published work (H_2O/EtOH/THF mixture, phosphate buffer at pH 7.2). A high fluorescence enhancement is obtained upon protonation of the amine group of the aza-crown ether indicating that the PET effect is supressed. However, no treating with STX did not show any fluorescence enhancement (**Figure S1**, ESI). This negative result raises two fundamental questions: i) Is the complex stability (Kd) of the complexation of STX in the crown ether sufficient to detect STX

in the micromolar range? ii) If STX is complexed, does it supress the PET effect or have any other influence on the photophysical properties?

Since the concentration of STX is limited by the certified reference material ($6.63*10^{-5}$ M stock solution) and it is not possible to obtain STX in higher concentrations, we investigated if a fluorescence enhancement can be obtained using structurally similar compounds at higher concentration (200x higher). **Figure 7.1b** summarizes the surrogate compounds used to simulate STX as they are all subunites of STX itself and cover the whole molecule. Above all, guanidinium is known to has a high binding affinity to 27-crown-9 and was proposed in previous work to be the structural compound of STX to inhibit PET [253 259]. Additionally, we evaluated K^+ and NH_4^+ and ethylenediamine because they are known for their binding affinity to the 18-aza-6-crown.

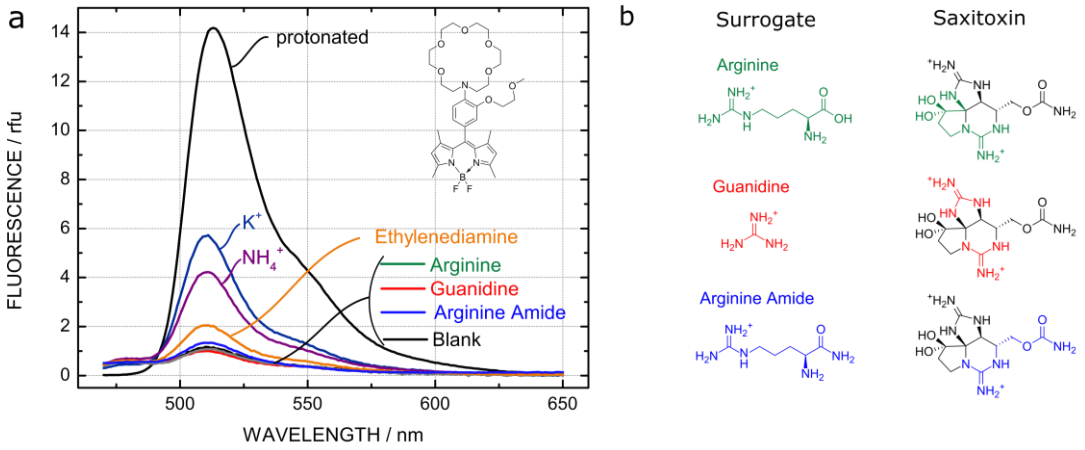

Figure 7.1: a: Normalized emission spectra of the BODIPY fluorophore (10^{-8} M) with surrogates (10 mM) in a mixture of H_2O/EtOH/THF (2/1/1) at pH 7.2. **b:** Structural similar surrogates used to simulate STX at higher concentrations (10 mM).

A high fluorescence increase can be observed in the presence of 10 mM K^+ or NH_4^+, whereas a less pronounced response is caused by ethylenediamine (**Figure 7.1a, Figure S - 7.2**). However, we did not obtain any significant increase in fluorescence upon adding the surrogates. The same experiment was conducted in a DMSO/H_2O (4+1) mixture as it is known, that the PET effect is more pronounced in more polar solvents. Again no significant increase of fluorescence using this surrogates was observable (**Figure S - 7.3**).

The complexation behaviour is highly depending on two factors – the solvent and the size of the cavity and the analyte. Generally, crown ethers show the highest binding constants in MeOH and the lowest in aqueous solution as and a higher ratio of organic solvents are beneficial for the complexation[41]. The low complexation in water is due to a too strong tendency to undergo hydration of the ion instead of getting complexed as the hydration shell around the ion needs to be stripped off [44]. MeOH or other organic solvents are much weaker solvating mediums and therefore hydration competes less with complexation yielding stability constants around three to four decades higher than in water.

Another important parameter besides the solvent is the size of the crown cavity and the guest ion. As size of the of 18-crown-6 is between 2.6-3.2 Å it shows optimal interaction with K^+ ion (2.66 Å) and NH_4^+ (2.86 Å) [44]. The corresponding stability constants of these in H_2O are lg*K* 2.05 for K^+ and and lg*K* 1.44 for NH_4^+ [41,80]. As the ammonium ion is more substituted, the stability constants lowers since the ion gets sterically hindered to fit into the crown ether [80]. This trend is observable in our data for K^+, NH_4^+ and ethylenediamine and the surrogates. The amine group of the latter is highly substituted which consequently prevent the complexation.

However, reported STX sensitive fluoroionophores which were used in aqueous solution show a binding constant 1000x higher than for K^+ [256,255]. Additionally, it was reported that complex stabilities of STX are higher in pure H_2O than in an EtOH/H_2O mixture which is in contrast to the trend of measured binding constants of all crown-ions interactions in different solvents [255].

The published utilized fluoroionophore for STX measurements in water is based on a coumarin dye, with which it was possible to measure concentrations of STX in the micromolar range with 137 mM NaCl and 2.7 mM KCl as background [255]. Na^+ and K^+ did not "turn on" the sensor even though an aza-18-crown-6 was used as the recognition unit. In this work STX binds to the receptor and inhibits the PET in a K^+ background that is 27 times higher, whereas K^+ does not turn on the sensor.

7.2.2 Fluorescence Background from STX

We synthesized this STX sensitive coumarin indicator dye as described in literature and response to STX was tested under conditions similar to those reported (**Figure 7.2a**). However, we could not observe any immediate increase in fluorescence with STX, but observed an increase in fluorescence intensity and a slight blue shift over

the course of 20 minutes, similar to the published work. However, as a blank sample without any indicator was measured we detected that STX itself starts to fluorescence upon illumination at 330 nm. This emission at 390 nm is shifted compared to the coumarin emission at 401 nm and superimposition with the coumarin fluorescence could explain the blue shift of the emission of the probe which is untypical for PET-indicators (**Figure 7.2**). Excitation spectra and emission spectra of both the coumarin dye and the STX illumination product are very similar and overlap over a broad range (**Figure S - 7.4**). The STX decomposition product shows excitation and emission peaks of 334 and 390 nm, respectively. This corresponds to the fluorescent decomposition product that is usually obtained during the pre- or post-column oxidation of the HPLC-fluorescence detection method, where STX is chemically oxidized to a fluorescent purine derivate (**Figure 7.2b**) [250] [251] [260]. From this experiment, we concluded that the increase of fluorescence is not caused by inhibition of the PET effect by STX. Instead, we were able to determine that this increase in fluorescence can be attributed to a photooxidation product of STX itself.

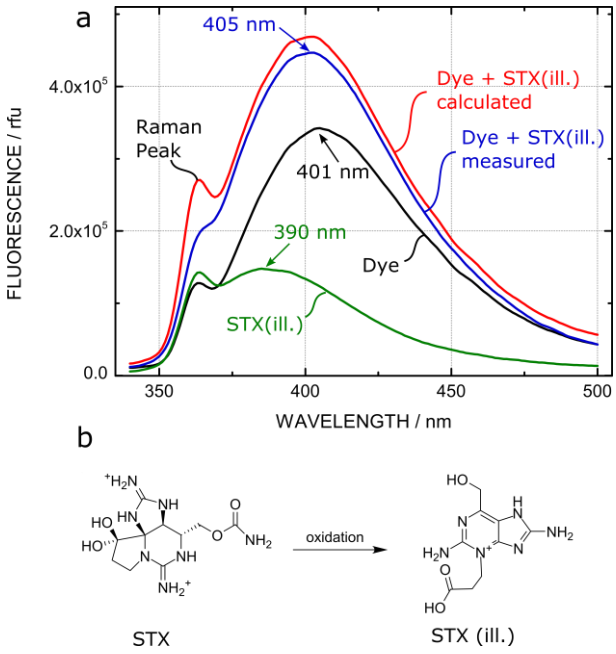

Figure 7.2: a: Fluorescence spectra of STX ($1.6*10^{-5}$ M), the coumarin dye (10^{-6} M), the dye + STX measured, and the dye + STX calculated. The measured fluorescence enhancement of dye + STX is not based on the complexation of STX but on the additional fluoresence **b:** Structure of STX and the fluorescence oxidation product.

To investigate the formation of this fluorescent STX product, we recorded the emission spectra of a buffered solution (pH = 7.2) of STX alone (**Figure S - 7.1**). When STX is stored without exposing to light, no increase in fluorescence is observed. In contrast, strong fluorescence is detectable after illumination with UV light. The fluorescence intensity of the oxidation product after illumination of STX with different intensities in the fluorimeter clearly shows, that the formation of this fluorescent STX product is highly dependent on the intensity of the applied UV light and that STX does not form this product by simple exposure to ambient air (**Figure S - 7.5**).

It should be stated that the group of Gawley et al. also detected this background fluorescence of STX, but interpreted it as a trace impurity of the STX solution and did not observe its increase during their measurements [258]. In our opinion, attributing the fluorescence increase of STX using the coumarin indicator to PET inhibition is a misinterpretation of data. The STX product shows very similar excitation and emission spectra to the used coumarin indicator and an addition of both fluorescence spectra explains the observed fluorescence enhancement by STX. Moreover, fluorescence enhancement due to STX oxidation can explain the observed blue shift of the emission in our measurement and in literature which is untypical for PET-indicators [256] [257]. With this in mind and comparison of published stability constants of STX-crown interaction with well-known ion-crown complexations, we believe that the measurement of STX using this method in water is not achievable in the environmental necessary concentration range.

However, crown ether sensors for STX based on other fluorophores have been developed in the literature and work at different excitation/emission wavelengths. For these probes the fluorescence increase is not influenced by this background fluorescence [259]. It is also important to note, that Gawley et al. in their earlier works were using non-aqueous solutions or a very high percentage of organic solvents which would be beneficial for the complexation of STX and much higher STX concentrations were used for the measurements.

7.3 Conclusion

A critical examination of the optical detection of STX using complexing fluorophore indicators in aqueous media is presented. An attempt to improve the detection method by using a new fluoroionophore which shows significant inhibition of the PET effect with K^+ or NH_4^+ ions was not successful. Testing structural similar compounds as STX in higher concentration also did not yield in a positive result. When reproducing literature where STX was detected in aqueous solution using a coumarin indicator dye, we discovered an artefact which was misinterpreted as response to STX. This artefact can be attributed to the intrinsic fluorescence of a known oxidative degradation product which is usually observed after chemical oxidation. We were able to identify UV light to be the reason for this oxidation. With this finding, it is possible to directly detect STX using this catalytic photooxidation which is currently under investigating in our laboratory and will be presented in the near future.

Acknowledgment

Financial support from European Commission ("Schema" Project No. 614002) is gratefully acknowledged. We gratefully acknowledge Dr. Sherwood Hall from the U.S. Food and Drug Administration (FDA) for critical discussion on the matter of STX detection.

7.4 Materials and Methods

Saxitoxin dihydrochloride ($6.63*10^{-5}$ M in $3*10^{-3}$ M HCl) was purchased as certified reference material from the National Research Council Canada (www.nrc-cnrc.gc.ca). KCl and NH_4Cl were obtained from Roth (www.carlroth.com). Guanidine hydrochloride, L-Arginine monohydrochloride and L-Argininamide dihydrochloride and Ethylendiamine were purchased from Sigma-Aldrich (www.sigmaaldrich.com). All other chemicals were obtained from TCI-Europe (www.tcichemicals.com). Synthesis of the BODIPY indicator was conducted as reported elsewhere [151]. Synthesis of the coumarin fluorophore was conducted similarly to that described in literature [255]. Luminescence spectra were measured on a Fluorolog-3 luminescence spectrometer (Horiba). Fluorescence kinetic

measurements were performed in a stirred and sealed micro quartz-cuvette from Hellma (www.hellma-analytics.com). All measurements were performed in buffered solution (phosphate buffer, 50 mM, pH = 7.2). Measurements with surrogates were performed in EtOH/THF/H_2O (1/1/2) and DMSO/H_2O (4/1) with a dye concentration of 10^{-8} M, surrogate concentration of $1*10^{-2}$ M and a phosphate buffer (pH = 7.2, 50 mM).

7.5 Supporting Information

Response of BODIPY Fluoroionophore to STX

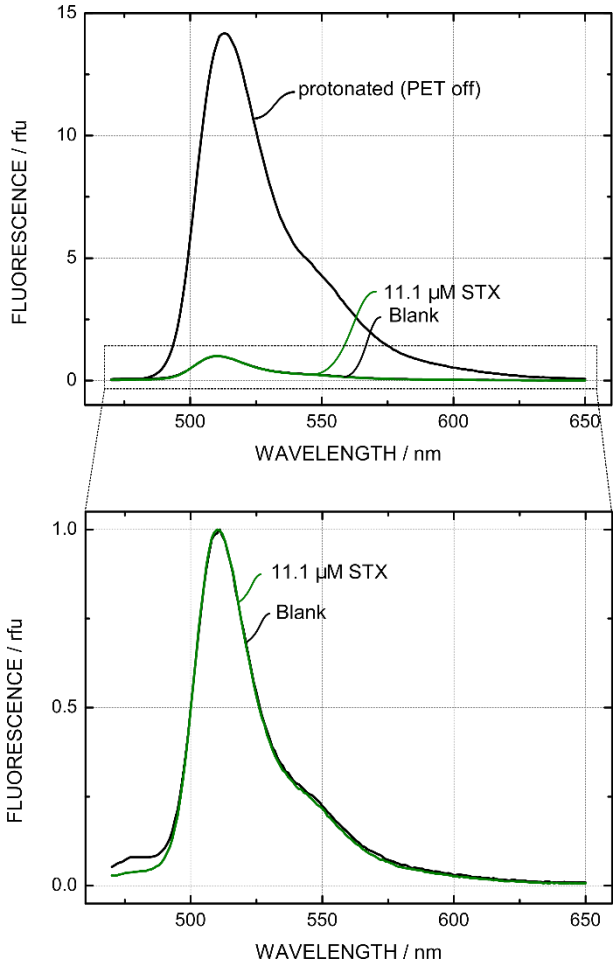

Figure S - 7.1: Fluorescence response of the BODIPY fluorophore with STX. **Top:** Fluorescence can be turned on completly by acidificiation with HCl. STX does not show any respsone in the micromolar range. **Bottom:** Closeup to the emission spectra of the blank and STX.

Response of BODIPY Fluoroionophore to Surrogates

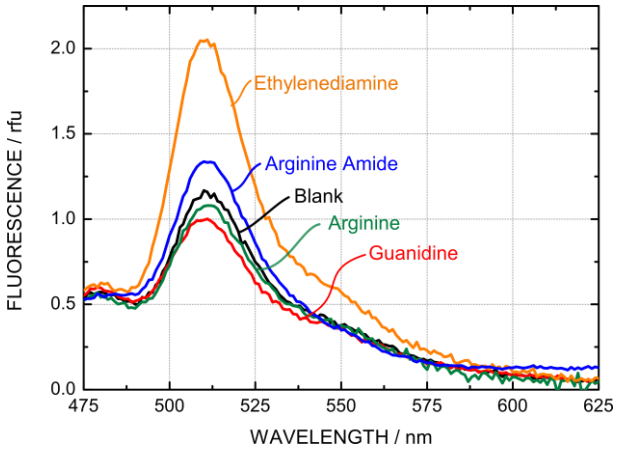

Figure S - 7.2: Normalized emission spectra of the BODIPY fluorophore (10^{-8} M) with surrogates (10 mM) in a mixture of H_2O/EtOH/THF (2/1/1) at pH 7.2.

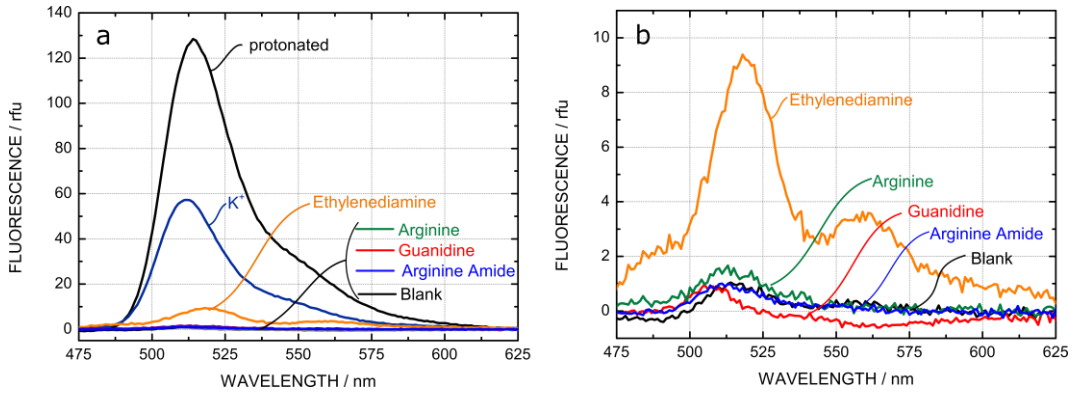

Figure S - 7.3: a: Normalized emission spectra of the BODIPY fluorophore (10^{-8} M) with surrogates (10 mM) in a mixture of DMSO/H_2O (4/1/) at pH 7.2. **b:** Zoom in.

STX Artefact

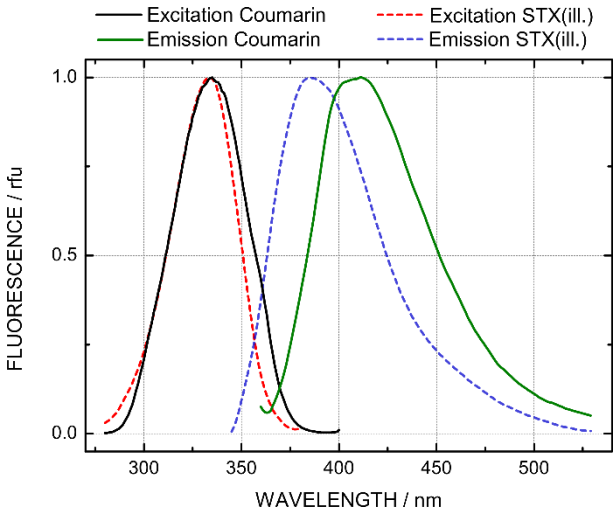

Figure S - 7.4: Excitation and emission spectra of the coumarin fluorophore and STX degradation product after illumination.

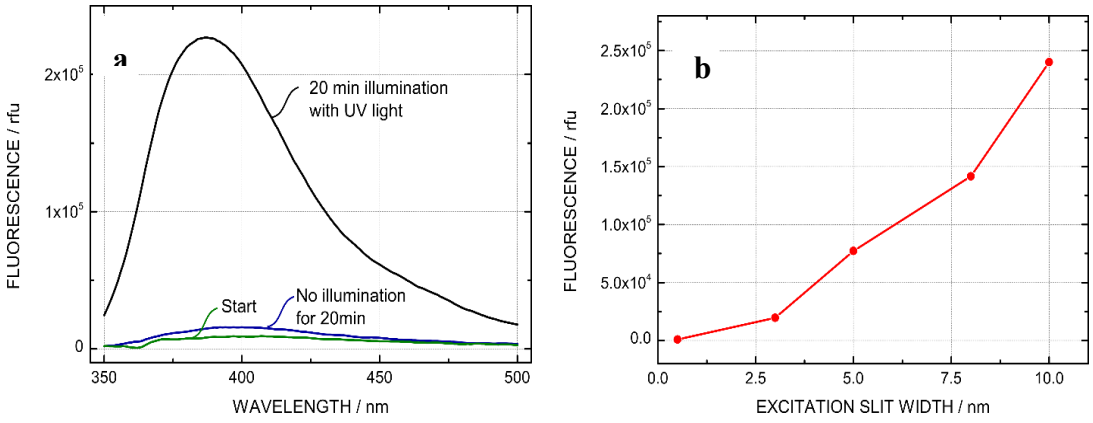

Figure S - 7.5: a. Emission spectra of a buffered solution of STX ($1.6*10^{-5}$ M) after illumination and after storage in darkness. **b.** Intensity of the emission maxima of the fluorescent product after excitation with different excitation slits (different UV light intensities)

Future Prospect and Outlook

As presented in this manuscript, is not possible to detect STX with fluorogenic crown ethers in aqueous solution. However, the degradation of STX to an intrinsically fluorescent product is of high interest as it enables direct measurement and does not require any additional indicator dye to interact with the analyte.

The mechanism of the degradation using UV light is not clear as STX does not absorb light. However, it is known that the degradation is caused by oxidation of STX and is routinely used in standardized analysis of STX using HPLC. Hereby, the toxin is oxidized before or after separation on the column using tedious reaction procedures with strong chemicals (e.g. H_2O_2) and heat programs.[261] One way to overcome the use of toxic and harsh oxidation agents is the use of photosensitizers which can produce singlet oxygen ($^1O_2$).[262]

Photosensitizers absorb light and are excited to a singlet state with higher energy, which then can undergo ISC to an excited triplet state (**Figure 2.1** on p.10). Molecular oxygen can then collide with the photosensitizer and the energy of the triplet state is transferred to O_2 forming the highly reactive $^1O_2$ species (**Figure 7.3**). Singlet oxygen is a very reactive species of molecular oxygen which can be used as an oxidising agent in chemical reactions or to selectively destroy tumor cells (photodynamic therapy).[263] Photosensitized generation is a simple and controllable method for the production of $^1O_2$, requiring only oxygen, light of an appropriate wavelength and a photosensitizer capable of absorbing this light.

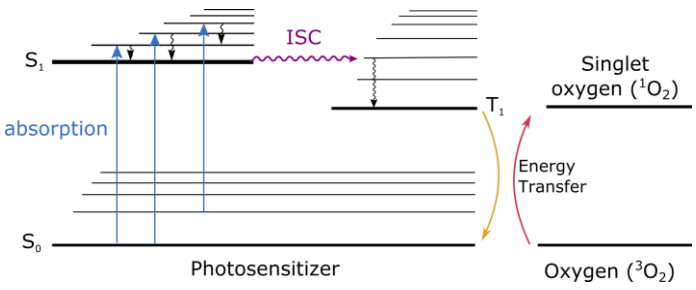

Figure 7.3: Schematic illustration of the function principle of a photosensitizer. The photosensitizer absorbs light and gets excited to an excited triplet state after intersystem crossing (ISC). The energy is then transferred to a ground state oxygen (triplet oxygen $^3O_2$) which gets excited to a highly reactive singlet oxygen species ($^1O_2$)

Based on the fact that STX forms a fluorescent product after oxidation, we attempted to develop a method to determine the concentration of STX in water using $^1O_2$. This is the first purely optical based method as both the generation and the detection of this STX product is based on photosensitization and fluorescence measurements.

The photosensitizer is added to an aqueous solution of STX and then illuminated at its excitation maximum to generate $^1O_2$ which should then oxidize STX. The same sample is then illuminated at the excitation maximum of the STX degradation product (334 nm, **Figure S - 7.4**) and its emission it detected (390 nm). Therefore, it is important that the absorption and emission of the photosensitizer is > 400 nm to prevent from any interference.

The fluorescein derivate Rose Bengal (RB) meets these criteria and its solubility in water and high $^1O_2$ yield makes it a perfect candidate for this application (**Figure 7.4**).[264]

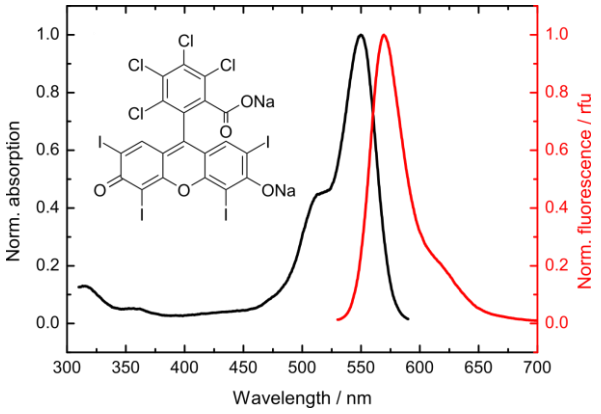

Figure 7.4: Structure and normalized absorption/emission spectra of the photosensitizer Rose Bengal

A cuvette containing a buffered solution (pH 7.4) of Rose Bengal and STX was placed in a fluorimeter with a stirring bar and a fluorescence spectrum was recorded (λex = 310 nm). As shown in **Figure 7.5**, at 0 min there is only the Raman peak of water (A) and the fluorescence of Rose Bengal (D) visible. Afterwards, the sample is illuminated for a certain amount of time with 550 nm which is the excitation maximum of Rose Bengal. Recording an emission spectrum after 30 min (λex = 310 nm) shows the formation of the STX degradation product (B). Additionally, Rose Bengal shows photobleaching (D) as the emission decreases. However, another emission peak is visible at 500 nm (C) which could be another emission of a degradation product of Rose Bengal.

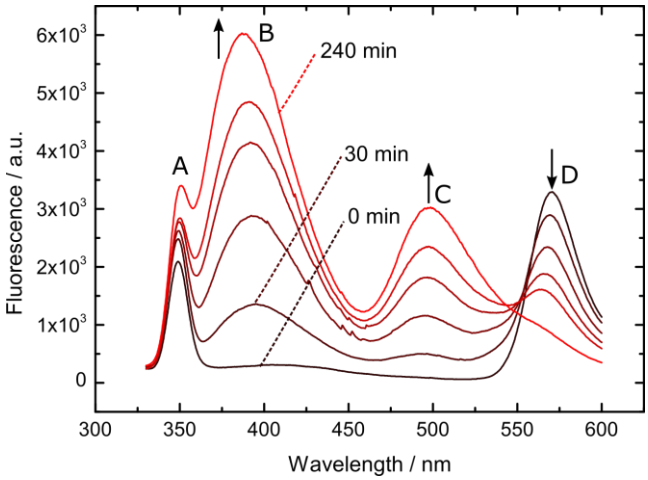

Figure 7.5: Fluorescence emission spectra of a sample containing STX (1.6 µM) and Rose Bengal (0.3 mM) in a phosphate buffer (100 mM, pH 7.4) at different times. Excitation was performed at 310 nm. **A:** Raman peak of H_2O. **B:** increasing emission of the STX degradation product that is formed while illumination of the photosensitizer. **C:** Increasing fluorescence product of a degradation product of Rose Bengal. **D:** Decreasing emission of Rose Bengal.

To validate if this method can be used for quantification of STX, we prepared samples with different STX concentrations, while keeping the photosensitizer concentration constant. Illumination was performed for 10, 30 and 60 min (**Figure 7.6 a-c**). A calibration curve can be obtained by taking the fluorescence maxima of the STX degradation product at 390 nm vs. the concentration of STX (**Figure 7.6 d-f**).

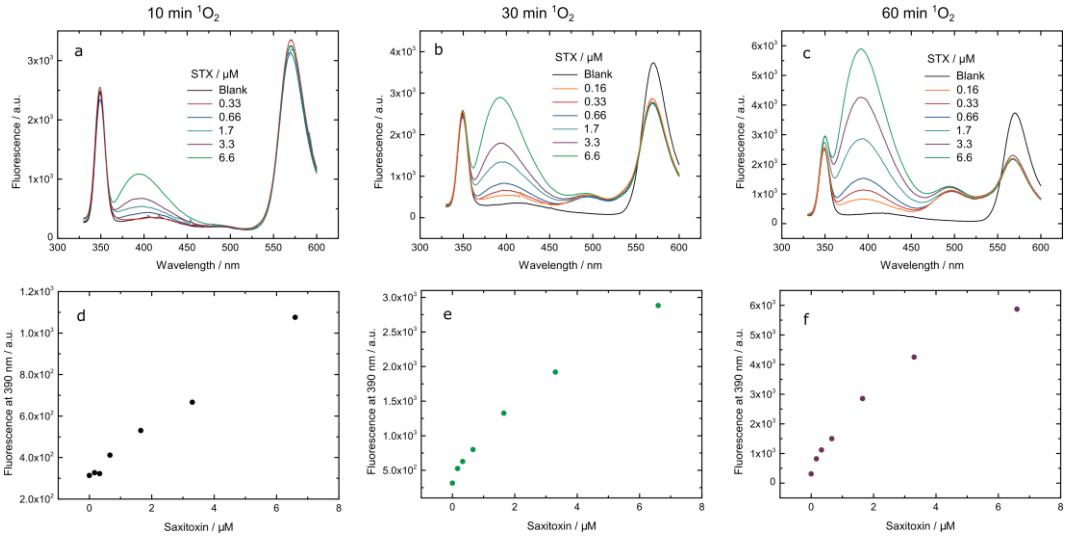

Figure 7.6: Oxidation of different concentrations of STX using Rose Bengal as photosensitizer. Emission spectra (excitation at 310 nm) were recorded after a generation of $^1O_2$ (illumination at 550

nm) for 10, 30 or 60 min (**a, b**, **c** respectively). Calibration curve is obtained by taking the fluorescence at the maximum of the STX degradation product at 390 nm (**d, e, f**).

A longer time for generation of $^1O_2$ increases the amount of fluorescent STX product and therefore a higher sensitivity can be achieved. However, as the amount of generated $^1O_2$ is dependent on the amount of absorbed photons, it is possible to use light with higher intensity to reduce the amount of time. This was achieved by using Power-LED (535 nm) instead of the lamp of the fluorimeter. A comparison of the efficiency of the $^1O_2$ production is shown in **Figure 7.7a**. The Power-LED with a higher intensity generates more $^1O_2$ and therefore oxidizes more STX in the same time as the fluorimeter lamp. Thus, it is possible to reduce the reaction time. However, Rose Bengal is also prone to photobleaching due to its highly efficient absorption of light which results in less production of $^1O_2$ over time. Using the Power-LED, Rose Bengal is almost completely destroyed after 60 min of illumination (**Figure 7.7b**).

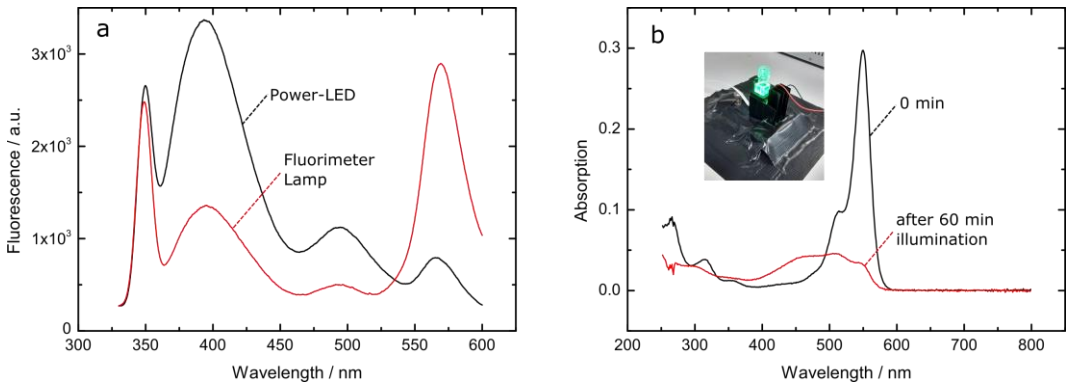

Figure 7.7: a: Comparison of a Power-LED and the lamp of the fluorimeter for generation of photosensitized $^1O_2$. A sample with 1.7 µM STX and 0.3 mM Rose Bengal was illuminated for 30 min followed by recording an emission spectrum to determine produced STX degradation product. **b:** Absorption spectra of Rose Bengal dissolved in water before and after illumination with the Power-LED (535 nm, 35 µmol m^2 s^{-1}). The insert shows a photographic image of the illuminated cuvette with the LED.

Additionally, oxidations were performed at different pH values using the Power-LED and a STX concentration of 1.7 µM. As shown in **Figure 7.8**, the oxidation is highly dependent on the pH value of the sample. At low pH values, only minor degradation

of STX can be detected after 45 minutes of illumination. Likewise, at higher pH (10), no oxidation of STX is visible. However, at a neutral pH (7.4), a highly efficient and fast oxidation of STX takes place.

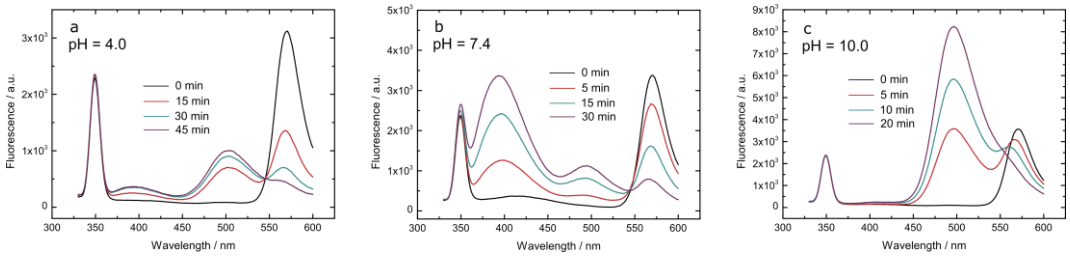

Figure 7.8: pH dependency of the generation of fluorescent STX degradation product. pH values were (**a**) 4.0 (acetic acid buffer), (**b**) 7.4 (phosphate buffer) and (**c**)10.0 (MES buffer).

Using photosensitizers, it is possible to efficiently generate an intrinsically fluorescent derivate product of STX. The reaction time can be reduced by applying highly intense light-sources in order to generate highly reactive $^1O_2$ species more efficiently, which can then oxidize STX. This method can be easily miniaturized, as LEDs are available for both the excitation of Rose Bengal and the STX product and also photodetectors to measure the emission of STX. This method represents a promising alternative to the pre- or post-column oxidation method which is currently routinely used.

8 Summary and Conclusion

This thesis demonstrated the potential of optical technology for measuring various analytes based on cation recognition. Different sensing materials and sensing concepts were developed for measuring K^+, Na^+ and dissolved ammonia and several applications were demonstrated ranging from marine monitoring to live cell imaging.

We established a straightforward and efficient synthetic strategy leading to a range of fluorescent indicator dyes with tuneable properties. These dyes combine selective aza-crown ether receptors and bright and photostable tetraaryl-BODIPY chromophores. Several representatives show absorption and emission in the red/NIR part of the spectrum, high molar absorption coefficients and fluorescence quantum yields. By employing different receptor units, we were able to develop sensors for of a variety of different analytes and additionally tune the sensitivity and selectivity.

It was demonstrated that the polymer matrix in which the fluoroionophores are embedded can further improve the sensor performance or even determine the sensitivity towards analytes. Incorporating the dye into a polymer matrix yielded robust and reproducible sensors, which can be used for continuous measurements as they show a rapid and fully reversible response. Importantly, the new materials are applicable in a variety of formats, including planar sensor foils and spots, fiber-optic (micro)sensors and water-dispersible nanosensors.

Moreover, referenced sensing material can be prepared and enable measurements with a commercially available compact phase fluorimeter. Nanoparticles, which can be prepared via a simple precipitation procedure, showed efficient intracellular uptake by multiple cell lines and enabled visualisation of ion fluxes using fluorescence imaging techniques. Innovation potential of the new material was demonstrated by modification of the polymer sensor membrane to transfer an K^+ ion sensor to an NH_3 gas sensor by measuring the corresponding NH_4^+ ion.

Due to the high potential of and need for reliable ion sensors in many scientific fields, the improvements achieved during this thesis take optical sensors one step closer to becoming valuable analytical tools in the future.

Part III

Appendix

A Curriculum Vitae

Bernhard Müller

Current Address	Plüddemanngasse 36, A-8010 Graz, Austria
Permanent Address	Ritzersdorf 47, A-4113 St.Martin im Mühlkreis
Date of Birth	28.11.1988 in Linz
Nationality	Austrian
E-Mail	ber.mueller@gmx.at

Education

04/2014 – 08/2017	**PhD student** in Technical Chemistry at Graz University of Technology, Topic: *Fluoroionophores for Optical Ion Sensing – From Synthesis to Applications*. Supervisor: Prof. Ingo Klimant, Co-supervision Dr. Sergey Borisov
02/2012 - 02/2014	**Master program** in Technical Chemistry at Graz University of Technology and Karl-Franzens University Graz (NAWI Project). Thesis: *Covalent Linkage of pi-Extended Pt(II)-Porphyrins to Silicone Matrices – A Convenient Way to Obtain Optical Trace Oxygen* Sensors. Supervisor: Prof. Ingo Klimant
10/2008 - 03/2012	**Bachelor program** in Chemistry; Graz University of Technology and Karl-Franzens University Graz (NAWI Project), Thesis: *Synthesis and Characterization of Polymer Matrices for Optical Oxygen Sensors.* Supervisor: Prof. Ingo Klimant
09/2000 - 06/2007	**A-Level** at Bundesrealgymnasium Rohrbach, Upper Austria

Internships and Collaborations

08/2016	Internship for three weeks at the Biosciences Institute (University College Cork, Ireland) supervised by Prof. Dmitri Papkovsky and Dr. Ruslan Dmitriev. Topic: *Live cell microscopy imaging and evaluation of new K^+-sensitive*

	fluorescent sensing materials for high-performance intracellular K^+ biosensors.
08/2011 - 09/2011	Internship for two months at Syracuse University (NY, USA) supervised by Prof. Michael Sponsler. Topic: *Synthesis of an Electron Reservoir Tri-Ruthenium Complex for Dye-Sensitized Solar Cells.*

Awards and Scholarships

04/2017	Best Speaker Award at DocDays Conference 2017 NAWI Graz; Graz, Austria
12/2012	Academic Merit-Based Scholarship

Publications in Peer Reviewed Journals

Müller, B. J., Steinmann, N; Borisov, S. M. & Klimant, I.; *Ammonia Sensing with Fluoroionophores – a Promising Way to Minimize Interferences Caused by Volatile Amines*; Chemical Communication, submitted

Müller, B. J. *; Zhdanov, A. V. *****; Borisov, S. M.; Foley, T.; Okkelman, I.A.; Tsytsarev, V.; Tan, Q.; Erzurumlu, R.S.; Chen, Y.; Zhang, H.; Toncelli, C.; Klimant, I.; Papkovsky, D.B. & Dmitriev, R.I.; *Nanoparticle-based Fluoroionophore for Analysis of Potassium Ion Dynamics in 3D-Tissue Models and In Vivo*; Nature Materials; under review. ***equal contributions**

Hollauf, M.; Zach, P.W.; Borisov, S.M.; **Müller, B. J.**; Beichel, D.; Tscherner, M.; Köstler, S.; Hartmann, P.; Knall, A.C. & Trimmel, G.; *Dye functionalized-ROMP based terpolymers for the use as a light up-converting material via triplet-triplet annihilation*; J. Mater. Chem. C., under review

Müller, B. J., Rappitsch, T; Staudinger, C; Borisov, S. M. & Klimant, I.; *Sodium-Selective Fluoroionophore-based Optodes for Seawater Salinity Measurements*; Analytical Chemistry, accepted

Müller, B. J., Mistlberger, G. & Klimant, I. *New insights in the determination of Saxitoxin in water with fluorogenic crown ethers*; Bioanalytical and Analytical Chemistry, under review

Müller, B. J., Borisov, S. M. & Klimant, I. *Red- to NIR-Emitting, BODIPY-Based, K^+-Selective Fluoroionophores and Sensing Materials.* Adv. Funct. Mater. 26, 7697–7707 (**2016**)

Müller, B. J.; Burger, T.; Borisov, S. M. & Klimant, I.; *High performance optical trace oxygen sensors based on NIR-emitting benzoporphyrins covalently coupled to silicone matrixes*; Sensors and Actuators B: Chemical, 216, 527–534 (**2015**)

Dmitriev, R.I., Borisov S.M., Dussmann H., Sun S., **Müller B.J.**, Prehn J., Baklaushev V.P., Klimant I. & Papkovsky D.B.; *Versatile conjugated polymer nanoparticles for high-resolution O2 imaging in 2D and 3D cell models and tissues*; ACS Nano, 5, 5275–5288 (**2015**)

Hutter, L. H*****.; **Müller, B. J.***; Koren, K.; Borisov, S. M. & Klimant, I.; *Robust optical oxygen sensors based on polymer-bound NIR-emitting platinum(II)–benzoporphyrins*; J. Mater. Chem. C., 2, 7589–7598. (**2014**) ***equal contributions**

Zoidl, M.; **Müller, B.**; Torvisco, A.; Tysoe, C.; Benazza, M.; Siriwardena, A.; Withers, S. G. & Wrodnigg, T. M.; *Concise synthesis of C-1-cyano-iminosugars via a new Staudinger/aza Wittig/Strecker multicomponent reaction strategy*; Bioorganic & Medicinal Chemistry Letters, 24, 2777–2780. (**2014**)

Oral Presentations

Müller, B. J.; Tribuser, L.; Rappitsch, T.; Steinmann, N.; Dmitriev, R.; Borisov, S. M. & Klimant, I.; *Optical Ion Sensors – A modular system for fluorescence indicators and their applications as sensing materials*; DocDays 2017 NAWI Graz; Graz, Austria; **2017**. **Best speaker award**

Müller, B.J.; Borisov, S.M.; Klimant, I.; *Fluorescence Optical Sensors for the Measurement of K^+ Ions;* JungchemikerInnenforum Austrian Society of Analytical Chemistry (ASAC) 2016; Graz, Austria; **2016**

Müller, B.J.; Borisov, S. M.; Klimant, I.; *Fluorescent K^+ Sensor Materials;* DocDays 2016 NAWI Graz; Graz, Austria; **2016**

Müller, B.J.; Sun, S.; Hutter, L.H..; Borisov, S.M.; Klimant, I.; *Advanced optical oxygen sensor materials based on NIR-emitting benzoporphyrins covalently grafted to polymers;* 13th YoungChem - International Congress of Young Chemists; Cracow, Poland; **2015**

Müller, B.J.; Hutter, L.H.; Koren, K.; Borisov, S.M.; Klimant, I.; *Optical (trace) oxygen sensors based on NIR-emitting benzoporphyrins covalently linked to polymers;* Europt(r)ode XII - XII conference on optical chemical sensors and biosensors; Athens, Greece; **2014**

Poster Presentations

Tribuser, L.; **Müller, B. J.**; Borisov S.M. & Klimant, I.; *Fluorescent Ca^{2+} Indicator Dyes for Optical Sensing*; DocDays 2017 NAWI Graz; Graz, Austria; **2017**

Müller, B.J.; Steinmann N.; Hörler B.; Lechner J.; Heupl L.; Borisov S.; Klimant, I.; *Fluorescent potassium sensors for water using BODIPY dyes with aza-crown-ether immobilised in hydrogel matrixes;* Europt(r)ode XIII - Conference on optical chemical sensors and biosensors; Graz, Austria; **2016**

Müller, B.J.; Mistlberger G.; Klimant, I.; *Optical detection of the marine biotoxin saxitoxin;* Europt(r)ode XIII - Conference on optical chemical sensors and biosensors; Graz, Austria; **2016**

Müller, B.J.; Mistlberger, G.; Klimant, I.; *Saxitoxin detection: A simple alternative to post column oxidation and bio assays*.13th International Estuarine Biogeochemistry Symposium; Bordeaux, France; **2015**

Zieger, S. E.; Mistlberger, G.; **Müller, B.J.;** Troi. L., Holly, C.; Klimant, I.; *Multi-channel miniaturized algae detection unit as an early warning system*. 13th International Estuarine Biogeochemistry Symposium; Bordeaux, France; **2015**

Müller, B.J.; Mistlberger G.; Klimant, I.; *Saxitoxin – Evaluation of a new potential detection method;* Anakon 2015; Graz, Austria; **2015**

Mistlberger G.; **Müller, B.J.**; Holly, C.; Klimant, I.; *Multi-Channel miniaturized algae detection module;* 2015 Aquatic Sciences Meeting; Granada, Spain; **2015**

Müller, B.J.; Mistlberger G.; Klimant, I.; *Evaluation of different optical detection methods for the marine biotoxin saxitoxin;* 2015 Aquatic Sciences Meeting; Granada, Spain; **2015**

Müller, B.J.; Basner A.; Sponsler M.B.; *Synthesis of an electron reservoir tri-ruthenium complex for dye sensitized solar cells;* Summer REU Symposium; Syracuse, USA; **2011**

B List of Figures

C List of Tables

D Abbreviations

BODIPY	Borondipyrromethenes
CTD	Conductivity, Temperature and Depth
DLR	Dual Lifetime Referencing
EEG	Electroencephalography
FBS	Fetal Bovine Serum
FI	Fluoroionophore
FLIM	Fluorescence Lifetime Imaging Microscopy
ICT	Intramolecular Charge Transfer
ISC	Intersystem Crossing
ISE	Ion Selective Electrode
LED	Light Emitting Diode
NIR	Near Infrared
PET	Photoinduced Electron Transfer
PET-foil	Polyethylene terephthalate foil
PSU	Practical Salinity Unit
QY	Quantum Yield
STEM	Scanning Transmission Electron Microscopy
TCSPC	Time-Correlated Single Photon Counting
UV-VIS	Ultraviolet–Visible Spectroscopy
VSDI	Voltage-Sensitive Dye Optical Imaging

E References

(1) Gründler, P. *Chemische Sensoren*, 1st ed.; Springer-Verlag Berlin Heidelberg, 2004.

(2) Borisov, S. M.; Wolfbeis, O. S. *Chem. Rev.* **2008**, *108* (2), 423–61.

(3) Homola, J. *Chem. Rev.* **2008**, *108* (2), 462–493.

(4) Oliver, N. S.; Toumazou, C.; Cass, A. E. G.; Johnston, D. G. *Diabet. Med. J. Br. Diabet. Assoc.* **2009**, *26* (3), 197–210.

(5) Lee, B. *Opt. Fiber Technol.* **2003**, *9* (2), 57–79.

(6) Li, M.; K. Cushing, S.; Wu, N. *Analyst* **2015**, *140* (2), 386–406.

(7) Muehlethaler, C.; Leona, M.; Lombardi, J. R. *Anal. Chem.* **2016**, *88* (1), 152–169.

(8) Schlücker, S. *Angew. Chem. Int. Ed.* **2014**, *53* (19), 4756–4795.

(9) Burgess, L. W. *Sens. Actuators B Chem.* **1995**, *29* (1), 10–15.

(10) Razeghi, M.; Nguyen, B.-M. *Rep. Prog. Phys.* **2014**, *77* (8), 082401.

(11) McDonagh, C.; Burke, C. S.; MacCraith, B. D. *Chem. Rev.* **2008**, *108* (2), 400–422.

(12) Ruedas-Rama, M. J.; Walters, J. D.; Orte, A.; Hall, E. A. H. *Anal. Chim. Acta* **2012**, *751*, 1–23.

(13) Schäferling, M. *Angew. Chem. Int. Ed.* **2012**, *51* (15), 3532–3554.

(14) Valeur, B. *Molecular Fluorescence: Principles and Applications*; Wiley-VCH Verlag GmbH, 2001.

(15) Lakowicz, J. R. *Principles of Fluorescence Spectroscopy*.

(16) Quaranta, M.; Borisov, S. M.; Klimant, I. *Bioanal. Rev.* **2012**, *4* (2–4), 115–157.

(17) Weller, A. *Pure Appl. Chem.* **1968**, *16* (1).

(18) Silva, A. P. de; Rupasinghe, R. A. D. D. *J. Chem. Soc. Chem. Commun.* **1985**, No. 23, 1669–1670.

(19) A. Bissell, R.; Silva, A. P. de; Nimal Gunaratne, H. Q.; Mark Lynch, P. L.; M. Maguire, G. E.; Samankumara Sandanayake, K. R. A. *Chem. Soc. Rev.* **1992**, *21* (3), 187–195.

(20) Silva, A. P. de; Gunnlaugsson, T.; Rice, T. E. *Analyst* **1996**, *121* (12), 1759–1762.

(21) Aigner, D.; Freunberger, S. A.; Wilkening, M.; Saf, R.; Borisov, S. M.; Klimant, I. *Anal. Chem.* **2014**, *86* (18), 9293–9300.

(22) Gareis, T.; Huber, C.; Wolfbeis, O. S.; Daub, J. *Chem. Commun.* **1997**, *0* (18), 1717–1718.

(23) Yokoi, H.; Nakano, T.; Fujita, W.; Ishiguro, K.; Sawaki, Y. *J. Am. Chem. Soc.* **1998**, *120* (48), 12453–12458.

(24) Bissell, R. A.; de Silva, A. P.; Thilak, W.; Fernando, M. L.; Patuwathavithana, S. T.; Shantha, T. K.; Samarasinghe, D. *Tetrahedron Lett.* **1991**, *32* (3), 425–428.

(25) Lehn, J.-M. *Supramolecular Chemistry: Concepts and Perspectives*; Wiley-VCH Verlag GmbH, 1995.

(26) Ma, X.; Zhao, Y. *Chem. Rev.* **2015**, *115* (15), 7794–7839.

(27) Del Valle, E. M. M. *Process Biochem.* **2004**, *39* (9), 1033–1046.

(28) Ramaiah, D.; Neelakandan, P. P.; Nair, A. K.; Avirah, R. R. *Chem. Soc. Rev.* **2010**, *39* (11), 4158–4168.

(29) Barrow, S. J.; Kasera, S.; Rowland, M. J.; del Barrio, J.; Scherman, O. A. *Chem. Rev.* **2015**, *115* (22), 12320–12406.

(30) Xue, M.; Yang, Y.; Chi, X.; Zhang, Z.; Huang, F. *Acc. Chem. Res.* **2012**, *45* (8), 1294–1308.

(31) Tsukanov, A. V.; Dubonosov, A. D.; Bren, V. A.; Minkin, V. I. *Chem. Heterocycl. Compd.* **2008**, *44* (8), 899–923.

(32) Schneider, H.-J. *Angew. Chem. Int. Ed. Engl.* **1991**, *30* (11), 1417–1436.

(33) Buschmann, H.-J. *Inorganica Chim. Acta* **1992**, *195* (1), 51–60.

(34) Shamsipur, M.; Talebpour, Z.; Alizadeh, N. *J. Solut. Chem.* **2003**, *32* (3), 227–238.

(35) Blair, S.; Kempen, E.; Brodbelt, J. *J. Am. Soc. Mass Spectrom.* **1998**, *9* (10), 1049–1059.

(36) Hirose, K. *J. Incl. Phenom. Macrocycl. Chem.* **2001**, *39* (3–4), 193–209.

(37) Piekarski, H.; Taniewska-Osińska, S.; Biernat, J. F. *Inorganica Chim. Acta* **1986**, *124* (3), 115–120.

(38) Pedersen, C. J. *Angew. Chem. Int. Ed. Engl.* **1988**, *27* (8), 1021–1027.

(39) Gokel, G. W.; Leevy, W. M.; Weber, M. E. *Chem. Rev.* **2004**, *104* (5), 2723–2750.

(40) Jana, S.; Suresh, V.; Lepore, S. D. *Synlett Acc. Rapid Commun. Synth. Org. Chem.* **2015**, *26* (14), 1977–1980.

(41) Arnaud-Neu, F.; Delgado, R.; Chaves, S. *Pure Appl. Chem.* **2003**, *75* (1).

(42) Gokel, G. W.; Goli, D. M.; Minganti, C.; Echegoyen, L. *J. Am. Chem. Soc.* **1983**, *105* (23), 6786–6788.

(43) Saalfrank, R. W.; Löw, N.; Kareth, S.; Seitz, V.; Hampel, F.; Stalke, D.; Teichert, M. *Angew. Chem. Int. Ed.* **1998**, *37* (1–2), 172–175.

(44) Pedersen, C. J.; Frensdorff, H. K. *Angew. Chem. Int. Ed. Engl.* **1972**, *11* (1), 16–25.

(45) Harris, D. C. *Quantitative Chemical Analysis*, 8th ed.; W.H. Freeman: New York, 2010.

(46) Bobacka, J.; Ivaska, A.; Lewenstam, A. *Chem. Rev.* **2008**, *108* (2), 329–351.

(47) Meyerhoff, M. E.; Fraticelli, Y. M. *Anal. Chem.* **1982**, *54* (5), 27–44.

(48) Bakker, E.; Diamond, D.; Lewenstam, A.; Pretsch, E. *Anal. Chim. Acta* **1999**, *393* (1–3), 11–18.

(49) Bakker, E.; Bühlmann, P.; Pretsch, E. *Chem. Rev.* **1997**, *97* (8), 3083–3132.

(50) Oesch, U.; Ammann, D.; Simon, W. *Clin. Chem.* **1986**, *32* (8), 1448–1459.

(51) Meyerhoff, M. E.; Fraticelli, Y. M.; Greenberg, J. A. *Clin. Chem.* **1982**, *28* (9), 1973–1978.

(52) Bakker, E.; Crespo, G.; Grygolowicz-Pawlak, E.; Mistlberger, G.; Pawlak, M.; Xie, X. *Chimia* **2011**, *65* (3), 141–149.

(53) Bakker, E.; Lerchi, M.; Rosatzin, T.; Rusterholz, B.; Simon, W. *Anal. Chim. Acta* **1993**, *278* (2), 211–225.

(54) Bühlmann, P.; Pretsch, E.; Bakker, E. *Chem. Rev.* **1998**, *98* (4), 1593–1688.

(55) Xie, X.; Bakker, E. *Anal. Bioanal. Chem.* **2015**, *407* (14), 3899–3910.

(56) Mistlberger, G.; Gaston, C. A.; Bakker, E. *Annu. Rev. Anal. Chem.* **2014**, *7* (1), 483–512.

(57) Huber, C.; Werner, T.; Krause, C.; Wolfbeis, O. S.; Leiner, M. J. P. *Anal. Chim. Acta* **1999**, *398* (2–3), 137–143.

(58) Krause, C.; Werner, T.; Huber, C.; Wolfbeis, O. S.; Leiner, M. J. P. *Anal. Chem.* **1999**, *71* (8), 1544–1548.

(59) Krause, C.; Werner, T.; Huber, C.; Wolfbeis, O. S. *Anal. Chem.* **1999**, *71* (23), 5304–5308.

(60) Ishikawa, J.; Sakamoto, H.; Otomo, M. *Analyst* **1998**, *123* (2), 201–207.

(61) Lan, B. T. T.; Tóth, K. *Anal. Sci.* **1998**, *14* (1), 191–197.

(62) Sanchez-Pedreño, C.; Ortuño, J. A.; Albero, M. I.; Garcia, M. S.; Valero, M. V. *Anal. Chim. Acta* **2000**, *414* (1–2), 195–203.

(63) Panchenko, P. A.; Fedorov, Y. V.; Fedorova, O. A.; Jonusauskas, G. *Dyes Pigments* **2013**, *98* (3), 347–357.

(64) Bozdemir, O. A.; Guliyev, R.; Buyukcakir, O.; Selcuk, S.; Kolemen, S.; Gulseren, G.; Nalbantoglu, T.; Boyaci, H.; Akkaya, E. U. *J. Am. Chem. Soc.* **2010**, *132* (23), 8029–8036.

(65) Hartley, J. H.; James, T. D.; Ward, C. J. *J. Chem. Soc. [Perkin 1]* **2000**, No. 19, 3155–3184.

(66) Callan, J. F.; de Silva, A. P.; Magri, D. C. *Tetrahedron* **2005**, *61* (36), 8551–8588.

(67) Carter, K. P.; Young, A. M.; Palmer, A. E. *Chem. Rev.* **2014**, *114* (8), 4564–4601.

(68) Li, J.; Yim, D.; Jang, W.-D.; Yoon, J. *Chem. Soc. Rev.* **2016**.

(69) Yin, J.; Hu, Y.; Yoon, J. *Chem. Soc. Rev.* **2015**, *44* (14), 4619–4644.

(70) Shin, E. J. *Chem. Lett.* **2002**, *31* (7), 686–687.

(71) Gunnlaugsson, T.; Nieuwenhuyzen, M.; Richard, L.; Thoss, V. *J. Chem. Soc. Perkin Trans. 2* **2002**, *0* (1), 141–150.

(72) Alonso, M.-T.; Brunet, E.; Juanes, O.; Rodríguez-Ubis, J.-C. *J. Photochem. Photobiol. Chem.* **2002**, *147* (2), 113–125.

(73) de Silva, A. P.; de Silva, S. A. *J. Chem. Soc. Chem. Commun.* **1986**, No. 23, 1709–1710.

(74) de Silva, A. P.; Nimal Gunaratne, H. Q.; Samankumara Sandanayake, K. R. A. *Tetrahedron Lett.* **1990**, *31* (36), 5193–5196.

(75) Kondo, S.; Takahashi, T.; Takiguchi, Y.; Unno, M. *Tetrahedron Lett.* **2011**, *52* (3), 453–457.

(76) Wolfbeis, O. S. *J. Mater. Chem.* **2005**, *15* (27–28), 2657.

(77) Borisov, S. M.; Klimant, I. *The Analyst* **2008**, *133* (10), 1302–1307.

(78) Zhou, X.; Su, F.; Gao, W.; Tian, Y.; Youngbull, C.; Johnson, R. H.; Meldrum, D. R. *Biomaterials* **2011**, *32* (33), 8574–8583.

(79) Schwarze, T.; Müller, H.; Ast, S.; Steinbrück, D.; Eidner, S.; Geißler, F.; Kumke, M. U.; Holdt, H.-J. *Chem. Commun.* **2014**, *50* (91), 14167–14170.

(80) Rüdiger, V.; Schneider, H.-J.; Solov'ev, V. P.; Kazachenko, V. P.; Raevsky, O. A. *Eur. J. Org. Chem.* **1999**, *1999* (8), 1847–1856.

(81) Treibs, A.; Kreuzer, F.-H. *Justus Liebigs Ann. Chem.* **1968**, *718* (1), 208–223.

(82) Boens, N.; Leen, V.; Dehaen, W. *Chem Soc Rev* **2012**, *41* (3), 1130–1172.

(83) Ziessel, R.; Ulrich, G.; Harriman, A. *New J. Chem.* **2007**, *31* (4), 496–501.

(84) Ulrich, G.; Ziessel, R.; Harriman, A. *Angew. Chem. Int. Ed.* **2008**, *47* (7), 1184–1201.

(85) Sui, B.; Yue, X.; Tichy, M. G.; Liu, T.; Belfield, K. D. *Eur. J. Org. Chem.* **2015**, *2015* (6), 1189–1192.

(86) Hirata, T.; Terai, T.; Komatsu, T.; Hanaoka, K.; Nagano, T. *Bioorg. Med. Chem. Lett.* **2011**, *21* (20), 6090–6093.

(87) Atilgan, S.; Ozdemir, T.; Akkaya, E. U. *Org. Lett.* **2008**, *10* (18), 4065–4067.

(88) Loudet, A.; Burgess, K. *Chem. Rev.* **2007**, *107* (11), 4891–4932.

(89) Molecular Probes®, Labeling & Detection Technologies | Thermo Fisher Scientific http://www.thermofisher.com/at/en/home/brands/molecular-probes.html (accessed Apr 11, 2017).

(90) Ast, S.; Schwarze, T.; Müller, H.; Sukhanov, A.; Michaelis, S.; Wegener, J.; Wolfbeis, O. S.; Körzdörfer, T.; Dürkop, A.; Holdt, H.-J. *Chem. – Eur. J.* **2013**, *19* (44), 14911–14917.

(91) Burnell, J. M.; Scribner, B. H.; Uyeno, B. T.; Villamil, M. F. *J. Clin. Invest.* **1956**, *35* (9), 935–939.

(92) Elkinton, J. R.; Winkler, A. W. *J. Clin. Invest.* **1944**, *23* (1), 93–101.

(93) Hille, B. *Prog. Biophys. Mol. Biol.* **1970**, *21*, 1–32.

(94) Eagle, H. *Science* **1955**, *122* (3168), 501–514.

(95) Whelton, P. K.; He, J.; Cutler, J. A.; Brancati, F. L.; Appel, L. J.; Follmann, D.; Klag, M. J. *JAMA* **1997**, *277* (20), 1624–1632.

(96) Gadsby, D. C.; Niedergerke, R.; Page, S. *Nature* **1971**, *232* (5313), 651–653.

(97) Hodgkin, A. L. *Biol. Rev.* **1951**, *26* (4), 339–409.

(98) Näbauer, M.; Kääb, S. *Cardiovasc. Res.* **1998**, *37* (2), 324–334.

(99) Tusa, J. K.; He, H. *J. Mater. Chem.* **2005**, *15* (27–28), 2640–2647.

(100) Doane, T. L.; Burda, C. *Chem. Soc. Rev.* **2012**, *41* (7), 2885–2911.

(101) Silva, A. P. de; Moody, T. S.; Wright, G. D. *Analyst* **2009**, *134* (12), 2385–2393.

(102) Meuwis, K.; Boens, N.; De Schryver, F. C.; Gallay, J.; Vincent, M. *Biophys. J.* **1995**, *68* (6), 2469–2473.

(103) He, H.; Mortellaro, M. A.; Leiner, M. J. P.; Fraatz, R. J.; Tusa, J. K. *J. Am. Chem. Soc.* **2003**, *125* (6), 1468–1469.

(104) Carpenter, R. D.; Verkman, A. S. *Eur. J. Org. Chem.* **2011**, *2011* (7), 1242–1248.

(105) Magzoub, M.; Padmawar, P.; Dix, J. A.; Verkman, A. S. *J. Phys. Chem. B* **2006**, *110* (42), 21216–21221.

(106) Padmawar, P.; Yao, X.; Bloch, O.; Manley, G. T.; Verkman, A. S. *Nat. Methods* **2005**, *2* (11), 825–827.

(107) Zhou, X.; Su, F.; Gao, W.; Tian, Y.; Youngbull, C.; Johnson, R. H.; Meldrum, D. R. *Biomaterials* **2011**, *32* (33), 8574–8583.

(108) Kong, X.; Su, F.; Zhang, L.; Yaron, J.; Lee, F.; Shi, Z.; Tian, Y.; Meldrum, D. R. *Angew. Chem. Int. Ed.* **2015**, n/a-n/a.

(109) Malval, J.-P.; Leray, I.; Valeur, B. *New J. Chem.* **2005**, *29* (8), 1089–1094.

(110) Baruah, M.; Qin, W.; Vallée, R. A. L.; Beljonne, D.; Rohand, T.; Dehaen, W.; Boens, N. *Org. Lett.* **2005**, *7* (20), 4377–4380.

(111) Namkung, W.; Padmawar, P.; Mills, A. D.; Verkman, A. S. *J. Am. Chem. Soc.* **2008**, *130* (25), 7794–7795.

(112) Zhou, X.; Su, F.; Tian, Y.; Youngbull, C.; Johnson, R. H.; Meldrum, D. R. *J. Am. Chem. Soc.* **2011**, *133* (46), 18530–18533.

(113) Zhao, W.; Carreira, E. M. *Chem. – Eur. J.* **2006**, *12* (27), 7254–7263.

(114) Yang, S. K.; Shi, X.; Park, S.; Ha, T.; Zimmerman, S. C. *Nat. Chem.* **2013**, *5* (8), 692–697.

(115) Umezawa, K.; Nakamura, Y.; Makino, H.; Citterio, D.; Suzuki, K. *J. Am. Chem. Soc.* **2008**, *130* (5), 1550–1551.

(116) Deutsch, C.; Taylor, J. S.; Wilson, D. F. *Proc. Natl. Acad. Sci. U. S. A.* **1982**, *79* (24), 7944–7948.

(117) Aigner, D.; Borisov, S. M.; Petritsch, P.; Klimant, I. *Chem. Commun.* **2013**, *49* (21), 2139–2141.

(118) Fercher, A.; Borisov, S. M.; Zhdanov, A. V.; Klimant, I.; Papkovsky, D. B. *ACS Nano* **2011**, *5* (7), 5499–5508.

(119) Das, S.; Suresh, P. K.; Desmukh, R. *Nanomedicine Nanotechnol. Biol. Med.* **2010**, *6* (2), 318–323.

(120) Sharma, U. K.; Verma, A.; Prajapati, S. K.; Pandey, H.; Pandey, A. C. *Appl. Nanosci.* **2014**, *5* (2), 143–155.

(121) Dillen, K.; Vandervoort, J.; Van den Mooter, G.; Ludwig, A. *Int. J. Pharm.* **2006**, *314* (1), 72–82.

(122) Borisov, S. M.; Mayr, T.; Mistlberger, G.; Waich, K.; Koren, K.; Chojnacki, P.; Klimant, I. *Talanta* **2009**, *79* (5), 1322–1330.

(123) Borisov, S. M.; Mayr, T.; Klimant, I. *Anal. Chem.* **2008**, *80* (3), 573–582.

(124) Borisov, S. M.; Würth, C.; Resch-Genger, U.; Klimant, I. *Anal. Chem.* **2013**, *85* (19), 9371–9377.

(125) Klimant, I.; Huber, C.; Liebsch, G.; Neurauter, G.; Stangelmayer, A.; Wolfbeis, O. S. In *New Trends in Fluorescence Spectroscopy*; Valeur, P. B., Brochon, D. J.-C., Eds.; Springer Series on Fluorescence; Springer Berlin Heidelberg, 2001; pp 257–274.

(126) Hortmann, A. G.; Robertson, D. A.; Gillard, B. K. *J. Org. Chem.* **1972**, *37* (2), 322–324.

(127) Kong, X.; Su, F.; Zhang, L.; Yaron, J.; Lee, F.; Shi, Z.; Tian, Y.; Meldrum, D. R. *Angew. Chem. Int. Ed.* **2015**, *54* (41), 12053–12057.

(128) Rappitsch, T. Optical Ion Sensors - Development of New Indicators for K^+ and Na^+ Sensing. Masterthesis, Graz Unversity of Technology, Austria: Graz, Austria, **2017.**

(129) McDonagh, C.; Burke, C. S.; MacCraith, B. D. *Chem. Rev.* **2008**, *108* (2), 400–22.

(130) Glud, R. N.; Ramsing, N. B.; Gundersen, J. K.; Klimant, I. *Oceanogr. Lit. Rev.* **1997**, *3* (44), 191.

(131) Rosenzweig, Z.; Kopelman, R. *Anal. Chem.* **1995**, *67* (15), 2650–2654.

(132) Song, A.; Parus, S.; Kopelman, R. *Anal. Chem.* **1997**, *69* (5), 863–867.

(133) Kosch, U.; Klimant, I.; Wolfbeis, O. S. *Fresenius J. Anal. Chem.* **1999**, *364* (1–2), 48–53.

(134) Kühl, M. *Methods Enzymol.* **2005**, *397*, 166–199.

(135) Koren, K.; Kühl, M. *Sens. Actuators B Chem.* **2015**, *210*, 124–128.

(136) Holst, G.; Grunwald, B. *Sens. Actuators B Chem.* **2001**, *74* (1–3), 78–90.

(137) Koren, K.; Jakobsen, S. L.; Kühl, M. *Sens. Actuators B Chem.* **2016**, *237*, 1095–1101.

(138) Minta, A.; Tsien, R. Y. *J. Biol. Chem.* **1989**, *264* (32), 19449–19457.

(139) Hirata, T.; Terai, T.; Yamamura, H.; Shimonishi, M.; Komatsu, T.; Hanaoka, K.; Ueno, T.; Imaizumi, Y.; Nagano, T.; Urano, Y. *Anal. Chem.* **2016**, *88* (5), 2693–2700.

(140) Matsui, A.; Umezawa, K.; Shindo, Y.; Fujii, T.; Citterio, D.; Oka, K.; Suzuki, K. *Chem. Commun.* **2011**, *47* (37), 10407–10409.

(141) Kim, M. K.; Lim, C. S.; Hong, J. T.; Han, J. H.; Jang, H.-Y.; Kim, H. M.; Cho, B. R. *Angew. Chem. Int. Ed.* **2010**, *49* (2), 364–367.

(142) Silva, A. P. de; Gunaratne, H. Q. N.; Gunnlaugsson, T.; Nieuwenhuizen, M. *Chem. Commun.* **1996**, No. 16, 1967–1968.

(143) Sarkar, A. R.; Heo, C. H.; Park, M. Y.; Lee, H. W.; Kim, H. M. *Chem. Commun.* **2014**, *50* (11), 1309–1312.

(144) Martin, V. V.; Rothe, A.; Diwu, Z.; Gee, K. R. *Bioorg. Med. Chem. Lett.* **2004**, *14* (21), 5313–5316.

(145) Meier, S. D.; Kovalchuk, Y.; Rose, C. R. *J. Neurosci. Methods* **2006**, *155* (2), 251–259.

(146) Valeur, B.; Leray, I. *Coord. Chem. Rev.* **2000**, *205* (1), 3–40.

(147) De Silva, A. P.; Gunaratne, H. N.; Gunnlaugsson, T.; Huxley, A. J.; McCoy, C. P.; Rademacher, J. T.; Rice, T. E. *Chem. Rev.* **1997**, *97* (5), 1515–1566.

(148) Kuhn, M. A.; Haugland, R. P. Fluorescent ion-selective diaryldiaza crown ether conjugates. US5405975 A, April 11, 1995.

(149) Buchholz, F.; Buschmann, N.; Cammann, K. *Sens. Actuators B Chem.* **1992**, *9* (1), 41–47.

(150) He, H.; Mortellaro, M. A.; Leiner, M. J. P.; Young, S. T.; Fraatz, R. J.; Tusa, J. K. *Anal. Chem.* **2003**, *75* (3), 549–555.

(151) Müller, B. J.; Borisov, S. M.; Klimant, I. *Adv. Funct. Mater.* **2016**, *26* (42), 7697–7707.

(152) Schultz, R. A.; White, B. D.; Dishong, D. M.; Arnold, K. A.; Gokel, G. W. *J. Am. Chem. Soc.* **1985**, *107* (23), 6659–6668.

(153) HydroMed Products http://www.advbiomaterials.com/products/hydrophilic/hydromed.html (accessed Nov 23, 2016).

(154) Rurack, K.; Sczepan, M.; Spieles, M.; Resch-Genger, U.; Rettig, W. *Chem. Phys. Lett.* **2000**, *320* (1–2), 87–94.

(155) Kollmannsberger, M.; Rurack, K.; Resch-Genger, U.; Daub, J. *J. Phys. Chem. A* **1998**, *102* (50), 10211–10220.

(156) Qin, W.; Baruah, M.; Sliwa, M.; Van der Auweraer, M.; De Borggraeve, W. M.; Beljonne, D.; Van Averbeke, B.; Boens, N. *J. Phys. Chem. A* **2008**, *112* (27), 6104–6114.

(157) Accorsi, G.; Verri, G.; Bolognesi, M.; Armaroli, N.; Clementi, C.; Miliani, C.; Romani, A. *Chem. Commun.* **2009**, No. 23, 3392–3394.

(158) Borisov, S. M.; Würth, C.; Resch-Genger, U.; Klimant, I. *Anal. Chem.* **2013**, *85* (19), 9371–9377.

(159) Harvey, H. W. *J. Mar. Biol. Assoc. U. K.* **1956**, *35* (1), 289–289.

(160) Millero, F. J.; Feistel, R.; Wright, D. G.; McDougall, T. J. *Deep Sea Res. Part Oceanogr. Res. Pap.* **2008**, *55* (1), 50–72.

(161) Caspers, H. *Int. Rev. Gesamten Hydrobiol. Hydrogr.* **1970**, *55* (1), 167–167.

(162) Müller, T. J. In *Methods of Seawater Analysis*; Grasshoff, K., Kremling, K., Ehrhardt, M., Eds.; Wiley-VCH Verlag GmbH, 1999; pp 41–73.

(163) Eilers, J. M.; Sullivan, T. J.; Hurley, K. C. *Hydrobiologia* **1990**, *199* (1), 1–6.

(164) Huber, C.; Klimant, I.; Krause, C.; Werner, T.; Mayr, T.; Wolfbeis, O. S. *Fresenius J. Anal. Chem.* **2000**, *368* (2–3), 196–202.

(165) He, H.; Jenkins, K.; Lin, C. *Anal. Chim. Acta* **2008**, *611* (2), 197–204.

(166) Tribuser, L. Synthesis of new fluorscent indicator dyes and receptors for optical ion sensors. Masterthesis, Graz Unversity of Technology, Austria: Graz, Austria, **2017.**

(167) Aigner, D.; Dmitriev, R. I.; Borisov, S. M.; Papkovsky, D. B.; Klimant, I. *J. Mater. Chem. B* **2014**, *2* (39), 6792–6801.

(168) Jenkins, J.; Borisov, S. M.; Papkovsky, D. B.; Dmitriev, R. I. *Anal. Chem.* **2016**, *88* (21), 10566–10572.

(169) Post, R. L.; Merritt, C. R.; Kinsolving, C. R.; Albright, C. D. *J. Biol. Chem.* **1960**, *235*, 1796–1802.

(170) Bellot-Saez, A.; Kékesi, O.; Morley, J. W.; Buskila, Y. *Neurosci. Biobehav. Rev.* **2017**, *77*, 87–97.

(171) Shieh, C. C.; Coghlan, M.; Sullivan, J. P.; Gopalakrishnan, M. *Pharmacol. Rev.* **2000**, *52* (4), 557–594.

(172) Agarwal, R.; Afzalpurkar, R.; Fordtran, J. S. *Gastroenterology* **1994**, *107* (2), 548–571.

(173) Lindinger, M. I. *J. Mol. Cell. Cardiol.* **1995**, *27* (4), 1011–1022.

(174) Jørgensen, P. L. *Physiol. Rev.* **1980**, *60* (3), 864–917.

(175) Comes, N.; Serrano-Albarrás, A.; Capera, J.; Serrano-Novillo, C.; Condom, E.; Ramón Y Cajal, S.; Ferreres, J. C.; Felipe, A. *Biochim. Biophys. Acta* **2015**, *1848* (10 Pt B), 2477–2492.

(176) Kitazono, T.; Faraci, F. M.; Taguchi, H.; Heistad, D. D. *Stroke* **1995**, *26* (9), 1713–1723.

(177) Yang, Y.; Huang, J.; Yang, X.; Quan, K.; Xie, N.; Ou, M.; Tang, J.; Wang, K. *Chem. Commun.* **2016**, *52* (76), 11386–11389.

(178) Yaron, J. R.; Gangaraju, S.; Rao, M. Y.; Kong, X.; Zhang, L.; Su, F.; Tian, Y.; Glenn, H. L.; Meldrum, D. R. *Cell Death Dis.* **2015**, *6*, e1954.

(179) Yaron, J. R.; Rao, M. Y.; Gangaraju, S.; Zhang, L.; Kong, X.; Su, F.; Tian, Y.; Glenn, H. L.; Meldrum, D. R. *Biochem. Biophys. Res. Commun.* **2016**, *472* (3), 545–550.

(180) Depauw, A.; Dossi, E.; Kumar, N.; Fiorini-Debuisschert, C.; Huberfeld, G.; Ha-Thi, M.-H.; Rouach, N.; Leray, I. *Chem. – Eur. J.* **2016**, *22* (42), 14902–14911.

(181) Song, G.; Sun, R.; Du, J.; Chen, M.; Tian, Y. *Chem. Commun.* **2017**, *53* (41), 5602–5605.

(182) Specht, E. A.; Braselmann, E.; Palmer, A. E. *Annu. Rev. Physiol.* **2017**, *79* (1), 93–117.

(183) Cella Zanacchi, F.; Lavagnino, Z.; Perrone Donnorso, M.; Del Bue, A.; Furia, L.; Faretta, M.; Diaspro, A. *Nat. Methods* **2011**, *8* (12), 1047–1049.

(184) Sarder, P.; Maji, D.; Achilefu, S. *Bioconjug. Chem.* **2015**, *26* (6), 963–974.

(185) Wolfbeis, O. S. *Angew. Chem. Int. Ed.* **2013**, *52* (38), 9864–9865.

(186) S.Wolfbeis, O. *Chem. Soc. Rev.* **2015**, *44* (14), 4743–4768.

(187) Dmitriev, R. I.; Borisov, S. M.; Düssmann, H.; Sun, S.; Müller, B. J.; Prehn, J.; Baklaushev, V. P.; Klimant, I.; Papkovsky, D. B. *ACS Nano* **2015**, *9* (5), 5275–5288.

(188) Nazarenus, M.; Zhang, Q.; Soliman, M. G.; Del Pino, P.; Pelaz, B.; Carregal-Romero, S.; Rejman, J.; Rothen-Rutishauser, B.; Clift, M. J. D.; Zellner, R.; Nienhaus, G. U.; Delehanty, J. B.; Medintz, I. L.; Parak, W. J. *Beilstein J. Nanotechnol.* **2014**, *5*, 1477–1490.

(189) Pelaz, B.; Jaber, S.; de Aberasturi, D. J.; Wulf, V.; Aida, T.; de la Fuente, J. M.; Feldmann, J.; Gaub, H. E.; Josephson, L.; Kagan, C. R.; Kotov, N. A.; Liz-Marzán, L. M.; Mattoussi, H.; Mulvaney, P.; Murray, C. B.; Rogach, A. L.; Weiss, P. S.; Willner, I.; Parak, W. J. *ACS Nano* **2012**, *6* (10), 8468–8483.

(190) Nel, A. E.; Mädler, L.; Velegol, D.; Xia, T.; Hoek, E. M. V.; Somasundaran, P.; Klaessig, F.; Castranova, V.; Thompson, M. *Nat. Mater.* **2009**, *8* (7), 543–557.

(191) Sapsford, K. E.; Algar, W. R.; Berti, L.; Gemmill, K. B.; Casey, B. J.; Oh, E.; Stewart, M. H.; Medintz, I. L. *Chem. Rev.* **2013**, *113* (3), 1904–2074.

(192) Algar, W. R.; Prasuhn, D. E.; Stewart, M. H.; Jennings, T. L.; Blanco-Canosa, J. B.; Dawson, P. E.; Medintz, I. L. *Bioconjug. Chem.* **2011**, *22* (5), 825–858.

(193) Pignatello, R.; Ferro, M.; De Guidi, G.; Salemi, G.; Vandelli, M. A.; Guccione, S.; Geppi, M.; Forte, C.; Puglisi, G. *Int. J. Pharm.* **2001**, *218* (1–2), 27–42.

(194) Kondrashina, A. V.; Dmitriev, R. I.; Borisov, S. M.; Klimant, I.; O'Brien, I.; Nolan, Y. M.; Zhdanov, A. V.; Papkovsky, D. B. *Adv. Funct. Mater.* **2012**, *22* (23), 4931–4939.

(195) Dmitriev, R. I.; Papkovsky, D. B. *Methods Appl. Fluoresc.* **2015**, *3* (3), 034001.

(196) Dmitriev, R. I.; Kondrashina, A. V.; Koren, K.; Klimant, I.; Zhdanov, A. V.; Pakan, J. M. P.; McDermott, K. W.; Papkovsky, D. B. *Biomater. Sci.* **2014**, *2* (6), 853–866.

(197) Dmitriev, R. I.; Zhdanov, A. V.; Nolan, Y. M.; Papkovsky, D. B. *Biomaterials* **2013**, *34* (37), 9307–9317.

(198) Dmitriev, R. I.; Borisov, S. M.; Kondrashina, A. V.; Pakan, J. M. P.; Anilkumar, U.; Prehn, J. H. M.; Zhdanov, A. V.; McDermott, K. W.; Klimant, I.; Papkovsky, D. B. *Cell. Mol. Life Sci.* **2015**, *72* (2), 367–381.

(199) Napp, J.; Behnke, T.; Fischer, L.; Würth, C.; Wottawa, M.; Katschinski, D. M.; Alves, F.; Resch-Genger, U.; Schäferling, M. *Anal. Chem.* **2011**, *83* (23), 9039–9046.

(200) Karamchand, L.; Kim, G.; Wang, S.; Hah, H. J.; Ray, A.; Jiddou, R.; Koo Lee, Y.-E.; Philbert, M. A.; Kopelman, R. *Nanoscale* **2013**, *5* (21), 10327–10344.

(201) Koo Lee, Y.-E.; Ulbrich, E. E.; Kim, G.; Hah, H.; Strollo, C.; Fan, W.; Gurjar, R.; Koo, S.; Kopelman, R. *Anal. Chem.* **2010**, *82* (20), 8446–8455.

(202) Mahe, M. M.; Aihara, E.; Schumacher, M. A.; Zavros, Y.; Montrose, M. H.; Helmrath, M. A.; Sato, T.; Shroyer, N. F. *Curr. Protoc. Mouse Biol.* **2013**, *3* (4), 217–240.

(203) Okkelman, I. A.; Dmitriev, R. I.; Foley, T.; Papkovsky, D. B. *PLOS ONE* **2016**, *11* (12), e0167385.

(204) Dmitriev, R. I.; Papkovsky, D. B. *Methods Mol. Biol. Clifton NJ* **2015**, *1254*, 55–71.

(205) Ivanov, A. I. *Methods Mol. Biol. Clifton NJ* **2008**, *440*, 15–33.

(206) Bestvater, F.; Spiess, E.; Stobrawa, G.; Hacker, M.; Feurer, T.; Porwol, T.; Berchner-Pfannschmidt, U.; Wotzlaw, C.; Acker, H. *J. Microsc.* **2002**, *208* (Pt 2), 108–115.

(207) Pawlicki, M.; Collins, H. A.; Denning, R. G.; Anderson, H. L. *Angew. Chem. Int. Ed.* **2009**, *48* (18), 3244–3266.

(208) Tsytsarev, V.; Arakawa, H.; Borisov, S.; Pumbo, E.; Erzurumlu, R. S.; Papkovsky, D. B. *J. Neurosci. Methods* **2013**, *216* (2), 146–151.

(209) Kocsis, J. D.; Malenka, R. C.; Waxman, S. G. *J. Physiol.* **1983**, *334*, 225–244.

(210) Grinvald, A.; Hildesheim, R. *Nat. Rev. Neurosci.* **2004**, *5* (11), 874–885.

(211) Dmitriev, R. I.; Ropiak, H. M.; Yashunsky, D. V.; Ponomarev, G. V.; Zhdanov, A. V.; Papkovsky, D. B. *FEBS J.* **2010**, *277* (22), 4651–4661.

(212) Zhdanov, A. V.; Dmitriev, R. I.; Papkovsky, D. B. *Cell. Mol. Life Sci. CMLS* **2011**, *68* (5), 903–917.

(213) Dmitriev, R. I.; Papkovsky, D. B. *FEBS Lett.* **2015**, *589* (1), 138–144.

(214) Tsytsarev, V.; Maslov, K. I.; Yao, J.; Parameswar, A. R.; Demchenko, A. V.; Wang, L. V. *J. Neurosci. Methods* **2012**, *203* (1), 136–140.

(215) Zhdanov, A. V.; Okkelman, I. A.; Golubeva, A. V.; Doerr, B.; Hyland, N. P.; Melgar, S.; Shanahan, F.; Cryan, J. F.; Papkovsky, D. B. *Cell. Mol. Life Sci.* **2017**, *74* (1), 141–151.

(216) Behrendt, J. M.; Wang, Y.; Willcock, H.; Wall, L.; McCairn, M. C.; O'Reilly, R. K.; Turner, M. L. *Polym. Chem.* **2013**, *4* (5), 1333–1336.

(217) West, S. J.; Ozawa, S.; Seiler, K.; Tan, S. S. S.; Simon, W. *Anal. Chem.* **1992**, *64* (5), 533–540.

(218) Steinmann, N. Development of Optical Ammonia Sensors using Fluoroionophores. Masterthesis, Graz Unversity of Technology, Austria: Graz, Austria, **2017.**

(219) Timmer, B.; Olthuis, W.; Berg, A. van den. *Sens. Actuators B Chem.* **2005**, *107* (2), 666–677.

(220) Rhines, T. D.; Arnold, M. A. *Anal. Chim. Acta* **1990**, *231*, 231–235.

(221) Moreno, J.; Arregui, F. J.; Matias, I. R. *Sens. Actuators B Chem.* **2005**, *105* (2), 419–424.

(222) Nakano, N.; Kobayashi, Y.; Nagashima, K. *Analyst* **1994**, *119* (9), 2009–2012.

(223) Mills, A.; Wild, L.; Chang, Q. *Mikrochim. Acta* **1995**, *121* (1–4), 225–236.

(224) Preininger, C.; Mohr, G. J.; Klimant, I.; Wolfbeis, O. S. *Anal. Chim. Acta* **1996**, *334* (1–2), 113–123.

(225) Preininger, C.; Mohr, G. J. *Anal. Chim. Acta* **1997**, *342* (2–3), 207–213.

(226) Waich, K.; Mayr, T.; Klimant, I. *Meas. Sci. Technol.* **2007**, *18* (10), 3195–3201.

(227) Strobl, M.; Walcher, A.; Mayr, T.; Klimant, I.; Borisov, S. M. *Anal. Chem.* **2017**, *89* (5), 2859–2865.

(228) Waich, K.; Borisov, S.; Mayr, T.; Klimant, I. *Sens. Actuators B Chem.* **2009**, *139* (1), 132–138.

(229) Widmer, S.; Dorrestijn, M.; Camerlo, A.; Urek, Š. K.; Lobnik, A.; Housecroft, C. E.; Constable, E. C.; Scherer, L. J. *Analyst* **2014**, *139* (17), 4335–4342.

(230) Mayr, T.; Borisov, S. M.; Abel, T.; Enko, B.; Waich, K.; Mistlberger, G.; Klimant, I. *Anal. Chem.* **2009**, *81* (15), 6541–6545.

(231) Schaude, C.; Meindl, C.; Fröhlich, E.; Attard, J.; Mohr, G. J. *Talanta* **2017**, *170*, 481–487.

(232) Trinkel, M.; Trettnak, W.; Reininger, F.; Benes, R.; O'Leary, P.; Wolfbeis, O. S. *Anal. Chim. Acta* **1996**, *320* (2–3), 235–243.

(233) Werner, T.; Klimant, I.; Wolfbeis, O. S. *Analyst* **1995**, *120* (6), 1627–1631.

(234) Malins, C.; Landl, M.; Šimon, P.; MacCraith, B. D. *Sens. Actuators B Chem.* **1998**, *51* (1–3), 359–367.

(235) Grady, T.; Butler, T.; MacCraith, B. D.; Diamond, D.; McKervey, M. A. *Analyst* **1997**, *122* (8), 803–806.

(236) Lobnik, A.; Wolfbeis, O. S. *Sens. Actuators B Chem.* **1998**, *51* (1–3), 203–207.

(237) Mohr, G. J.; Nezel, T.; Spichiger-Keller, U. E. *Anal. Chim. Acta* **2000**, *414* (1–2), 181–187.

(238) Chen, X.; Dai, Y.; Li, Z.; Zhang, Z.; Wang, X. *Fresenius J. Anal. Chem.* **2001**, *370* (8), 1048–1051.

(239) Rodríguez, A. J.; Zamarreño, C. R.; Matías, I. R.; Arregui, F. J.; Cruz, R. F. D.; May-Arrioja, D. A. *Sensors* **2014**, *14* (3), 4060–4073.

(240) Duong, H. D.; Rhee, J. I. *Sens. Actuators B Chem.* **2014**, *190*, 768–774.

(241) Waich, K.; Mayr, T.; Klimant, I. *Talanta* **2008**, *77* (1), 66–72.

(242) Abel, T.; Ungerböck, B.; Klimant, I.; Mayr, T. *Chem. Cent. J.* **2012**, *6* (1), 124–124.

(243) Ozawa, S.; Hauser, P. C.; Seiler, K.; Tan, S. S. S.; Morf, W. E.; Simon, W. *Anal. Chem.* **1991**, *63* (6), 640–644.

(244) Gawley, R. E.; Pinet, S.; Cardona, C. M.; Datta, P. K.; Ren, T.; Guida, W. C.; Nydick, J.; Leblanc, R. M. *J. Am. Chem. Soc.* **2002**, *124* (45), 13448–13453.

(245) Kao, C. Y. *Algal Toxins in Seafood and Drinking Water*; Academic Press: San Diego, 1993.

(246) Hackett, J. D.; Wisecaver, J. H.; Brosnahan, M. L.; Kulis, D. M.; Anderson, D. M.; Bhattacharya, D.; Plumley, F. G.; Erdner, D. L. *Mol. Biol. Evol.* **2013**, *30* (1), 70–78.

(247) Evans, M. H. *Br. J. Pharmacol.* **1969**, *36* (3), 426–436.

(248) Cusick, K. D.; Sayler, G. S. *Mar. Drugs* **2013**, *11* (4), 991–1018.

(249) Jellett, J. F.; Marks, L. J.; Stewart, J. E.; Dorey, M. L.; Watson-Wright, W.; Lawrence, J. F. *Toxicon Off. J. Int. Soc. Toxinology* **1992**, *30* (10), 1143–1156.

(250) Bates, H. A.; Rapoport, H. *J. Agric. Food Chem.* **1975**, *23* (2), 237–239.

(251) Bates, H. A.; Kostriken, R.; Rapoport, H. *J. Agric. Food Chem.* **1978**, *26* (1), 252–254.

(252) Lawrence, J. F.; Niedzwiadek, B.; Menard, C. *J. AOAC Int.* **2004**, *87* (1), 83–100.

(253) Kyba, E. P.; Helgeson, R. C.; Madan, K.; Gokel, G. W.; Tarnowski, T. L.; Moore, S. S.; Cram, D. J. *J. Am. Chem. Soc.* **1977**, *99* (8), 2564–2571.

(254) Gawley, R. E.; Zhang, Q.; Higgs, P. I.; Wang, S.; Leblanc, R. M. *Tetrahedron Lett.* **1999**, *40* (30), 5461–5465.

(255) Kele, P.; Orbulescu, J.; Calhoun, T. L.; Gawley, R. E.; Leblanc, R. M. *Tetrahedron Lett.* **2002**, *43* (25), 4413–4416.

(256) Kele, P.; Orbulescu, J.; Gawley, R. E.; Leblanc, R. M. *Chem. Commun. Camb. Engl.* **2006**, No. 14, 1494–1496.

(257) Orbulescu, J.; Kele, P.; Kotschy, A.; Leblanc, R. M. *J. Mater. Chem.* **2005**, *15* (30), 3084–3084.

(258) Gawley, R. E.; Shanmugasundaram, M.; Thorne, J. B.; Tarkka, R. M. *Toxicon Off. J. Int. Soc. Toxinology* **2005**, *45* (6), 783–787.

(259) Gawley, R. E.; Mao, H.; Haque, M. M.; Thorne, J. B.; Pharr, J. S. *J. Org. Chem.* **2007**, *72* (6), 2187–2191.

(260) Indrasena, W. M.; Gill, T. A. *Anal. Biochem.* **1998**, *264* (2), 230–236.

(261) Jf, L.; C, M.; Cf, C.; S, H. *J. - Assoc. Off. Anal. Chem.* **1990**, *74* (2), 404–409.

(262) Kochevar, I. E.; Redmond, R. W. *Methods Enzymol.* **2000**, *319*, 20–28.

(263) DeRosa, M. C.; Crutchley, R. J. *Coord. Chem. Rev.* **2002**, *233*, 351–371.

(264) Paczkowski, J.; Lamberts, J. J. M.; Paczkowska, B.; Neckers, D. C. *J. Free Radic. Biol. Med.* **1985**, *1* (5), 341–351.